

Electronic and optical properties of nanomaterials

- PhD thesis -

by Ferdinand Schulz

2013



University of Osnabrueck

Physics Department

Contents

1. Introduction	
1.1 Graphene	5
1.2 Carbon nanotubes	14
1.3 Basic electronic structure of graphene and carbon nanotubes	23
2. Theoretical background	
2.1 DFT	28
2.2 GWA	32
2.3 Bethe-Salpeter equation and optical spectrum	35
3. Planar nanostructures of various materials	
3.1 Graphene	40
3.2 Boron nitride, boron arsenide and boron phosphide	44
3.3 Optoelectronic materials: AlN, AlAs, AlP and GaN	55
3.4 SiC and GeC	68
4. Nanotubes and nanoribbons	
4.1 Carbon nanotubes	75
4.2 Boron nitride, boron arsenide and boron phosphide nanotubes	84
4.3 Nanotubes of optoelectronic materials	106
4.4 SiC and GeC nanotubes	133
5. Heterostructures of nanomaterials	
5.1 Boron nitride embedded in graphene	147
5.2 GaN embedded in planar AlN	155
6. Summary	164
7. References	166

1. Introduction

Nanotechnology plays a crucial role nowadays for high tech industries of all sectors , ranging from new promising materials which weigh less but are stronger and capable, new optical devices to innovative approaches to biotechnology. It can be seen as new revolution in materials science after the discovery of synthetic materials like plastic, polyethylene or kevlar. But what exactly means nanotechnology or nanomaterials ? One already knows from media that it is about small particles with amazing properties. But speaking precisely in terms of solid state physics, the fundamental difference between conventional materials and nano materials ist that nano materials exhibit a characteristic microstructure. In contrast to crystals like diamond or silicon, where the atoms in the unit cell replicate in all three room directions x,y,z , in the case of nanomaterials atoms only propagate periodically in for example one or two directions. Famous examples for this are carbon nanotubes and the Nobel-prize winning graphene. In carbon nanotubes, atoms arrange cylindrically and propagate only in one direction, and in graphene atoms arrange hexagonally in a one-layer plane. Both are based on graphite, but their special microscopic structure causes properties which are far superior to graphite.

The materials which get most attention from science are definitely carbon-based systems, namely graphene and carbon-nanotubes. But the correspondence between diamond as conventional crystal on one side and graphene and carbon nanotubes as corresponding nanostructures can be extended to a vast class of other materials. The main goal of my work is to investigate the properties of nanostructures resulting from important bulk crystals such as GaN, AlAs, silicon In order to accomplish to this , I will make use of theoretical methods and computer simulation, more precisely ab initio methods. This provides the big advantage of making first predictions about materials behavior without laboratory . Especially for these system this is quite helpful because the systems regarded here are very challenging in their experimental measurement and in their synthesis . Also companies nowadays make heavy use of ab initio software to investigate novel materials, famous examples include Acceryls Materials studio [1] and Quantum Wise [2] . Experimental methods would require a lot of time and money, whereas computer simulation provides realistic predictions in a very fast time.

The theoretical methods used in this work are mainly density functional theory (DFT) and many body perturbation theory (MBPT) . If one would simply use the Schrödinger equation based on the potential of the lattice, the electric interaction between the electrons in the system would be totally neglected, and this would cause unrealistic results. The electron-electron interaction plays a decisive role in theoretical solid state physics. The first step in our calculations is DFT [3] , which still handles the problem in one particle formalism, but

adds a correction term to the Hamiltonian, which is calculated by self consistent iteration. In the next chapter this will be discussed in more detail. But experiments have shown that the DFT method systematically underestimates the band gap of semiconductors. One of the fundamental reasons for this is that DFT was developed mainly for obtaining the electronic structure of the ground state, using a very simplified model for the electron-electron interaction. Excited states are not the primary aim of DFT.

A more advanced method, which corrects DFT, is the so called GW-approximation (GWA). This approach initially considers the electron-electron interaction in its full two-particle Fock-space representation. Similar to DFT, a one particle expression is derived for the electron-electron interaction, but the term used by GWA yields much better results for the electronic structure above the ground state. One first calculates the band structure by DFT, and based on the obtained results corrections from GWA are added. Having calculated the GWA band structure of a system, one has already a solid and realistic basis for the electron structure of the system. The final step in the calculations carried out in this work is inserting the resulting electronic bands in the so called Bethe-Salpeter-equation (BSE). In contrast to DFT and GWA, the Bethe Salpeter equation treats the electron-electron interaction explicitly in two-particle formalism, and the coulomb interaction between electrons is investigated in its full form in Fock space representation. The only restriction made by BSE is that only the interaction between electrons and holes is taken into account, which expresses formally in the way that only product states between valence and conduction bands are regarded. The reason for this is that the main focus of interest in BSE are electron-hole excitations. Additionally, BSE is mainly restricted to semiconductors because its is based on electron-hole excitations, and consequently only semiconducting system are considered in my work. Based on the energy eigenvalues, many body eigenstates and matrix elements received from solving the BSE, one is able to calculate the optical spectrum by using the dipole operator.

The main program package used in this work is Exciton [4], [5]. Excitons main areas of application are DFT, GWA and BSE calculation, with final calculation of the optical spectrum. It is written in Fortran and conceived for use on parallel computation on clusters. For the numerical setup Gaussian orbitals as well as plane wave basis sets are used. I preferred Gaussian orbitals for DFT calculations and plane waves for GWA due to better numerical efficiency. More details about the program Exciton are specified in [6].

The second program package used here is the well known program SIESTA [7]. Its main capabilities consist of self-consistent DFT electronic band structure and also geometry optimization. The later capability is the one being most important for this work. Starting with a given unit cell and atomic positions, and corrects and optimizes the atomic positions to make them physical reasonable. The underlying principle behind this is relaxation of the atomic coordinates, because in nature physically stable states are those having the minimum total energy. Based on this, the program executes a variation of atomic coordinates in order to minimize total energy, where the total energy is regarded as functional of the atoms position. The numerical procedure used is the conjugate-gradient method. Relaxing the atoms positions is crucial if one considers defects, because one does not know the exact structure of the unit cell in those cases. Therefore one inserts the defect atoms at the

planned positions, and SIESTA provides the exact structure of all atoms in the unit cell after relaxation.

In the first chapter of the work an introduction to Nanotechnology and basic electronic properties of graphene and carbon nanotubes is given. Following this, the second chapter describes the theoretical methods used here in detail. Then the third chapter presents the results obtained for graphene and graphene-like planar nanostructures, and the chapter four discusses the properties of carbon nanotubes and nanotubes from other materials. Finally, chapter five deals with defects and heterostructures of planar nanomaterials

1.1 Graphene

The new wonder material graphene draws a lot of attention from media because its amazing physical properties with give it great prospects for new applications. Recently, in 2010, Andre Geim and Konstantin Novoselov were awarded with Nobel Prize in Physics for their ground-breaking work about graphene [8]. They succeeded in isolating single graphene layers from graphite and transferred the graphene on top of SiO₂ of silicon wafer [9]. This process was decisive because SiO₂ is electrically insulating and does not influence graphene electronics, in contrast to graphene epitaxially grown on other substrates. Before that graphene could only be grown on substrates with significantly distort the electronic structure of it, and this process was used since the 1970s [10]. But the history of graphene started much earlier. In 1947, P.R Wallace investigated the electronic structure of graphene [11], but of course he did not regard it in our modern view as graphene, but rather as one layer of graphite. The term graphene was invented by Hans-Peter Boehm [12], who combined graphite with the suffix -ene when describing single layer carbon foils in 1962 [13].

Precisely speaking, graphene is one layer honeycomb lattice with an interatomic distance of approximately 0.142 nanometers [14]. The carbon atoms are chemically bonded by the sp²-bond [15], which causes a strong chemical bond between the atoms. Naturally graphene always occurs in graphite, because one layer of graphite is nothing else than graphene, but not freestanding.

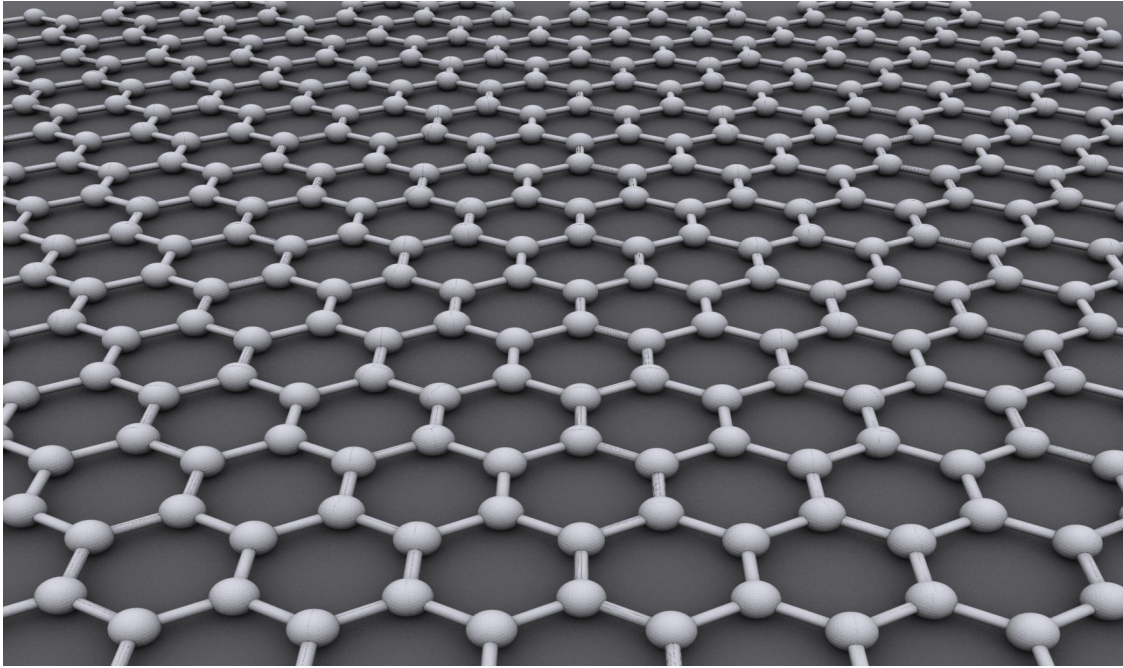


Figure 1.1 Graphene, taken from Wikipedia

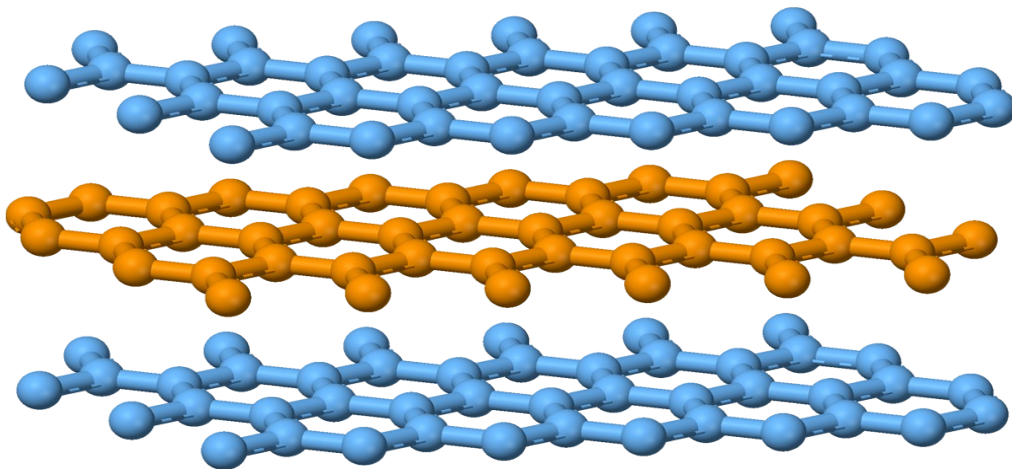


Figure 1.2 Graphite, taken from Wikipedia

But in order to be stable, theoretical calculations predict that the graphene sheet should at least have the size of 20nm, and it becomes most stable when containing over 24,000 carbon atoms [16].

The most striking aspect of graphenes properties is its zero band gap. Thus is electronically a zero band gap semiconductor or semimetal, which means its behavior is close to that of

a semiconductor, but at the same time also close to that of a metal. Experiments revealed that graphene possesses a very high electron mobility at room temperature, exceeding $15,000 \text{ cm}^2/(\text{V}\cdot\text{s})$ [15]. Symmetry of the experimentally measured conductance indicates that the mobility for electrons and holes is nearly equal [17].

Applications

Furthermore, graphene exhibits interesting optical properties. It absorbs white light at a rate of approximately 2.3%, which is much more than one would expect for monolayer material containing a lot of vacuum [18]. But graphene's optical absorption can be saturated if the input intensity is high enough, which takes place for the visible to infrared spectrum. This effect is called saturable absorption, and it's very important for mode locking in fiber lasers. A graphene-based saturable absorber has already been realized for fullband mode locking. See [19], [20]. Saturable absorption is also expected to occur in the microwave and Terahertz band, which might lead to applications for graphene in modulators, polarizers, microwave signal processing and broad band wireless network access networks [21]. Moreover, graphene offers possibility for electrochromic devices because its optical and electronic properties can be tuned electrically [22,23] as follows: Electric stimulus controls oxidation and reduction of graphene, and the grade of oxidation influences the electronic and optical properties of it. Additionally, a photonic crystal based on graphene has been manufactured, using a 633 nm He-Ne laser as the light source. [24]

The mechanical behavior of graphene is amazing as well, as it seems to be the strongest material available today. Graphene proved to have a breaking strength more than 100 times more than a steel film with the same thickness in experiments [25], and it has a tensile modulus of 1 TPa [26]. It is a very light material, weighing only 0.77 milligrams per square metre, but the Nobel announcement illustrated its strength but stating that 1 square meter graphene hammock would support a 4 kg cat with a weight similar to that of one of the cat's whiskers, 0.77 mg [25]. But the most problematic circumstance hindering graphene's commercial applications is its very costly manufacture [27], but recent developments could change this soon [28]. Graphene has been processed into a form of paper, called graphene paper (GP), by a research department from the University of Technology Sydney. Lead Researcher Ali Reza Ranjbari commented: "The exceptional mechanical properties of synthesised GP render it a promising material for commercial and engineering applications. "Not only is it lighter, stronger, harder and more flexible than steel it is also a recyclable and sustainable manufacturable product that is eco-friendly and cost effective in its use." [29]. The results would allow for lighter and stronger cars and planes using less fuel and generating less pollution, as well as being cheaper to run and being ecologically sustainable. As large aerospace companies have already started to use carbon fibers and carbon-based materials, graphene paper could be the next material of interest.

One of the most interesting applications of graphene is its use for field effect transistors. Due to its high carrier mobility and low noise, graphene is considered as channel in field effect transistors. Thus researchers are looking for ways to transfer graphene to the substrate of interest [30]. In 2008 the smallest transistor so far consisting of only one atom in thickness

and 10 atoms in width was produced [31]. Graphene transistors operating at GHz frequencies were fabricated and characterized by IBM in December 2008 [32]. P-type as well as n-type graphene processors have been achieved in May 2009 [33]. Finally, a complementary inverter containing n-type and p-type graphene was reported [34].

Another possible application of graphene is its use as transparent conductor, which means a material which lets light pass through freely as well as conducting well electrically. Graphene's high electrical conductivity and high optical transparency make it suitable for that. Concrete areas of application could be touchscreens, LCDs and organic light-emitting diodes (OLEDs). In comparison to indium tin oxide, which is used today for those purposes, graphene exhibits superior mechanical properties, for example higher mechanical strength and better flexibility, and also graphene films can be deposited from solution over large areas [35], [36]. In practice, an OLED with a graphene anode has been constructed [37].

Additionally, graphene has drawn attention regarding photovoltaics. As mentioned before, graphene is a transparent conductor, which means it can be used as for transporting electric current in solar systems without absorbing the incoming light [38]. But graphene might also work as photoactive material in solar cells. In its natural state, graphene is not suitable for this due to its zero bandgap, but if its bandgap is tuned up to 1.4-1.9 eV, it can be used as photoactive material. Solar cells incorporating metallic graphene as conductive electrodes and semiconducting graphene as photoactive material are proposed by P. Mukhopadhyay and R. K. Gupta [39]. Research from the Institute of Photonics Sciences (ICFO) in Spain has revealed that graphene could transform light into energy much more efficiently than the current standard material silicon. In contrast to silicon generation only one current driving electron per absorbed photon, graphene can produce multiple electrons for each absorbed photon. So solar cells based on graphene might offer an efficiency of 60%, which is twice of the maximum theoretical efficiency of silicon based systems [40].

Moreover, another application where graphene might provide an excellent material for are sensors, especially sensors for detecting gaseous molecules. In contrast to ordinary solids filling space in all three dimensions, graphene has a 2-dimensional structure with a lot of vacuum surrounding it, which means it possesses much more contact points with incoming gas molecules. But unfortunately, graphene in its pure form cannot absorb molecules due to the lack of dangling points on its surface [41]. This obstacle can be overcome by functionalizing graphene by coating it with a thin polymer layer, which absorbs the gaseous molecules. The absorption locally changes the electrical resistance of graphene, which is very advantageous for electrical measurements because of its high electrical conductivity and low noise [42].

Another very important field of graphene's technological use is energy storage. Its extremely high surface area to mass ratio suggests to use it as material for the conductive plates of ultracapacitors. Such ultracapacitors are believed to surpass the current ultracapacitors in terms of energy storage density [43].

Finally, graphene offers amazing possibilities for use in biotechnology. Due to its large

surface area, atomic thickness as well as its modifiable chemistry and molecularly gatable structure, graphene sheets can be functionalized by antibodies for microbial and mammalian detection and diagnosis devices [44] . But the most biomedical ambitious application graphene is considered for is rapid electronic DNA sequencing. This could be performed by integration of graphene layers as nanoelectrodes into a nanopore [45] .

Production

Despite of all mentioned great things graphene can do, the biggest challenge which must be handled for its use is its production. At the moment graphene can only be synthesized at low rates and its very costly. Therefore productions methods fill in a fundamental role for graphene technologies, and I present some of the in the following :

- The first method to obtain is the one which was used in the Nobel prize for graphene. This method, called exfoliation, takes a graphite flake and puts the sticky side of a plastic adhesive tape over the flake, and the pulls the tape away with the graphite caught by the tape, splitting the graphite flake up. By repeating the process, the resulting fragments become smaller and smaller to the point when the fragments contain single layers graphite, which is just graphene [46] .



Figure 1.3 Graphene, a graphene transistor and the tape used by Andre Geim (Nobel museum Stockholm)

The tape with graphite flakes containing graphene are dissolved in acetone, and after few further steps, these are sedimented on a silicon wafer. The the monolayer graphene are searched using an optical microscope. This procedure was simplified one year later avoiding the solution of the graphite flakes in liquid, and it become possible to obtain relatively large crystallites through this. It is also called scotch tape or drawing method [47] .

- Heating up silicon carbide (SiC) at high temperatures ($> 1,100$ Celsius) under low pressure (ca. $10e-6$ torr) results in exptixial growth of graphene [48] . The dimensions of grown graphene depend on SiC substrate, and the face of the SiC substrate used plays a crucial role thickness, mobility and carrier density of the obtained graphene. This production

method was important for observing many important properties like for example its electronic band structure, which was first visualized with graphene obtained by this method [49], [50], [51].

- Graphene can also be obtained by sonication of graphite dissolved in a proper liquid. The remaining non-graphene compounds can be removed using centrifugation. This was realized first by Hernandez et al. [52]. but later was later heavily improved by other groups, especially by the Italian group of Alberto Mariani [53]. Mariani's group attained the highest concentration of graphene in a liquid by using suitable ionic liquid as dissolving medium, namely 5.33mg/ml [54].
- Furthermore, burning magnesium in dry ice (carbon dioxide) causes graphene sheets formation, which was reported by Narayan Hosmane from Northern Illinois University in the United States 2011 in a paper [55]. Following this, the company Graphene Technologies has developed a process for scalable production of graphene making use of endothermic reactions between Group I and II and carbon-containing gases [56].
- At last, graphite oxide draws lot of attention concerning graphene synthesis. Graphite oxide is hydrophilic, and, when dissolving in water, breaks up into flakes which are mostly only one atomic layer thick (!!!). Those flakes are not far away from being graphene, they just need to be chemically reduced. This can be achieved by exposing them to hydrazine [57], hydrogen plasma [58] or Xenon flash [59]. However, these methods cause defects in the resulting graphene, which has much lower conductivity than expected [60]. Treating the graphite oxide flakes with a DVD laser provides high quality graphene at low cost [61].

But graphene, as mentioned at the beginning, is not the only planar nanomaterial of interest for research. For example, boron nitride also forms hexagonal planar structures, called nanomesh, which were discovered first at the University of Zurich, Switzerland, in 2003 [62]. Exposing rhodium or ruthenium to borazine under ultra-high vacuum at high temperatures leads to self assembled formation of nanomesh sheets. Its structure is the same like that of graphene, but instead of carbon atoms, boron and nitride are arranged alternating in a hexagonal lattice :

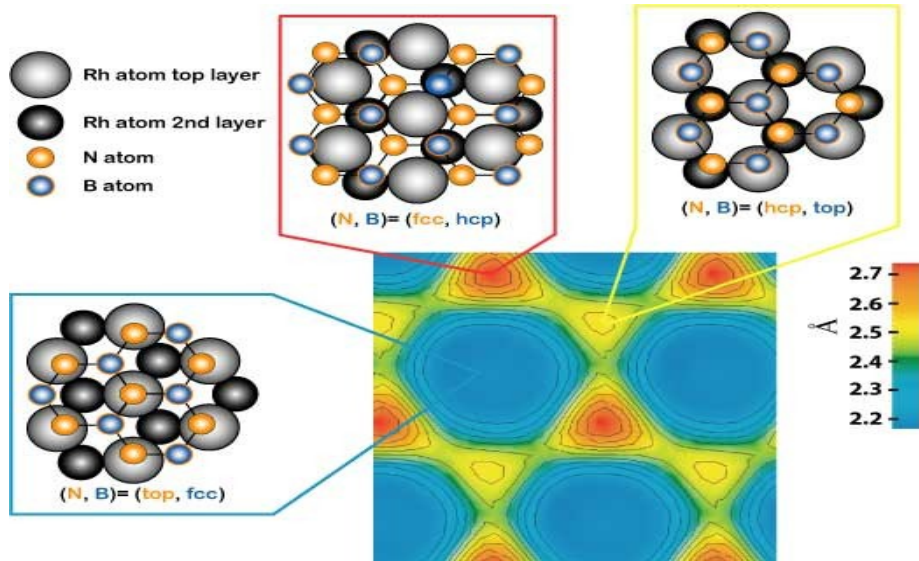


Figure 1.4 Boron nitride nanomesh grown on ruthenium , taken from Wikipedia (Dr. Peter Blaha)

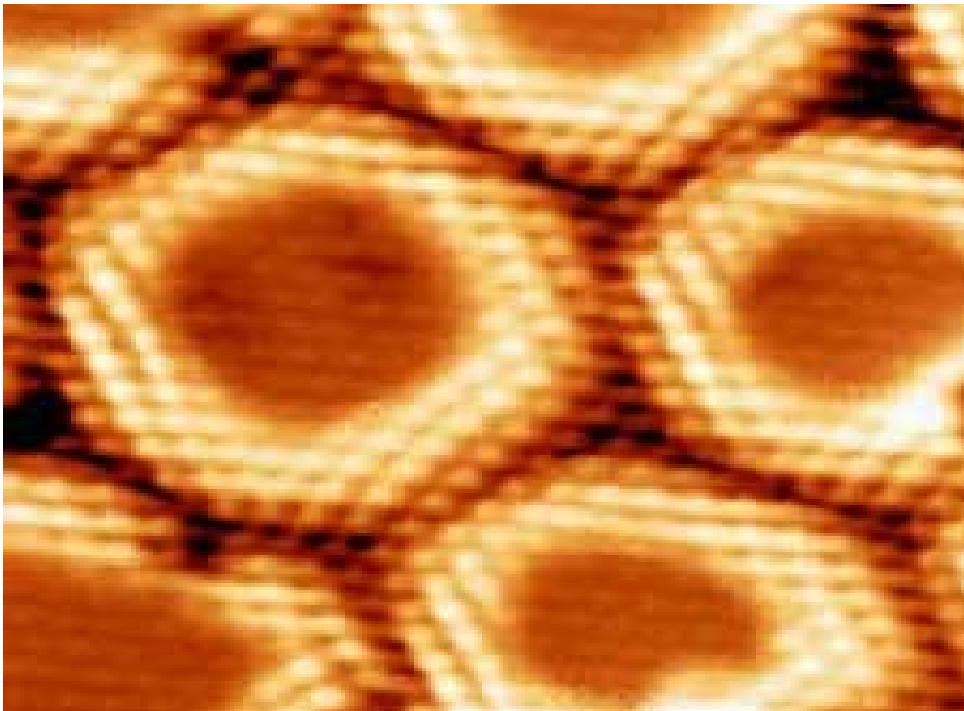


Figure 1.5 STM image of nanomesh, taken from Wikipedia (Martina Corso and Roland Widmer)

Due to its wide space between planar sheets and negligible interplanar interaction, nano-mesh might be of interests for applications regarding molecular electronics, memory elements, photochemistry and optical devices [63], [64], [65]. Additionally, graphene-like nanostructures of silicon are considered by science. Hexagonal monolayers have been assumed theoretically some time ago [66], and were observed experimentally by growth on Ag(111) [67], [68]. The term used for them is *silicene*, analogous to graphene. Theoretical calculations suggest that silicene might be very useful as field effect transistor and also for hydrogen storage [69].

1.2 Carbon Nanotubes

Carbon nanotubes are one dimensional nanostructures where carbon atoms arranged hexagonally form a hollow cylinder. They derive from planar graphene, because they can be thought as graphene sheet rolled up to a hollow cylinder. In order to specify them, a pair of integers (n,m) called *chirality* are used. They determine the way graphene sheets are rolled up to build the nanotube. The image below illustrates this:

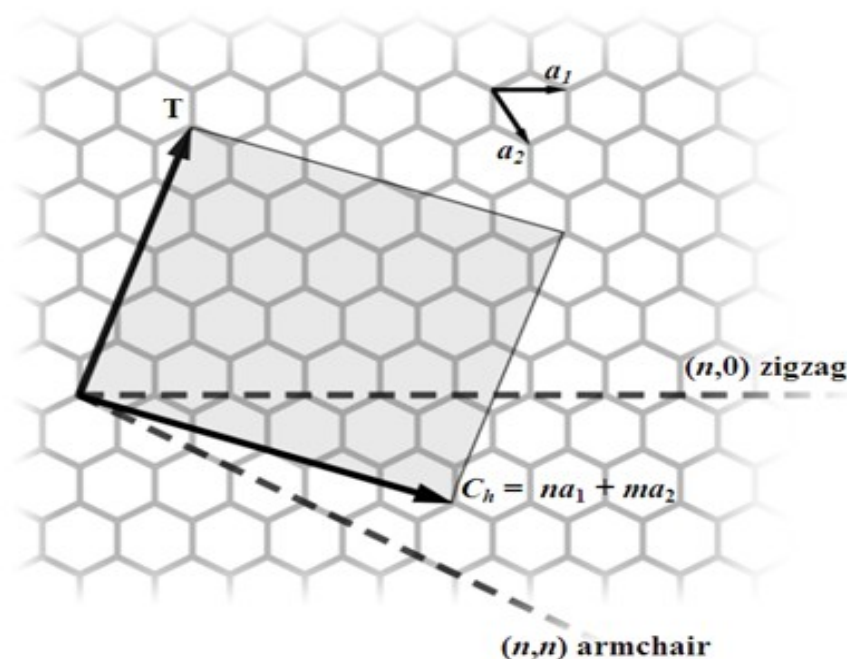


Figure 1.6 Nanotube chirality, taken from Wikipedia

Here a a_1 and a_2 denote the hexagonal lattice vectors of planar graphene. The carbon nanotube is obtained by rolling up graphene along the chiral vector C_h given by

$$C_h = n \cdot a_1 + m \cdot a_2 \quad (1.1)$$

Following this, the nanotubes diameter d is

$$d = \frac{|C_h|}{\pi} = \frac{a}{\pi} \cdot \sqrt{n^2 + nm + m^2} \quad (1.2)$$

with $a = \sqrt{3} \cdot a_{cc}$, where a_{cc} denotes the interatomic of graphene, which is approximately

$$a_{cc} \approx 1.42 \text{ \AA} \quad (1.3)$$

There two often considered cases of nanotubes, which are called *armchair* and *zigzag*. Armchair nanotubes are given in the case that $n = m$, and zigzag in the case $m = 0$. They take the form (n,n) and $(n,0)$, respectively. Below are visualizations

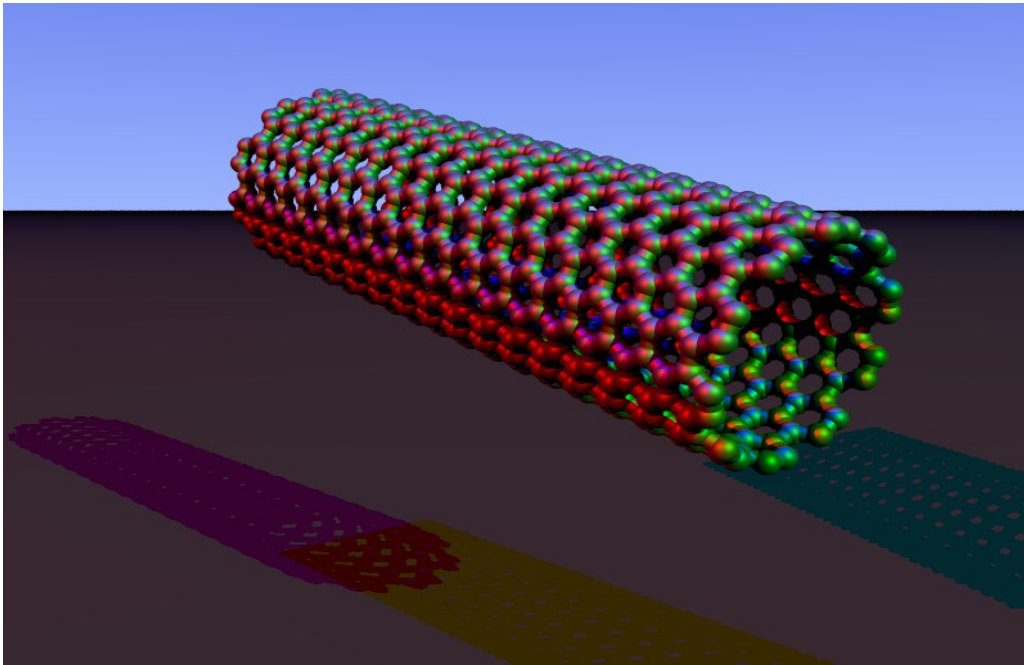


Figure 1.7 Armchair nanotube, taken from Wikipedia

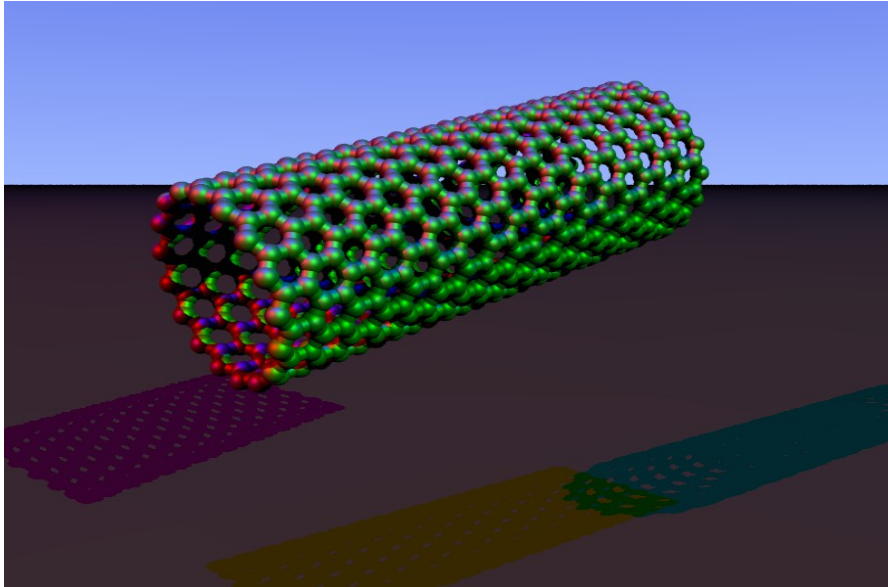


Figure 1.8 Zigzag nanotube, taken from Wikipedia

Later we will see that armchair and zigzag differ significantly in their electronic structure. But carbon nanotubes can also occur *multi-walled*, which means that multiple nanotubes sit inside each other :

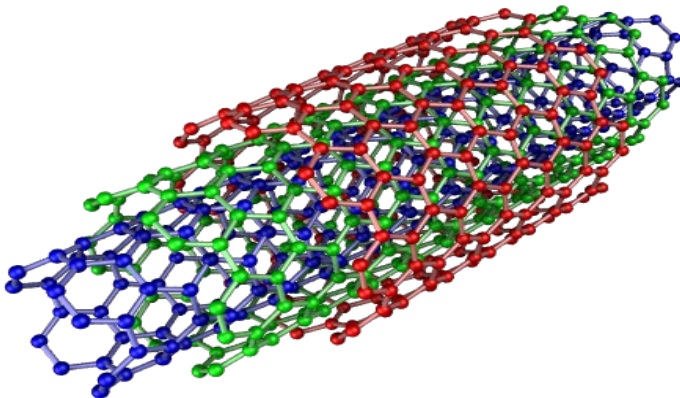


Figure 1.9 Multi-walled nanotube, taken from Wikipedia

In this work, I only investigate single-walled nanotubes . Another important structures related to nanotubes are nanoribbons. They can be viewed as rolled out nanotubes or as stripes from graphene. In order to describe them, the same specifications (n,m) as for nanotubes are used.

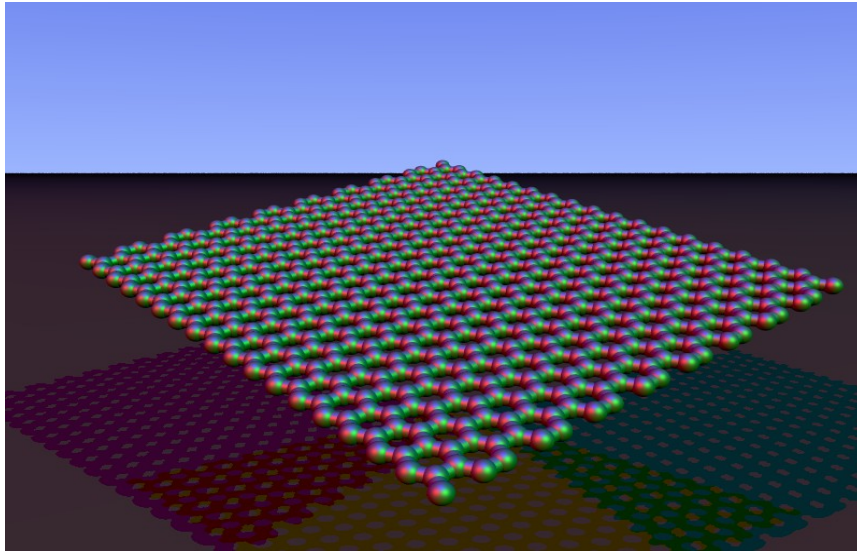


Figure 1.10 Nanoribbon, from Wikipedia

The discovery of nanotubes is very interesting and there is a lot of discussion about it. Mostly, the discovery of carbon nanotubes is credited for Sumio Iijima who described carbon nanotubes in 1991. But this is not 100% correct, as pointed out in an editorial written by Marc Monthieux and Vladimir Kuznetsov in the journal *Carbon* in 2006 [70]. Detection of carbon nanotubes tube structures dates back to 1952, when L.V. Radushkevich and V.M.Lukyanovich published images of tubes of carbon atoms with a diameter of 50nm in the Soviet Journal of Physical Chemistry [71]. The publication was written in Russian and the Cold War prevented science from the West to notice him. Later, in 1979, John Abrahamson revealed carbon nanotubes in a conference paper at the 14th Biennial Conference of carbon at Pennsylvania State University. He obtained them from carbon anodes during arc discharge, but instead of calling them nanotubes, he referred to them as carbon fibers [72]. In 1981, a group of Soviet scientists produced carbon nanotubes by thermocatalytical disproportionation of carbon monoxide. After evaluating the TEM images X-ray patterns, they depicted them "carbon multilayer tubular crystals". They suggested that they are formed by rolling up graphene layers in different configurations, namely circular (armchair) and spiral (general (n,m)) [73].

One of the most famous aspects of carbon nanotubes are their excellent mechanical properties. Due to their strong covalent sp^2 bonds, their tensile strength and elastic modulus exceed conventional materials by far. For instance, in 2000 a multiwalled carbon nanotube was measured to possess a tensile strength of 63 gigapascals [74]. Another study in 2008 showed that individual carbon nanotubes can have strengths up to 100 GPa, as expected from theoretical calculations [75]. Despite having a low density of only 1.3-1.4 g/cm^3 , they exhibit a specific strength ranging up to 48,000 kNm/kg , which is the best of currently available materials, whereas high carbon steel only has 154 kNm/kg [76]. Furthermore, carbon nanotubes hardness is amazing. They prove to have a bulk modulus of 462 to 546 GPa, exceeding even diamond which has 420 GPa [77].

The electronic structure of nanotubes strongly depends on their chirality, and can be predicted by her. If for a given chirality (n,m) the difference $n-m$ is a multiple of 3, then the nanotube shows metallic behavior, otherwise it is a semiconductor [78]. This will be discussed later in this work. But this approach is only very basic and neglects curvature effects, and therefore sometimes fails for nanotubes with small diameters. For example, a $(5,0)$ nanotube should be expected to be semiconducting using this approach, but experiments reveal that this nanotube is metallic in fact.

Furthermore, nanotubes exhibit interesting thermal properties. Along their axis, they prove to be very good thermal conductors, following the so called "ballistic conduction" regime. Experiments showed that a single-walled nanotube has a room temperature thermal conductivity of around $3500 \text{ W}/(\text{m}\cdot\text{K})$ along its axis, exceeding the thermal conductivity of the well known good thermal conductor copper by far, which only has $385 \text{ W}/(\text{m}\cdot\text{K})$ [79]. In contrast to this, the thermal conductivity of them across their axis is only about $\text{W}/(\text{m}\cdot\text{K})$, comparable to that of soil [80]. Carbon nanotubes are thermally stable at temperatures up to 2800 Celsius in vacuum and 750 Celsius in air [81].

Applications

Like graphene, carbon nanotubes promise a lot of applications. For instance, they offer great potential for new strong materials. They have already been used as composite fibers in polymers in order to improve their strength. Zyvex Technologies has built a 54' maritime vessel, called the Piranha Unmanned Surface Vessel, significantly improving its structural perforce through use of carbon nanotubes. The boats weighs only 8,000 lb, but it can carry a payload of 15,000 lb over a range of 2,500 miles [82]. Additionally, Amroy Europe Oy produces carbon nanoepoxy resins incorporating carbon nanotubes under the trademark Hybonite, which are up to 30% stronger than other composite materials. Its areas of applications already include wind turbines, marine paints and a lot of sport equipment like skis, ice hockey sticks, baseball bats, hunting arrows and surfboards [83]. Moreover, carbon nanotubes are proposed for use in clothes, combat jacktes and even in space elevators due to their superior mechanical properties [84]. However, their use in space elevators still requires a lot of technological development. Ballistic vests containing carbon nanotubes for better protection against gunfire are under development [85].

Another possible application of carbon nanoutubes are field-effect transistors based on them, called carbon nanotube field effect transistors (CNTFETs). They have been demonstrated at room temperature and can perform digital switching using only one electron [86]. But one very big challenge for their production is to separate metallic nanotubes away from semiconducting ones, because semiconductors are desired for use. IBM found a way to handle this problem in 2001, called "constructive destruction", which automatically destroys metallic nanotubes on the wafer [87]. However, carbon nanotubes are far away from replacing conventional CMOS technology.

Furthermore, nanotubes can be used to manufacture new kind of superior wires and cables. Wires based on carbon nanotubes and nanotube-polymer have been realized which show

a specific conductivity exceeding that of copper and aluminum [88], [89] .

Another amazing applications of nanotubes is their use in a new class of batteries, called *paper batteries* . They consist of cellulose which fill up the space, and carbon nanotubes act as electrodes [90] . Lithium ions fill the role as electrolyte. Those batteries exhibit many advantages over existing batteries, as there are light, thin and flexible. If they can be produced in newspaper size , they would provide enough energy to power a car [91] . In addition, carbon nanotube electrodes can improve the efficiency of ultracapacitors according to research having been made by MIT Laboratory for Electromagnetic and Electronic Systems [92] .

Moreover, carbon nanotubes draw attention regarding their use for military. Multi-walled carbon nanotubes can absorb microwaves and are therefore useful as radar-absorbing material. The University of Michigan investigated the application of carbon nanotubes for stealth technologies, and they found that carbon nanotubes not only absorb light, but also do not reflect or scatter visible light, which makes aircrafts hard to see. In practice, carbon nanotubes could be painted on an aircraft [93] .

Nanotubes play a crucial role for constructing microsystems and micromachines. For instance, a new memory device based on carbon nanotubes called *NRAM* has been invented by the company Nantero Inc. [94] . In this memory device, 0 and 1 are represented by high or low electrical resistivity of two carbon nanotubes. In each memory unit, there are two carbon nanotubes. In the 1 state, they are connected and therefore conduct electricity well, whereas in the 0 state, they stay separated from each other and have low electrical conductivity.

In addition, nanomotors can be constructed using carbon nanotubes. These motors are very small, at magnitude of molecules, and generate very small forces down to the order of piconewtons [95], [96] . First approaches used thermal gradient principles to control motion, but these have some drawbacks compared to other micromotors. A new technology, called *Electron windmill* has overcome many obstacles and largely improved nanotube motors. An electron windmill consists of an outer (18,0) carbon nanotube and an inner (6,4) inner carbon nanotube, and applying a voltage causes a wind of electrons. When interacting with the inner nanotube, these electrons get an angular momentum and therefore produce a tangential force on the inner nanotube causing it to rotate [97] . No metallic plates or gates are needed. This approach is very promising for further applications.

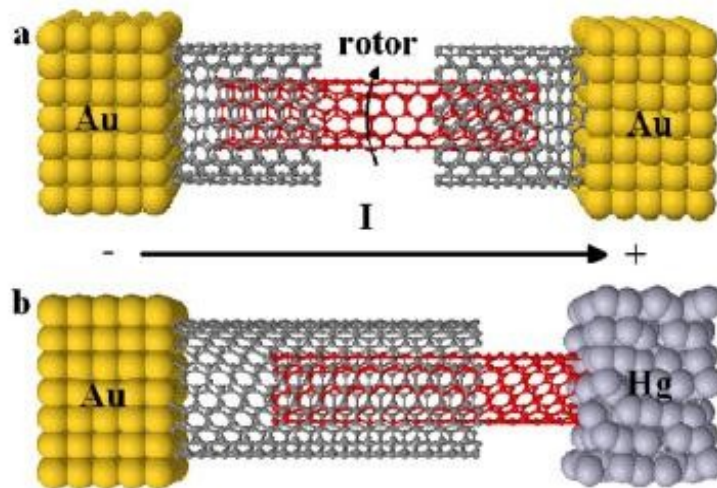


Figure 1.11 Conventional nanotube motor and electron windmill below, taken from S. W. D., Bailey, I. Amanatidis and C. J. Lambert (2008). "Carbon Nanotube Electron Windmills: A Novel Design for Nanomotors". *Physical Review Letters* 256802: 1-4.

Apart from that, carbon nanotubes also draw attention for their use as transparent conductors in touchscreens and flexible displays. Eikos Inc. in Franklin, Massachusetts and Unidym Inc. are working on carbon nanotube films in order to replace indium tin oxide (ITO). Printable water-based inks of carbon nanotubes are under development [98].

Finally, another amazing application of carbon nanotubes could be store energy mechanically. Flywheels can store huge amounts of energy when they rotate at very high speeds in vacuum suspended by magnetic bearings, from 20,000 to over 50,000 rpm [99]. Carbon nanotubes excellent strength would enable flywheels made with carbon nanotubes to rotate at extremely high speeds. Energy can be taken from the flywheels very efficiently by using electromagnetic fields. Furthermore, carbon nanotube springs can store big amounts of energy can exceed that of lithium ion batteries [100].

Production

But in order to realize all those amazing applications, production methods for carbon nanotubes are essential. One very important method of synthesizing carbon is *chemical vapor deposition* (CVD)- This method was used first in 1993 in order to produce carbon nanotubes [101]. In CVD, the carbon nanotubes are grown on a substrate using metal nanoparticles as catalysts, which pull out a nanotube getting longer and longer.

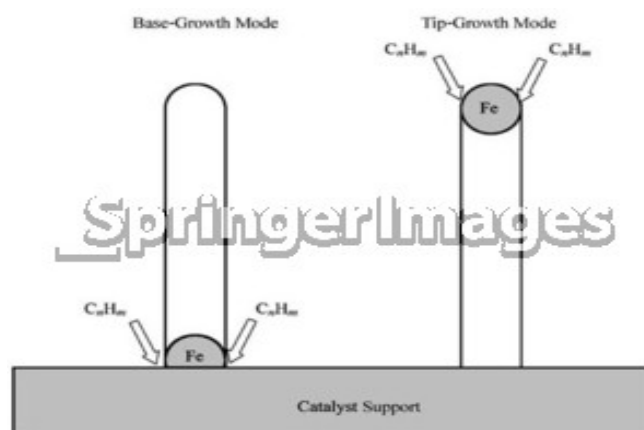


Figure 1.12 CVD carbon nanotube growth, taken from Springer Images

At the beginning, a substrate is prepared with the nanoparticle catalysts. The the substrate is heated up to 700 Celsius , and a carbon containing gas like methane, ethanol or acetylene flows into to reactor together with a process gas, for example, ammonia, nitrogen or hydrogen. Carbon breaks away from the gas and starts forming nanotubes at the metal nanoparticles [102] . Depending on the adhesion between the catalyst particles and the substrate, the catalyst nanoparticles either remain on the bottom of the substrate, or move into the direction of growth, drawing the growing carbon nanotube behind itself [103] . See Figure 1.12 for illustration. The metals used as catalysts are mostly nickel, cobalt and iron [104] , or a combination [105] . The diameter of the grown nanotubes is influenced by the size of the carbon nanoparticles.

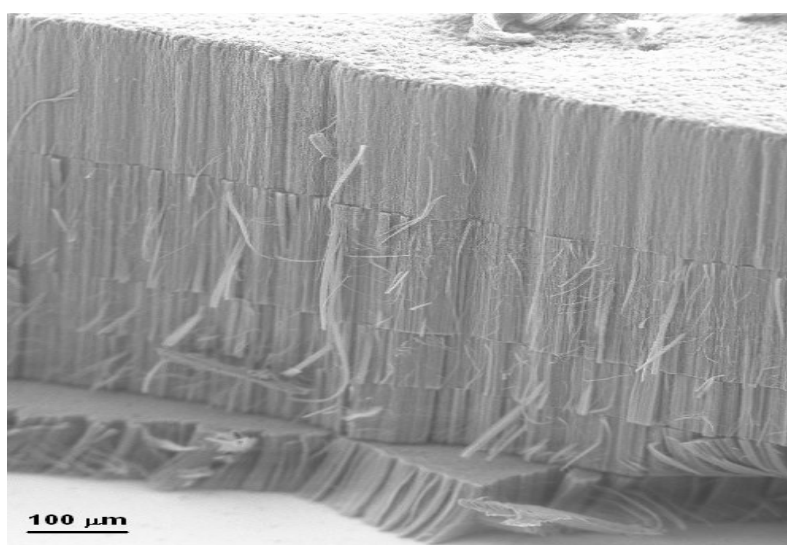


Figure 1.13 Image of carbon nanotubes grown on substrate, taken from nanotechweb.org (2006)

Adding water to the process can significantly improve the growth of the carbon nanotubes. This procedure is denoted as *Super-growth CVD* and was invented by Kenji Hata, Sumio Iijima and co-workers at AIST in Japan [106] .

A different approach for synthesis of carbon nanotubes is based on vaporization of carbon. The most important methods of that kind are:

- Arc discharge

In this method, a high current of around 100 Amperes passes through graphite electrodes. Due to the high temperatures achieved by this, the carbon in the negative electrodes sublimates and carbon nanotubes are formed, single-walled as well as multi-walled. This method was first used in 1991 [107] , but the first macroscopic production by this method was done in 1992 by two researchers at NECs Fundamental Research Laboratory [108] . The efficiency per weight is up to 30% [76] .

- Laser ablation

Another method to produce carbon nanotubes is to vaporize a graphite target in high temperature reactor using a pulsed laser, while an inert gas is blown into the reactor. The vapor condenses on the cooler sites of the reactor and multi-walled carbon nanotubes emerge [109] . Single-walled carbon nanotubes can be obtained by a combination of graphite and metal catalyst particles, preferably cobalt and nickel [110] .

- Plasma torch

This method makes use of plasma in order to vaporize carbon containing substances, in analogy to the arc discharge method. High frequency oscillating currents in a coil induces a plasma which is maintained by an inert gas. Metal catalysts are added for the nanotube growth process. Groups from the University of Sherbrooke and the National Research Council of Canada discovered this process in 2005 [111] . The production speed achieved is quite good being 2 grams of nanotubes per minute, which exceeds the speed of arc-discharge and laser ablation.

But there is a completely different approach for producing carbon nanotubes than the methods mentioned. These methods all try to synthesize carbon nanotubes directly from scratch, which is difficult and complicated. However, carbon nanotubes are closely related to graphene and can be thought as rolled up graphene. This idea is realized by a proposed method to synthesize carbon nanotubes, namely *Twisting graphene nanoribbons into carbon nanotubes* [112] .

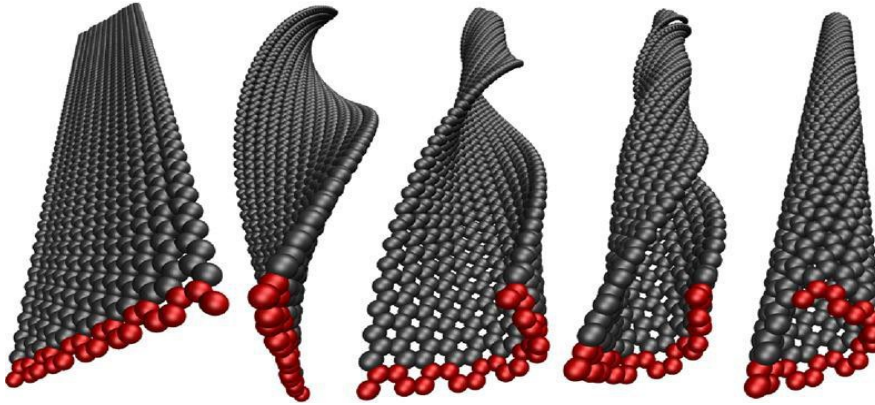


Figure 1.14 Rolling up graphene nanoribbons to carbon nanotubes, taken from [112]

As depicted in Figure 1.14, carbon nanotubes are formed by continuously twisting graphene nanoribbons. The twisting can be carried out in practice with paddle-type setups by applying appropriate voltages to electrodes. Chiralities of the resulting carbon nanotubes can be controlled by using graphene nanoribbons with suitable chirality, which is a huge advantage over all other methods, which produce mixtures of different nanotubes. There many very promising approaches for large scale cheap production of graphene, and as nanoribbons can be obtained easily from graphene, this method is very interesting for economic synthesis of carbon nanotubes .

1.3 Basic electronic structure of graphene and carbon nanotubes

In this chapter I want to provide a brief description of the electronic structure of graphene and carbon nanotubes based on tight binding considerations. As graphenes electronic structure is fundamental for carbon nanotubes, I start with graphene. Graphene is a hexagonal lattice consisting of 2 carbon atoms in its unit cell, as shown in the picture below:

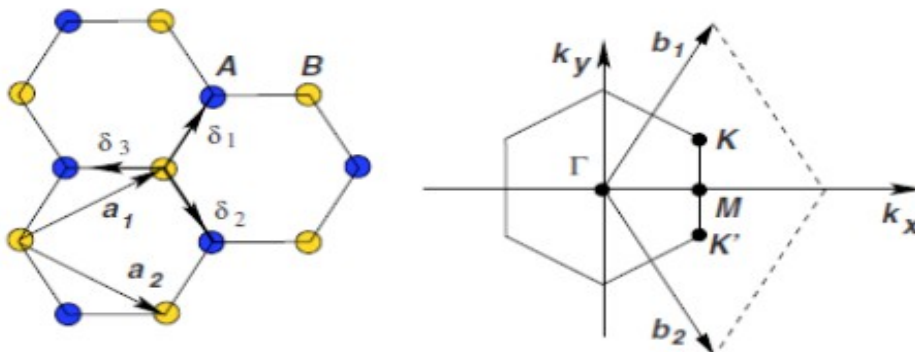


Figure 1.15 Unit cell of graphene and its reciprocal lattice, taken from thep-center.org

I will follow the approach in [113], which gives a very good introduction to graphene and nanotubes. With $a = \sqrt{3} \cdot a_{cc}$, where $a_{cc} \approx 1.42$ Angstrom is the distance between carbon atoms, the lattice vectors of graphene are :

$$a_1 = \left(\frac{\sqrt{3}}{2}; \frac{1}{2} \right) \cdot a, \quad a_2 = \left(\frac{\sqrt{3}}{2}; -\frac{1}{2} \right) \cdot a \quad (1.4)$$

The reciprocal lattice vectors are given by :

$$b_1 = \left(\frac{1}{\sqrt{3}}; 1 \right) \cdot \frac{2\pi}{a}, \quad b_2 = \left(-\frac{1}{\sqrt{3}}; -1 \right) \cdot \frac{2\pi}{a} \quad (1.5)$$

The carbon atoms in the graphene plane are bonded by the sp^2 hybridization. Carbon has 4 valence electrons, where the s, p_x, p_y orbitals form a strong sigma bond in the plane, but the p_z orbitals combine by pi bond. Graphenes mechanical properties mostly derive from the strong sigma bond. In the electronic structure, the p_z orbitals pointing out of the graphene sheet are isolated from the other orbitals and are thus decoupled from them. Therefore only the pi-bonding p_z orbitals are taken into account for the tight binding description of graphene. With the two basis atoms A and B of the hexagonal, the tight binding wavefunction can be written as linear combination of two functions belonging to A and B :

$$\psi(k, r) = c_A(k) P_A(k, r) + c_B(k) P_B(k, r) \quad (1.6)$$

with

$$P_A(k, r) = \frac{1}{\sqrt{(N_{cells})}} \sum_l e^{ik \cdot l} p_z(r - r_A - l) \quad (1.7)$$

$$P_B(k, r) = \frac{1}{\sqrt{(N_{cells})}} \sum_l e^{ik \cdot l} p_z(r - r_B - l) \quad (1.8)$$

where k denotes the wavevector, N_{cell} the number of unit cells, and l the cell position index. Inserting (1.6) into the Schrödinger equation yields the matrix diagonalization problem with energy E

$$\begin{pmatrix} H_{AA} - E & H_{AB} \\ H_{BA} & H_{BB} - E \end{pmatrix} \quad (1.9)$$

We restrict only to next neighbor interaction and set $H_{AA}=H_{BB}=0$ as energy reference. We obtain

$$H_{AB}=H_{BA}=-\gamma_0(1+e^{-ik\cdot a_1}+e^{-ik\cdot a_2})=-\gamma_0\cdot\alpha(k) \quad (1.10)$$

for the off-diagonal matrix elements, where γ_0 denotes the transfer integral between next neighbor pi-bond orbitals. It is approximately 2.9 eV. Solving the eigenvalue problem gives the dispersion relation

$$E_{1,2}(k)=\pm\gamma_0\cdot\sqrt{1+4\cos\left(\frac{\sqrt{3}}{2}k_x a\right)\cdot\cos\left(\frac{k_y a}{2}\right)+4\cos^2\left(\frac{k_y a}{2}\right)} \quad (1.11)$$

The positive and negative square root correspond to the conduction and valence band of graphene. At the K points of the Brillouin zone, the term becomes zero, which means that valence and conduction band touch each other. Figure 1.16 shows graphenes band structure:

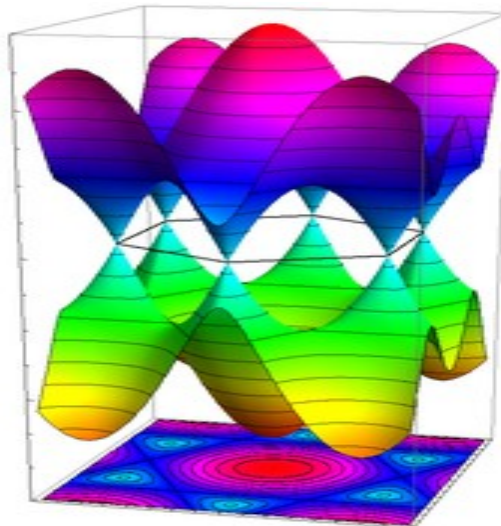


Figure 1.16 Band structure of graphene, taken from Wikipedia

The electronic structure of carbon nanotubes can be derived from graphene. Carbon nanotubes can be thought of as rolled up graphene, and this idea is used to obtain the band structure of them. When applying next neighbor tight binding to carbon nanotubes and neglecting curvature effects between the carbon atoms, one finds that the tight binding Hamiltonian of the carbon nanotube is the same as if one would roll the nanotube out to a stripe of graphene. This model is called zone folding approximation. We can get the electronic structure of the rolled out graphene stripe by taking that of graphene, but requiring periodic boundary conditions, because both ends of the stripe come together in the real nanotube. For a given chirality (n,m) , these are :

$$\psi_k(r + C_h) = e^{ik \cdot C_h} \psi_k(r) = \psi_k(r) \quad (1.12)$$

Consequently, the allowed k points must fulfill

$$k \cdot C_h = 2\pi \cdot q \quad (1.13)$$

with an integer q . The allowed k points form lines in the Brillouin zone, and these lines are taken as bands. If one of the k-point lines crosses a K point, then the nanotube is metallic, because conduction and valence band cross, otherwise the nanotube is a semiconductor. This can be checked easily by the condition

$$n - m = 3 \cdot l \quad (1.14)$$

, where l is an integer. Therefore if the difference $n-m$ is a multiple of 3, a K point is crossed by the band lines, and the nanotube is metal. In the case that $n-m$ cannot be divided by 3, the nanotube is an semiconductor. A direct consequence of this is that all armchair carbon nanotubes (n,n) are metallic, whereas zigzag nanotubes $(n,0)$ are metallic when n is multiple of 3. Here is an illustration of that method for a $(5,5)$ nanotube :

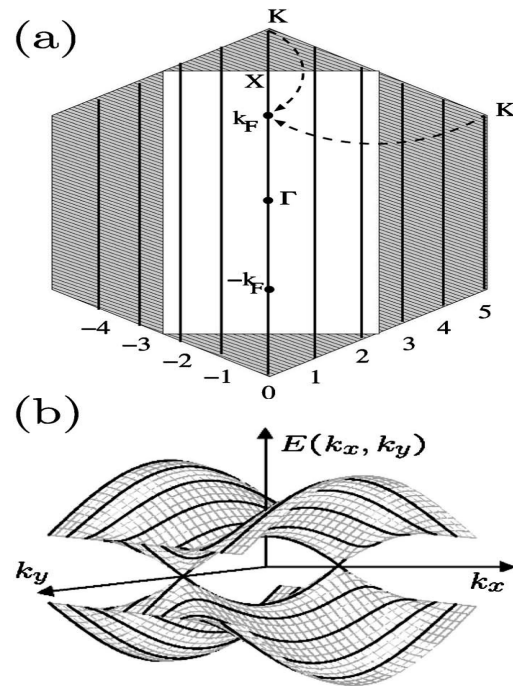


Figure 1.17 K-point lines in the Brillouin zone for a (5,5) nanotube (a) and the resulting electronic bands (b), taken from [113]

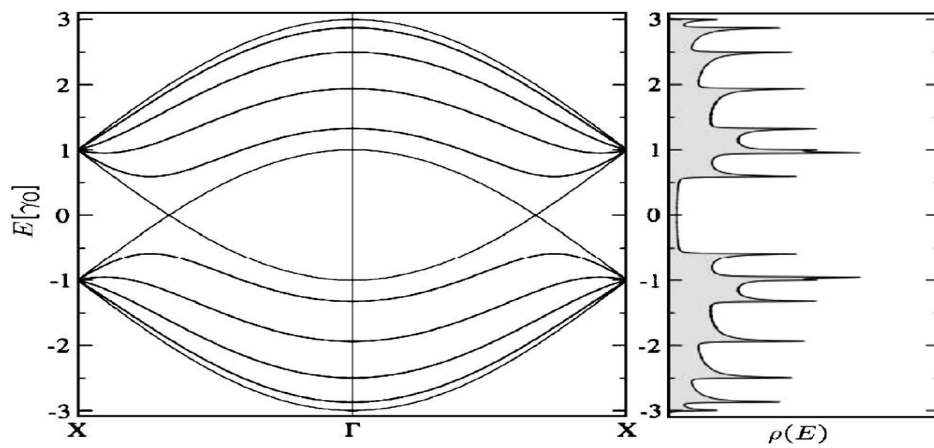


Figure 1.18 Band structure and density of states for a (5,5) nanotube, taken from [113]

2. Theoretical background

In this chapter, the theoretical concepts used in this work are discussed. The key problem in determining the electron structure is that electron-electron interaction must be taken into account in order to describe the systems properly. 2.1 gives an introduction to DFT, a very popular method which calculates the ground state of a many body system in good approximation by reducing the many body problem to an effective one-particle problem. In 2.2 , the GW-approximation is described, which is a very big improvement of DFT for examining the electronic structure beyond the ground state. Finally, the Bethe-Salpeter equation (BSE) and optical spectrum are explained in 2.3 .BSE is the final method used here, which deals with electron-hole excitations (*Excitons*), and its results are taken in order to compute the optical spectrum.

2.1 DFT

The density functional theory (DFT) plays a very important role in the computation of the ground state in many body systems [3]. It is the main approach to incorporate the interaction between electrons, and its basic idea is to express it by an effective potential, still remaining in the one particle formalism. If we consider a system with N electrons, then the complete Hamiltonian is

$$H = \sum_{i=1}^N \frac{p_i^2}{2m} + \sum_{i=1}^n V(r_i) + \sum_{i<j} \frac{e^2}{|r_i - r_j|} \quad (2.1)$$

Instead of solving the eigenvalue problem directly in the Fock space, which would be very time consuming, one considers the particle density

$$n_0(r) = \int d^3 r_1 \dots \int d^3 r_N \psi_0(x_1, \dots, x_N) \sum_{i=1}^N \delta(r - r_i) \psi_0(x_1, \dots, x_N) \quad (2.2)$$

The energy expectation value of a state is given by

$$E[\psi] = \frac{\langle \psi | H | \psi \rangle}{\langle \psi | \psi \rangle} \quad (2.3)$$

For simplicity, we restrict to normalized wavefunctions, so that the energy becomes only the matrix element of the Hamiltonian.

Considering the energy as functional of the particle makes sense, because the

Theorem of Hohenberg and Kohn (2.4)

states that ground state energy *uniquely* depends on the particle density. Furthermore, to the ground state density belongs exactly one ground state wave function. Thus all relations are unique and well-defined. But in order to proceed, we first need to express the energy in dependence from the particle density, with a special focus on the electron-electron interaction. The total energy consists of 3 parts, the kinetic energy, the potential energy and the electron-electron interaction :

$$E[n(r)] = T[n(r)] + V[n(r)] + U[n(r)] \quad (2.5)$$

$$T[n(r)] = \left\langle \psi \left| \sum_{i=1}^N \frac{p_i^2}{2m} \right| \psi \right\rangle \quad (2.6)$$

$$V[n(r)] = \left\langle \psi \left| \sum_{i=1}^N V(r_i) \right| \psi \right\rangle = \int d^3 r V(r) n(r) \quad (2.7)$$

$$U[n(r)] = \left\langle \psi \left| \frac{e^2}{2} \sum_{i \neq j} \frac{1}{|r_i - r_j|} \right| \psi \right\rangle \quad (2.8)$$

The term for the electron-electron interaction (2.8) is very complicated and has no relation to the electron density. In order to get an expression for (2.8) based on the particle density, one sets as approximation

$$U[n(r)] = \frac{e^2}{2} \int d^3 r \int d^3 r' \frac{n(r)n(r')}{|r - r'|} \quad (2.9)$$

This would be the classical electrostatic energy of the electron cloud. However, this approximation neglects quantum effects, and needs to be improved. Therefore a correction term $E_{xc}[n(r)]$ called *exchange correlation energy* is introduced :

$$U[n(r)] = \frac{e^2}{2} \int d^3 r \int d^3 r' \frac{n(r)n(r')}{|r-r'|} + E_{xc}[n(r)] \quad (2.10)$$

The exchange correlation energy consists of two parts, the so called exchange energy E_x and the correlation energy E_c :

$$E_{xc} = E_x + E_c \quad (2.11)$$

The most basic and popular for the exchange correlation energy is the so called local density approximation (*LDA*) . It starts from the free homogenous electron gas, also called *jellium*, to investigate the electron-electron interaction. Hartree-Fock calculations for the free homogenous electron gas provide the following exchange energy :

$$E_x[n(r)] = -\frac{3e^2}{4\pi} (3\pi^2)^{1/3} \int d^3 r (n(r))^{4/3} \quad (2.12)$$

But Hartree-Fock calculations assume single Slater-determinants as solutions. This simplification is corrected by the correlation energy, which is much more difficult to calculate. Throughout this work, we use the results from Ceperly and Alder, who calculated the correlation energy of the homogenous electron gas by quantum Monte Carlo simulations. This can be read in D. M. Ceperley and B. J. Alder (1980). "Ground State of the Electron Gas by a Stochastic Method". *Phys. Rev. Lett.* **45** (7): 566–569.

But there are some improvements over LDA, which are called GGA and Minnesota Functionals. GGA functionals not only depend on the particles density, but also on gradient of it. Minnesota functionals are even more extreme, involving terms of the Laplacian [114]

Now we regard the system in one-particle picture, because our goal is to find an appropriate one particle formalism to describe the electron-electron interaction. If the one-particle wavefunctions are ψ_i , then the ground state wave function can be approximated as Slater determinant

$$\psi(x_1, \dots, x_N) = \frac{1}{\sqrt{N!}} \cdot \det(\psi_i(x_j)) \quad (2.13)$$

The particle density becomes

$$n(r) = \sum_{i=1}^N |\psi_i(x)|^2 \quad (2.14)$$

Finally, using (2.11) and (2.12), we obtain the total energy functional

$$E[n(r)] = \sum_{i=1}^N \frac{-\hbar^2}{2m} \int d^3 r \bar{\psi}_i \nabla^2 \psi_i(r) + \int d^3 r V(r) n(r) + \frac{e^2}{2} \int d^3 r \int d^3 r' \frac{n(r)n(r')}{|r-r'|} + E_{xc}[n(r)] \quad (2.15)$$

After variational minimization of the energy functional with the constraint of normed wavefunctions, one receives the famous

Kohn-Sham equations

$$\left\{ \frac{-\hbar^2}{2m} \nabla^2 + V(r) + \int d^3 r' \frac{e^2}{|r-r'|} n(r') + \frac{\delta E_{xc}[n(r)]}{\delta n(r)} \right\} \psi_i(r) = \epsilon_i \psi_i(r) \quad (2.16)$$

for the ground state wavefunctions ψ_i and corresponding energies ϵ_i .

Thus the system can be regarded as one particle problem with an *effective potential*

$$V_{eff} = V(r) + \int d^3 r' \frac{e^2}{|r-r'|} n(r') + \frac{\delta E_{xc}[n(r)]}{\delta n(r)} \quad (2.17)$$

Solving (2.14) and (2.15) yields a band structure as result, the DFT band structure. The numerical procedure for DFT calculations is *self-consistent iteration*. One starts with an appropriate particle density and solves the Kohn-Sham equations. The resulting wavefunctions are taken to calculate the updated particle density and Kohn-Sham equations. Then the procedure is repeated again and again, until the obtained particle densities converge to a given convergence parameter.

The main basis sets used for all calculations are Gaussian orbitals and plane waves. Gaussian orbitals attach an orbital basis to the atoms, which is determined by the included decay constants and the maximum angular momentum L belonging to them. So for one decay constant, there are 10 orbitals in case of L=2, 4 orbitals in case of L=1, and one orbital in case of L=0. L=2 ist maximum in the program package *Exciton* being used here. Gaussian orbitals are often contracted in order to resemble atomic orbitals better.

Additionally, it is possible to use linear combinations of the atomic orbitals belonging to the atoms in the system as basis. This method is called linear combination of atomic orbitals (LCAO).

Secondly, plane waves are used. These are controlled by the energy cutoff, and by increa-

sing it, the precision can be enhanced systematically. Plane waves are mainly used for the following GW calculations in my work.

In all of this work, norm conserving ab-initio pseudopotentials are used.

2.2 GWA

The GWA method is big improvement over DFT in order to describe the electron-electron interaction concerning electronic states above the ground state . Despite being quite successful in predicting the ground state of quantum systems, DFT often fails for excited states and band gaps. For instance, band gaps in Si, GaAs, Ge etc are systematically underestimated, up to 100% in the case of Ge. In order to receive more realistic computational results, the much more accurate GWA method is used [115] . The starting point for deriving it is to consider a many body quantum system in the *Green function formalism*. In this formalism, the *one particle Green function* is defined as

$$G_1(1,2) = -i \langle N, 0 | T \hat{\psi}(1) \psi^\dagger(2) | N, 0 \rangle \quad (2.18)$$

and the *two particle Green function* by

$$G_2(12; 1'2') = -\langle N, 0 | T (\hat{\psi}(1) \hat{\psi}(2) \psi^\dagger(2') \psi^\dagger(1')) | N, 0 \rangle \quad (2.19)$$

using the field annihilation and creation operators, where

$$1, 2, \dots = (x_1, t), (x_2, t) \dots \quad (2.20)$$

are the particles coordinates including spin, $N, 0 >$ the ground state and T denotes time ordering operator. The particle field annihilation and creation operators create or remove at a room point x by generate the according particle states in the Fock space. The Green functions obey the following equation :

$$(2.21)$$

$$\left(i \frac{\partial}{\partial t} + \nabla^2 - V(r) - V_c(r) \right) G(xt, x't') + i \int \frac{e^2}{|r-r''|} G_2(x''t, x''t, xt, x't') dx'' = \delta(x, x') \delta(t, t')$$

But we need a closed set of equation, and therefore (2.20) is simplified by introducing the

so called *self energy* Σ :

$$\left(i\frac{\partial}{\partial t} + \nabla^2 - V(r) - V_C(r)\right)G_1(xt, x't') - \int \Sigma(xt, x''t'')G_1(x''t'', x't')dx''dt'' = \delta(x, x')\delta(t, t') \quad (2.22)$$

Here $V(r)$ denotes the potential of the lattice and $V_C(r)$ the classical electrostatic potential of the electrons between each other, which is the first term in the DFT effective potential. The equation above all depend on time, but we are interested in energy, and thus one makes a Fourier transformation of the time variable for getting an energy dependence. One obtains a new Hamiltonian for the wavefunctions :

$$\left(-\nabla^2 - V(r) - V_C(r)\right)\psi_m^{OP}(x) + \int \Sigma(x, x', \epsilon_m)\psi_m^{OP}(x')dx' = \epsilon_m\psi_m^{OP}(x) \quad (2.23)$$

In order to receive the self energy, one uses variational derivation, which can be read in full detail in [115]. The resulting equations are

Hedin's equations

$$\Sigma(12) = i \int G_1(13)W(1'4)\Gamma(32;4)d(34) \quad (2.24)$$

$$W(12) = \int v(13)\epsilon^{-1}(32)d(3) \quad (2.25)$$

$$\epsilon(12) = \delta(12) - \int v(13)P(32)d(3) \quad (2.26)$$

$$P(12) = -i \int G_1(23)G_1(42)\Gamma(34;1)d(34) \quad (2.27)$$

$$\Gamma(12;3) = \delta(12)\delta(13) + \int \frac{\delta\Sigma(12)}{\delta G_1(46)}G_1(75)\Gamma(67;3)d(4567) \quad (2.28)$$

The second term in (2.27) is very complicated and makes calculation difficult. Therefore in the so called *GW approximation (GWA)*, the second term in (2.27) is neglected. This gives simplified equations for the self energy :

$$\Sigma = iG_1W \quad (2.29)$$

$$W = v \epsilon^{-1} \quad (2.30)$$

$$\epsilon = \delta - vP \quad (2.31)$$

$$P = -iG_1 G_1 \quad (2.32)$$

$$\Gamma(12; 3) = \delta(12)\delta(13) \quad (2.33)$$

A self consistent calculation like in DFT would be very time-consuming and difficult to perform. Instead of this, the results from DFT are taken to construct the self energy. The Green function based on DFT results is

$$G_1^{DFT}(x, x', \omega) = \sum_n \frac{\psi_n^{DFT}(x) \overline{\psi_n^{DFT}(x')}}{E - E_n^{DFT} + i0^+ \text{sign}(E_n^{DFT} - E_F)} \quad (2.34)$$

All other quantities are then obtained using (2.33) as starting point. Finally, the GWA quasiparticle wavefunctions and energies from (2.22) can be computed by setting the wavefunctions as linear combinations of DFT wavefunctions, which gives us the Hamiltonian to be diagonalized :

$$\psi_m^{QP} = \sum_{n'} a_{n'}^m \psi_{n'}^{DFT} \quad (2.35)$$

$$H_{nn'}^{QP}(E) = E_n^{DFT} \delta_{nn'} + \langle \psi_n^{DFT} | \Sigma(E) - V_{XC} | \psi_{n'}^{DFT} \rangle \quad (2.36)$$

Numerical evaluation of the self requires a lot of computational effort, and becomes extremely time consuming in the case of large systems. In order to handle this obstacle, *dielectric model functions* have been developed. These describe the dielectric function with a simplified model rather than fully making a full calculation of the equations listed before. One of the most prominent of the ones of Hybertsen-Louie and of Bechstedt-Falter. However, these screening models have the big drawback that they assume one universal dielectric constant. In homogenous bulk systems, this makes sense, but it does not work in inhomogenous systems like surfaces or the nanosystems considered in this work. Due to that problem, the so called *LDA+GdW* model has been developed by Michael Rohlfing [116]. This model constructs the total dielectric response as sum of the responses of each atom in the unit cell, and an effective volume is attributed to each atom as a weight. All calculations in this work are based on LDA+GdW.

2.3 Bethe-Salpeter equation and optical spectrum

The final step in our calculations to solve the so called *Bethe-Salpeter equation* (BSE), in which the electron-electron interaction is calculated directly upon the previously obtained wavefunctions. Its key quantities are the *two-particle correlation functions* , defined by

$$L(12;1'2')=-G_2(12;1'2')+G_1(1,1')G_1(2,2') \quad (2.37)$$

and for free electron pairs

$$L_0(12;1'2')=G_1(1,2')G_1(2,1') \quad (2.38)$$

They obey the following equation of motion [117] , called the Bethe-Salpeter equation (BSE) :

$$L(12;1'2')=L_0(12;1'2')+\int d(3456)L_0(14;1'3)K(35;46)L(62;52') \quad (2.39)$$

Here the coordinates are denoted like in the previous chapter, the numbers 1,2 ... are an abbreviation for the space, including spin, and time coordinates, and $K(35;46)$ denotes the so called *electron-hole interaction kernel* . There four time variables here, referring to two particle creations and two particle creations respectively, but we restrict to simultaneous creation and annihilation, so that only two time variables remain. Furthermore, due to time homogeneity, only time differences are of interest, so that we effectively have to deal only with one time variable. Once again, we perform a Fourier transformation of the time variable in order to work in the relevant energy space. The free electron pair correlation function can be expressed by the wavefunctions and energies obtained by the GW calculation as follows:

$$L_0(12,1'2';\omega)=i\sum_{v,c}\left(\frac{\psi_c(x_1)\overline{\psi_v(x_1')}\psi_v(x_2)\overline{\psi_c(x_2')}}{\omega-(E_c-E_v)}-\frac{\psi_v(x_1)\overline{\psi_c(x_1')}\psi_c(x_2)\overline{\psi_v(x_2')}}{\omega+(E_c-E_v)}\right) \quad (2.40)$$

Under the assumption that the electron-hole excitations are long lived, the two particle correlation function can be written as

$$L(12,1'2';\omega)=i\sum_S\left(\frac{\chi_S(x_1,x_1')\overline{\chi_S(x_2',x_2)}}{\omega-\Omega_S}-\frac{\chi_S(x_2,x_2')\overline{\chi_S(x_1',x_1)}}{\omega+\Omega_S}\right) \quad (2.41)$$

, where S denotes the excited many body states and Ω_S the energies belonging to them. The electron-hole amplitudes in (2.40) are defined by

$$\chi_S(x,x')=-\langle N,0|\psi^\dagger(x')\hat{\psi}(x)|N,S\rangle \quad (2.42)$$

with many-body ground state N,0 and excited states N,S. The excited states can be assumed as linear combinations of electron-hole excitations:

$$|N,S\rangle=\sum_v^{\text{hole}}\sum_c^{\text{elec}}A_{vc}^S\hat{a}_v^\dagger\hat{b}_c^\dagger|N,0\rangle:=\sum_v^{\text{hole}}\sum_c^{\text{elec}}A_{vc}^S|vc\rangle \quad (2.43)$$

with electron and hole creators a,b. Expanding the field operators in the basis of the valence and conduction bands and using (2.42) yields the following expression for the electron-hole amplitudes:

$$\chi_S(x,x')=\sum_v^{\text{occ}}\sum_c^{\text{empty}}A_{vc}^S\psi_c(x)\overline{\psi_v(x')}+B_{vc}^S\psi_v(x)\overline{\psi_c(x')} \quad (2.44)$$

Inserting the equations above into the Bethe-Salpeter equation yields the following eigenvalue problem :

$$(E_c-E_v)A_{vc}^S+\sum_{v'c'}K_{vc,v'c'}^{AA}(\Omega_S)A_{v'c'}^S+\sum_{v'c'}K_{vc,v'c'}^{AB}(\Omega_S)B_{v'c'}^S=\Omega_S A_{vc}^S \quad (2.45)$$

$$\sum_{v'c'}K_{vc,v'c'}^{BA}(\Omega_S)A_{v'c'}^S+(E_c-E_v)B_{vc}^S+\sum_{v'c'}K_{vc,v'c'}^{BB}(\Omega_S)B_{v'c'}^S=-\Omega_S B_{vc}^S \quad (2.46)$$

with matrix elements

$$K_{vc,v'c'}^{AA}=i\int d(3456)\psi_v(x_4)\overline{\psi_c(x_3)}K(35,46;\Omega_S)\overline{\psi_{v'}(x_5)}\psi_{c'}(x_6) \quad (2.47)$$

$$K_{vc,v'c'}^{AB}=i\int d(3456)\psi_v(x_4)\overline{\psi_c(x_3)}K(35,46;\Omega_S)\overline{\psi_{v'}(x_6)}\psi_{c'}(x_5) \quad (2.48)$$

and similar formulas for K^{BA} and K^{BB} . The off-diagonal matrix elements K^{BA} and K^{AB} are very small and can be neglected. Therefore we can set $K^{AB} = K^{BA} = 0$, which decouples the eigenvalue problem (2.44) and (2.45). We restrict on solving (2.44) for the coefficients A , because these are the relevant ones providing the structure of the excited many body states. So the equation to be solved is (2.46), giving positive solutions.

But in order to solve (2.48), we have to know the electron-hole interaction kernel K before. K is given by [117]:

$$K(35;46) = \frac{\delta[V_{Coul}(3)\delta(3,4) + \Sigma(3,4)]}{\delta G_1(6,5)} \quad (2.49)$$

The derivative Coulomb interaction part can be computed easily because the Coulomb interaction is proportional to the particle density, which can be expressed by the Green function:

$$V_{Coul} \propto \rho v \quad (2.50)$$

$$\rho(1) = -i G(1,1^\dagger) \quad (2.51)$$

The functional derivative of the self energy using GWA reads

$$\frac{\delta(G_1 W)}{\delta G_1} = W + \frac{\delta W}{\delta G_1} \quad (2.52)$$

Fortunately, the second term of (2.52) is small and can be neglected. We obtain the electron-electron interaction kernel as

$$(2.53)$$

$$K(35;46) = -i \delta(3,4) \delta(5^-,6) v(3,6) + i \delta(3,6) \delta(4,5) W(3^\dagger,4) = K^x(35;46) + K^d(35;46)$$

In (2.53), the first part K^x is called exchange interaction term and controls details of the excitation spectrum, whereas the second term K^d is called direct interaction term and is respon-

sible for the attractive nature of the electron-electron interaction and the formation of excitons. The matrix elements of K can be calculated by

$$\begin{aligned} \langle \nu c | K^{AA,d}(\Omega_S) | \nu' c' \rangle &= \int dx dx' \overline{\psi_c(x)} \psi_{c'}(x) \psi_{\nu}(x') \overline{\psi_{\nu'}(x')} \frac{i}{2\pi} \int d\omega e^{-i\omega 0^+} W(r, r', \omega) \\ &\times \left[\frac{1}{\Omega_S - \omega - (E_c^{QP} - E_{\nu'}^{QP}) + i0^+} + \frac{1}{\Omega_S + \omega - (E_c^{QP} - E_{\nu}^{QP}) + i0^+} \right] \end{aligned} \quad (2.54)$$

and

$$\langle \nu c | K^{AA,x} | \nu' c' \rangle = \int dx dx' \overline{\psi_c(x)} \psi_{\nu}(x) v(r, r') \psi_{c'}(x') \overline{\psi_{\nu'}(x')} \quad (2.55)$$

The integration in (2.54) is carried out using a *plasmon-pole model* [118]. If the excitonic binding energies are much smaller than the characteristic screening frequencies, which is the case in most semiconductor crystals, then (2.54) is simplified to

$$\langle \nu c | K^{AA,d} | \nu' c' \rangle = - \int dx dx' \overline{\psi_c(x)} \psi_{c'}(x) \psi_{\nu}(x') \overline{\psi_{\nu'}(x')} W(r, r', \omega=0) \quad (2.56)$$

Finally we are able to determine the optical spectrum, after having obtained the excited states and their excitation energies. The crucial physical size for this is the dielectric function $\epsilon(\omega)$. With given polarization vector of the incoming light and the velocity operator

$$\vec{\lambda} = \frac{\vec{A}}{|\vec{A}|} \quad (2.57)$$

$$\vec{v} = \frac{i}{\hbar} [H, \vec{r}] \quad (2.58)$$

, the imaginary part of the dielectric function results from the optical transition matrix elements :

$$\epsilon_2(\omega) = \frac{16\pi e^2}{\omega^2} \cdot \sum_S |\vec{\lambda} \cdot \langle 0 | \vec{v} | S \rangle|^2 \delta(\omega - \Omega_S) \quad (2.59)$$

Taking only the free interband transitions without electron-hole interaction would yield the so called *free spectrum* , whereas including the electron-hole interaction gives the so called *coupled spectrum* .

3. Planar nanostructures of various materials

In this chapter, planar nanostructures of various materials are discussed. These are in analogy to graphene in their structure, but consist of different atoms. First the most prominent material graphene is investigated, followed by boron nitride, which is also a popular concerning nanostructures. Then optoelectronic materials are considered, which are very important for industrial applications. Finally the focus of attention goes to one-layer nanostructures of the classical semiconductors silicon and germanium, and their carbides.

3.1 Graphene

Graphene, which was introduced to large extent in the first chapter, will now be analyzed quantitatively. We start with its bandstructure obtained by DFT calculation, as well in its full 2-dimensional presentation as along characteristic points of the Brillouin zone:

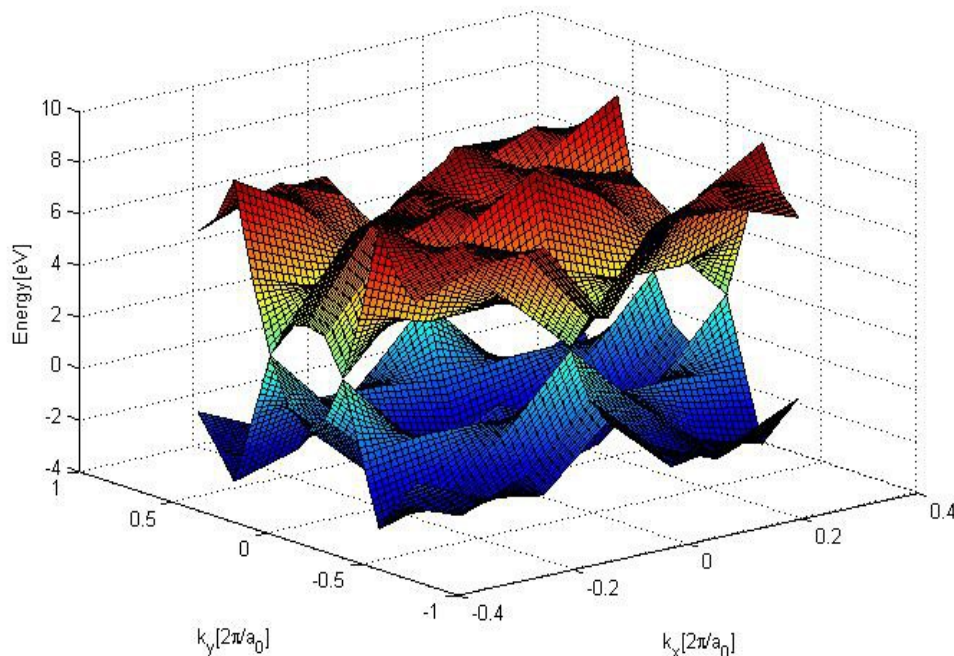


Figure 3.1 2-dimensional DFT band structure of graphene

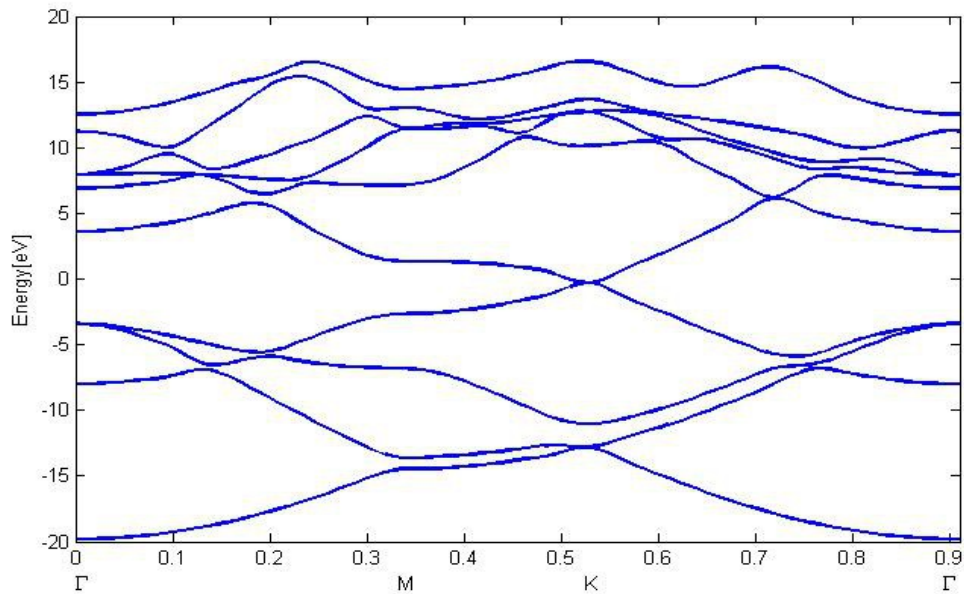


Figure 3.2 DFT band structure of graphene along characteristic k-points

One can clearly see that the valence and conduction touch at the k points, with a vanishing band gap of around 0.2eV. Thus graphene is a semimetal.

GWA and BSE calculations are quite troublesome, as a very high k-point resolution is required in order to obtain reliable results in the case of graphene. This is due to the circumstance that valence and conduction band touch. However, GWA calculation has been carried out by another group, yielding very interesting results for graphene. This can be read in Paolo E. Trevisanutto, Christine Giorgetti, Lucia Reining, Massimo Ladisa and Valerio Olevano (2008) " Ab Initio GW Many-Body Effects in Graphene " *PhysRevLett* 101, 226405 (2008).

Now we take a look at the silicon analog to graphene, silicene. For comparability, all systems in this work are assumed to have hexagonal structure. The lattice structure of it was computed by minimization of the total energy in dependence of the lattice constant, which is the method of choice in all of this work. Silicene possess the following structure, with a calculated interatomic distance of 2.26 Angstrom :

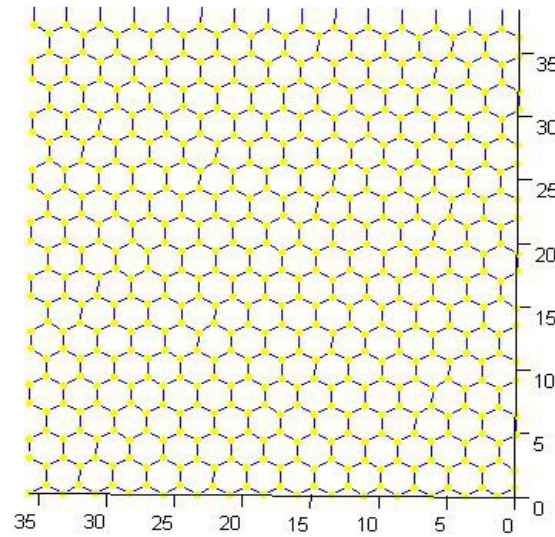


Figure 3.3 Silicene, silicon atoms in yellow

Its electronic structure is very similar to graphene, as shown below :

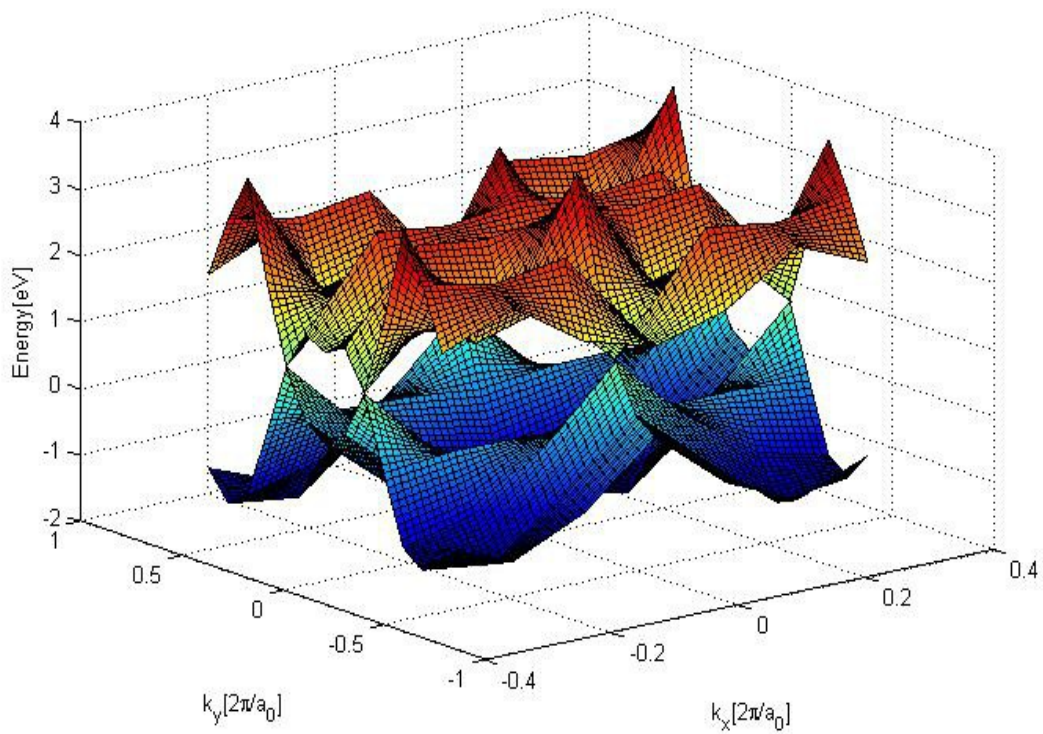


Figure 3.4 2-dimensional DFT band structure of silicene

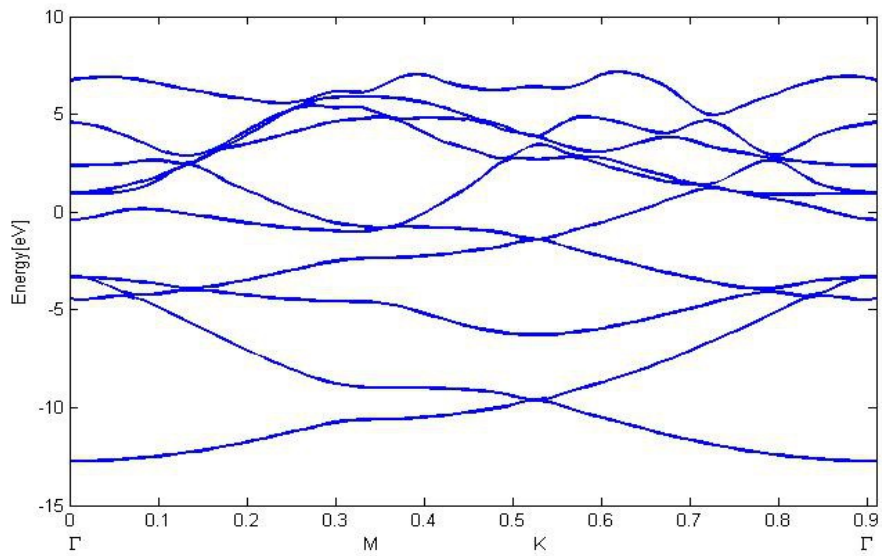


Figure 3.5 DFT band structure of silicene along Γ MK Γ

One realizes that the electronic structure of silicene is basically the same as the one of graphene. As in the case of graphene, valence and conduction band touch at K. Further considerations like GWA and BSE have been excluded, because the same difficulties arise due to the band gap closing at K.

3.2 Boron nitride, boron arsenide and boron phosphide

The second interesting material being investigated in this work is boron nitride. It possess a planar analog called nanomesh [62] mentioned in the first chapter, which offers many applications in electronics and optics [63],[64],[65]. Nanomesh is shown in the picture below

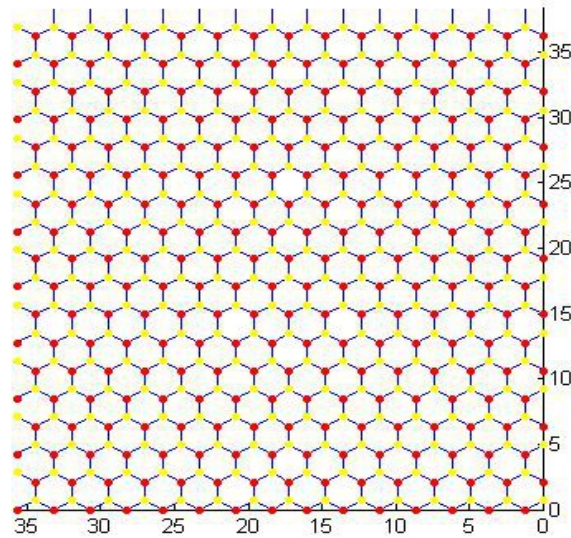


Figure 3.6 Boron nitride nanomesh, boron atoms in yellow, nitrogen atoms in red ; estimated interatomic distance 1.45 Angstrom

The geometric structure is the same hexagonal arrangement like in graphene, but having pairs of boron and nitrogen atoms instead of carbon atoms. DFT calculations yield the following band structure :

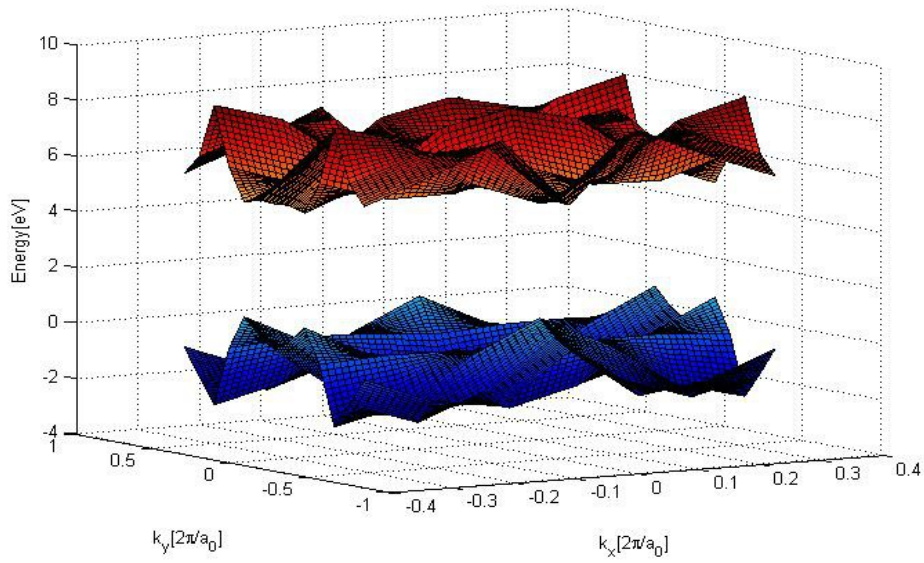


Figure 3.7 2-dimensional DFT band structure of boron nitride nanomesh

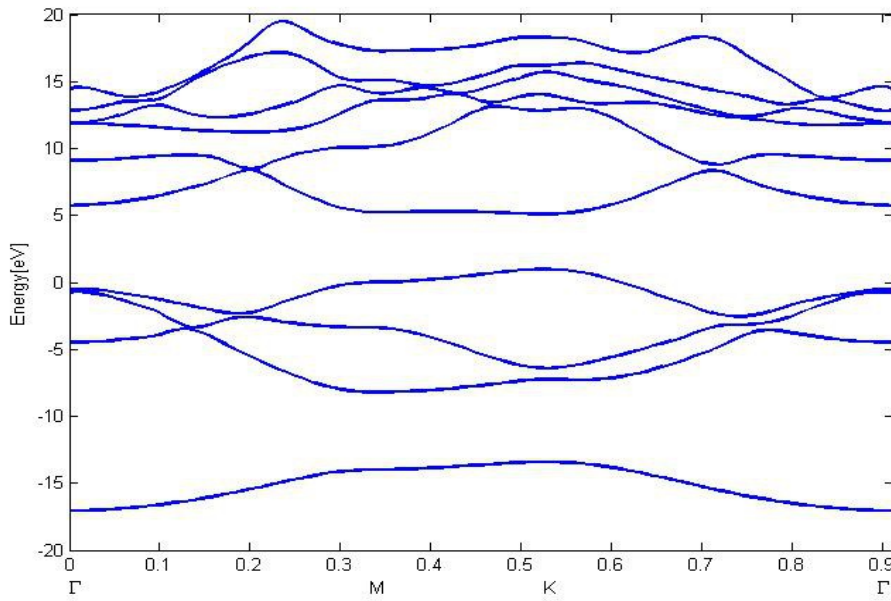


Figure 3.8 DFT band structure of boron nitride nanomesh along characteristic k points

The DFT bandstructure of boron nitride nanomesh is similar to that of graphene, both materials get their band gap at the K point . But in contrast to graphene, planar boron nitride exhibits a significant band gap of approximately 4.1 eV .

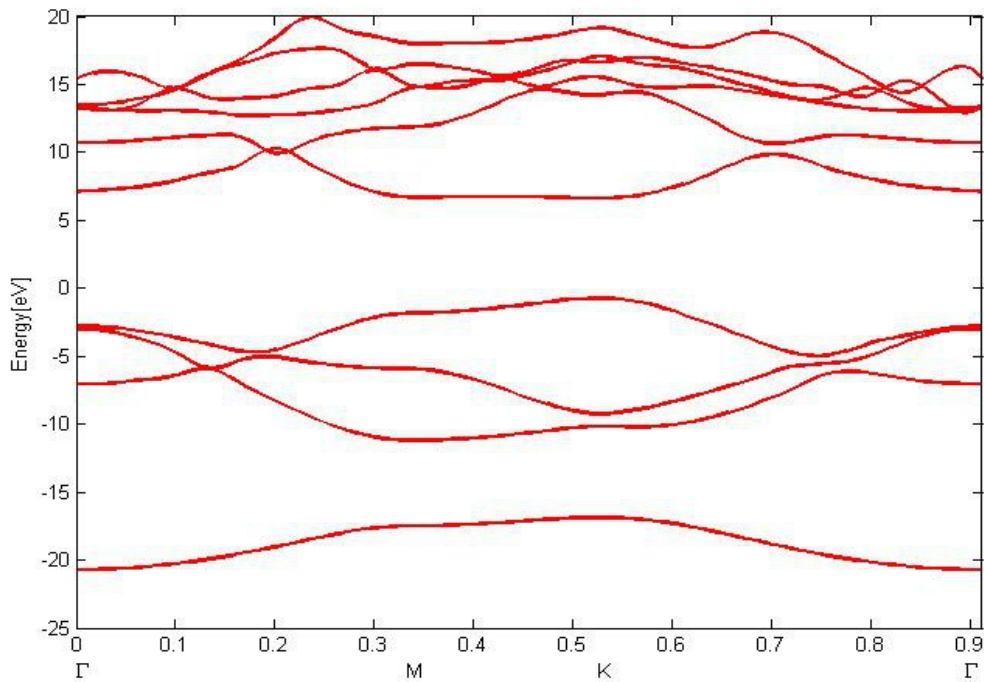


Figure 3.9 GWA band structure of boron nitride nanomesh along characteristic k points. Boron nitride nanomesh undergoes heavy corrections of its band structure by GWA, opening its band gap up to 7.35 eV. Bulk boron nitride has a band gap of only 5.05 eV. The GWA correction has an order of magnitude being around 2.6 eV, and showing very weak dispersion, sharply contrasting to graphene.

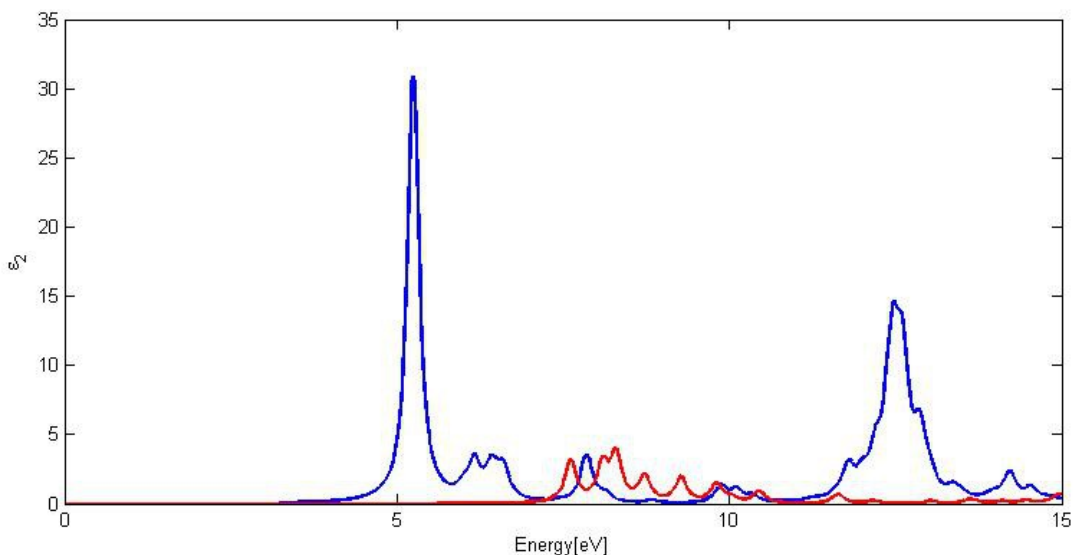


Figure 3.10 Optical spectrum of boron nitride nanomesh with wavevector z

In the case of a plane wave propagating along the z axis, the optical response is depicted in the figure above. The coupled spectrum has a sharp main peak at 5.25 eV, followed by small side peaks, and finally gets a second peak at 12.48 eV, which is much broader than the

first main peak. One immediately recognizes the strong impact of the electron-hole interaction, as the free spectrum differs from the coupled one in each aspect.

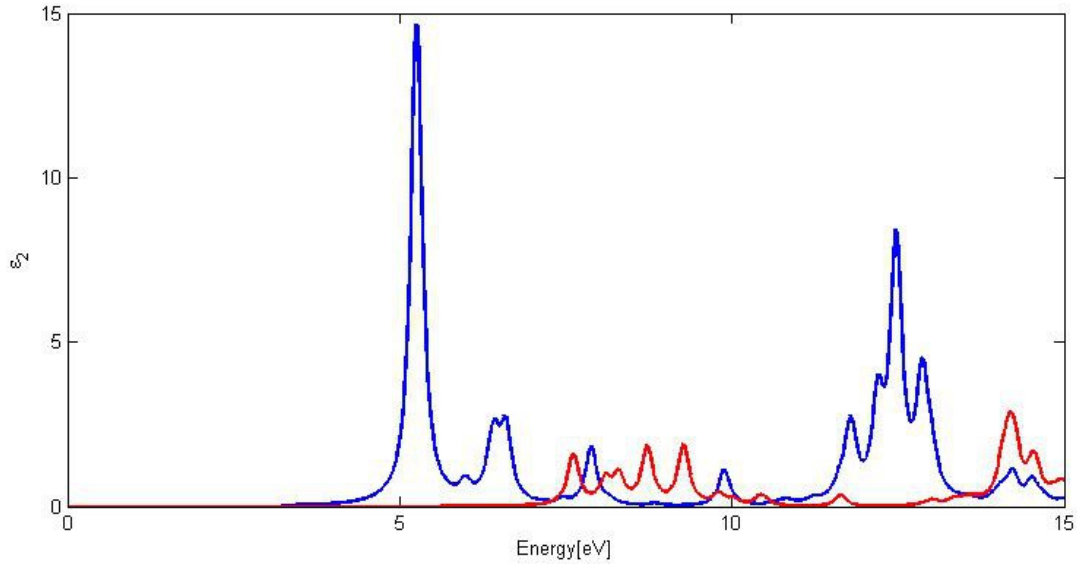


Figure 3.11 Optical spectrum of boron nitride nanomesh for wavevector y

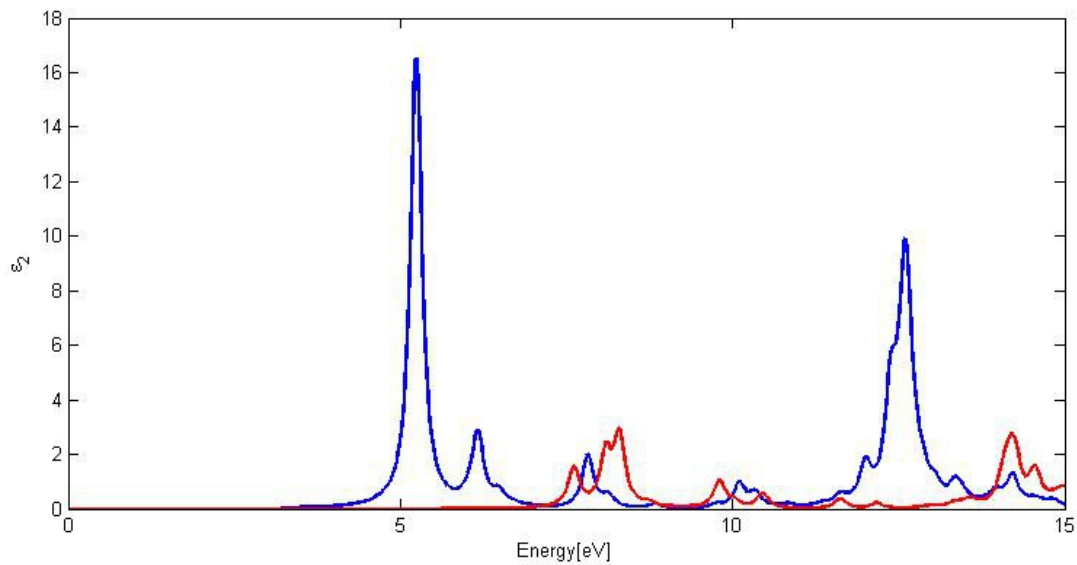


Figure 3.12 Optical spectrum of boron nitride nanomesh for wavevector x

The spectrum for wavevector y and x both show a sharp main peak at 5.25 eV, the same as in the case of wavevector z . Additionally, the second peak has the same position for all wavevectors, with the only difference that the second is broader in the case of wavevector x than in y . In comparison, graphene takes its main peak at 2.37 eV and the second peak at 12.25 eV.

Next we take a look at monolayer boron arsenide:

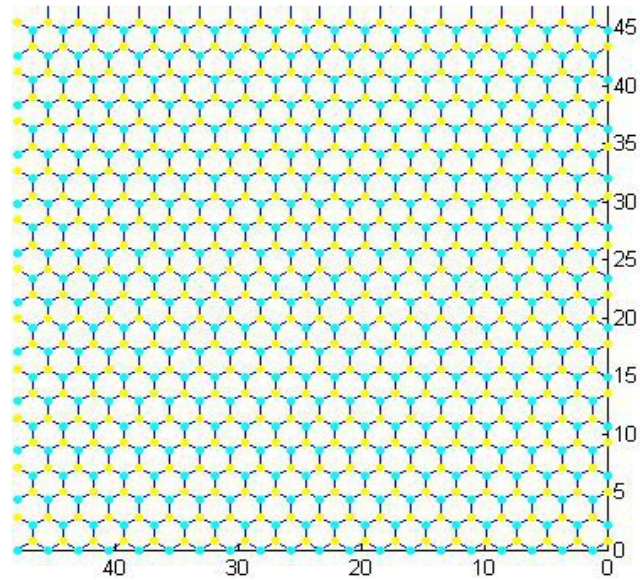


Figure 3.13 Monolayer boron arsenide, boron atoms in yellow and arsenic atoms in cyan ; estimated interatomic distance 1.97 Angstrom

DFT gives the following band structure :

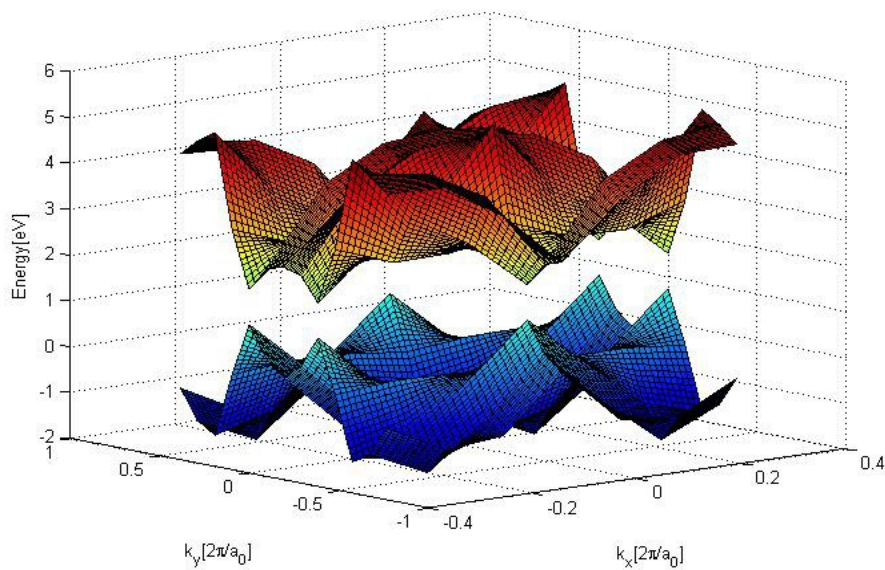


Figure 3.14 2-dimensional DFT band structure of monolayer boron arsenide

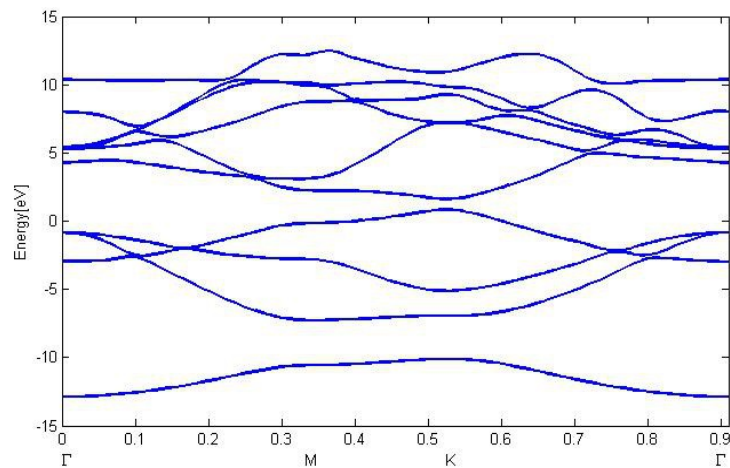


Figure 3.15 DFT band structure of monolayer boron arsenide along Γ MK Γ

The band gap received from DFT calculation is around 0.8 eV. GWA corrects the band structure as shown below:

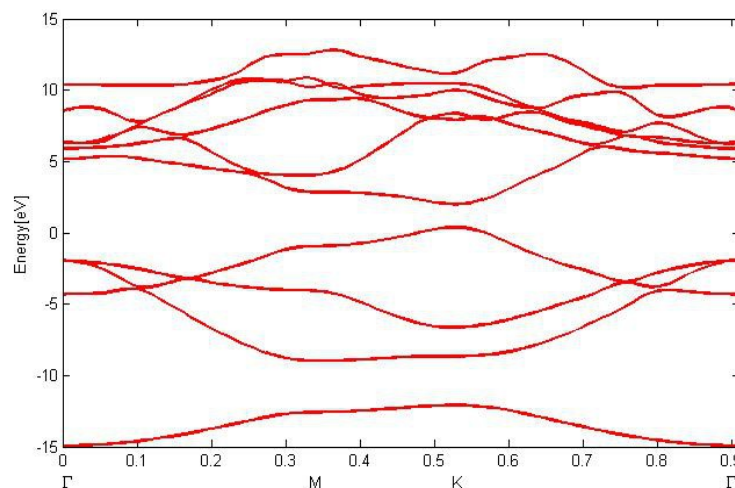


Figure 3.16 GWA band structure of monolayer boron arsenide along Γ MK Γ

The band gap doubles to around 1.62 eV under GWA corrections. The GWA vary in their strength, being strongest at Γ with 2 eV and weakest at K with only 0.8 eV. It seems obvious that monolayer boron arsenide has a much smaller band gap than boron nitride. Nevertheless, the size of the GWA corrections are similar to that of boron nitride, with the difference that the corrections for boron nitride show little dispersion. Compare this to bulk boron arsenide, which has band gap of 1.5 eV.

Concerning the optical response, we obtain the following dielectric function in the case of an incoming plane wave with wavevector z :

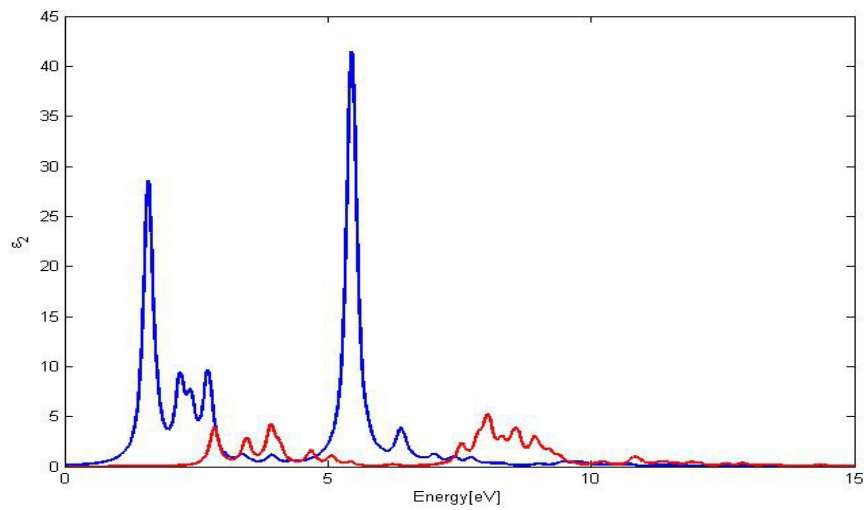


Figure 3.17 Optical spectrum of monolayer boron arsenide for wavevector z

The peaks for wavevector z are located at 1.59 eV, followed by side peaks, and at 5.45 eV. Thus the optical response of planar boron arsenide is at much lower frequencies than that of planar boron nitride, which is in accordance with the smaller band gap of boron arsenide.

Now lets have a look at what happens in the case of wavevector y and x :

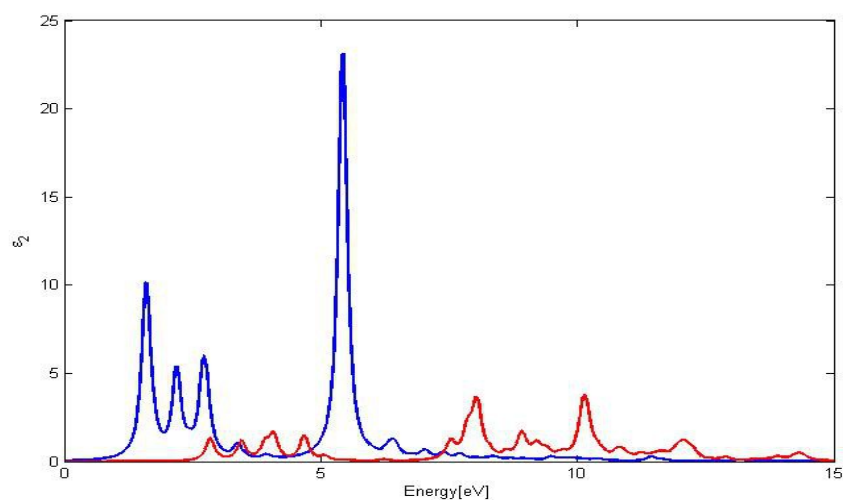


Figure 3.18 Optical spectrum of monolayer boron arsenide for wavevector y

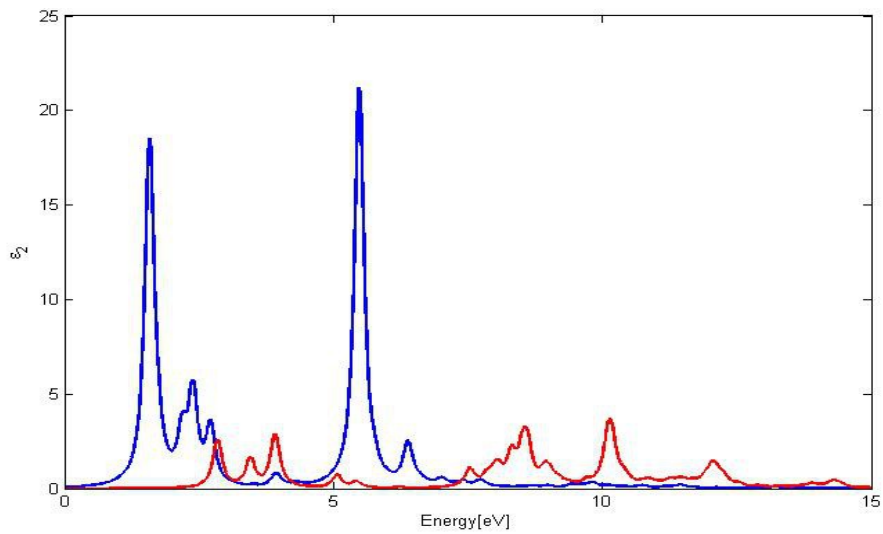


Figure 3.19 Optical spectrum of monolayer boron arsenide for wavevector x

One observes that the position of the peaks remains the same for wavevectors x and y. However, the strength of the peaks differs. In case of wavevector y, the second peak is considerably stronger than the first one, but in case of wavevector x the second peak is only a little stronger than the first peak. This averages in the case of wavevector z, as it can be considered as superposition of x and y.

Finally we regard planar boron phosphide :

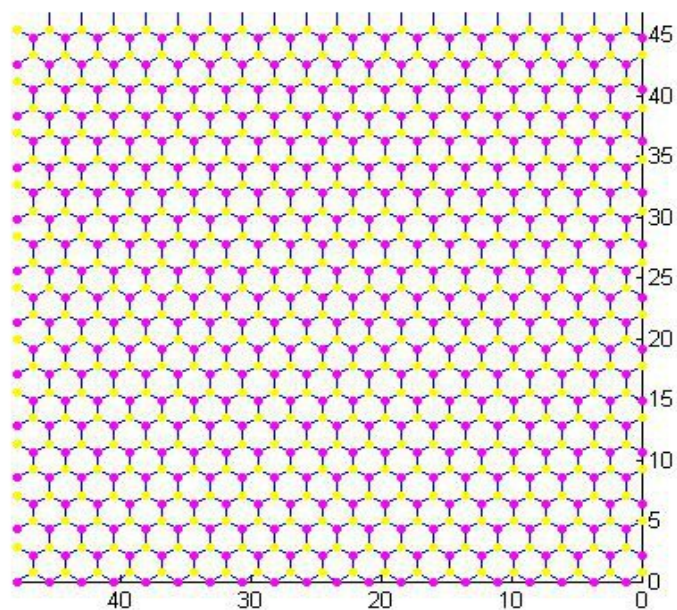


Figure 3.20 Planar boron phosphide, boron atoms yellow and phosphorous atoms magenta ;

estimated interatomic distance 1.87 Angstrom

An interatomic distance 1.87 Angstrom was calculated using SIESTA. For the band structure, DFT provides the following results :

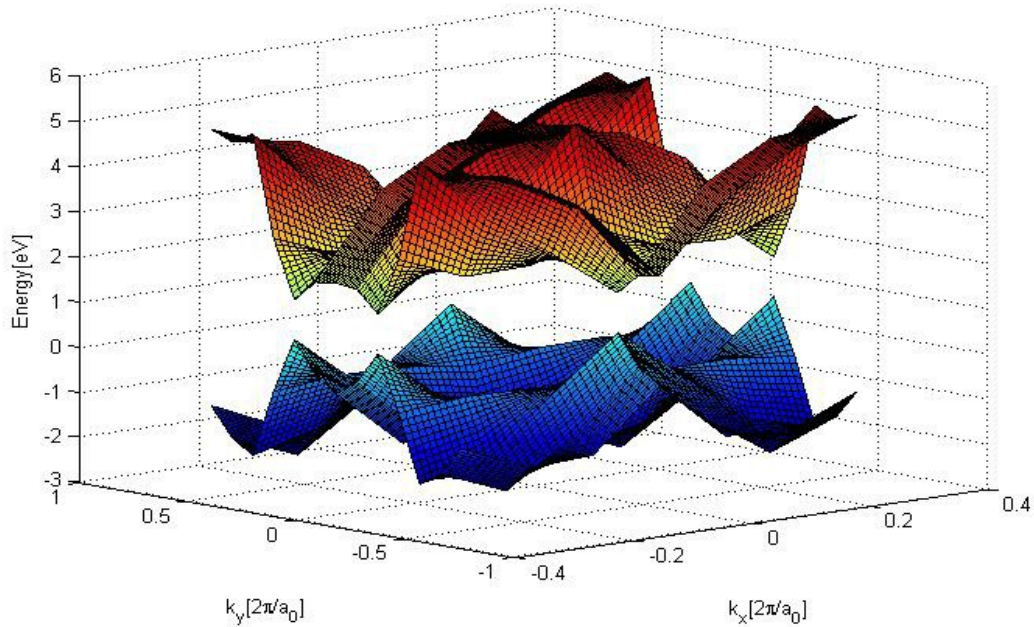


Figure 3.21 2-dimensional DFT band structure of planar boron phosphide

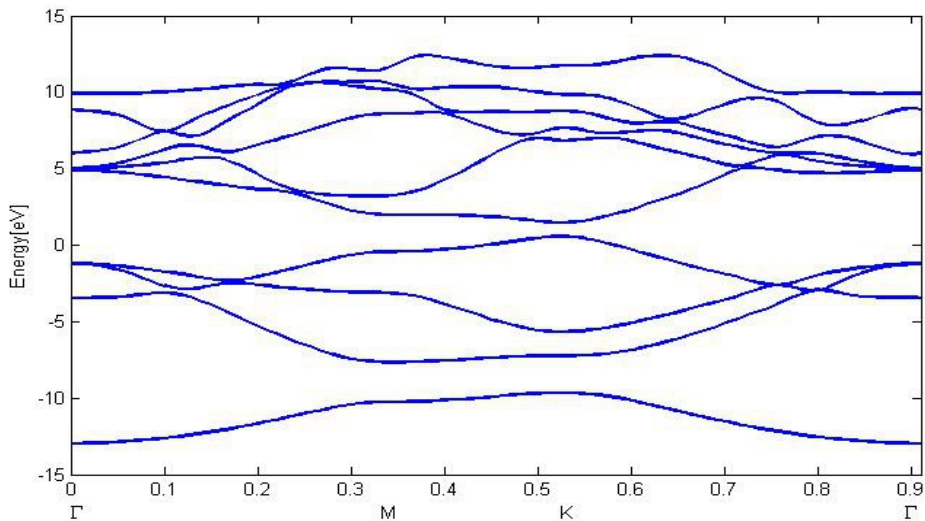


Figure 3.22 DFT band structure of planar boron phosphide along Γ MK Γ

The band structure runs a similar path as boron arsenide and boron nitride, getting its band gap at Γ . DFT states a band gap of around 0.9 eV. GWA provides this band structure:

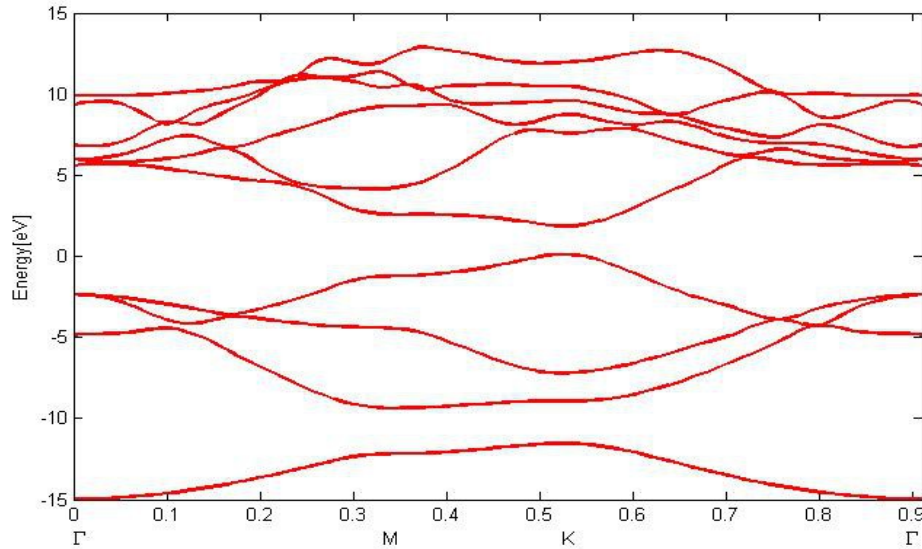


Figure 3.23 GWA band structure of planar boron phosphide along Γ MK Γ

GWA corrections enhance the band gap to 1.76 eV. This is less than the band gap of bulk boron phosphide, which is 2.1 eV. Thereby the corrections are roughly the same as the ones of planar boron arsenide. So one can draw the conclusion that the band gap of the materials considered decreases with the atomic number of the second atom. The strongest band gap is reached for boron nitride with 7.35 eV, followed by boron phosphide with 1.76 eV and boron arsenide with only 1.62 eV.

Finally, our focus of attention goes to the optical spectrum of boron phosphide. For an incoming plane wave with wavevector z , the dielectric function is

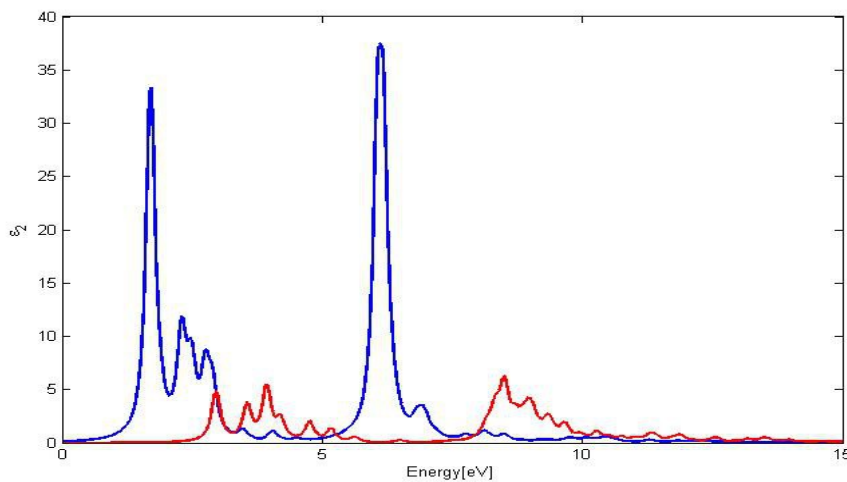


Figure 3.24 Optical spectrum of planar boron phosphide for wavevector z

As in the case of boron arsenide, we observe two strong peaks, at 1.7 eV with side peaks, and at 6.11 eV. This can be interpreted as consequence of the higher band gap of boron phosphide.

For other wavevectors, the optical spectra are :

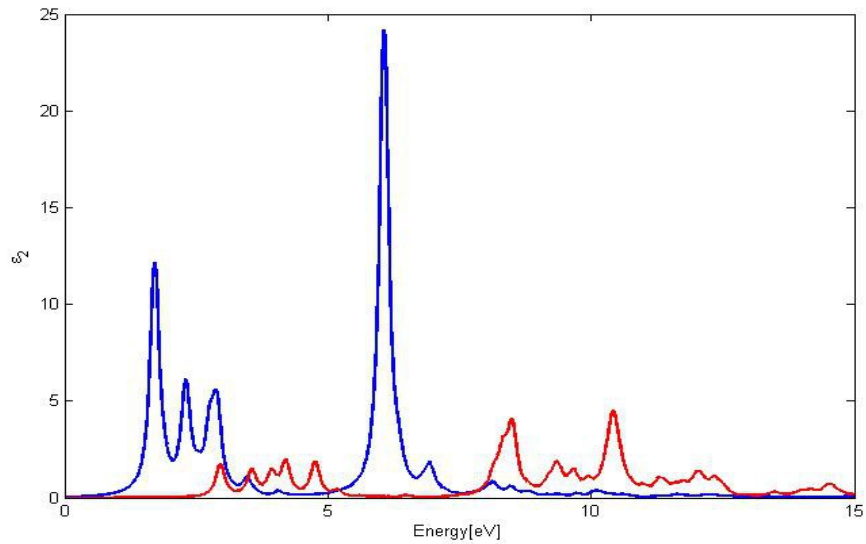


Figure 3.25 Optical spectrum of planar boron phosphide for wavevector y

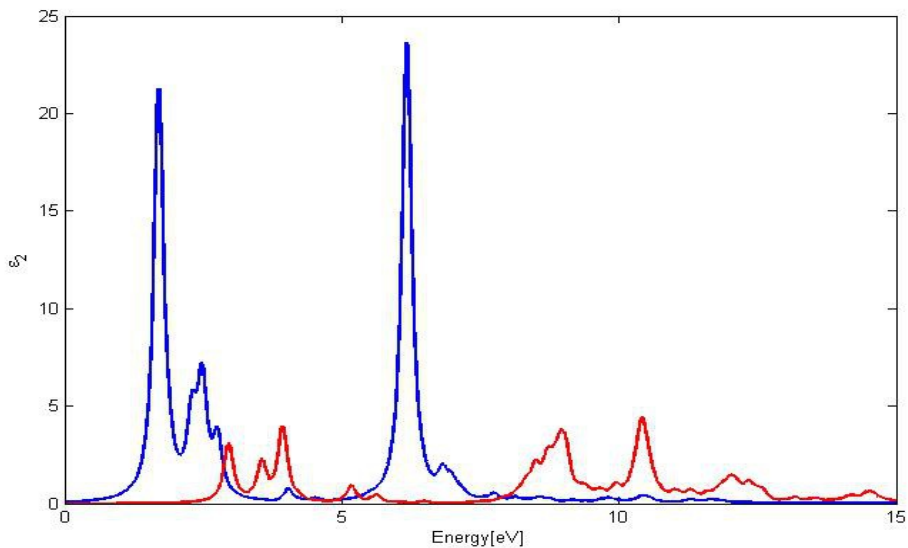


Figure 3.26 Optical spectrum of boron phosphide with wavevector x

Like in planar arsenide, the second peak is very high in the case wavevector y and less for wavevector x. This averages in wavevector z by superposition.

3.3 Optoelectronic materials: AlN, AlAs, AlP and GaN

The materials considered in this section play a crucial role for optoelectronics. AlN, AlAs, AlP and GaN have many applications in optics and electronics, most notably in light emitting diodes (LED). Therefore taking a look at their optical properties makes a lot of sense. In this section their planar nanostructures in analogy to graphene are regarded.

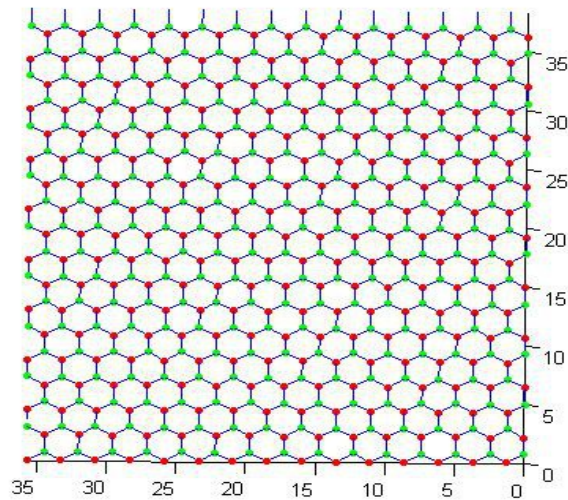


Figure 3.27 Planar AlN , aluminum atoms in red, nitrogen atoms in green ; estimated inter-atomic distance 1.8 Angstrom

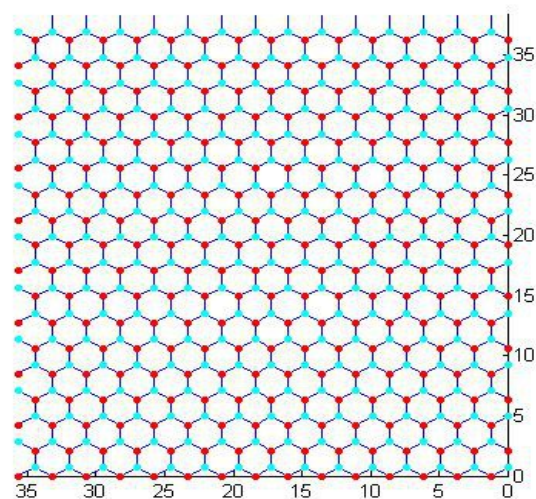


Figure 3.28 Planar AlAs, aluminium atoms in red, arsenide atoms in cyan ; estimated inter-atomic distance 2.39 Angstrom

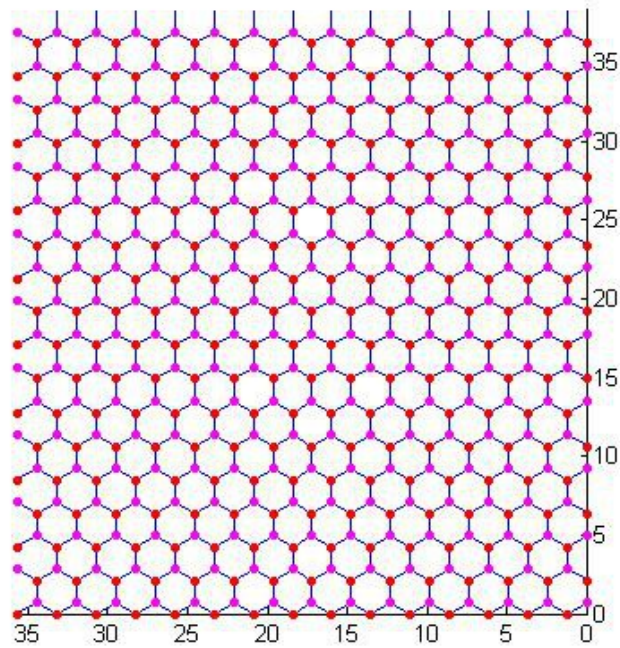


Figure 3.29 Planar AlP, aluminum atoms in red, phosphorous atoms in cyan ; estimated interatomic distance 2.27 Angstrom

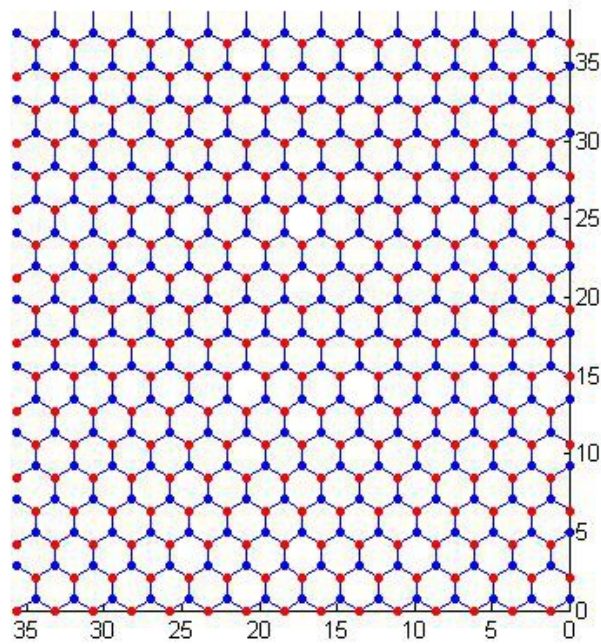


Figure 3.30 Planar GaN, gallium atoms in blue , nitrogen atoms in red ; estimated interatomic distance 1.94 Angstrom

We see hexagonal monolayers like graphene, whose units cell always consists of two atoms, Al and N, Al and As, Al and P or Ga and N. Lets take a look at the resulting band structures:

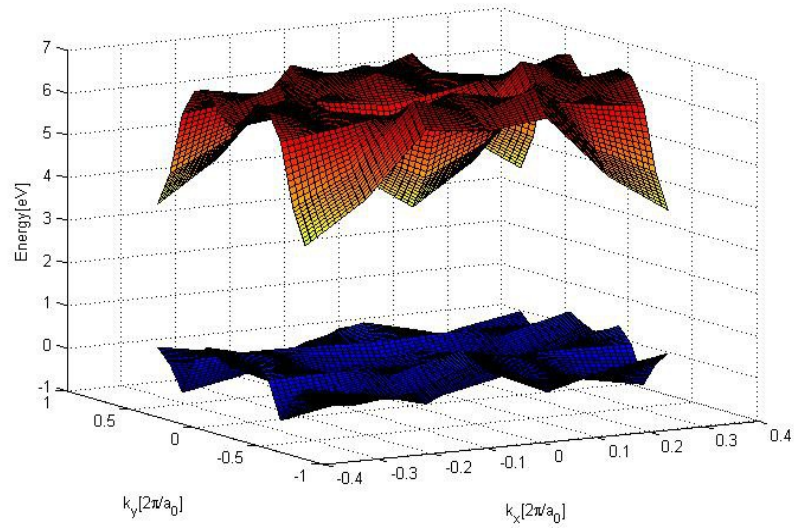


Figure 3.31 2-dimensional DFT band structure of planar AlN

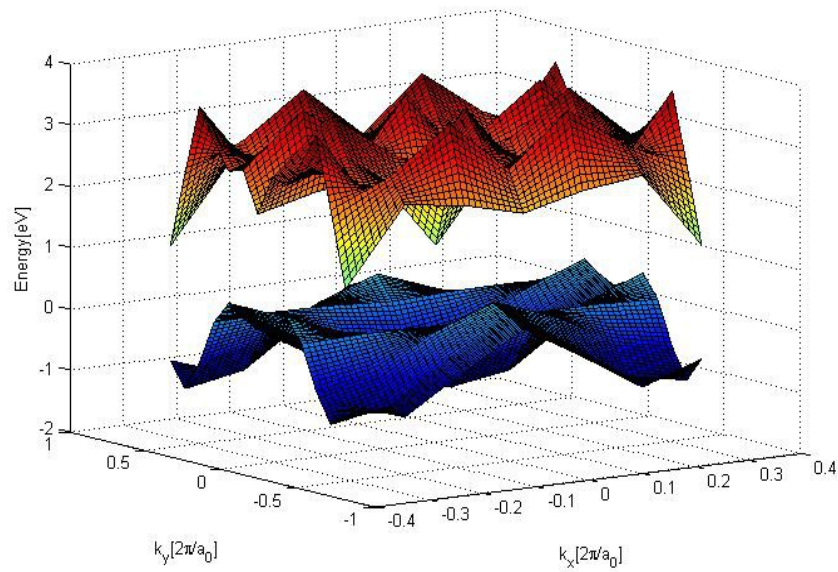


Figure 3.32 2-dimensional DFT band structure of planar AlAs

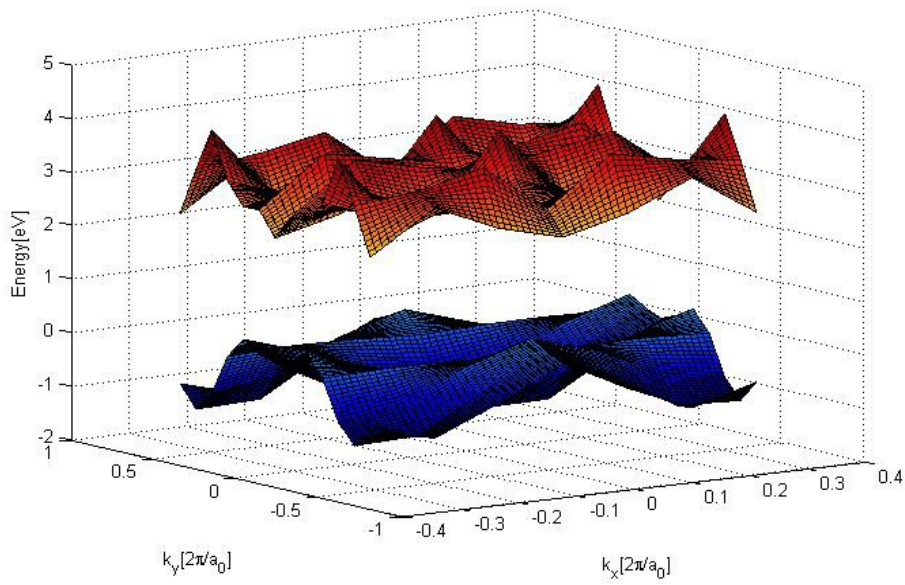


Figure 3.33 2-dimensional DFT band structure of planar AlP

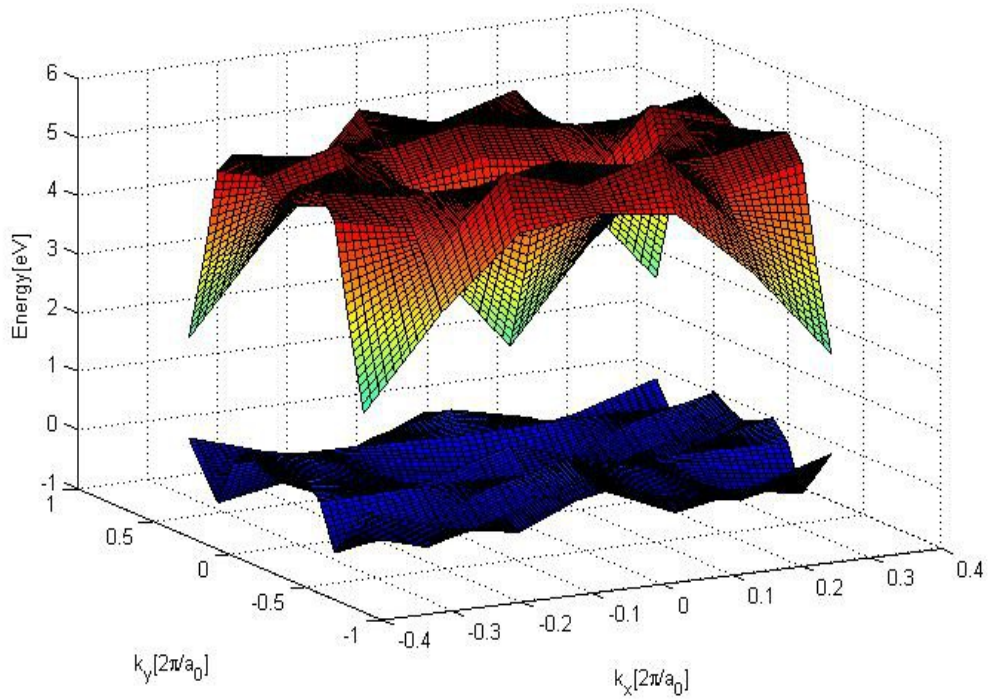


Figure 3.34 2-dimensional DFT band structure of planar GaN

Now we take a look at the DFT band structure along characteristic k point in order to get a more detailed view:

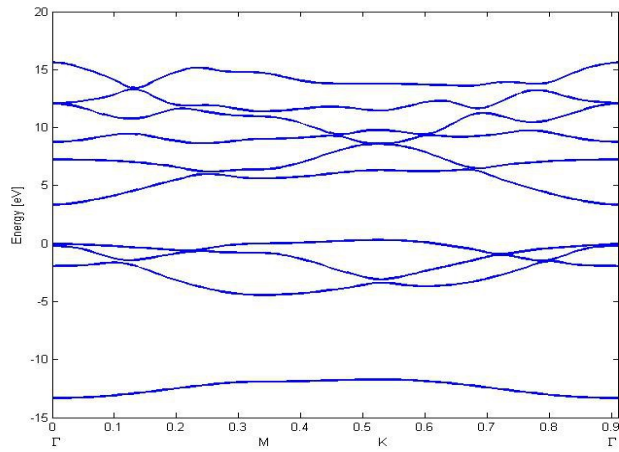


Figure 3.35 DFT band structure of planar AlN along Γ MK Γ

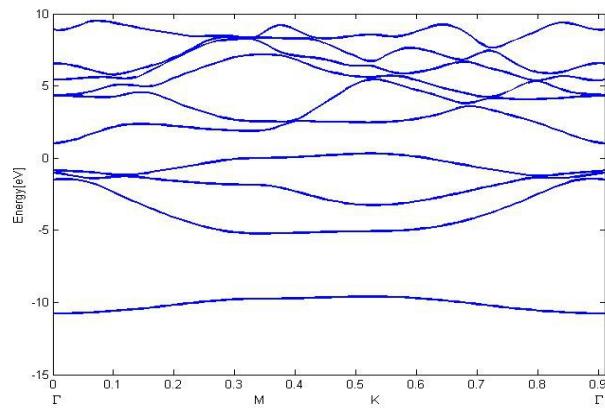


Figure 3.36 DFT band structure of planar AlAs along Γ MK Γ

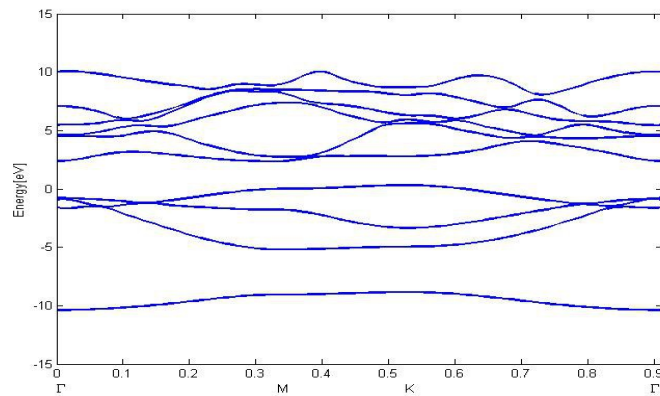


Figure 3.37 DFT band structure of planar AlP along Γ MK Γ

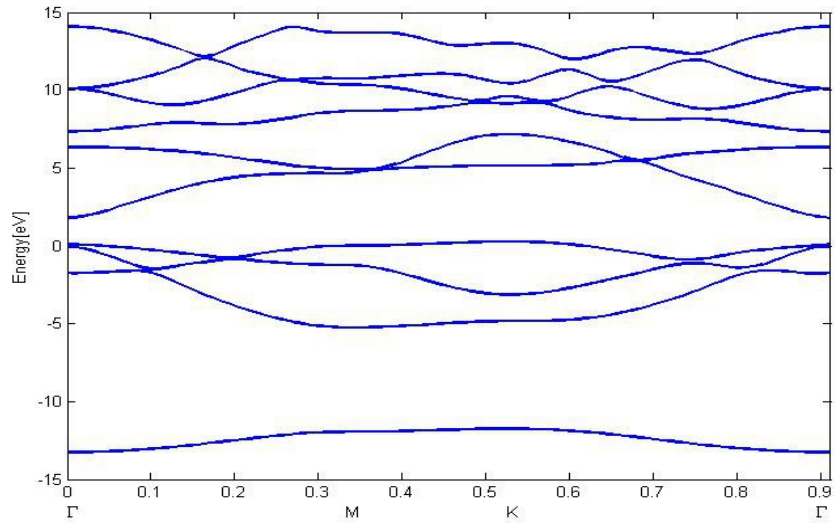


Figure 3.38 DFT band structure of planar GaN along Γ MK Γ

The most striking fact which one immediately observes is that the band structure of all materials significantly differs from that of graphene and boron nitride. Planar AlN has a band gap of 3.36 eV at Γ , whereas AlAs and AlP have indirect band gaps, 0.7 eV in the case of AlAs and 2.1 eV in the case of AlP. The plane nanomaterial GaN shows a band gap of approximately 0.9 eV at Γ . But now we regard the band structures resulting from GWA corrections :

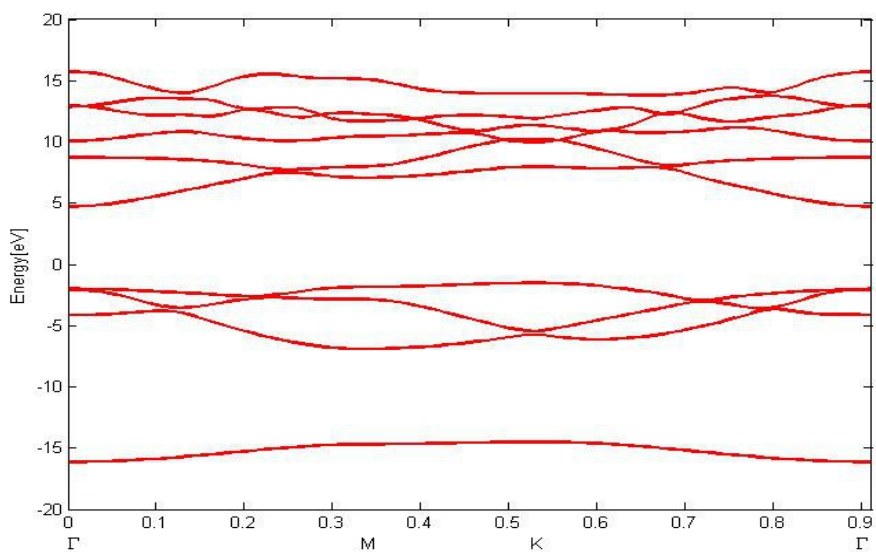


Figure 3.39 GWA band structure of planar AlN along Γ MK Γ

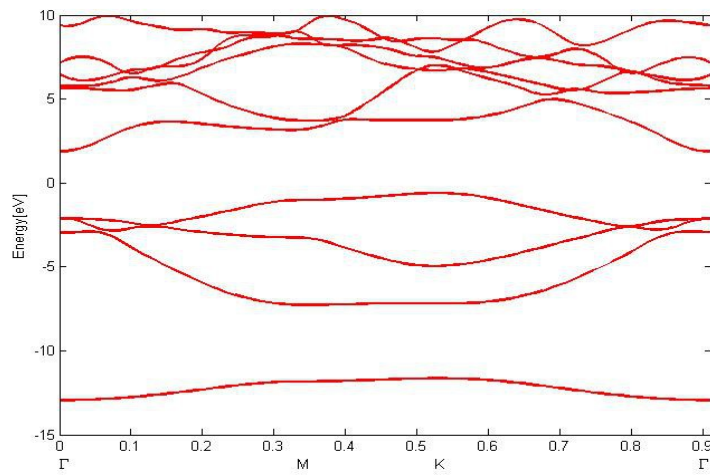


Figure 3.40 GWA band structure of planar AlAs along Γ MK Γ

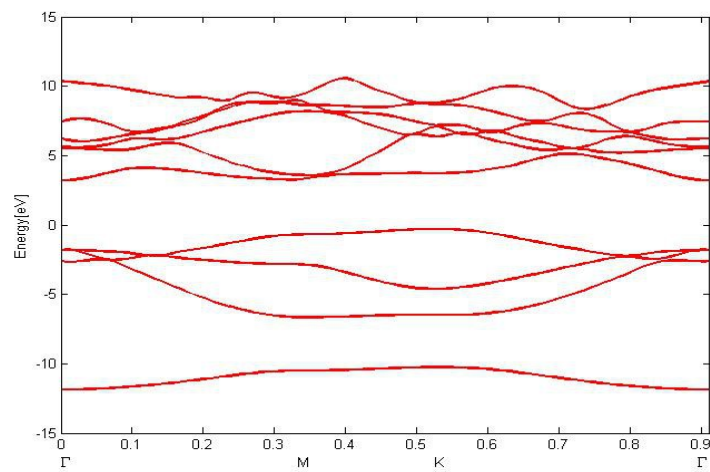


Figure 3.41 GWA band structure of planar AlP along Γ MK Γ

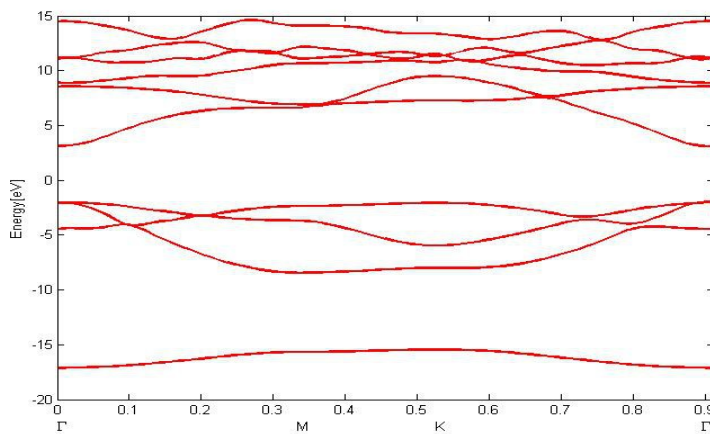


Figure 3.42 GWA band structure of planar GaN along Γ MK Γ

GWA correct strongly affect the band structure in all materials. AlN has a band gap of 6.7eV after GWA corrections, with corrections on the order of 3.2 eV , whereas the bulk crystal AlN has a band gap of 6.28 eV. AlAs has a band gap of 2.5 eV according to GWA with corrections being around 2 eV on average, with bulk AlAs having a band gap of 2.16 eV, which is also indirect. Moreover, GWA calculations yield a band gap of 3.5 eV with band corrections of around 1.7 eV in the case of planar AlP, in comparison with crystal AlP having an indirect band gap of 2.45 eV. Finally, in the case plane GaN a band gap of 5.15 eV together with corrections ranging from 3.3eV at Γ to 4.2 eV at K are predicted by GWA. This strongly exceeds conventional crystal GaN, which only has a band gap of 3.44 eV !!! One can realize the clear trend that band gap is the biggest for the nitrides AlN and GaN, an decreases with AlAs and AlP. The band gaps of planar AlN and GaN are clearly bigger than the ones of the corresponding bulk crystals , but in contrast, the band gap of planar AlP is even smaller than that of crystal AlP. For the optical spectrum the following results are obtained:

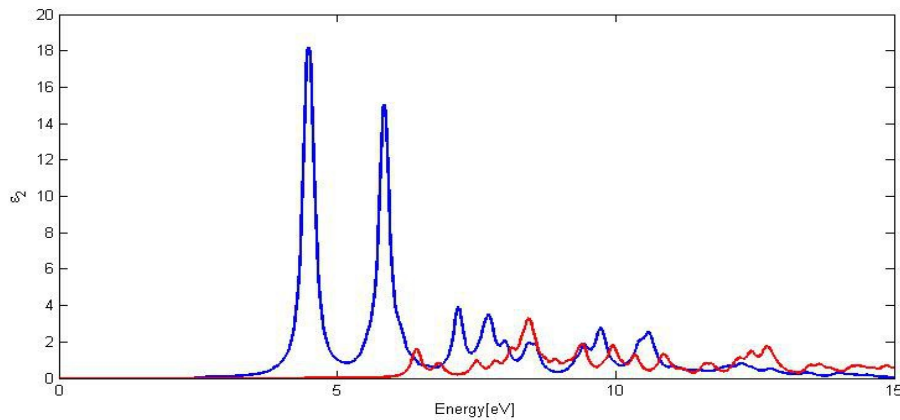


Figure 3.43 Optical spectrum of planar AlN for wavevector z

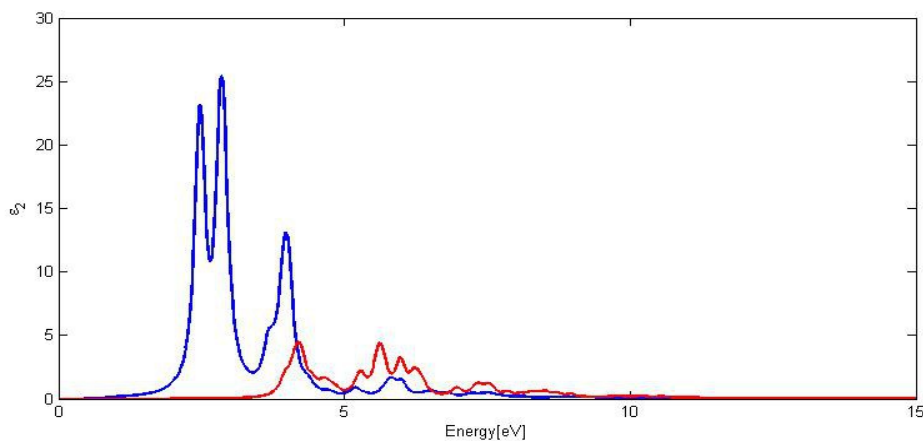


Figure 3.44 Optical spectrum of planar AlAs for wavevector z

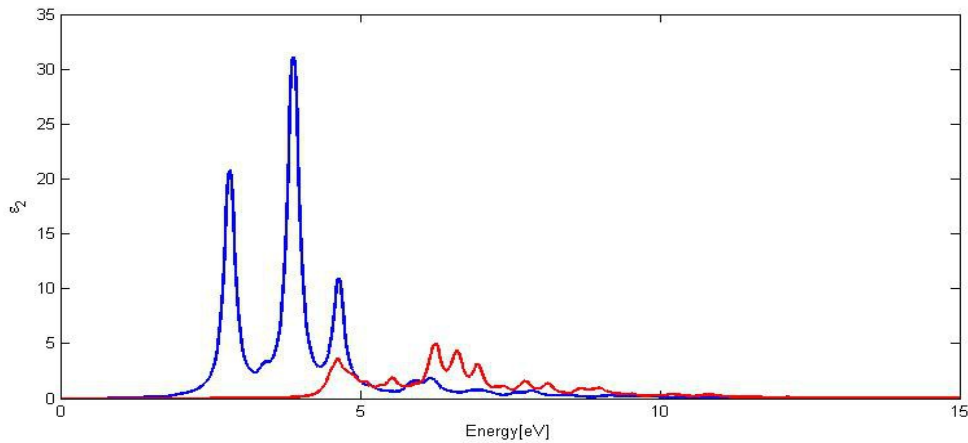


Figure 3.45 Optical spectrum of planar AlN for wavevector z

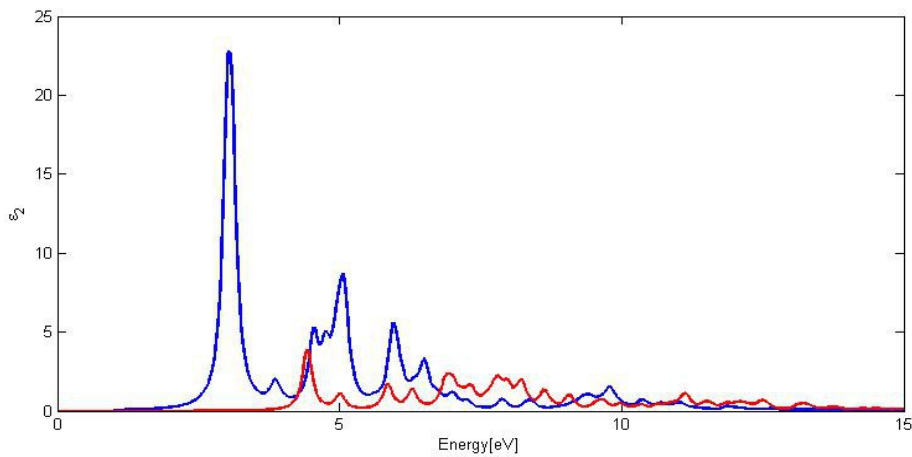


Figure 3.46 Optical spectrum of planar GaN with wavevector z

The spectrum of AlN has its main peak at 4.5 eV, followed by a second peak at 5.8 eV and smaller peaks thereafter. It is strongly affected by electron-hole interaction, which completely changes the spectrum. In the case of AlAs, we observe a double peak located at 2.47 eV and 2.85 eV, and a third peak at 4 eV. AlN possesses three peaks, where the main peak at 3.9 eV is flanked by two side peaks at 2.8 eV and 4.6 eV. Finally, planar GaN shows a main peak at 3 eV, followed by a broad second peak at 5 eV, and finally another wide peak at 6 eV. It is interesting that in the case of GaN, the structure of the spectrum is similar for the free and coupled cases, which means that electron-hole interactions primarily shift the free spectrum to lower energies. The position of the first peak correlates with the band gap; the higher the band gap, the higher is the energy of the first peak.

Now let's take a look at what happens if the incoming light has other wavevectors:

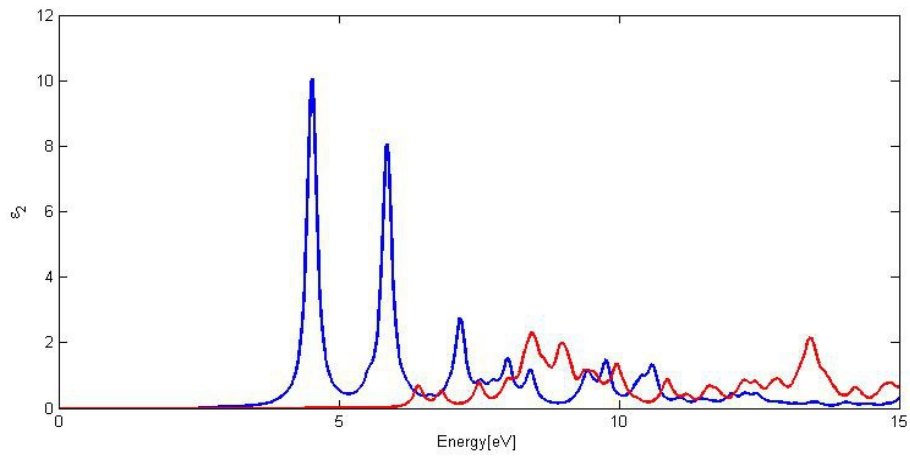


Figure 3.47 Optical spectrum of AlN for wavevector y

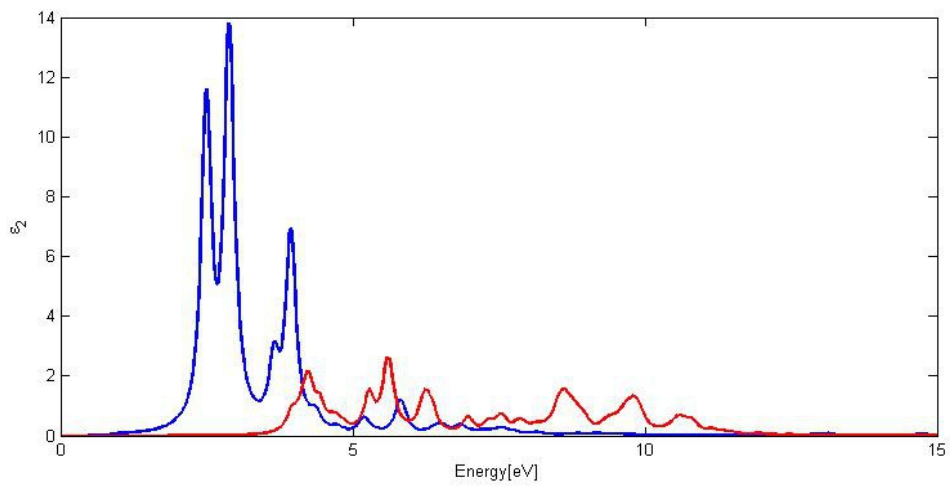


Figure 3.48 Optical spectrum of AlAs for wavevector y

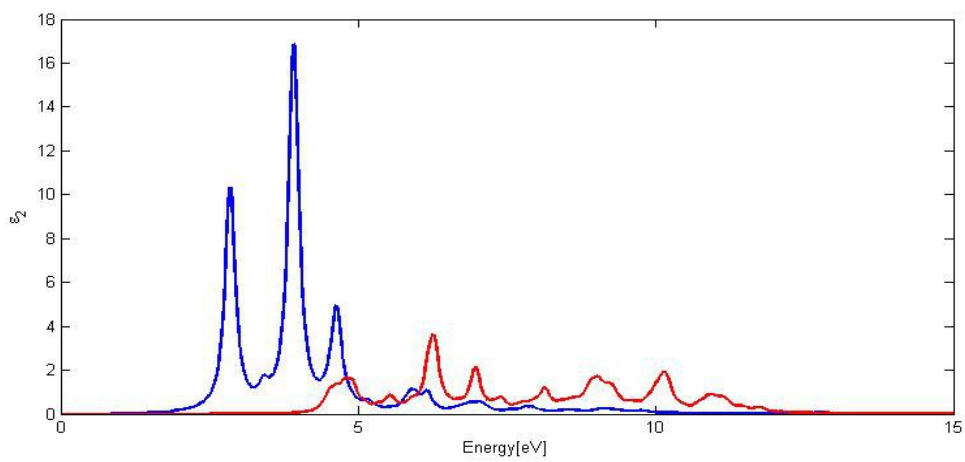


Figure 3.49 Optical spectrum of AlP for wavevector y

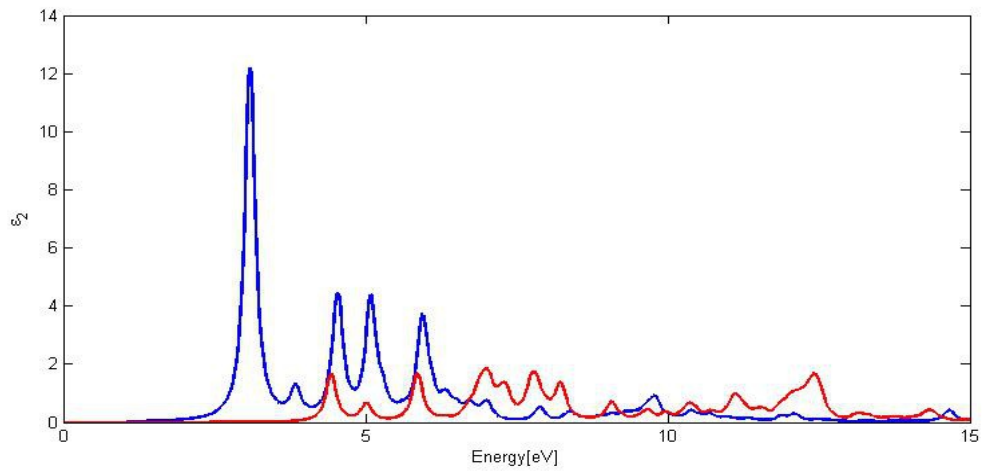


Figure 3.50 Optical spectrum of GaN for wavevector y

, and now the spectrum for wavevector x :

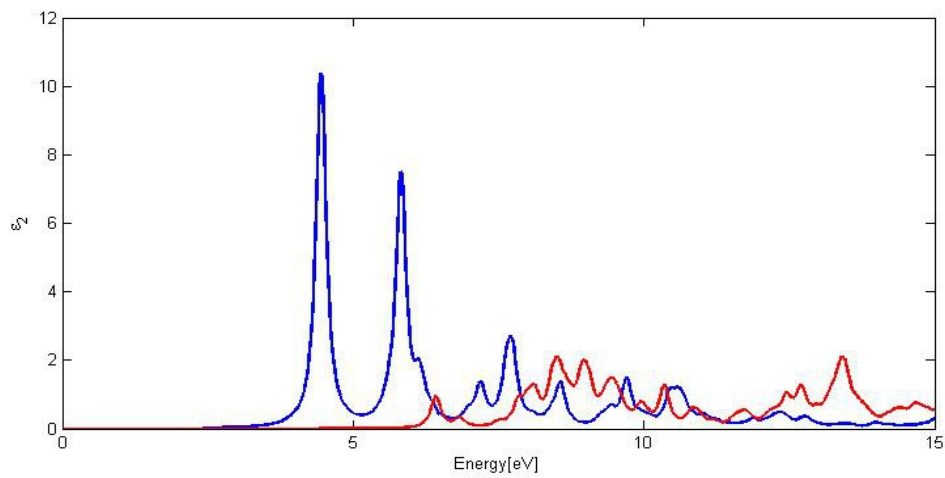


Figure 3.51 Optical spectrum of AlN for wavevector x

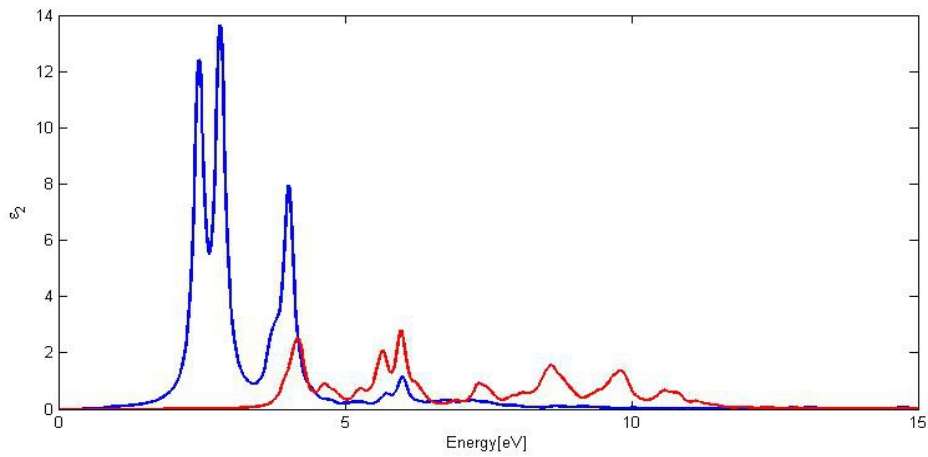


Figure 3.52 Optical spectrum of AlAs for wavevector x

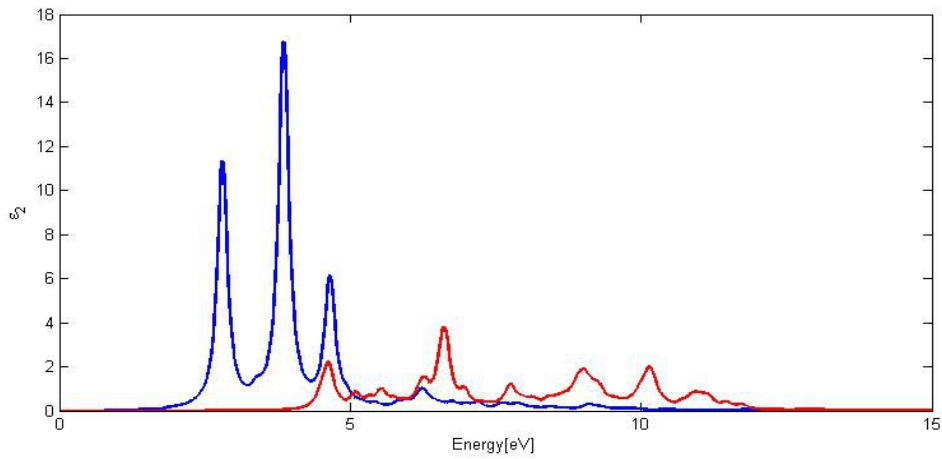


Figure 3.53 Optical spectrum of AlP for wavevector x

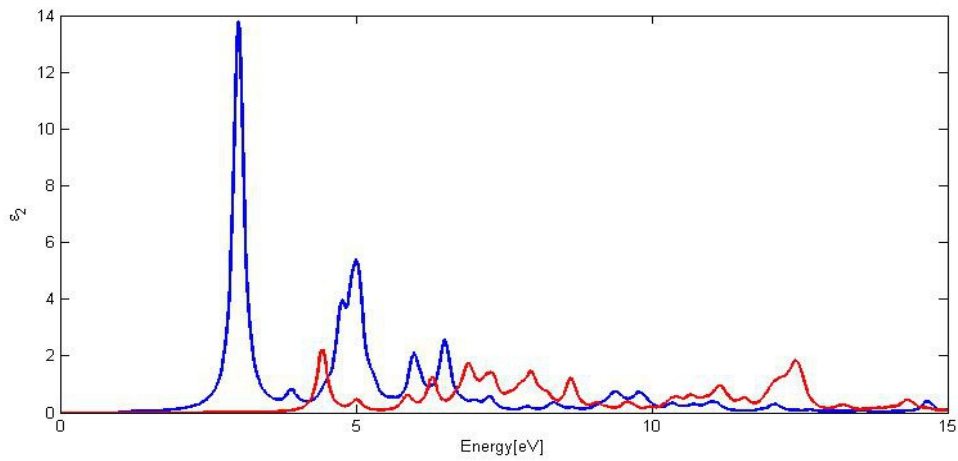


Figure 3.54 Optical spectrum of GaN for wavevector x

From the results we can conclude that the optical spectra for wavevectors x and y are similar in all materials. The spectra for wavevector z can be regarded as superposition of x and y as explained before, and thus the spectra of all wavevectors are similar to each other.

Finally, we take a look at silicon carbide SiC and its germanium counterpart GeC. Silicon carbide, popularly known as carborundum, has its most famous application as very hard material used for material processing and armor. Moreover, it is used for high power and high temperature, and it played a very important role in LED before the arrival of GaN, which is 10 to 100 times more efficient. Therefore we pay attention to the graphene-like nanostructures of SiC and its germanium counterpart GeC in this section.

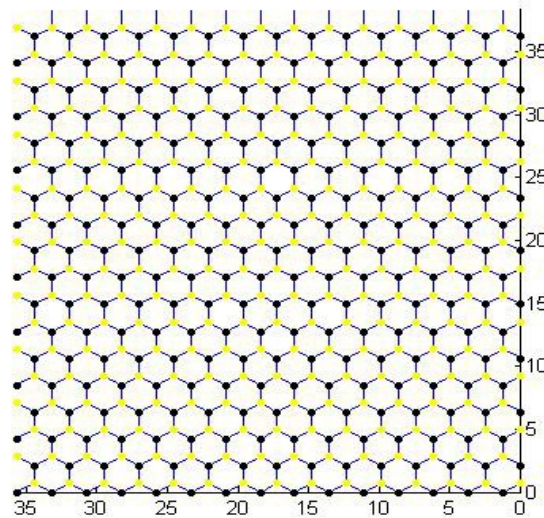


Figure 3.55 Planar SiC, silicon atoms in yellow and carbon atoms in black ; estimated interatomic distance 1.8 Angstrom

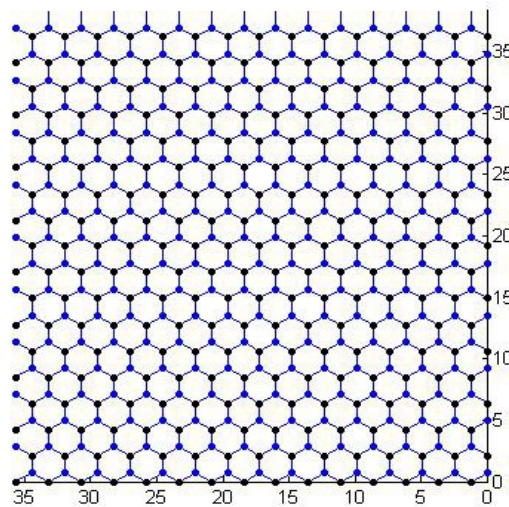


Figure 3.56 Planar GeC, germanium atoms in blue and carbon atoms in black ; estimated interatomic distance 1.85 Angstrom

DFT calculations lead to the following band structures :

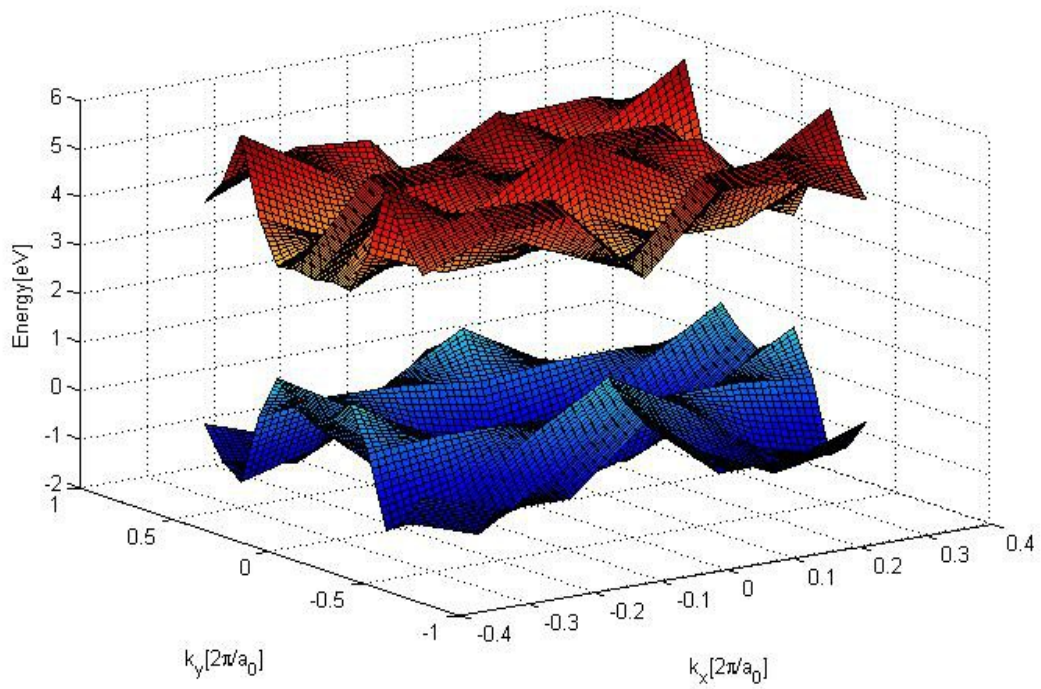


Figure 3.57 2-dimensional DFT band structure of planar SiC

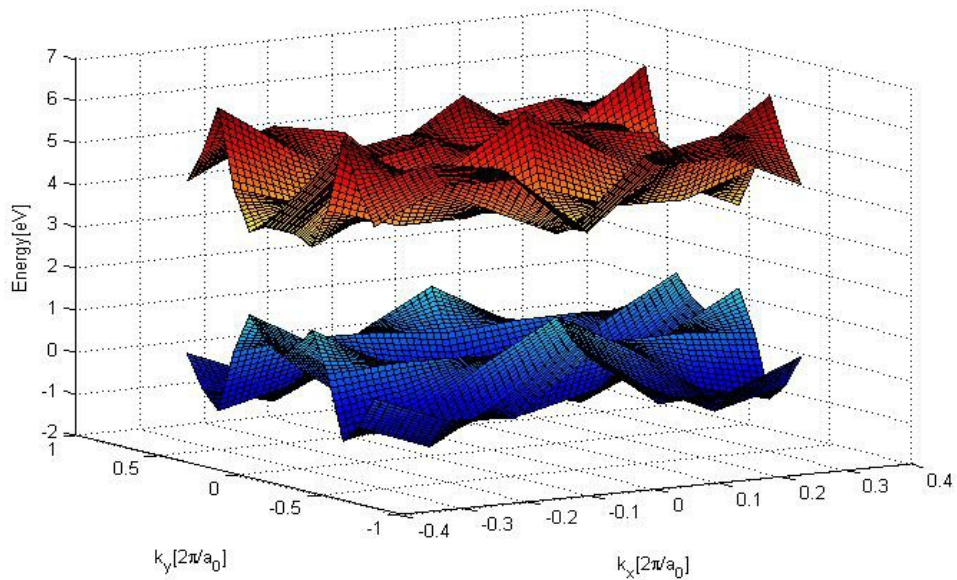


Figure 3.58 2-dimensional DFT band structure of planar GeC

Along lines these look :

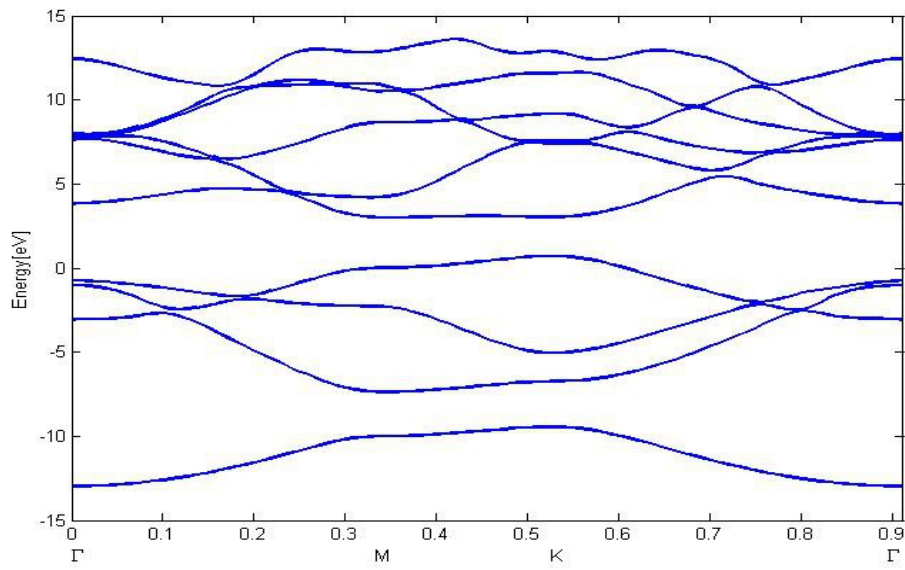


Figure 3.59 DFT band structure of SiC along Γ MK Γ

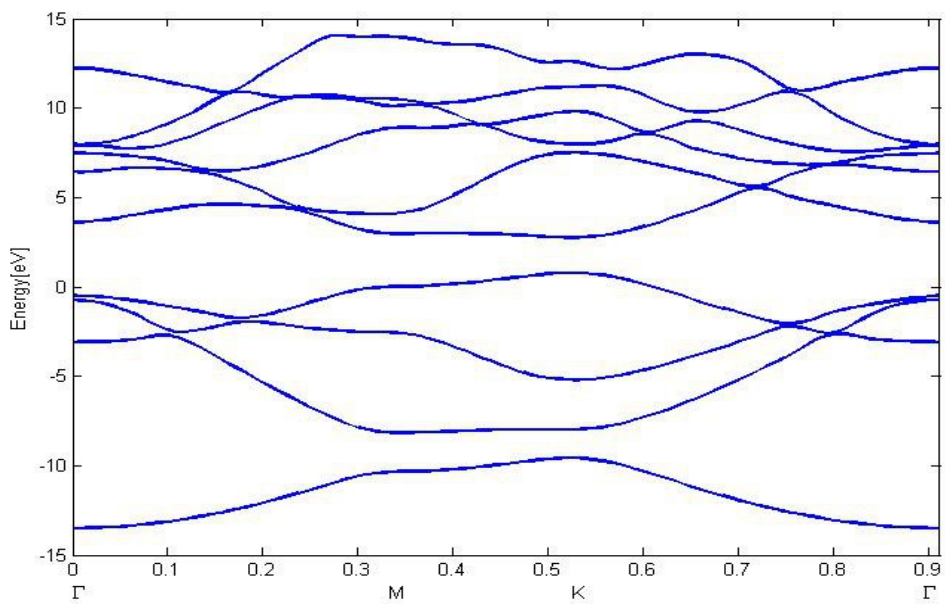


Figure 3.60 DFT band structure of GeC along Γ MK Γ

Planar SiC gets its band gap at K and it is around 0.14 eV according to DFT, and planar GeC has a band gap of around 2 eV at K.

GWA yields the following corrected band structures :

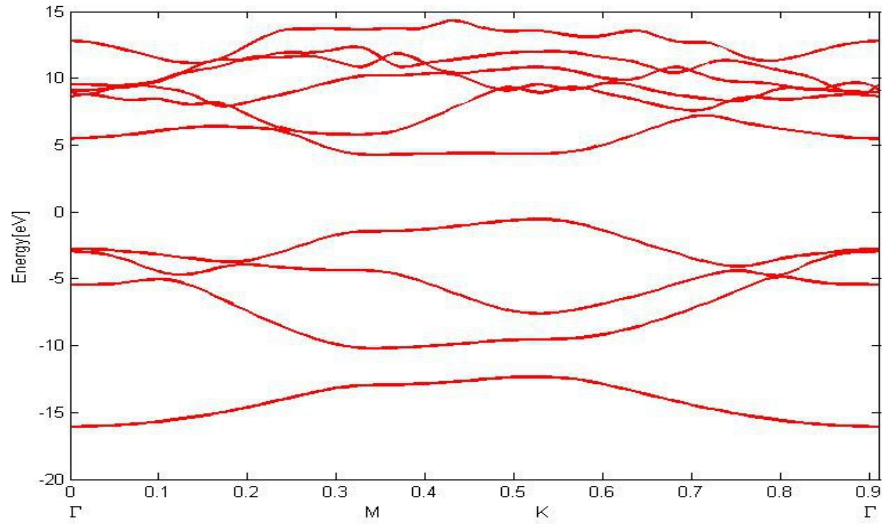


Figure 3.61 GWA band structure of SiC along Γ MK Γ

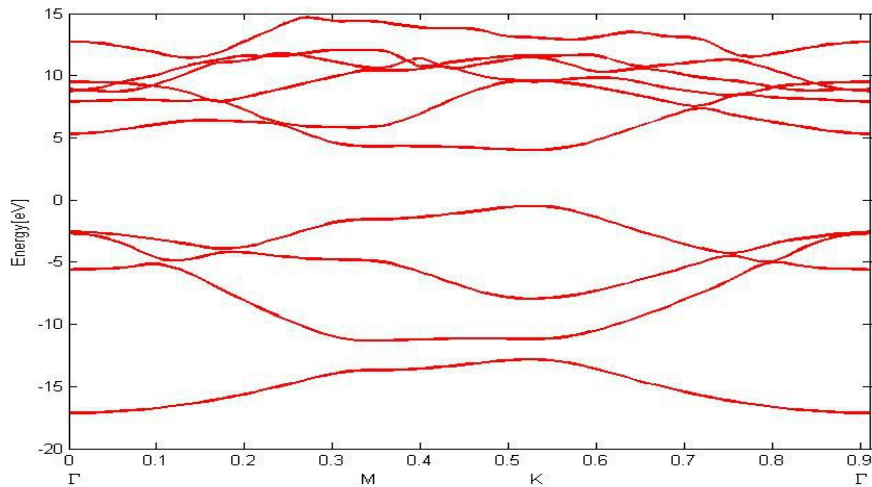


Figure 3.62 GWA band structure of GeC along Γ MK Γ

GWA corrections greatly affect the bandstructure of planar SiC, giving it an indirect band gap of 4.8 eV, with the maximum of the valence band at K and the minimum of the conduction band at M. The corrections are strong and show a lot of dispersion, ranging from 3.6 eV at Γ to 2.5 eV at K. In the case of planar GeC, a bandgap of 4.5 eV at Γ results, with GWA corrections being roughly the same as the ones of planar SiC. Finally, we can put this in comparison to crystal SiC having an indirect band gap of 2.3 eV and crystal GeC having an indirect band gap of 1.76 eV [119].

Now we draw our attention to the optical spectra of these materials for various wavevectors

of an incoming plane wave. We start with z :

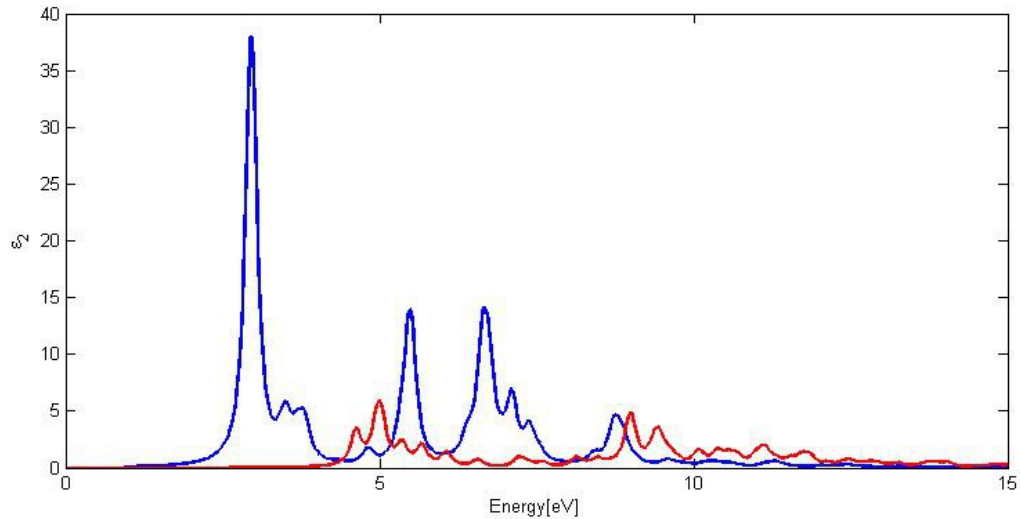


Figure 3.68 Optical spectrum of planar SiC for wavevector z

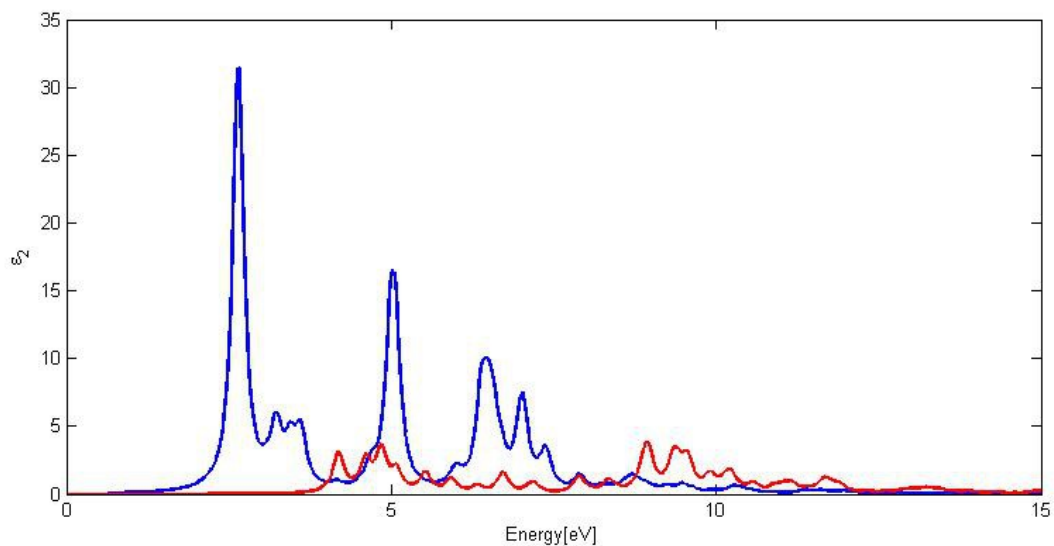


Figure 3.63 Optical spectrum of planar GeC for wavevector z

In both spectra 3 peaks emerge, where the main one comes first and is followed by two smaller peaks. Planar SiC possesses its main peak at 2.95 eV, followed by peaks at 5.48 eV and 6.67 eV. The main peak of planar GeC lies at 2.64 eV, with peaks coming after it at 5 eV and 6.47 eV. All peaks of SiC sit at higher frequencies than the ones of GeC, which is in ac-

cordance with the higher band gap of SiC.

For wavevector γ the spectra are :

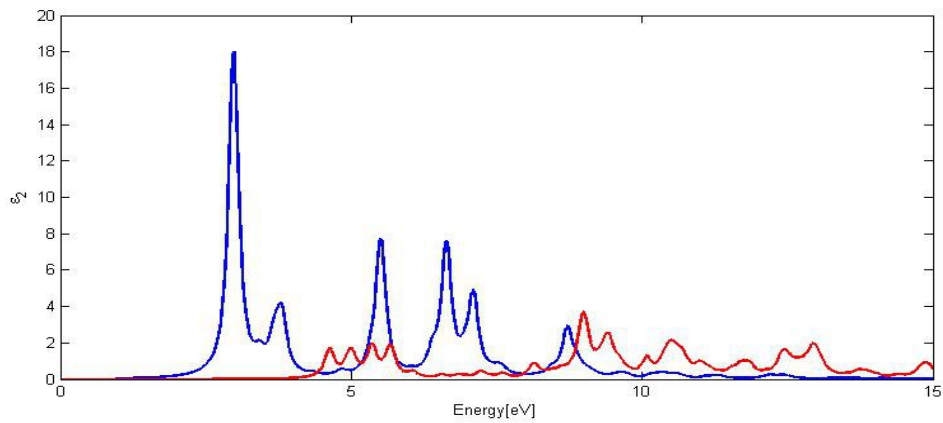


Figure 3.64 Optical spectrum of SiC for wavevector γ

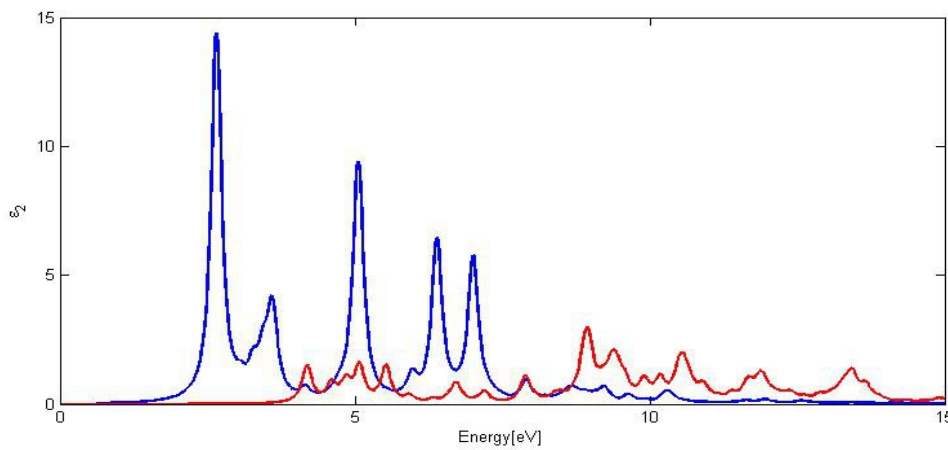


Figure 3.65 Optical spectrum of GeC for wavevector γ

and for wavevector x

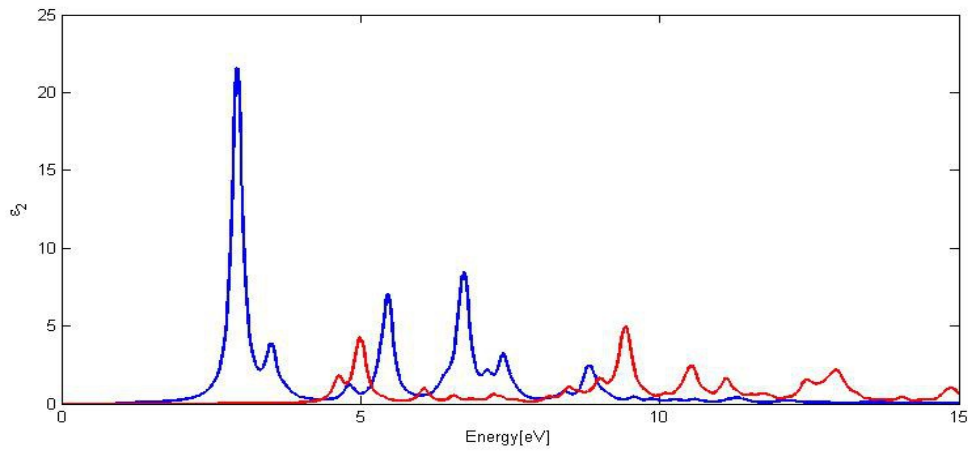


Figure 3.66 Optical spectrum of SiC for wavevector x

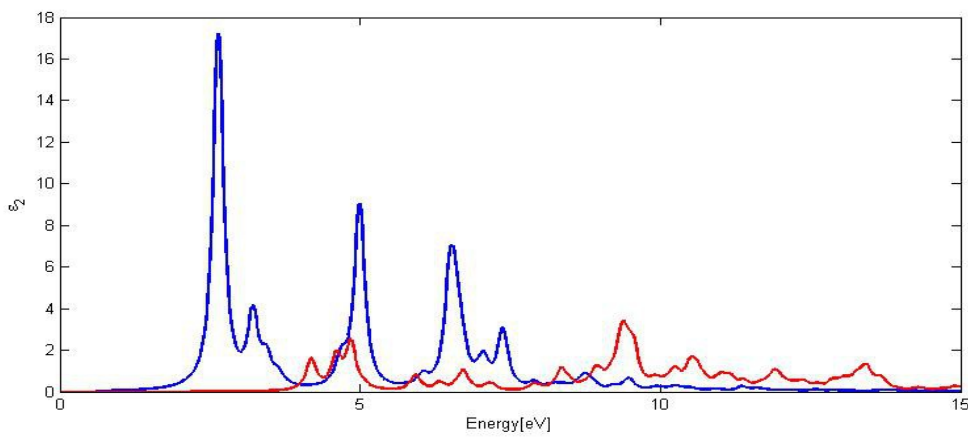


Figure 3.67 Optical spectrum of GeC for wavevector x

We realize that the spectra of wavevectors x, y, z are all roughly identical in both materials. The spectra of x and y are basically the same, and z is their superposition, and thus z should give a very similar spectrum.

4. Nanotubes of various materials

In this chapter, nanotubes and nanoribbons of the nanomaterials considered in the last chapter are examined. We follow the same order as in the last chapter, starting with carbon and boron nitride, then optoelectronic materials, silicon and germanium, and finish with SiC and GeC. These structures are one-dimensional, in contrast to the two-dimensional structures of the last chapter.

4.1 Carbon nanotubes

We start with semiconducting carbon nanotubes with chiralities $(7,0)$, $(8,0)$, $(10,0)$. As mentioned in the first chapter, only some chiralities are semiconducting, and therefore our focus of attention goes to zigzag nanotubes. Their lattice constant has been estimated to be 4.26, which corresponds to rolled up graphene. Let us visualize them first :

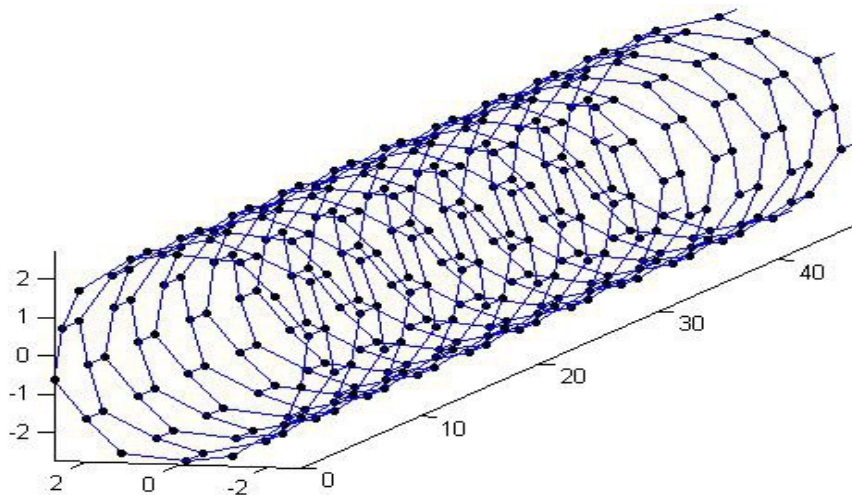


Figure 4.1 $(7,0)$ carbon nanotube, carbon atoms in black

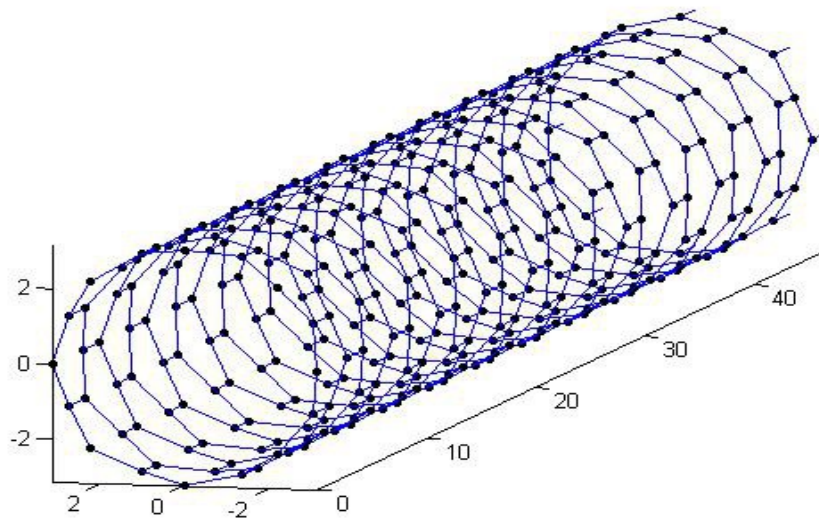


Figure 4.2 (8,0) carbon nanotube, carbon atoms in black

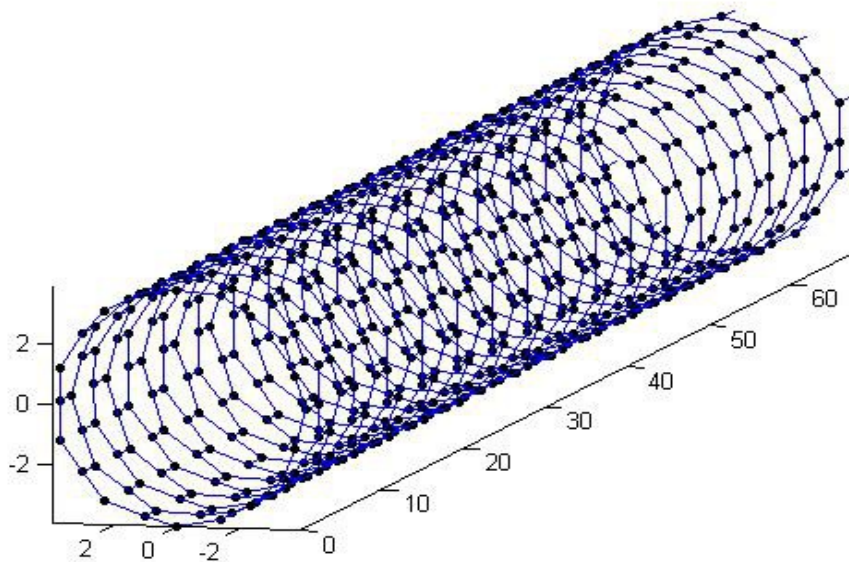


Figure 4.3 (10,0) carbon nanotube , carbon atoms in black

For these carbon nanotubes, DFT yields the following band structures :

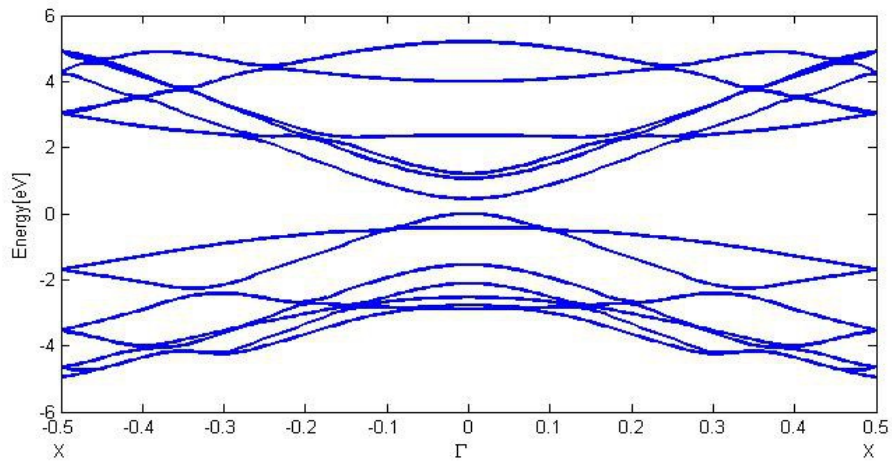


Figure 4.4 DFT bandstructure of a (7,0) carbon nanotube

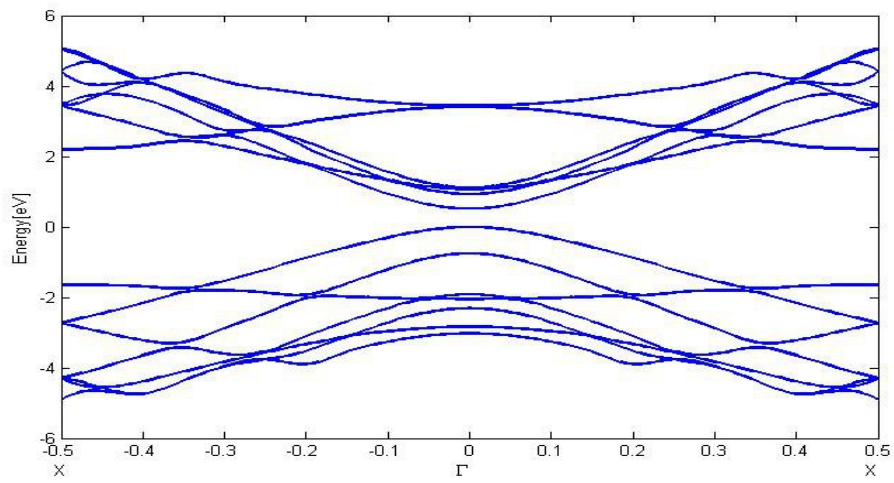


Figure 4.5 DFT bandstructure of a (8,0) carbon nanotube

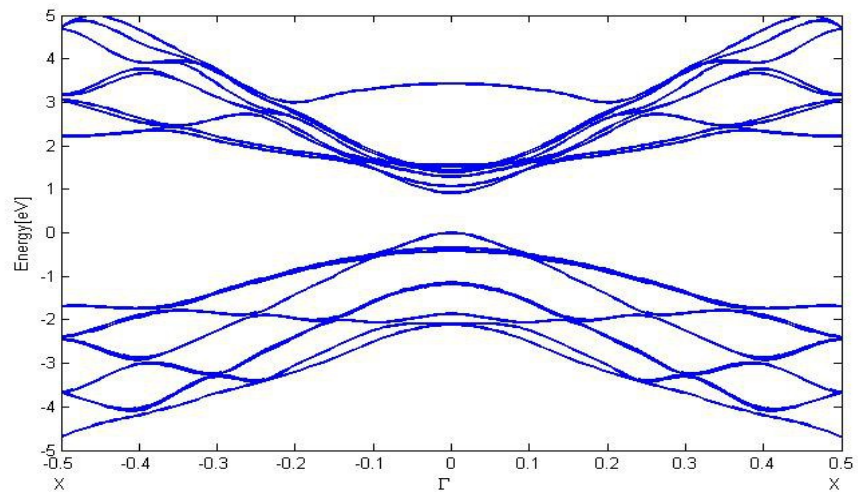


Figure 4.6 DFT band structure of a (10,0) carbon nanotube

The resulting DFT band gap for a (7,0) carbon nanotube is 0.45 eV, for a (8,0) carbon nanotube 0.52 eV and for a (10,0) carbon nanotube 0.92 eV.

Now lets take a look at the band structures GWA provides :

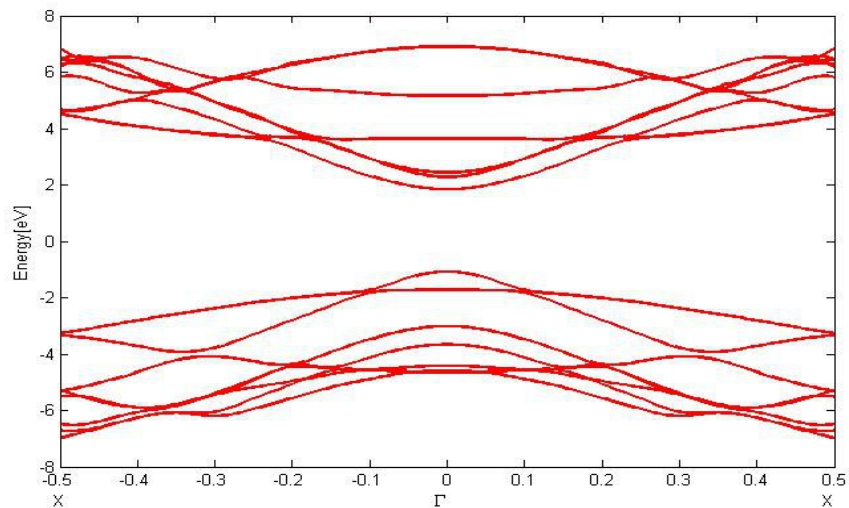


Figure 4.7 GWA band structure of a (7,0) carbon nanotube

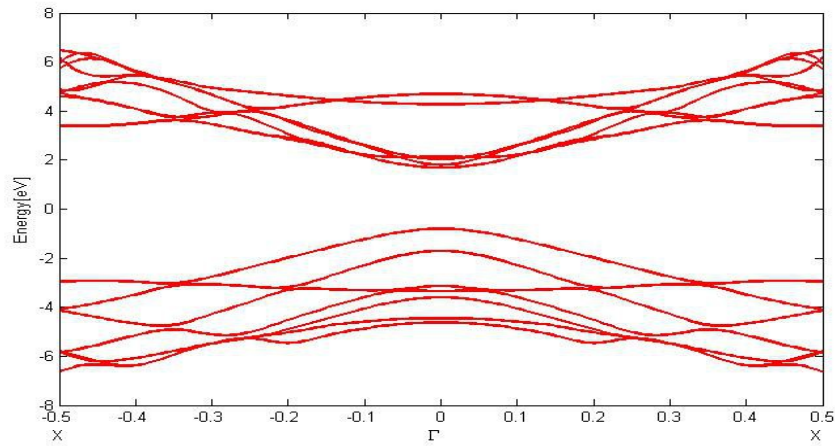


Figure 4.8 GWA band structure of a (8,0) carbon nanotube

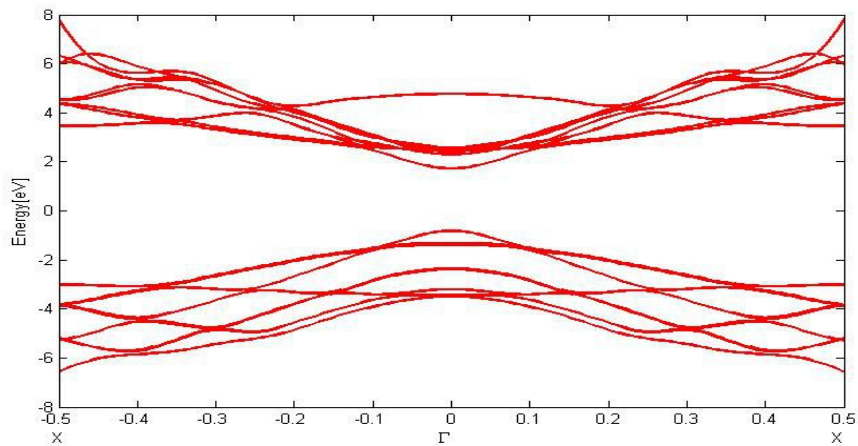


Figure 4.9 GWA band structure of a (10,0) carbon nanotube

In the DFT band structures one realizes the clear trend that the band gaps increase with the diameter of the zigzag carbon nanotube. However, GWA reverses this trend. GWA calculation gives a band gap of 2.92 eV for a (7,0) nanotube, 2.6 eV for a (8,0) carbon nanotube and 2.54 eV in the case of a (10,0) carbon nanotube. A possible explanation is that for smaller chirality parameter $(n,0)$ there are fewer allowed lines in the graphene band structure as explained in the first chapter, and so the allowed line can not come closer to the K point. GWA corrections are weakest at Γ and strongest at X for all nanotubes, and the corrections for the (7,0) carbon nanotube are significantly stronger than the ones for (8,0) and (10,0). They range from 2.3 eV to 3.1 eV for (7,0), whereas for (8,0) and (10,0) they range from 1.6 eV to 2.4 eV.

The optical spectrum for an incoming plane wave with propagation vector z is :

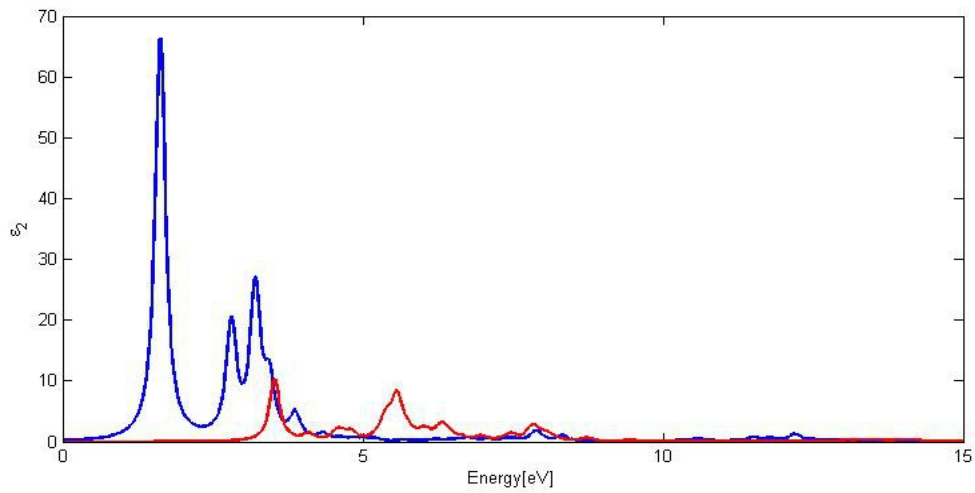


Figure 4.10 Optical spectrum of a (7,0) carbon nanotube with wavevector z

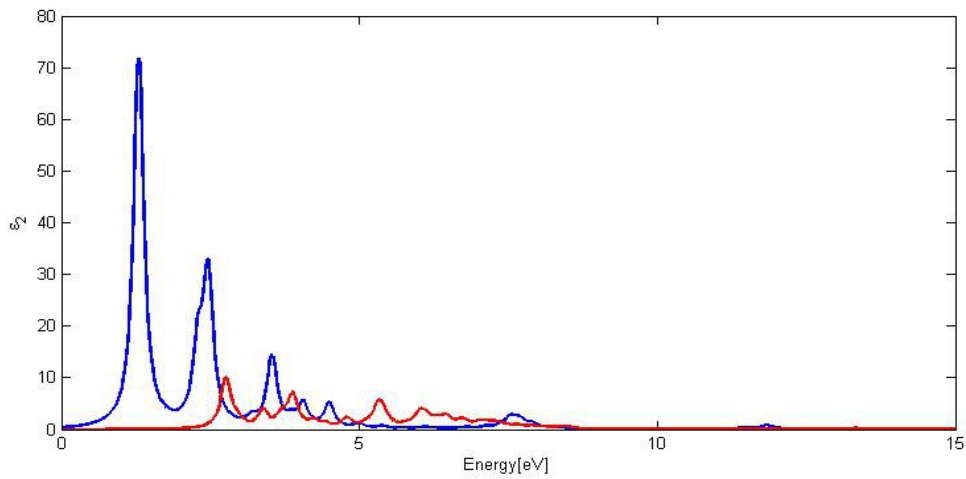


Figure 4.11 Optical spectrum of a (8,0) nanotube for wavevector z

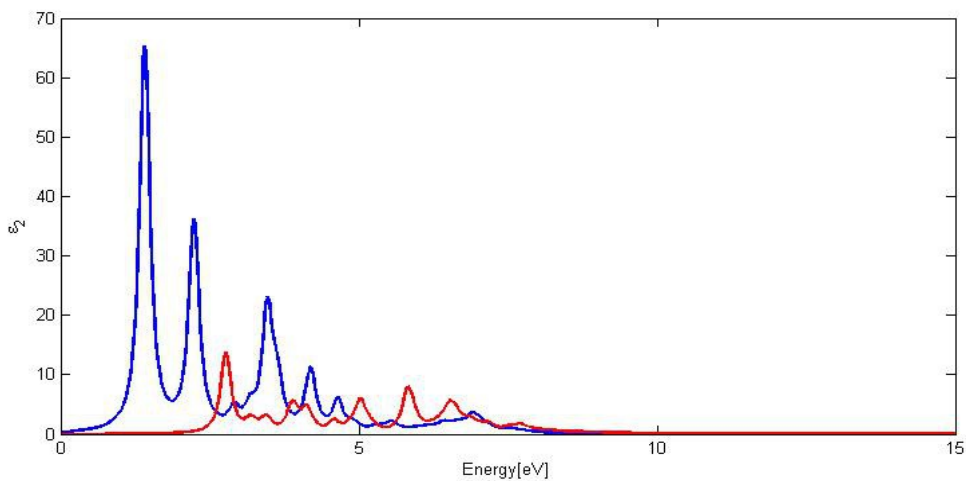


Figure 4.12 Optical spectrum of a (10,0) carbon nanotube for wavevector z

and for wavevector γ

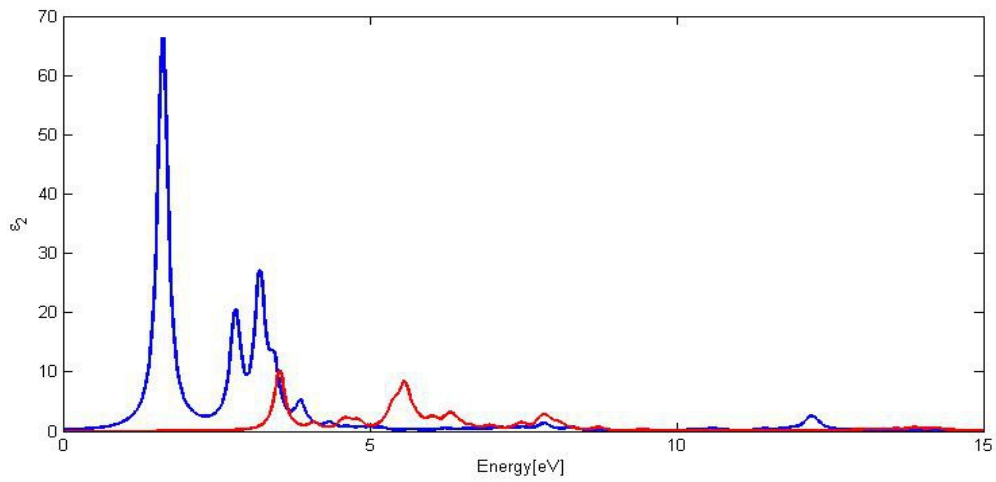


Figure 4.13 Optical spectrum of a (7,0) carbon nanotube for wavevector γ

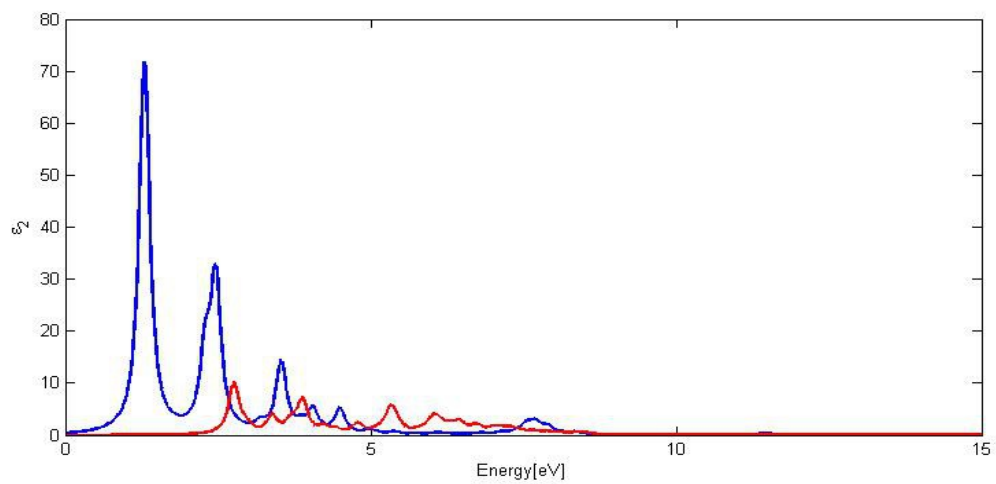


Figure 4.14 Optical spectrum of a (8,0) carbon nanotube for wavevector γ

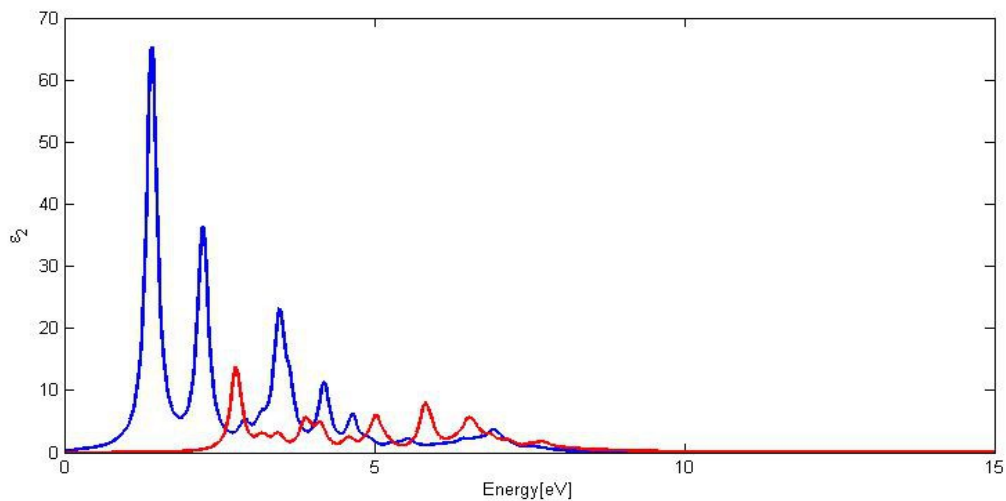


Figure 4.15 Optical spectrum of a (10,0) carbon nanotube for wavevector γ

The optical spectra for wavevectors z and y are nearly identical in all carbon nanotubes considered. In case of wavevectors z and y , the electric field vectors are x,y and x,z . The electric field vector is the most important one because it shows along the tube direction, and the contributions of y and z showing across the carbon nanotube are very similar due to symmetry considerations. Therefore the resulting spectra for wavevectors z and y are nearly equal. The (7,0) carbon nanotube exhibits its main peak at 1.63 eV, followed by a double peak at 2.81 eV and at 3.21 eV, the (8,0) nanotube has its main peak at 1.3 eV with peaks at 2.45 eV and at 3.53 eV coming after it, and the (10,0) carbon nanotube has its main peak at 1.41 eV which is followed by peaks at 2.23 eV and 3.47 eV. The first peak of the (7,0) carbon nanotube arrives at higher frequency that the ones of the other carbon nanotubes, which is consistent with the higher band gap of (7,0).

For wavevector x one gets

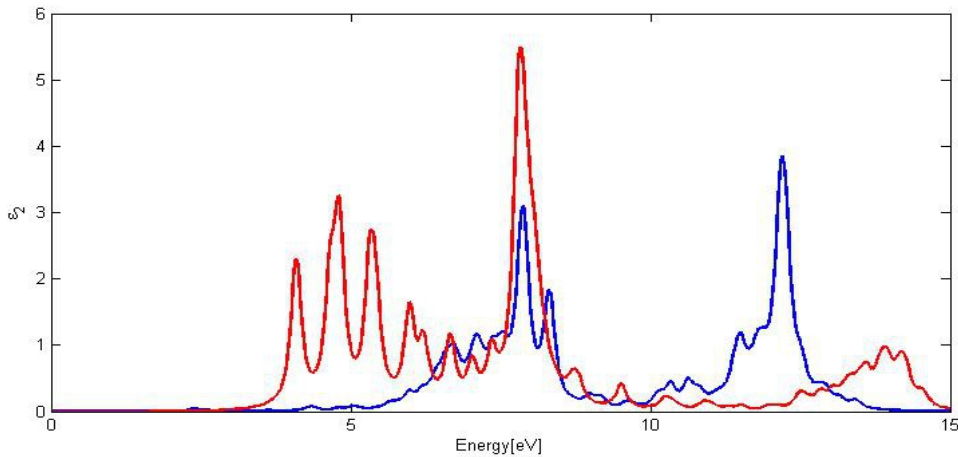


Figure 4.16 Optical spectrum of a (7,0) carbon nanotube for wavevector x

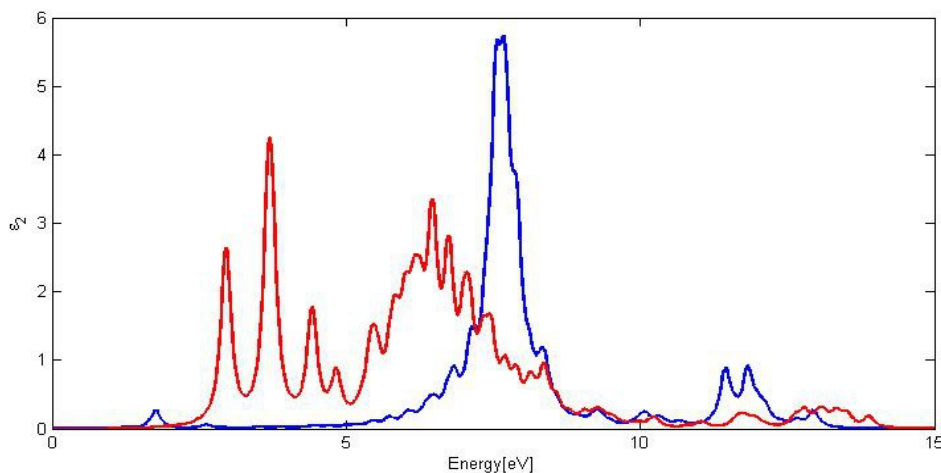


Figure 4.17 Optical spectrum of a (8,0) carbon nanotube for wavevector x

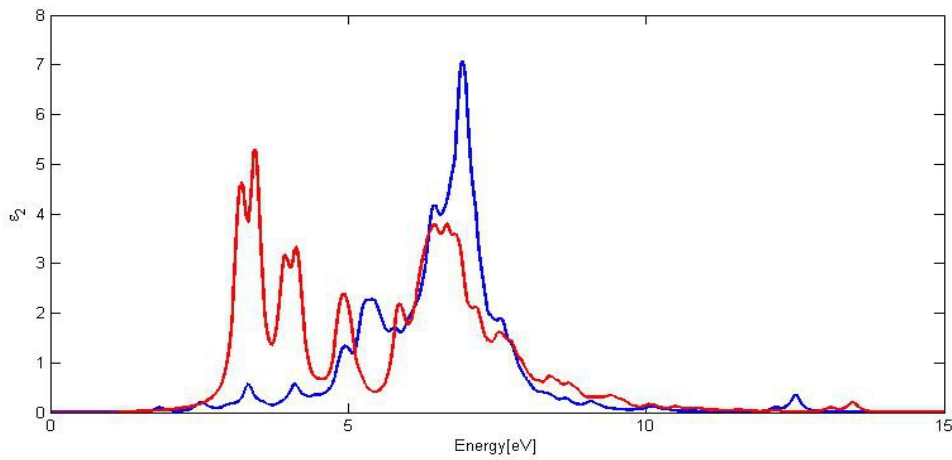


Figure 4.18 Optical spectrum of a (10,0) carbon nanotube for wavevector x

From the results depicted above we can see that the (7,0) has two peaks, the main one at 122eV and another peak before at 7.87 eV. The (8,0) carbon nanotube has its main peak at 7.67 eV, and (10,0) has a broad peak at 6.91 eV. Once again the same trend emerges that (7,0) peaks have the highest frequencies, declining for (8,0) and (10,0).

4.2 Boron nitride, boron arsenide and boron phosphide nanotubes

As next step, we take a look at boron nitride. Like carbons nanotubes for graphene, we can consider nanotubes for the planar boron nitride of 3.2 by rolling it up. Their lattice constant has been estimated to be 4.35 Angstrom. Boron nitride nanotubes look as shown below:

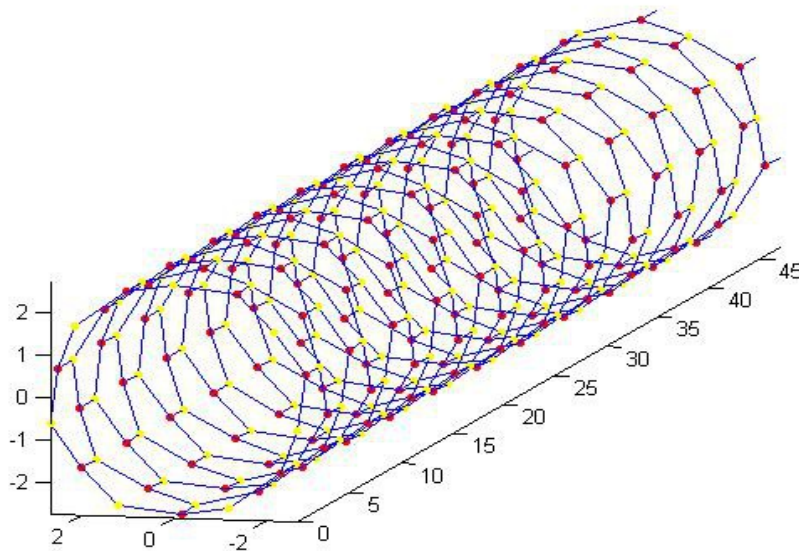


Figure 4.19 (7,0) boron nitride nanotube, boron atoms in yellow, nitrogen atoms in red

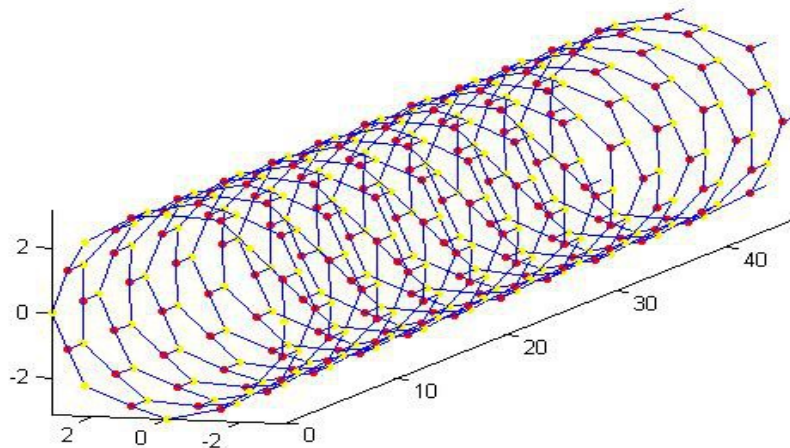


Figure 4.20 (8,0) boron nitride nanotube, boron atoms in yellow, nitrogen atoms in red

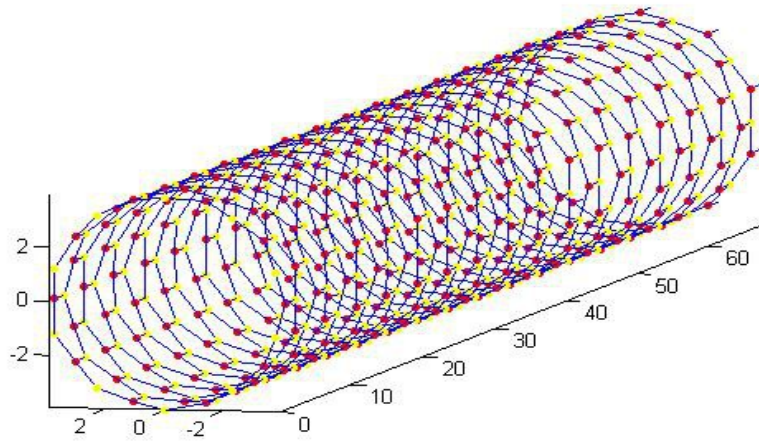


Figure 4.21 (10,0) boron nitride nanotube, boron atoms in yellow, nitrogen atoms in red

We regard the same chiralities like for carbon nanotubes, which are defined in analogy, as graphene and planar boron nitride have the same hexagonal lattice structure. DFT provides the following band structures for them :

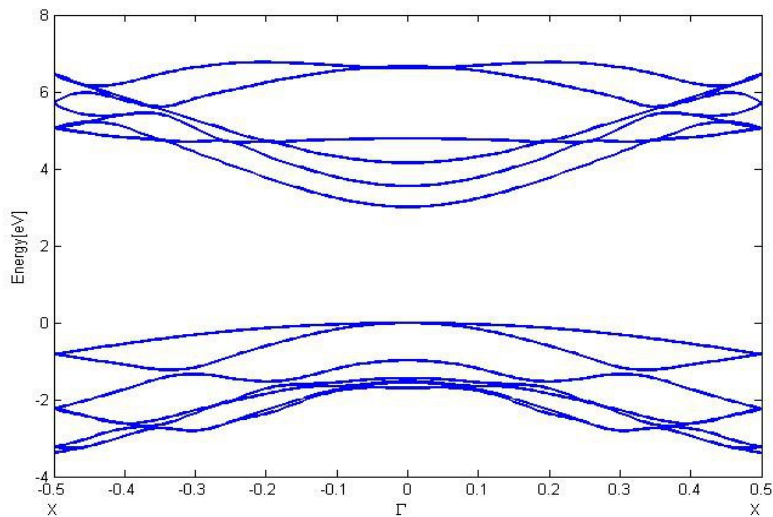


Figure 4.22 DFT band structure of a (7,0) boron nitride nanotube

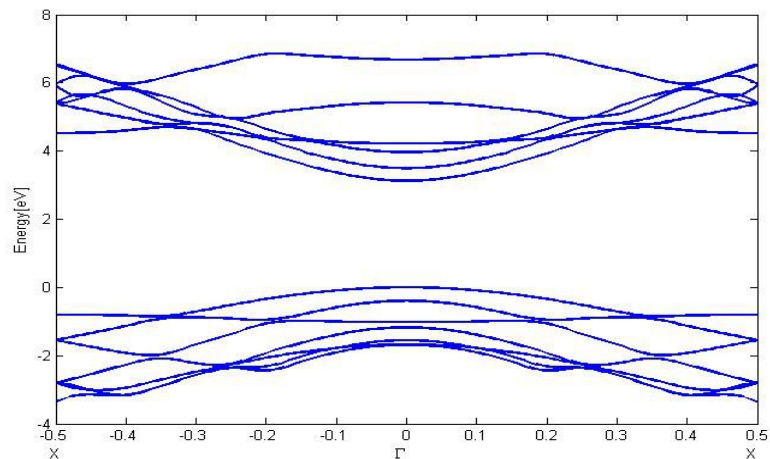


Figure 4.23 DFT band structure of a (8,0) boron nitride nanotube

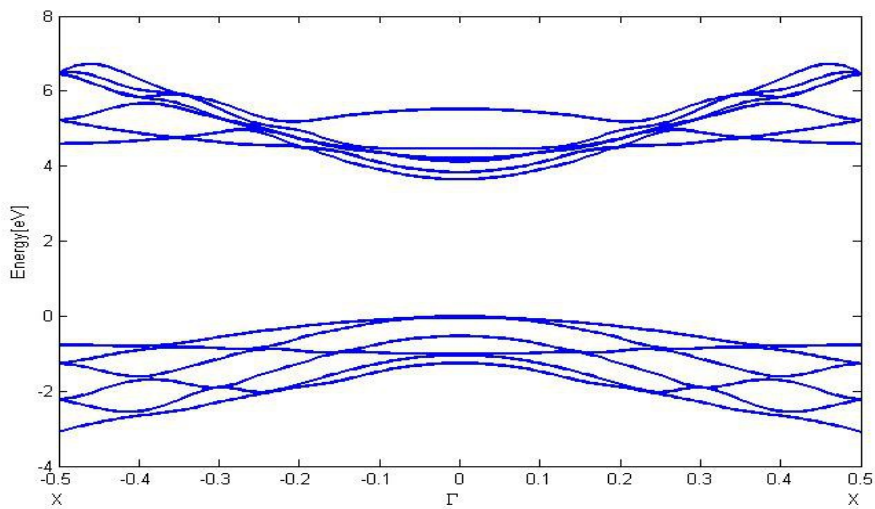


Figure 4.24 DFT band structure of a (10,0) boron nitride nanotube

One can conclude from the results above that the DFT band gaps increase with the diameter of the nanotubes. For a (7,0) boron nitride nanotube one gets an band gap of 3 eV, for a (8,0) nanotube one gets 3.12 eV and for a (10,0) nanotube one has a band gap of 3.64 eV according to DFT. But GWA yields quite different results, as it has done for carbon nanotubes. So lets look at the GWA band structures:

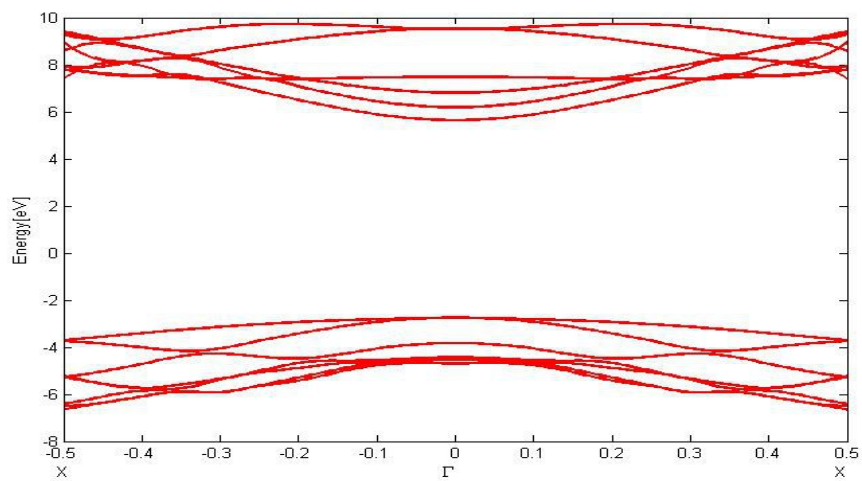


Figure 4.25 GWA band structure of a (7,0) boron nitride nanotube

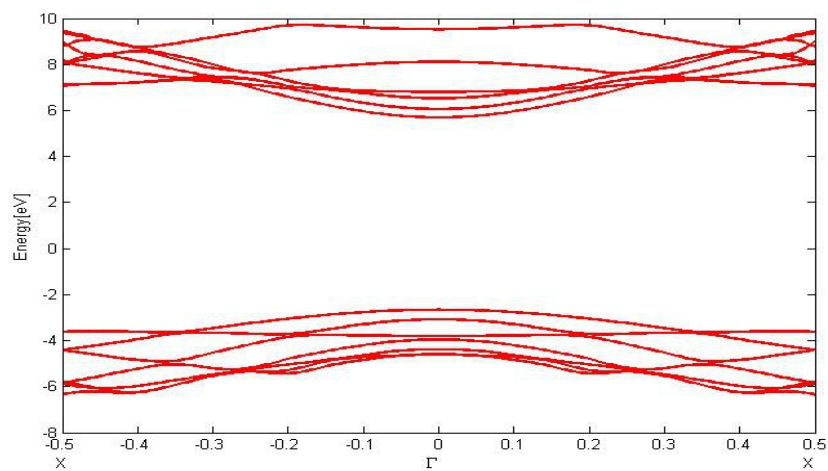


Figure 4.26 GWA band structure of a (8,0) boron nitride nanotube

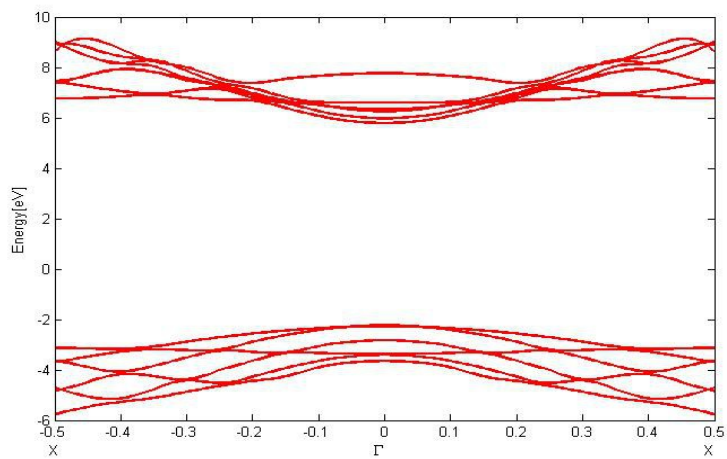


Figure 4.27 GWA band structure of a (10,0) boron nitride nanotube

The band structures obtained by GWA give different band gaps, in detail 8.4 eV for a (7,0) nanotube, 8.3 eV for a (8,0) nanotube and 8 eV for a (10,0). It follows that the GWA are not only huge in their magnitude, but also reverse the order of band gaps like for carbon nanotubes. According to GWA results, band gaps decrease with higher diameter. In contrast to carbon nanotubes, the GWA correction for boron nitride nanotubes show little dispersion. Their are strongest for the (7,0) nanotube with a great magnitude of approximately 5.3 eV , and weakest for the (10,0) nanotube with a size of 4.4 eV, which is still huge. Furthermore, the optic of them behaves as follows :

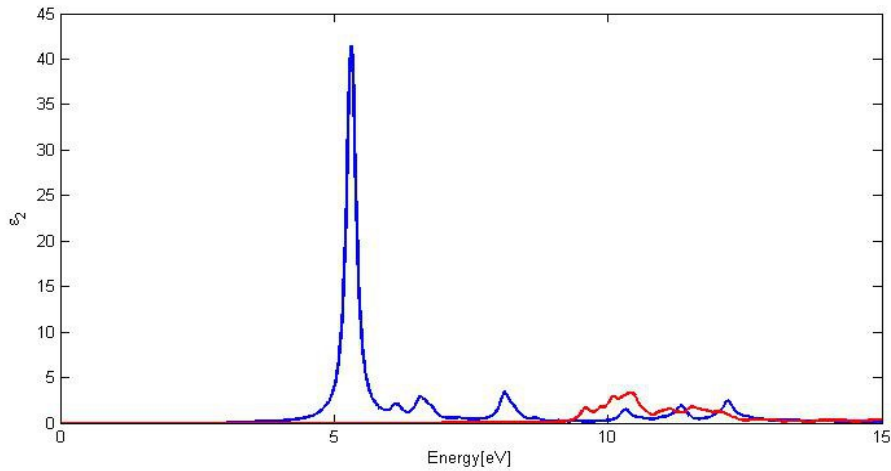


Figure 4.28 Optical spectrum of a (7,0) boron nitride nanotube for wavevector z

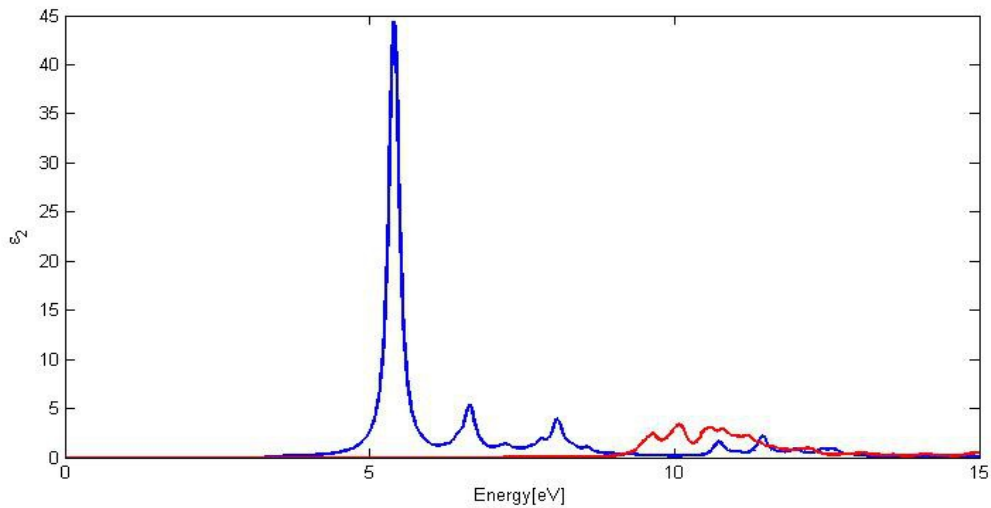


Figure 4.29 Optical spectrum of a (8,0) boron nitride nanotube for wavevector z

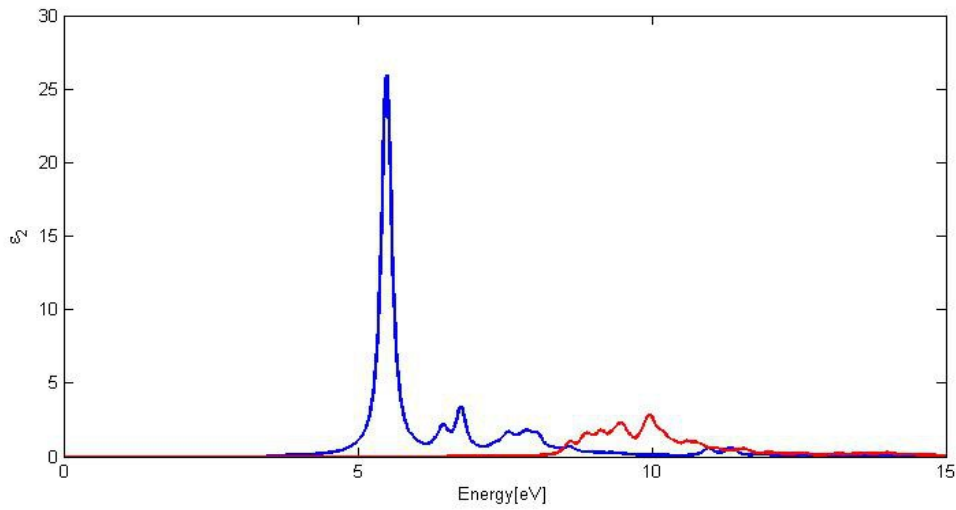


Figure 4.30 Optical spectrum of a (10,0) boron nitride nanotube for wavevector z

, and for wavevector y :

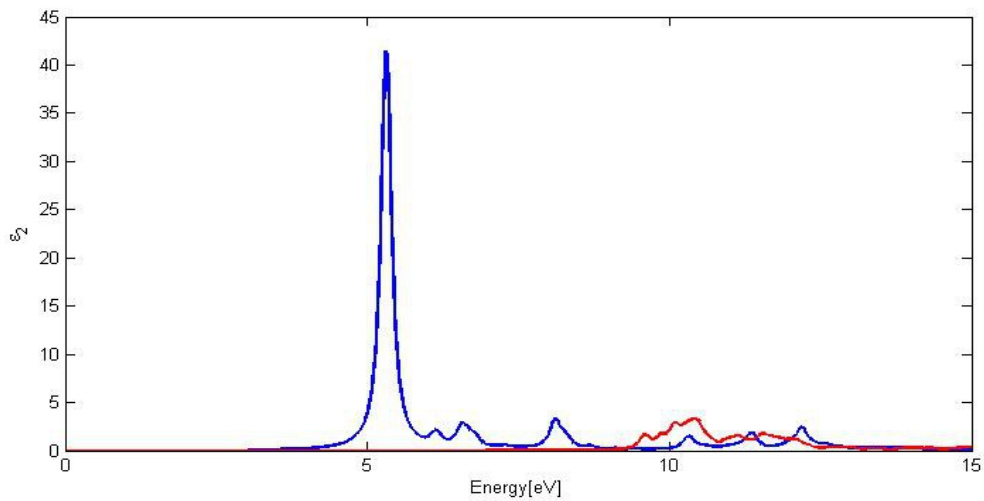


Figure 4.31 Optical spectrum of a (7,0) boron nitride nanotube for wavevector y

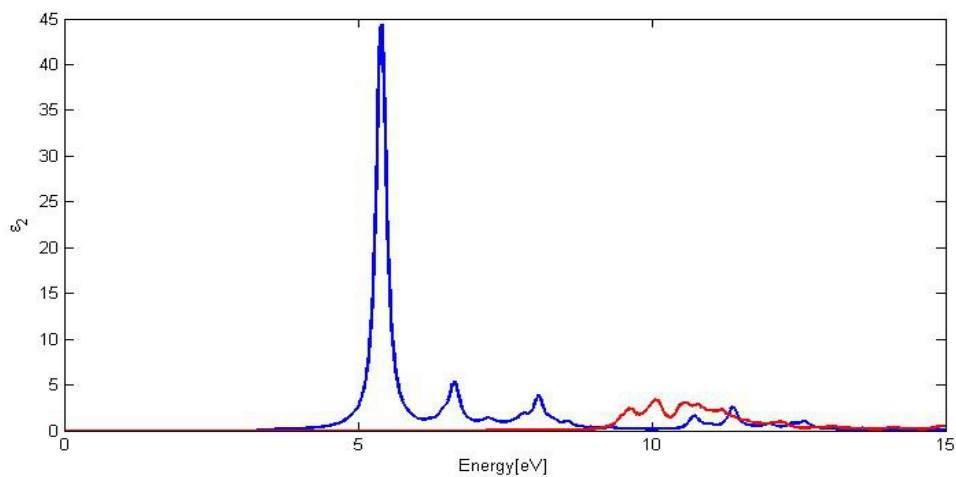


Figure 4.32 Optical spectrum of a (8,0) boron nitride nanotube for wavevector y

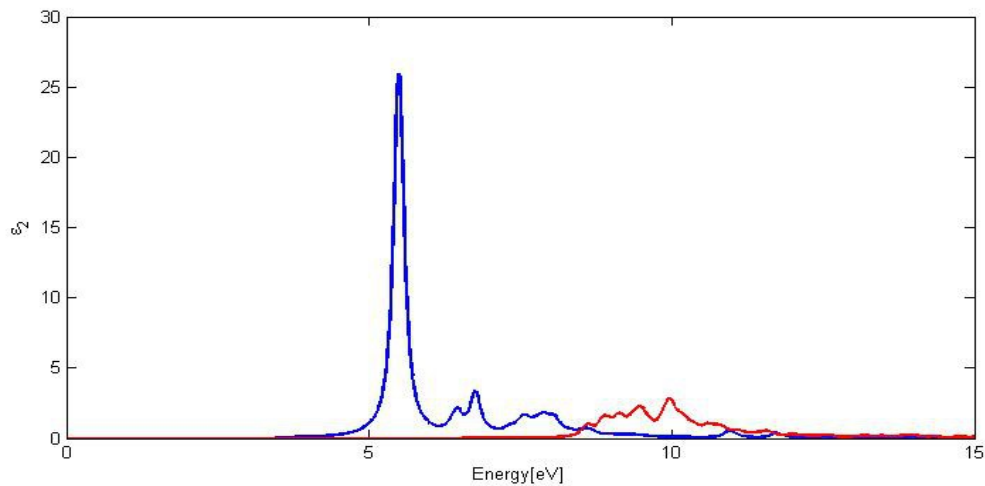


Figure 4.33 Optical spectrum of a (10,0) boron nitride nanotube for wavevector y

It seems obvious that the optical spectra for wavevectors z and y are nearly the same in all nanotubes, for the same reasons explained in the previous section about carbon nanotubes. All spectra exhibit one characteristic main peak. For the (7,0) nanotube, he is located at 5.3 eV, for the (8,0) nanotube at 5.4 eV and for the (10,0) nanotube at 5.5 eV. This can be explained by the circumstance that for the (7,0) nanotube the size of the electron-hole interaction is very strong, up to 5 eV for the first excited states, whereas for the (10,0) nanotube it maximally reaches 3.9 eV.

For wavevector x one receives these optical spectra:

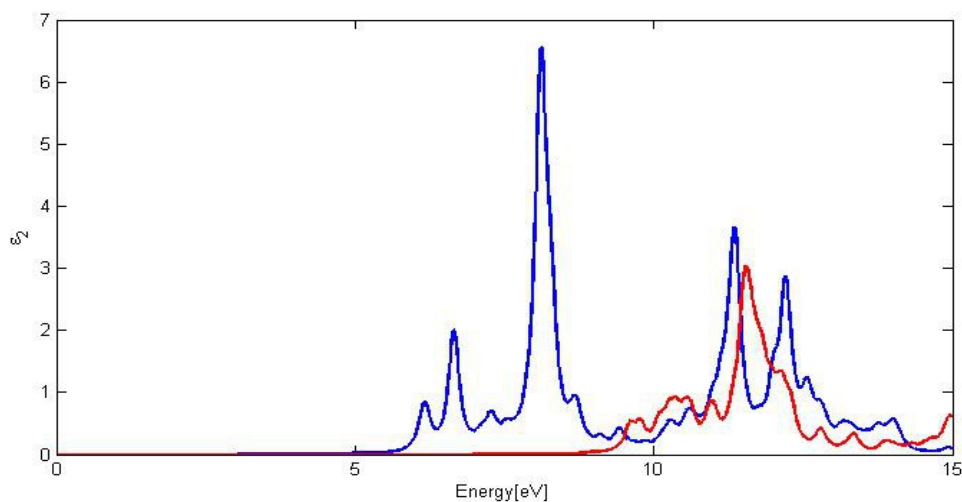


Figure 4.34 Optical spectrum of a (7,0) boron nitride nanotube for wavevector x

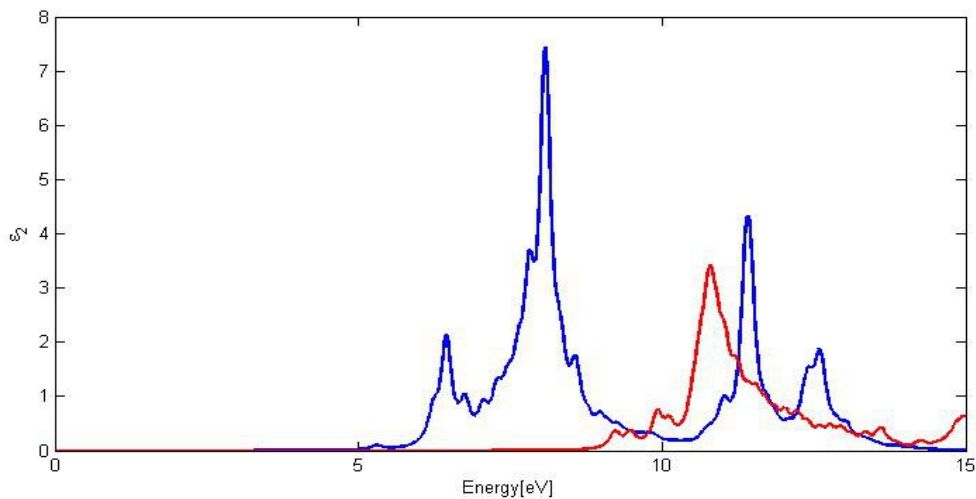


Figure 4.35 Optical spectrum of a (8,0) boron nitride nanotube for wavevector x

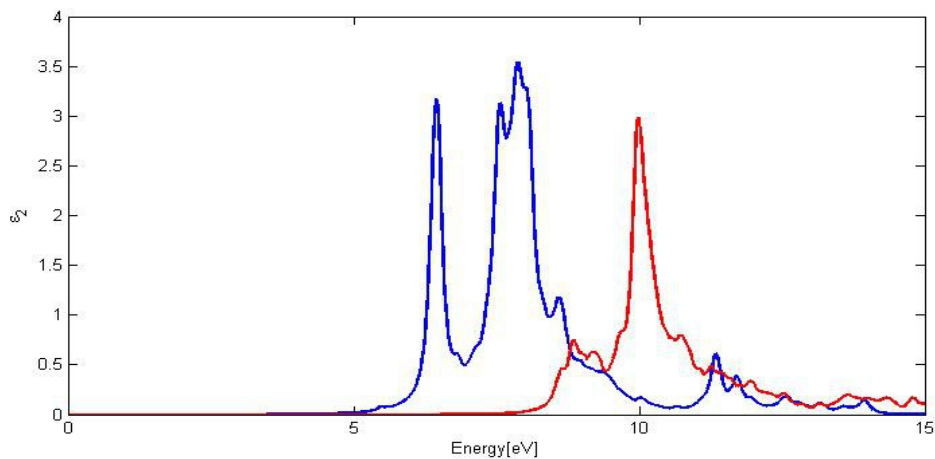


Figure 4.36 Optical spectrum of a (10,0) boron nitride nanotube for wavevector x

One sees that the (7,0) nanotube has its main peak at 8.12 eV, followed by smaller peaks at 11.34 eV and 12.1 eV, the (8,0) nanotube has its main peak at 8.07 eV with a second peak at 11.4 eV, and finally the (10,0) nanotube has a sharp peak at 6.46 eV together with a broad main peak around 7.88 eV. Consequently the position of the main peaks moves to lower frequencies for bigger diameter.

Next we look at nonotubes of boron arsenide :

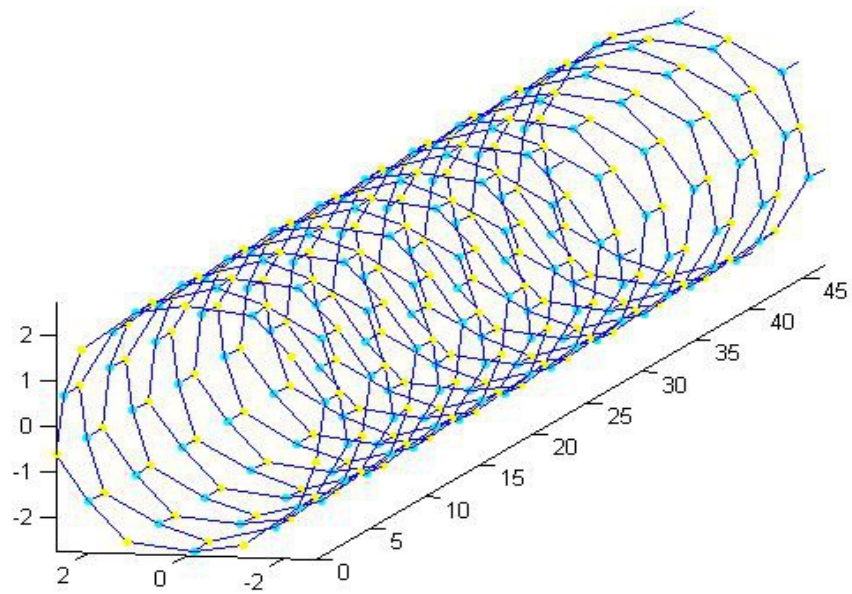


Figure 4.37 (7,0) boron arsenide nanotube, boron atoms yellow and arsenic atoms cyan

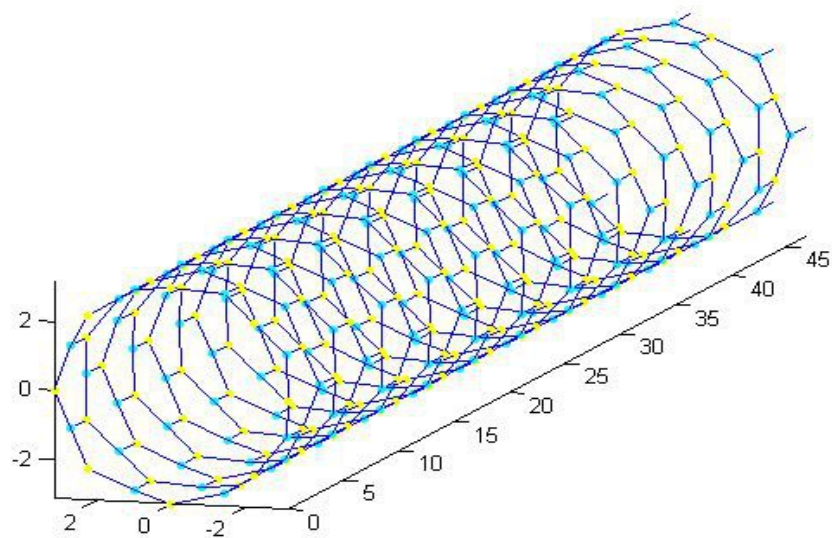


Figure 4.38 (8,0) boron arsenide nanotube, boron atoms yellow and arsenic atoms cyan

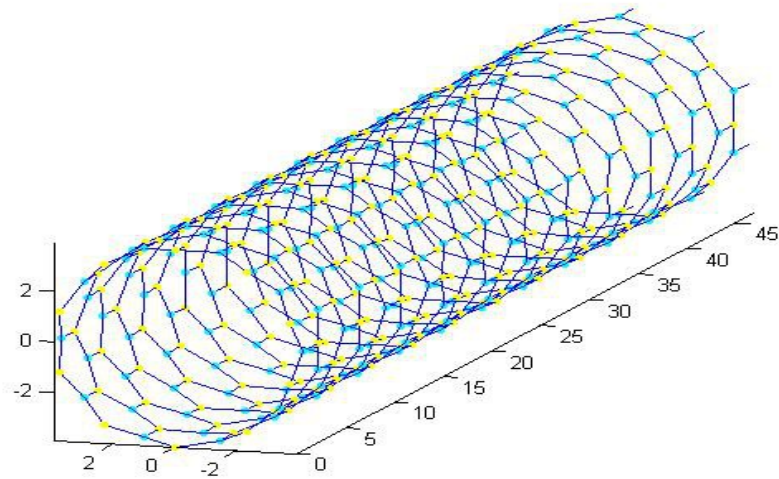


Figure 4.39 (10,0) boron arsenide nanotube, boron atoms yellow and arsenic atoms cyan

For boron arsenide nanotubes, a lattice constant of 5.91 Angstrom was computed. DFT calculation leads to the following band structures:

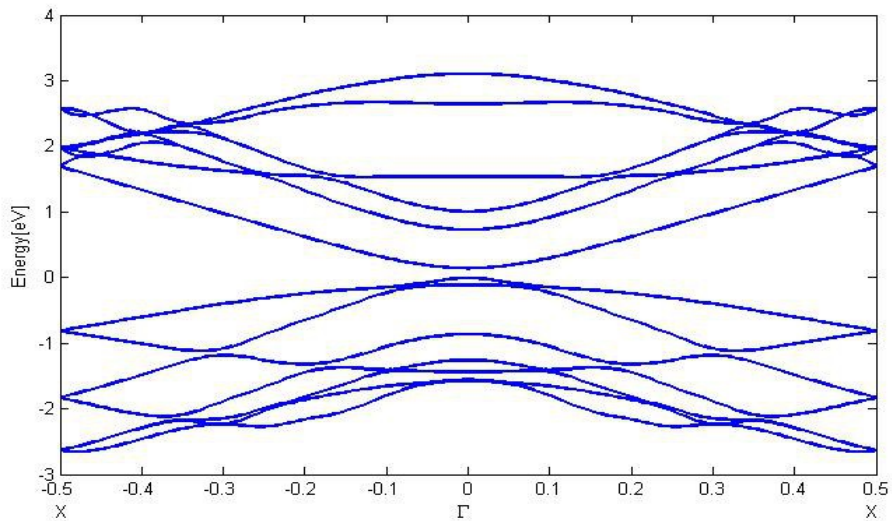


Figure 4.40 DFT band structure of a (7,0) boron arsenide nanotube

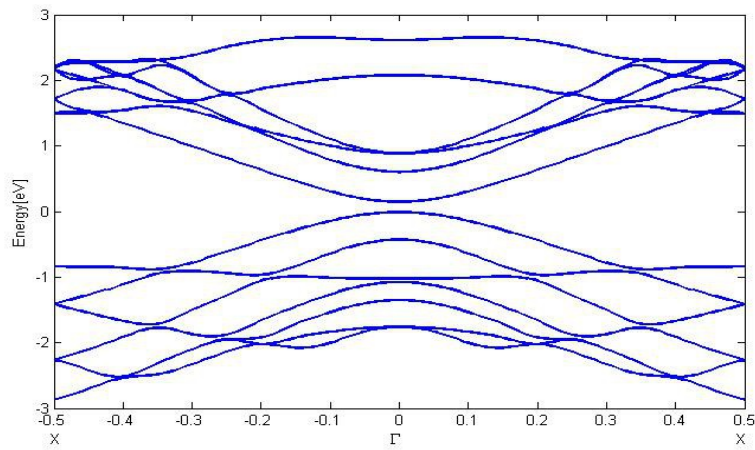


Figure 4.41 DFT band structure of a (8,0) boron arsenide nanotube

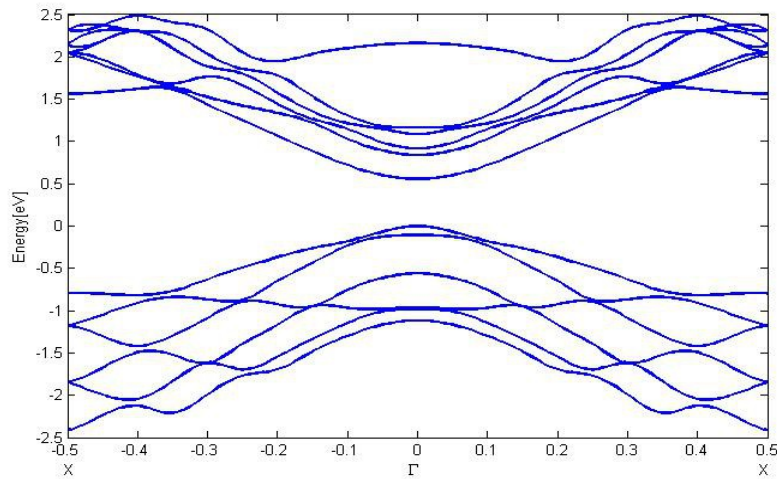


Figure 4.42 DFT band structure of a (10,0) boron arsenide nanotube

We find out a band gap of 0.15 eV for (7,0), 0.156 eV for (8,0) and 0.55 eV for (10,0) using DFT. These band structures are significantly corrected by GWA:

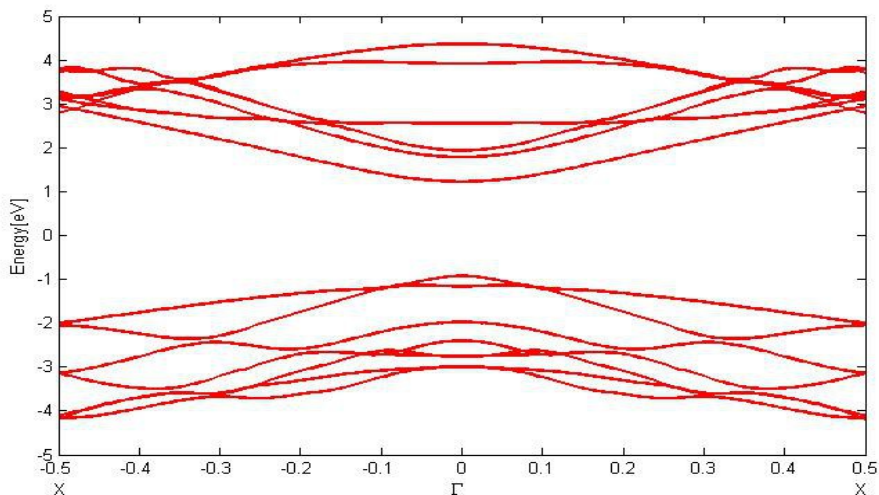


Figure 4.43 GWA band structure of a (7,0) boron arsenide nanotube

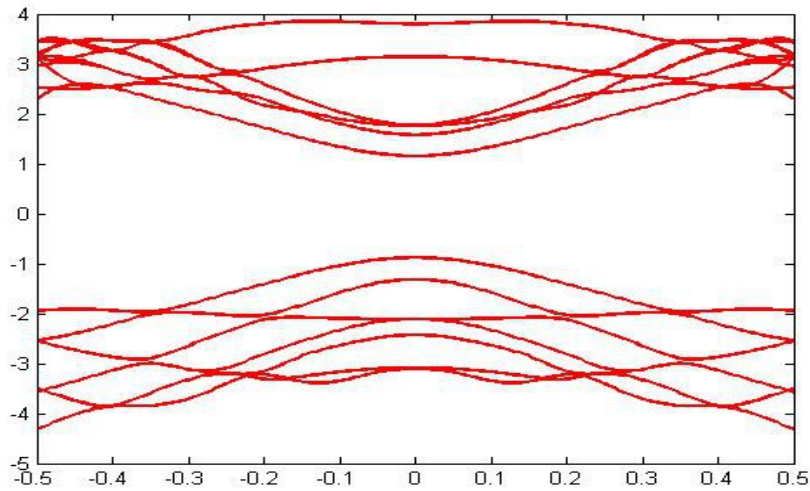


Figure 4.44 GWA band structure of a (8,0) boron arsenide nanotube

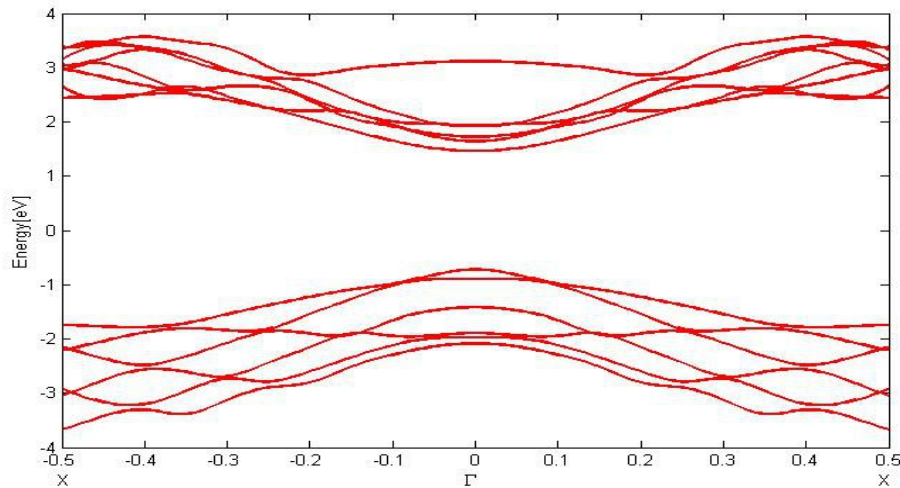


Figure 4.45 GWA band structure of a (10,0) boron arsenide nanotube

The band gaps get significantly increased by GWA corrections, namely 2.14 eV for the (7,0) nanotube, 2.03 eV for the (8,0) nanotube and 2.18 eV for the (10,0) nanotube. There seems to be no clear order of the band gap sizes, but however, the (10,0) nanotube has the largest band gap. The strength of GWA corrections slightly decreases for larger nanotube size, and for all nanotubes, the corrections show small dispersion, being strongest at Γ and weakest at X.

Now let's regard the optical properties of these nanotubes. For an incoming plane wave with wavevector z , their optical spectra are :

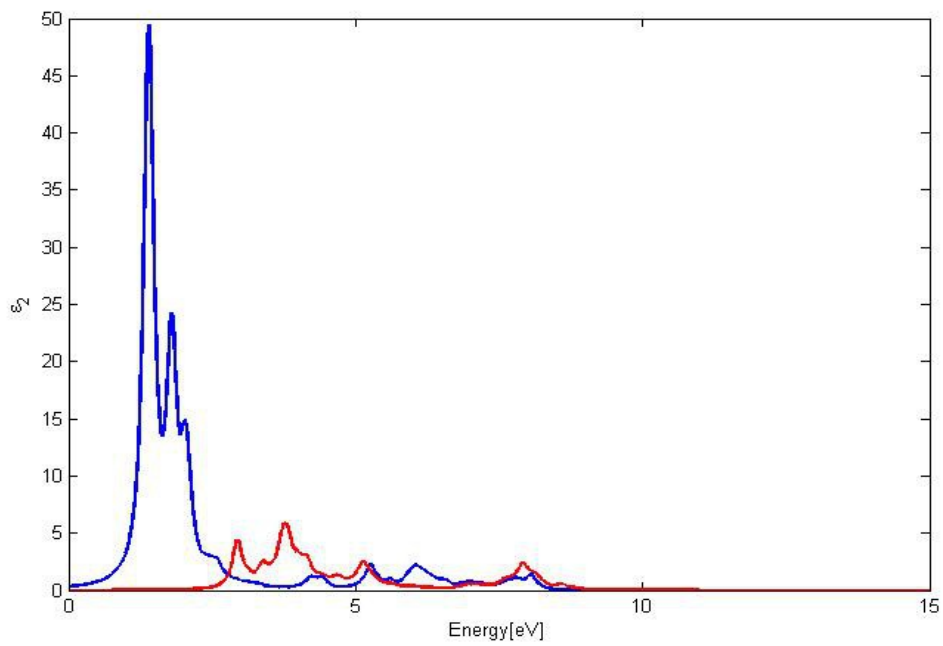


Figure 4.46 Optical spectrum of a (7,0) boron arsenide nanotube for wavevector z

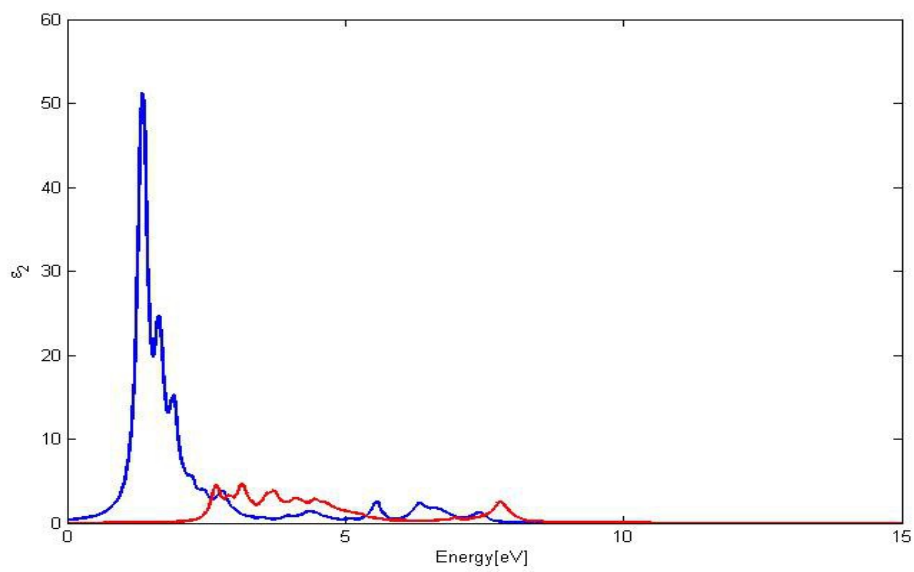


Figure 4.47 Optical spectrum of a (8,0) boron arsenide nanotube for wavevector z

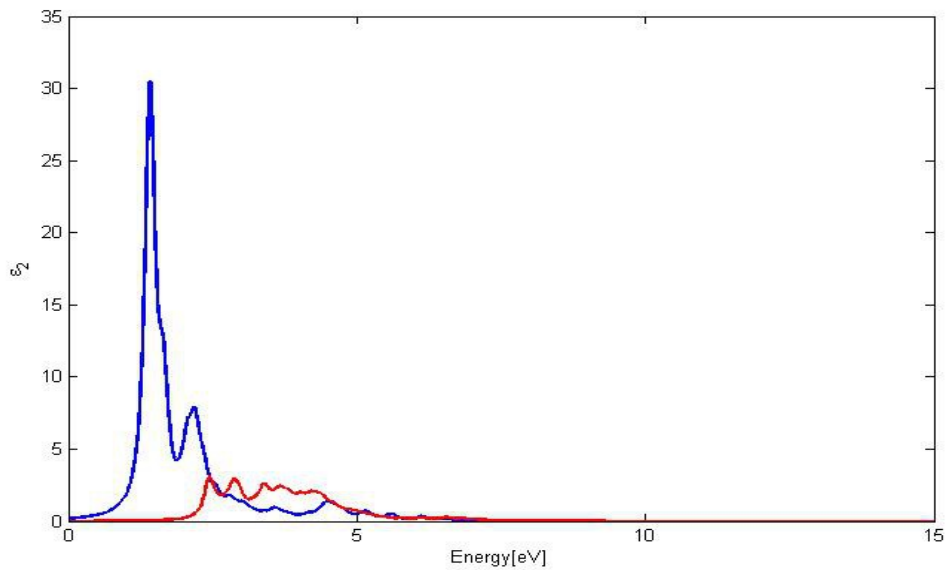


Figure 4.48 Optical spectrum of a (10,0) boron arsenide nanotube with wavevector z , with nearly identical spectra for wavevector y .

One can see that all spectra have sharp first peak followed by shoulder peaks. The main peak lies at 1.39 eV for the (7,0) nanotube, at 1.35 eV for the (8,0) nanotube and at 1.41 eV for the (10,0) nanotube. Thus the position of the peaks correlates with the band gap sizes, the larger the band gap, the larger the peak frequency, which makes sense.

In case of wavevector x , the dielectric functions are :

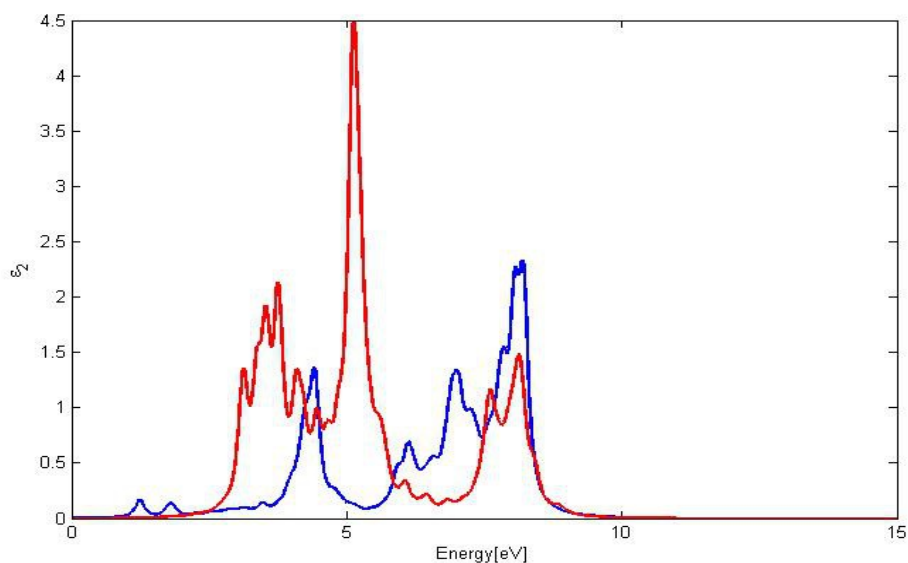


Figure 4.49 Optical spectrum of a (7,0) boron arsenide nanotube for wavevector x

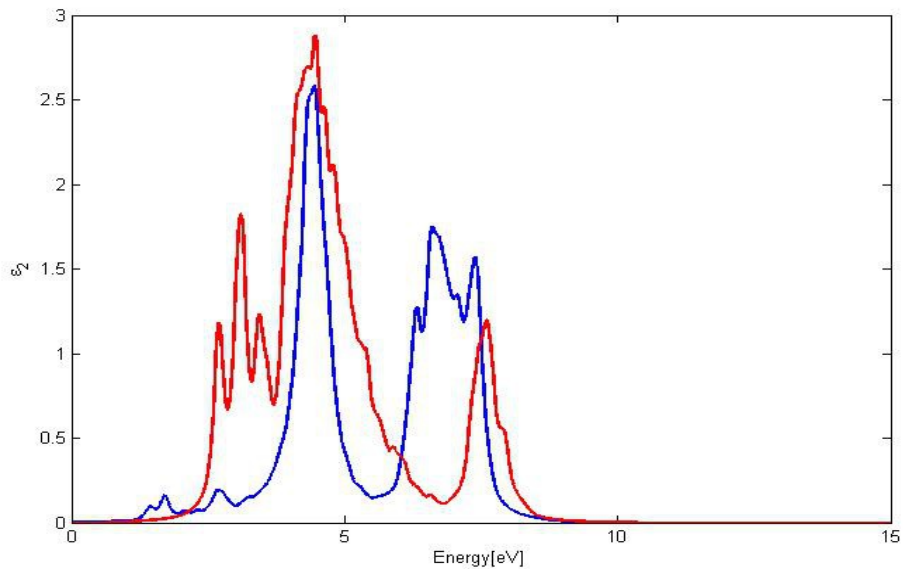


Figure 4.50 Optical spectrum of a (8,0) boron arsenide nanotube for wavevector x

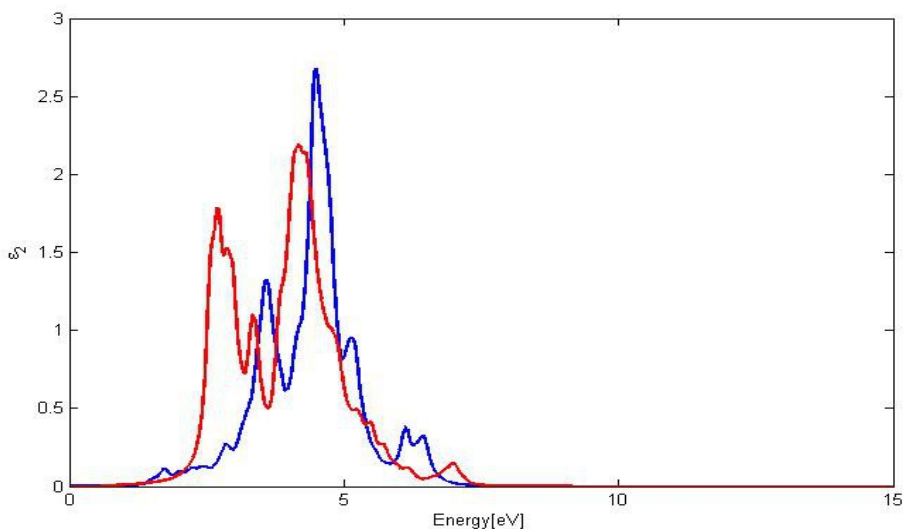


Figure 4.51 Optical spectrum of a (10,0) boron arsenide nanotube for wavevector x

In contrast to the case of wavevector z and y, the spectra belonging to wavevector x are broad and show many peaks, the most important ones being located at 1.37 eV and 8.19 eV for (7,0), at 4.52 eV, 6.61 and at 7.39 eV for (8,0), and at 3.58 eV and 4.48 eV for (10,0). It seems obvious that the spectrum of smaller nanotubes achieves higher frequencies, as the frequency of the highest-energy peak decreases for bigger nanotubes.

Furthermore, we examine boron phosphide nanotubes. Calculations have revealed a lattice

constant of 5.61 Angstrom for them:

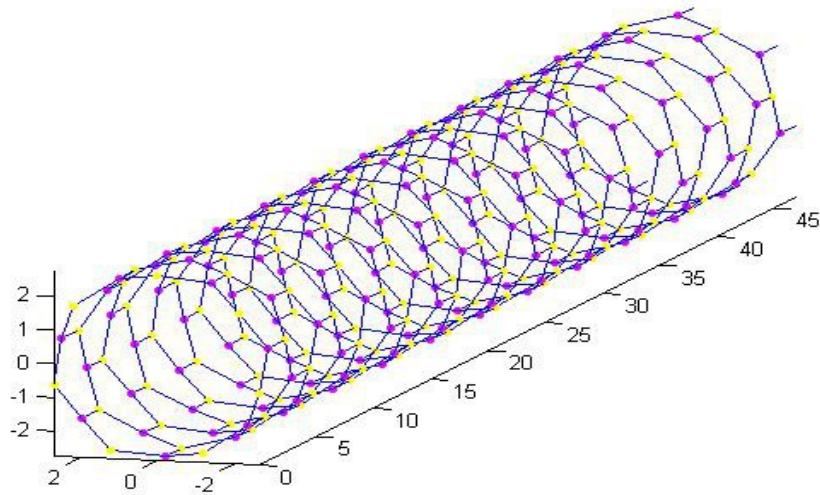


Figure 4.52 (7,0) boron phosphide nanotube, boron yellow and phosphorous magenta

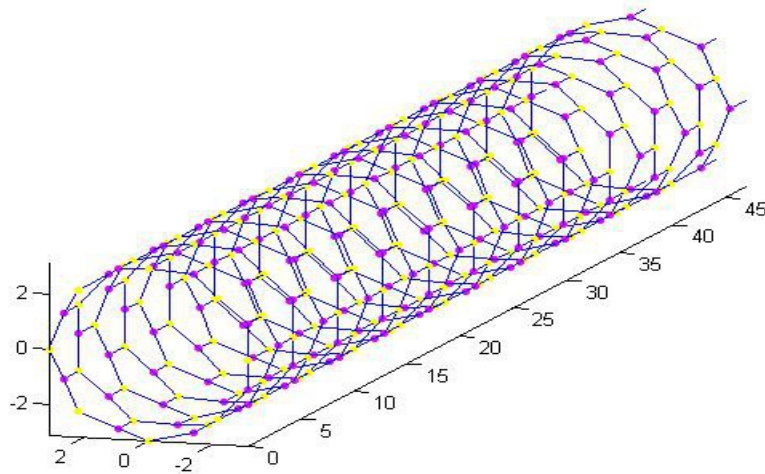


Figure 4.53 (8,0) boron phosphide nanotube, boron yellow and phosphorous magenta

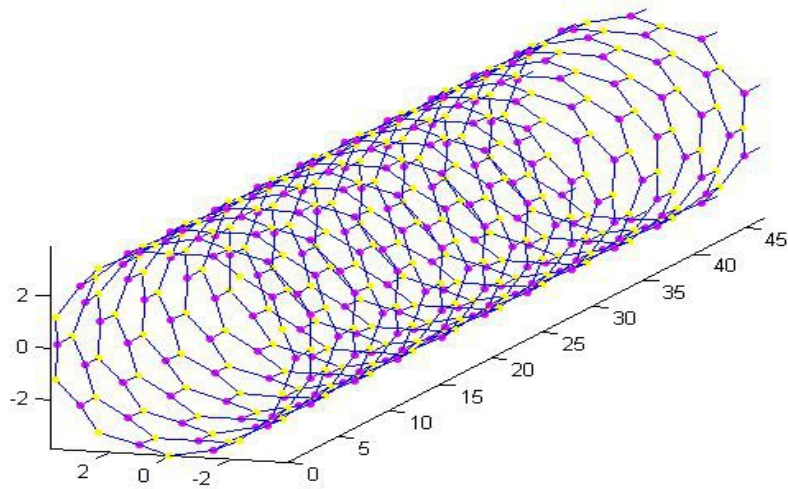


Figure 4.54 (10,0) boron phosphide nanotube, boron yellow and phosphorous magenta

Their electronic bandstructure is the following according to DFT :

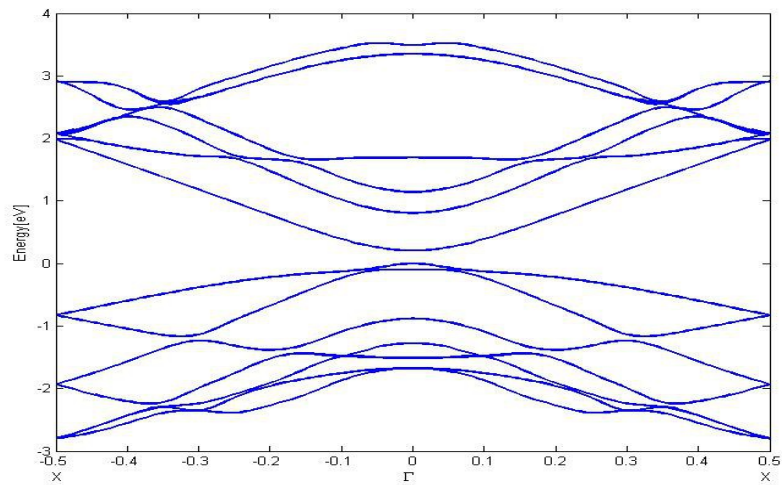


Figure 4.55 DFT band structure of a (7,0) boron phosphide nanotube

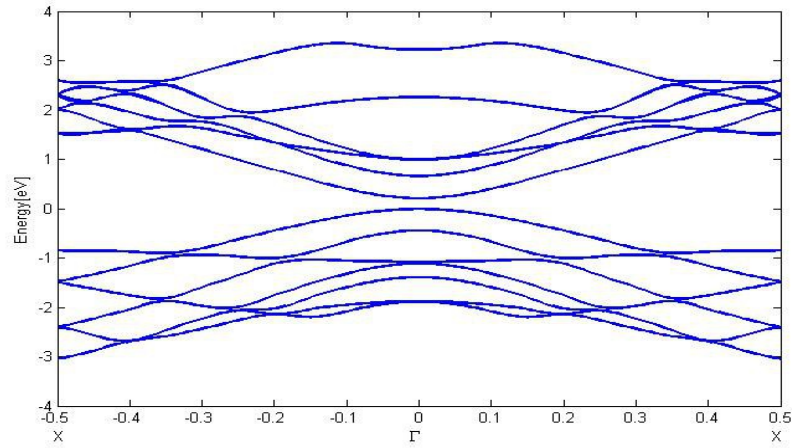


Figure 4.56 DFT band structure of a (8,0) boron phosphide nanotube

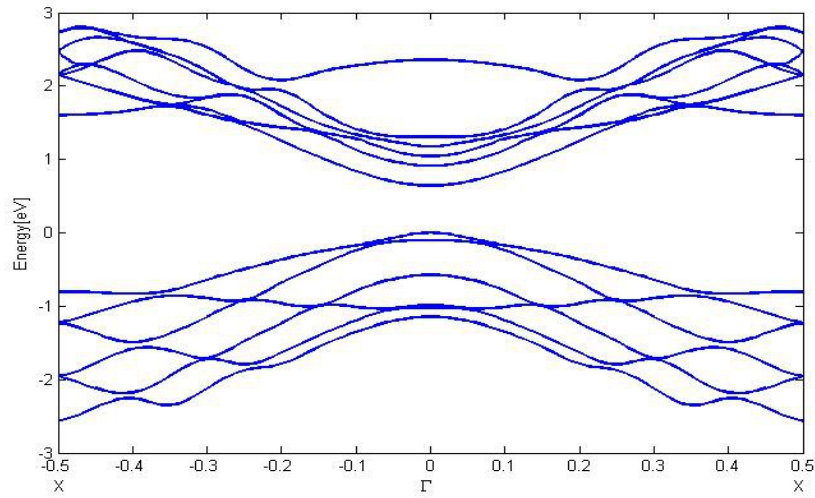


Figure 4.57 DFT band structure of a (10,0) boron phosphide nanotube

The band gaps obtained from DFT are similar to that of the boron arsenide nanotubes, but larger. A band gap of 0.2 eV for the (7,0) nanotube, 0.21 eV for the (8,0) nanotube and 0.64 eV for the (10,0) nanotube is predicted by DFT. Thus the (10,0) possesses by far the largest bandgap, like in the boron arsenide nanotubes. Let us take a look at the GWA band structures now :

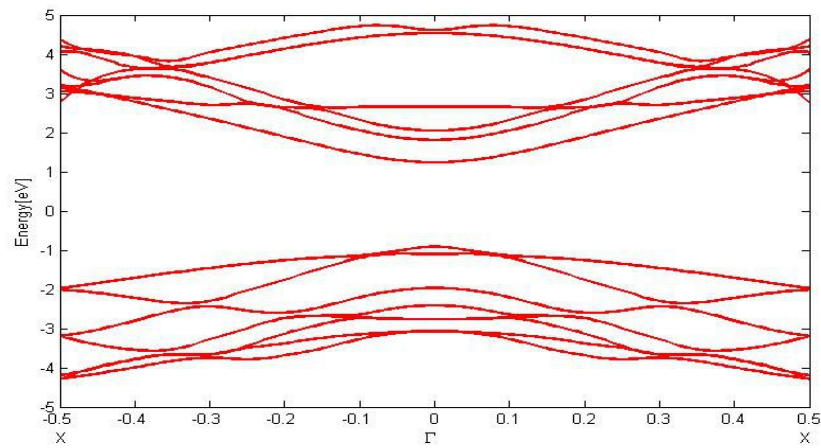


Figure 4.58 GWA band structure of a (7,0) boron phosphide nanotube

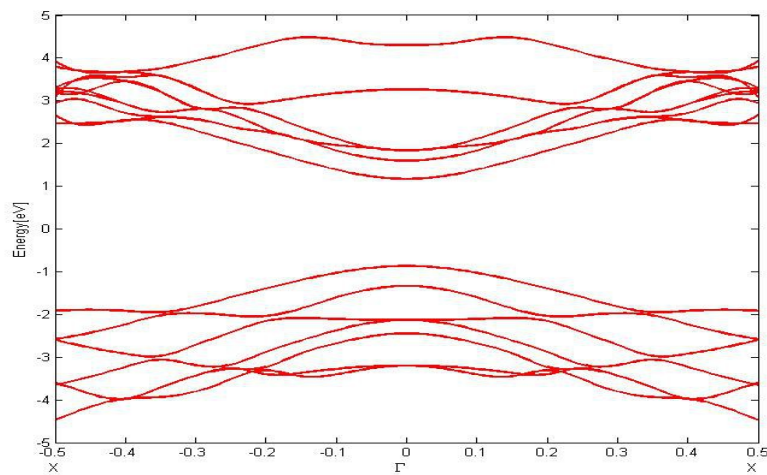


Figure 4.59 GWA band structure of a (8,0) boron phosphide nanotube

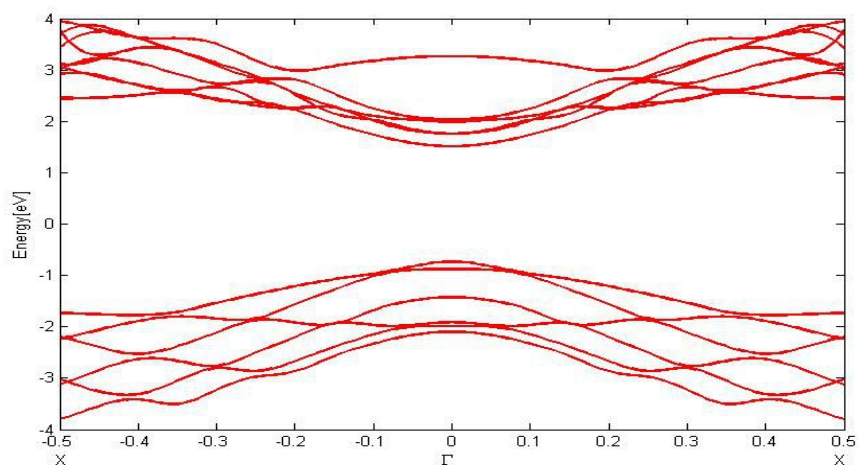


Figure 4.60 GWA band structure of a (10,0) boron phosphide nanotube

GWA gives a band gap of 2.15 eV for (7,0), 2.04 eV for (8,0) and 2.24 eV for (10,0). So under GWA corrections, the (10,0) still has the largest band gap. The strength of the GWA

corrections behaves in the same way as in the case of boron arsenide nanotubes. Dispersion of the corrections is small for all nanotubes, having their largest strength at X and their weakest at Γ . With increasing nanotube size, the magnitude of the GWA corrections gets smaller, from around 1.9 eV for the (7,0) nanotube to 1.6 eV for the (10,0) nanotube.

Moreover, their optical responses are shown below. For wavevector z, the optical spectra are :

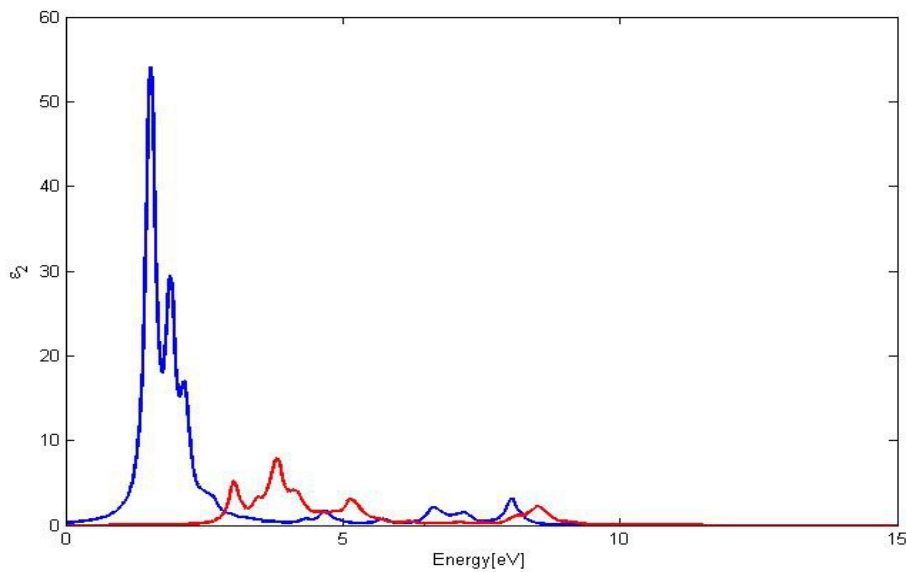


Figure 4.61 Optical spectrum of a (7,0) boron phosphide nanotube with wavevector z

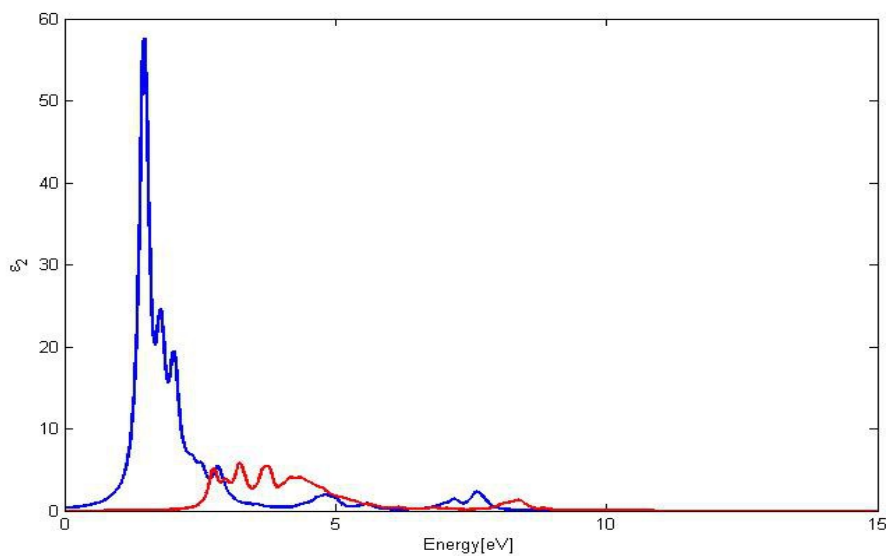


Figure 4.62 Optical spectrum of a (8,0) boron phosphide nanotube for wavevector z

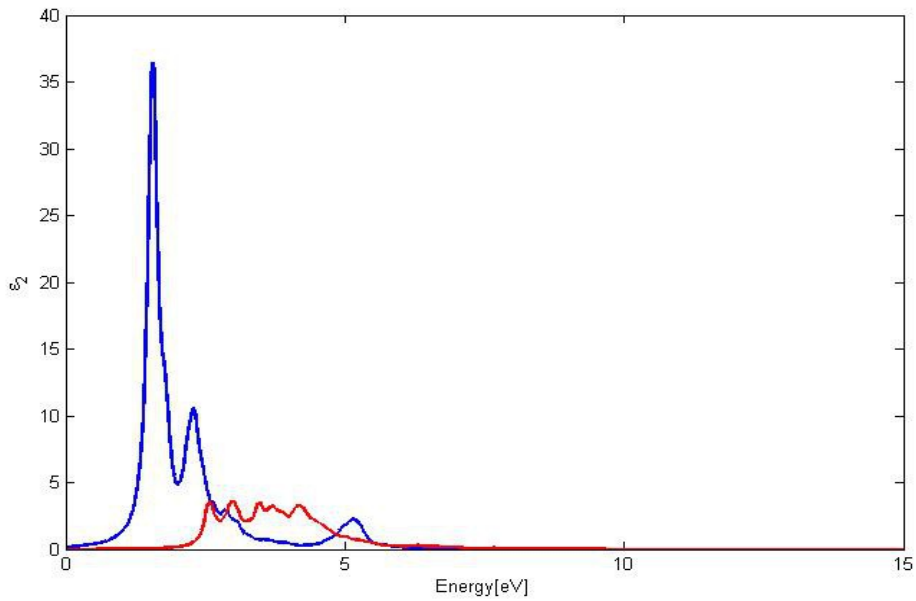


Figure 4.63 Optical spectrum of a (10,0) boron phosphide nanotube for wavevector z

All three spectra reveal one characteristic main peak, followed by shoulder. He is located at 1.53 eV for (7,0), at 1.47 eV for (8,0) and at 1.55 eV for (10,0). It follows that the larger the band gap is, the higher the frequency of the main peak is.

In case of wavevector x, the dielectric functions are :

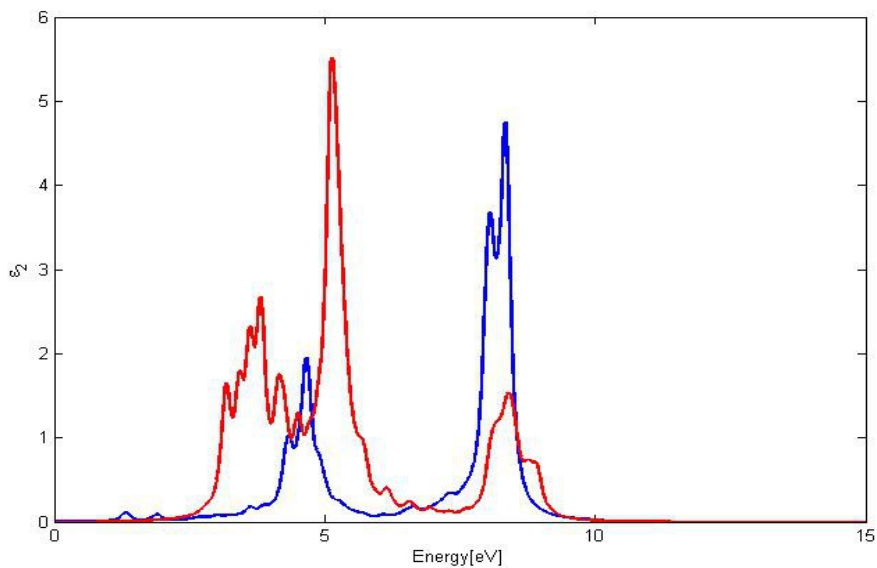


Figure 4.64 Optical spectrum of a (7,0) boron phosphide nanotube

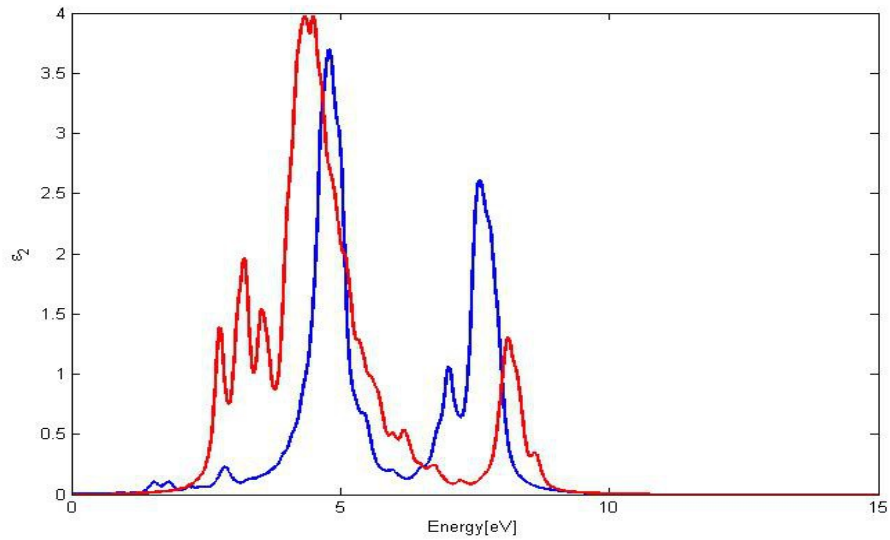


Figure 4.65 Optical spectrum of a (8,0) boron phosphide nanotube for wavevector x

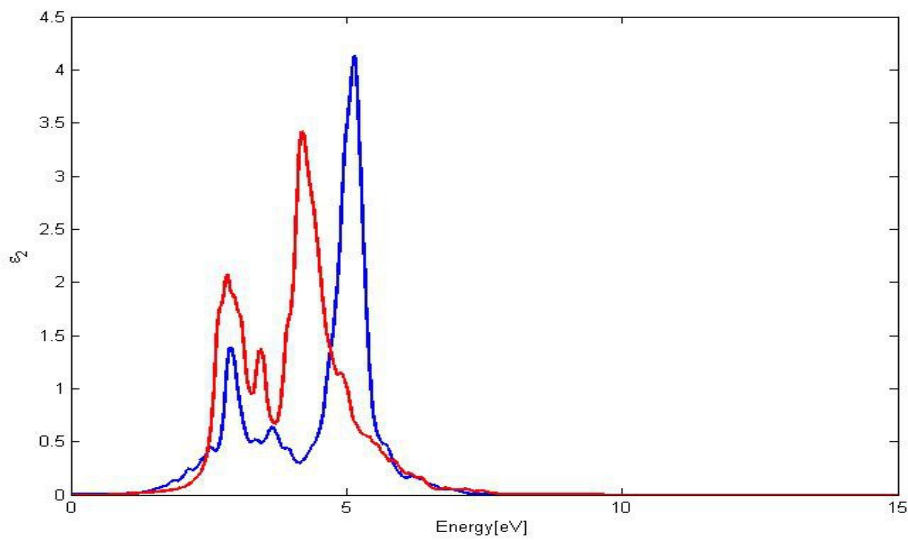


Figure 4.66 Optical spectrum of a (10,0) boron phosphide nanotube for wavevector x

The spectra for wavevector x exhibit 2 main peaks each, which lie at 4.66 eV and at 8.34 eV in case of (7,0), at 4.78 eV and at 7.59 eV in case of (8,0) and at 2.9 eV, 5.15 eV in case of (10,0). Thus we can conclude, like in the case of boron arsenide nanotubes, that the smaller nanotubes reach higher frequencies in their optical spectrum.

4.3 Nanotubes of optoelectronic materials

This section with the nanotubes belonging to the planar nanostructures discussed in chapter 3.3. Zigzag nanotubes of the materials AlN, AlAs, AlP and GaN are in the focus of investigation.

4.3.1 AlN nanotubes

We consider nanotubes of AlN with chiralities $(7,0)$, $(8,0)$ and $(10,0)$, defined in the same as for boron nitride and carbon nanotubes. For these nanotubes, a lattice constant of 5.40 Angstrom was found for AlN, 7.12 Angstrom for AlAs, 6.83 Angstrom for AlP and 6 Angstrom for GaN using SIESTA. Their structure is visualized below:

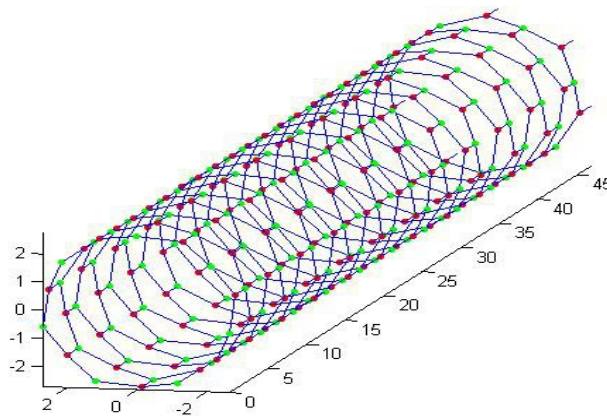


Figure 4.67 $(7,0)$ AlN nanotube, aluminum atoms in red and nitrogen atoms in green

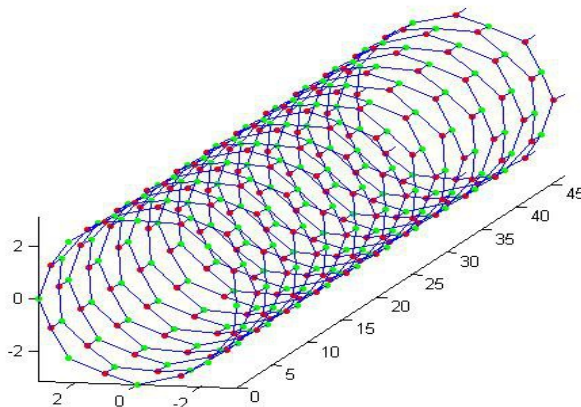


Figure 4.68 $(8,0)$ AlN nanotube, aluminum atoms in red and nitrogen atoms in green

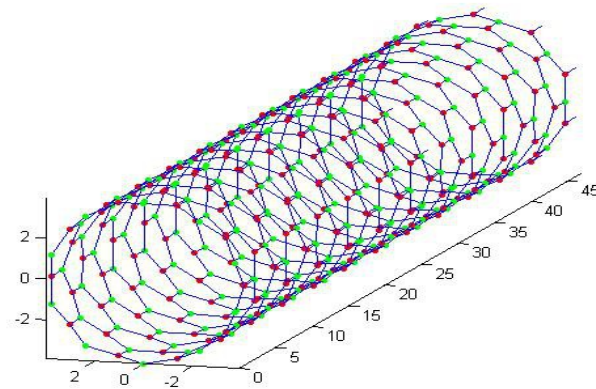


Figure 4.69 (10,0) AlN nanotube, aluminum atoms in red and nitrogen atoms in green

The following band structures were obtained for these nanotubes using DFT :

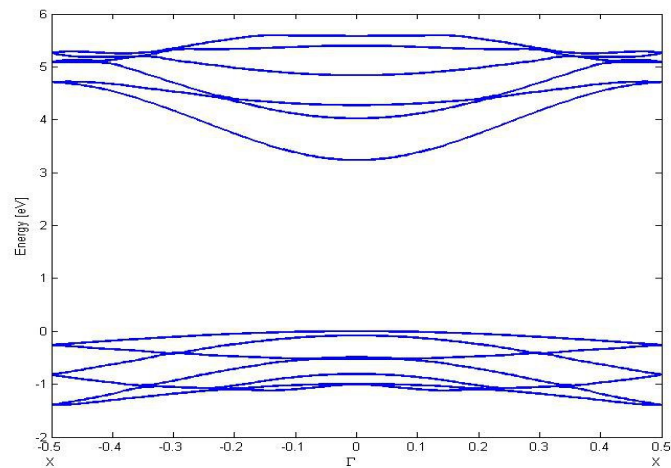


Figure 4.70 DFT band structure of a (7,0) AlN nanotube

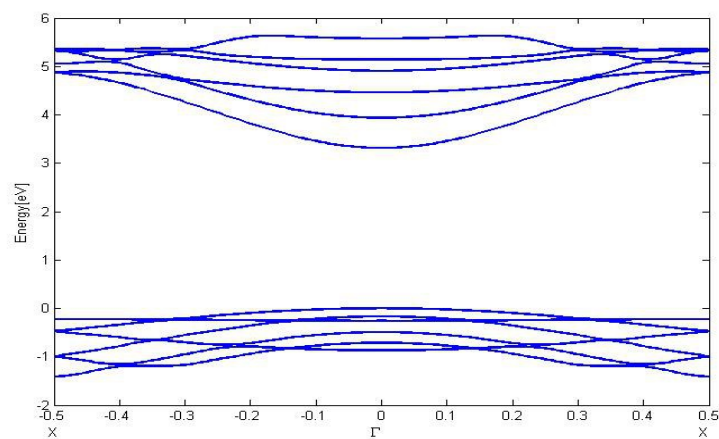


Figure 4.71 DFT band structure of a (8,0) AlN nanotube

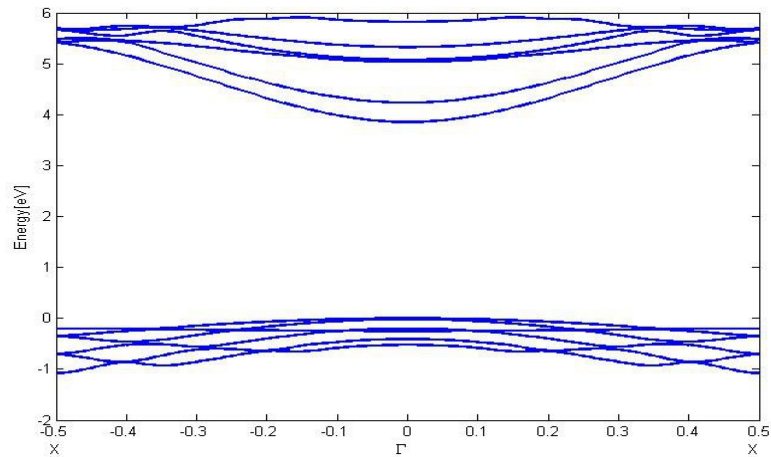


Figure 4.72 DFT band structure of a (10,0) AlN nanotube

DFT calculation yields a band gap of 3.23 eV for a (7,0) AlN nanotube, 3.31 eV for a (8,0) nanotube and 3.85 eV for a (10,0) nanotube. Thus the band gap increases according to DFT. Let us now regard the GWA band structures:

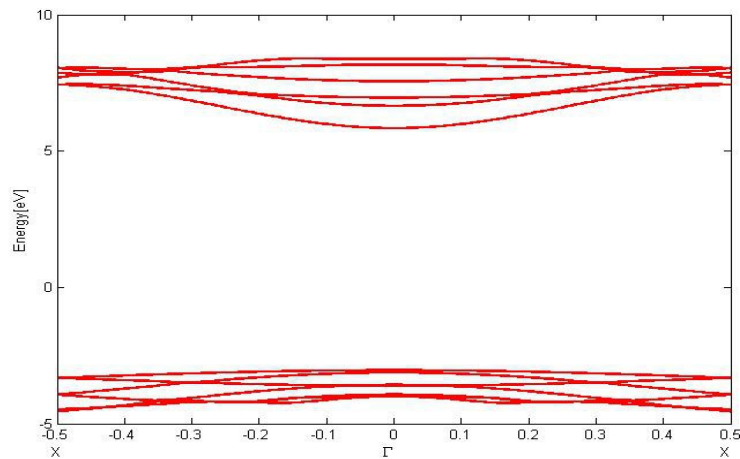


Figure 4.73 GWA band structure of a (7,0) AlN nanotube

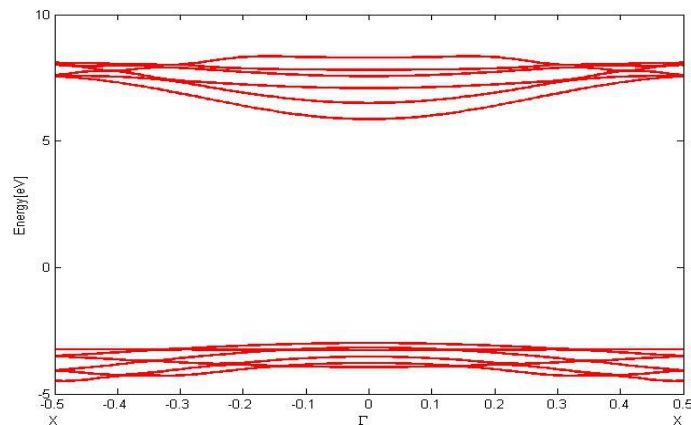


Figure 4.74 GWA band structure of a (8,0) AlN nanotube

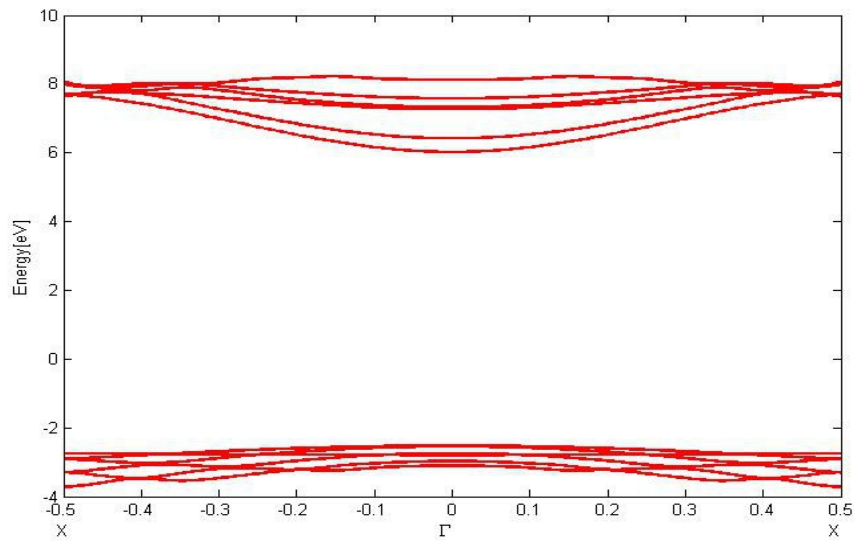


Figure 4.75 GWA band structure of a (10,0) AlN nanotube

GWA predicts a band gap of 8.88 eV for the (7,0) nanotube, 8.86 eV for the (8,0) nanotube and 8.5 eV for the (10,0) nanotube, which means GWA band gaps are higher for smaller diameter. The GWA corrections taking place are immense and have negligible dispersion. They affect the (7,0) nanotube most with approximately 5.4 eV, the (8,0) nanotube with 5.3 eV, and the (10,0) to lesser extent with around 4.5 eV.

After having discussed the band structures, our focus of attention goes to the optical spectra:

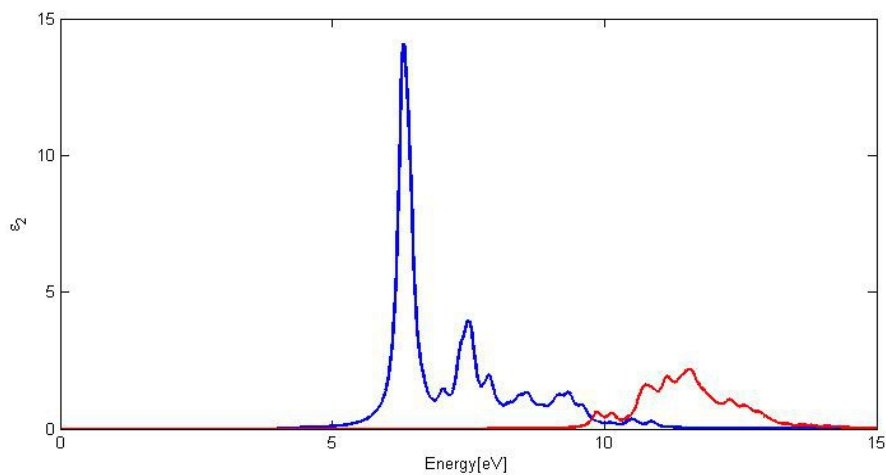


Figure 4.76 Optical spectrum of a (7,0) AlN nanotube with wavevector z

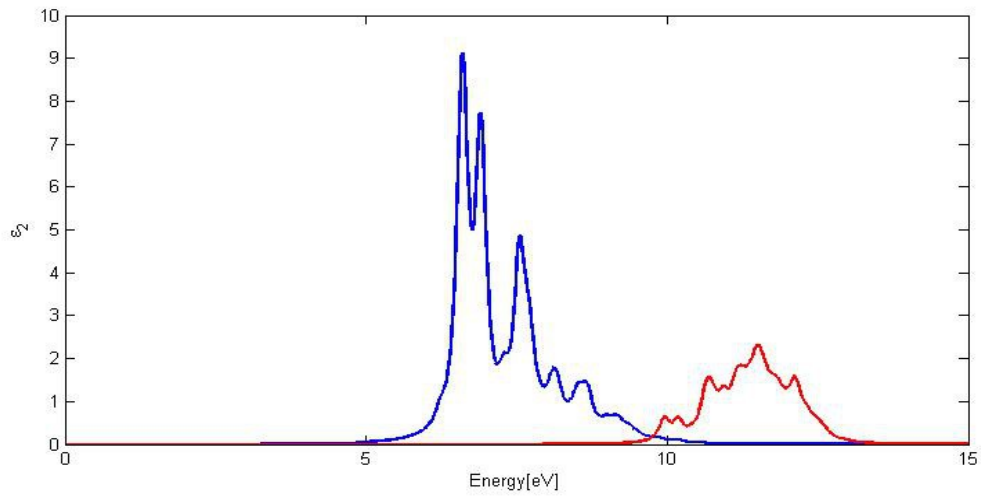


Figure 4.77 Optical spectrum of a (8,0) AlN nanotube with wavevector z

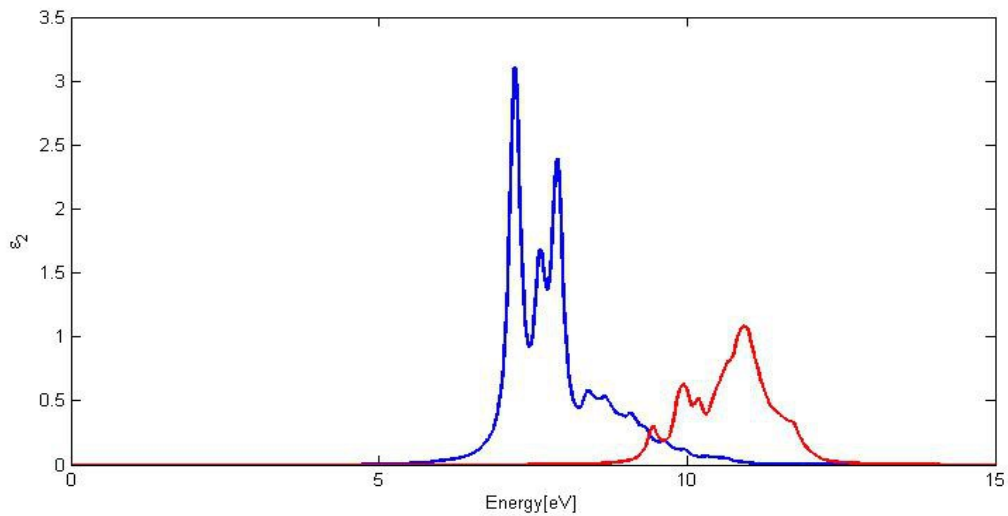


Figure 4.78 Optical spectrum of a (10,0) AlN nanotube with wavevector z

One can observe in the figures above that the (7,0) nanotube has its main peak at 6.31 eV, and after it a small peak at 7.49 eV. The (8,0) nanotube has double peak at 6.6 eV and 6.9 eV, finished with smaller peak at 7.55 eV, and the (10,0) nanotube reveals a kind of peak rock whose borders are the main peak at 7.2 eV and another strong peak at 7.9 eV. Consequently, the spectra goes to higher frequencies for bigger nanotube diameters in the case of wavevector z .

The spectra of wavevector are basically the same as for wvectors and are therefore not taken

into account separately. For wavevector x , the spectra are :

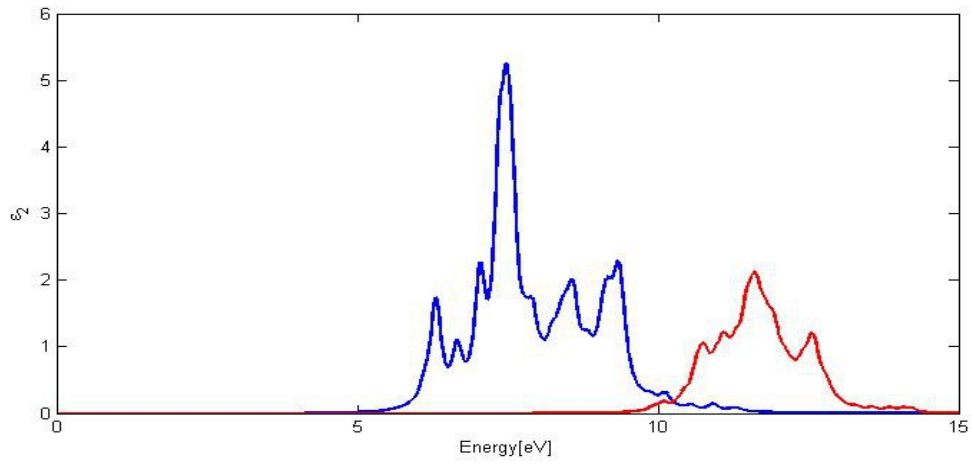


Figure 4.79 Optical spectrum of a (7,0) AlN nanotube with wavevector x

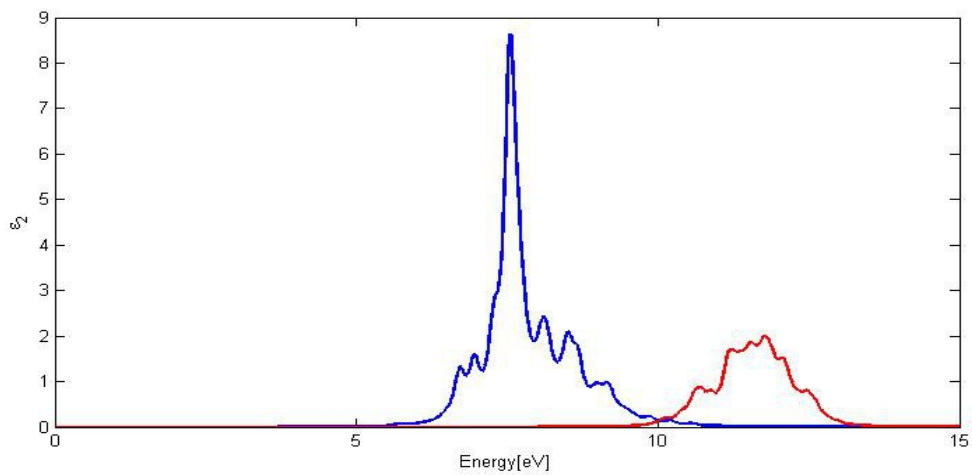


Figure 4.80 Optical spectrum of a (8,0) AlN nanotube with wavevector x

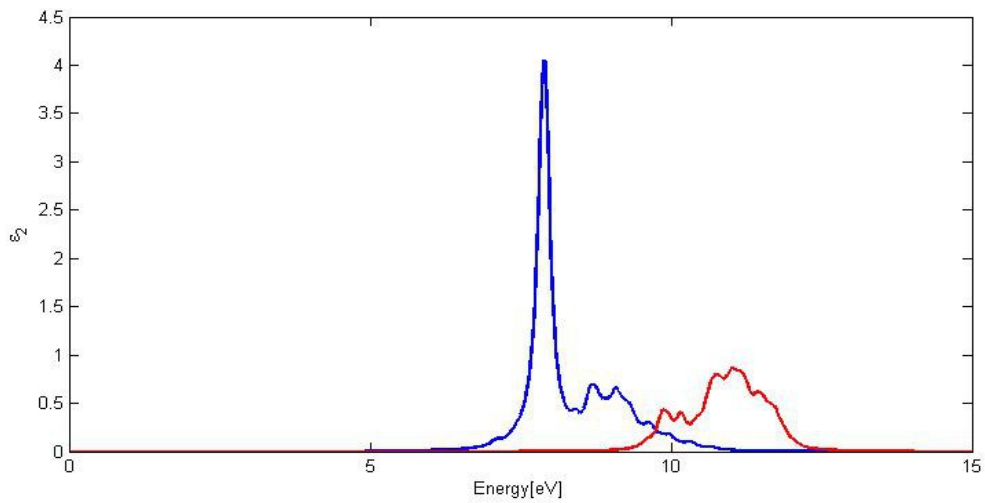


Figure 4.81 Optical spectrum of a (10,0) AlN nanotube with wavevector x

The frequencies of the main peaks get higher with bigger nanotube, being 7.48 eV for (7,0), 7.55 eV for (8,0) and 7.89 eV for (10,0). However, the width of the spectrum increases with the diameter, and the dielectric function still achieves notable values at higher frequencies.

4.3.2 AIAs nanotubes

As next step, we deal with the nanotubes corresponding to planar AIAs. Like for AlN, we consider the chiralities (7,0), (8,0) and (10,0). They look like this :

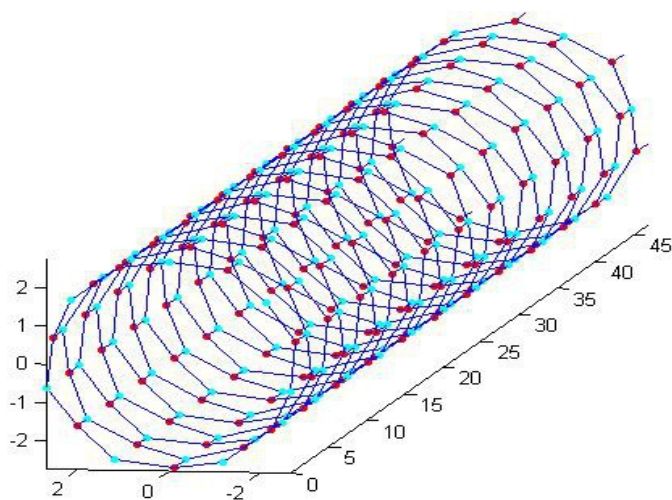


Figure 4.82 (7,0) AlAs nanotube, aluminum atoms in red and arsenic atoms in cyan

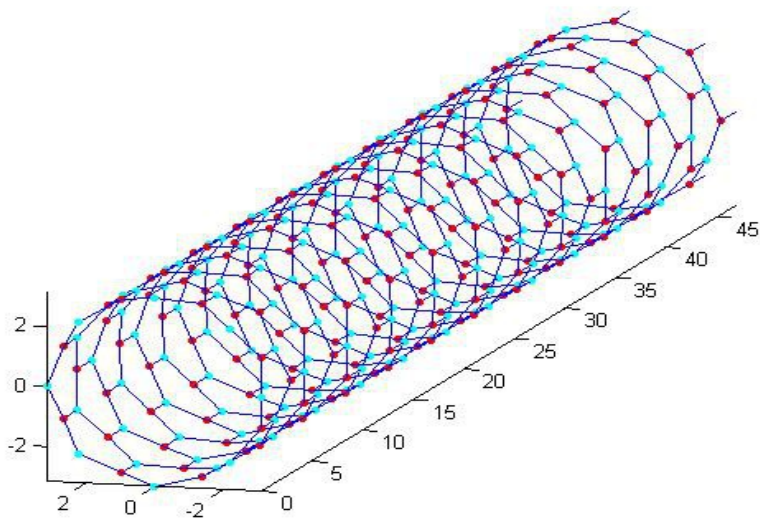


Figure 4.83 (8,0) AlAs nanotube, aluminum atoms in red and arsenic atoms in cyan

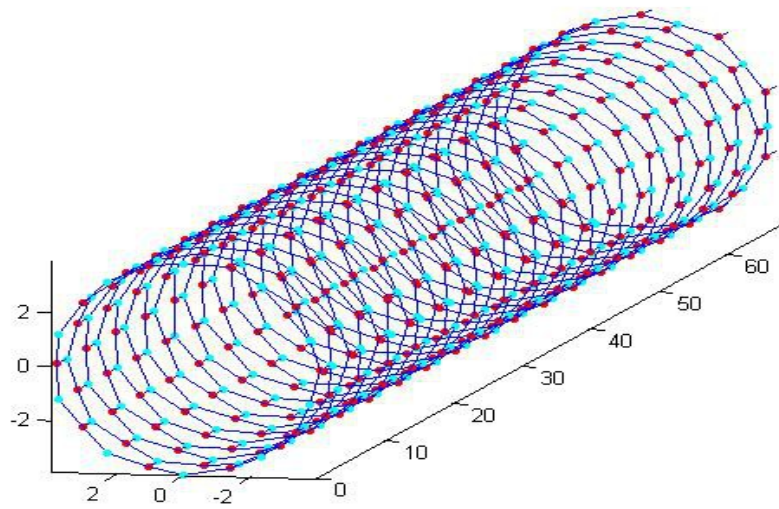


Figure 4.84 (10,0) AlAs nanotube, aluminum atoms in red and arsenic atoms in cyan

One obtains the following band structures from DFT :

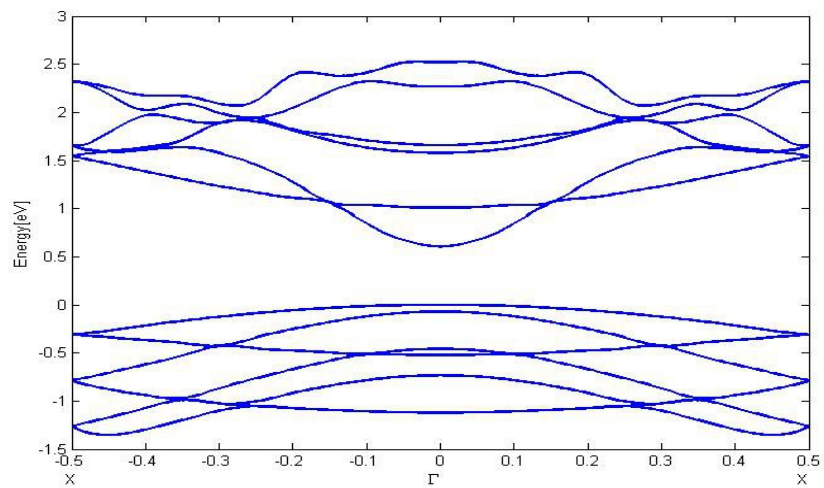


Figure 4.85 DFT band structure of a (7,0) AlAs nanotube

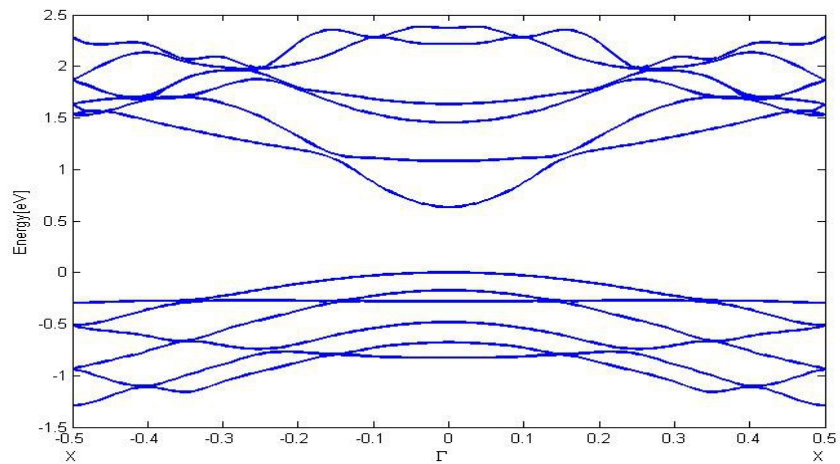


Figure 4.86 DFT band structure of a (8,0) AlAs nanotube

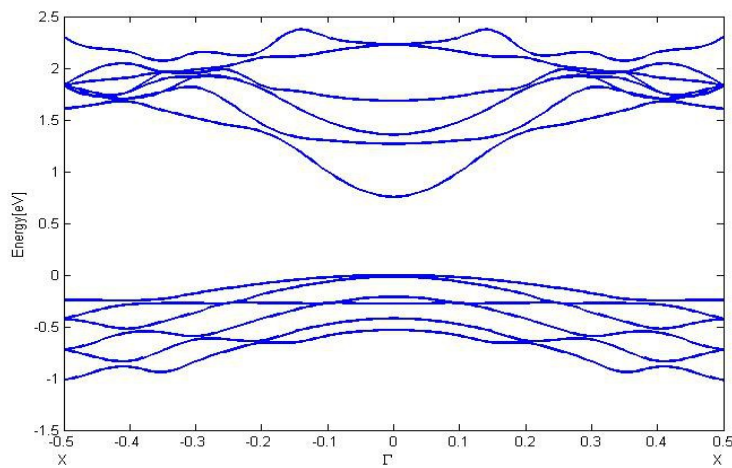


Figure 4.87 DFT band structure of a (10,0) AlAs nanotube

As consequence of the DFT results, the DFT band gap increases with the size of the nanotube, starting with 0.6 eV for (7,0) , then 0.63 eV for (8,0) and 0.75 eV for (10,0) . GWA provides the following corrected band structures:

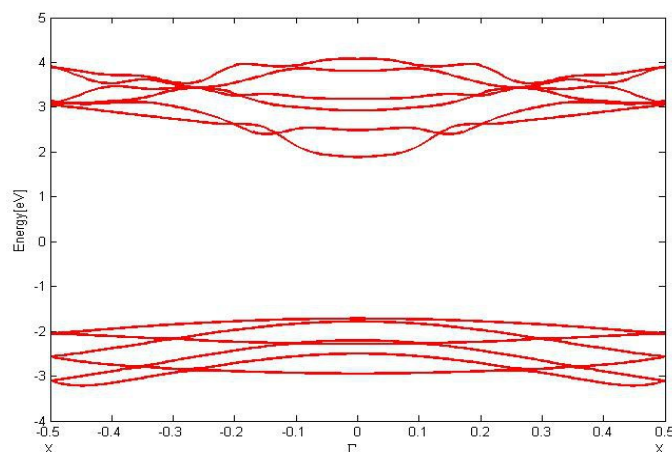


Figure 4.88 GWA band structure of a (7,0) AlAs nanotube

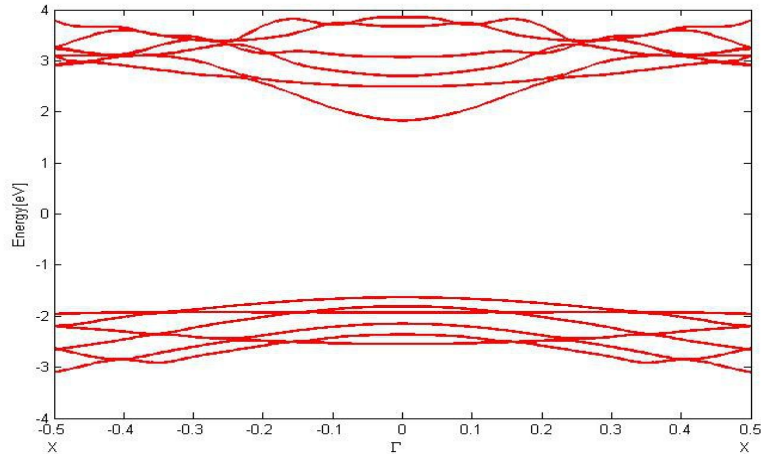


Figure 4.89 GWA band structure of a (8,0) AlAs nanotube

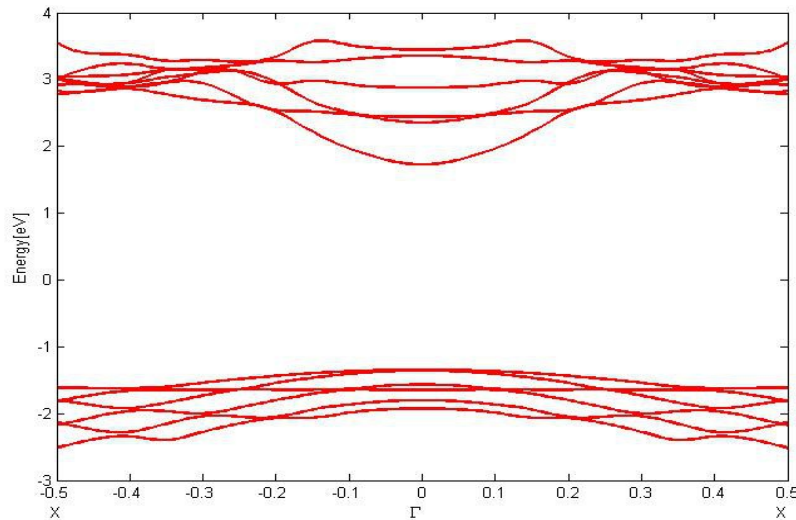


Figure 4.90 GWA band structure of a (10,0) AlAs nanotube

Once again, GWA corrections dramatically change the band structures. GWA yields a band gap of 3.6 eV for (7,0), 3.23 eV for (8,0) and 3.07 eV for the (10,0) AlAs nanotube. This means that the band gap decreases with the size of the nanotube for AlAs nanotubes, and the band gaps of the AlAs nanotubes are much smaller than of AlN nanotubes. The GWA corrections, showing little dispersion, make their strongest effect in the (7,0) nanotube with approximately 3 eV, declining with nanotube size to around 2.3 eV for the (10,0) nanotube.

These band structures lead to the optical spectra listed below. We start with the case of an incoming plane wave with wavevector, and the spectra for wavevector are nearly identical to them and are thus not listed separately. The spectra for wavevector z are :

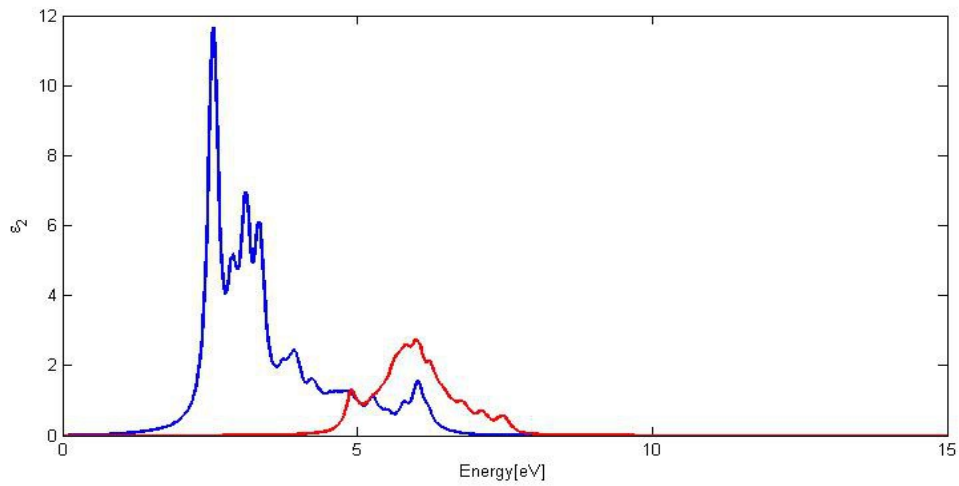


Figure 4.91 Optical spectrum of a (7,0) AlAs nanotube for wavevector z

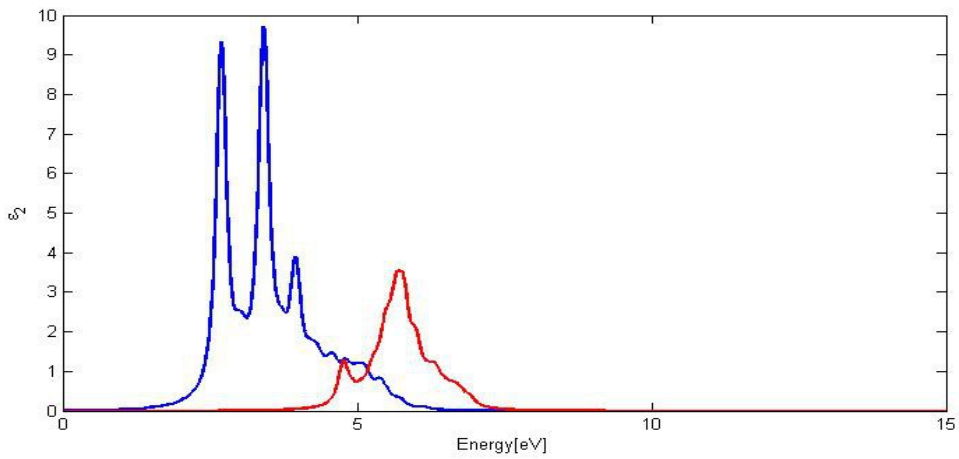


Figure 4.92 Optical spectrum of a (8,0) AlAs nanotube for wavevector z

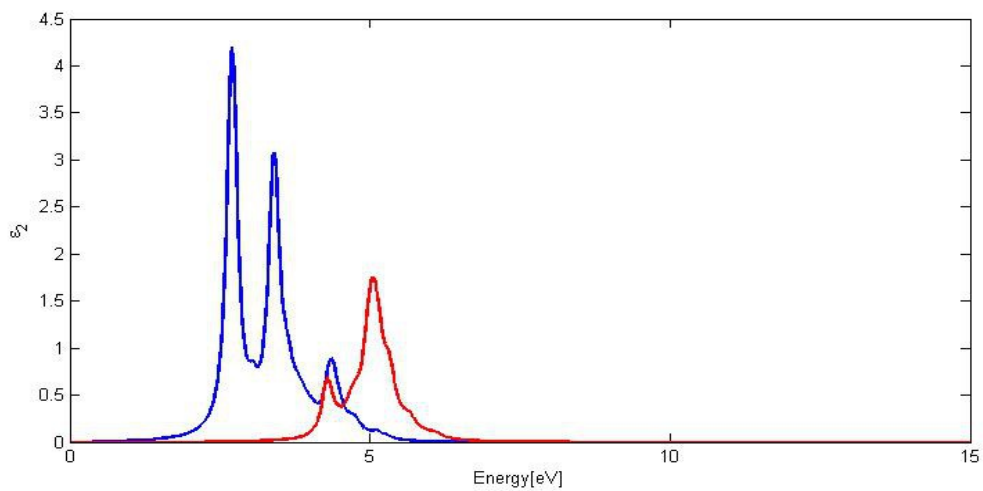


Figure 4.93 Optical spectrum of a (10,0) AlAs nanotube with wavevector z

From the figures above one realizes that the position of the peaks does not change much with the nanotube diameter, the peaks of (7,0) are located at 2.55 eV, 3.11 eV and 3.33 eV, for (8,0) they lie at 2.69 eV, 3.41 eV and 3.95 eV, and at 2.7 eV, 3.4 eV and 4.35 eV for the (10,0) nanotube. But another interesting aspect of the optical spectra is that for smaller size, the higher frequency area gets penetrated deeper and the hill around the peaks gets broader.

Additionally, a plane wave with wavevector x causes these optical responses:

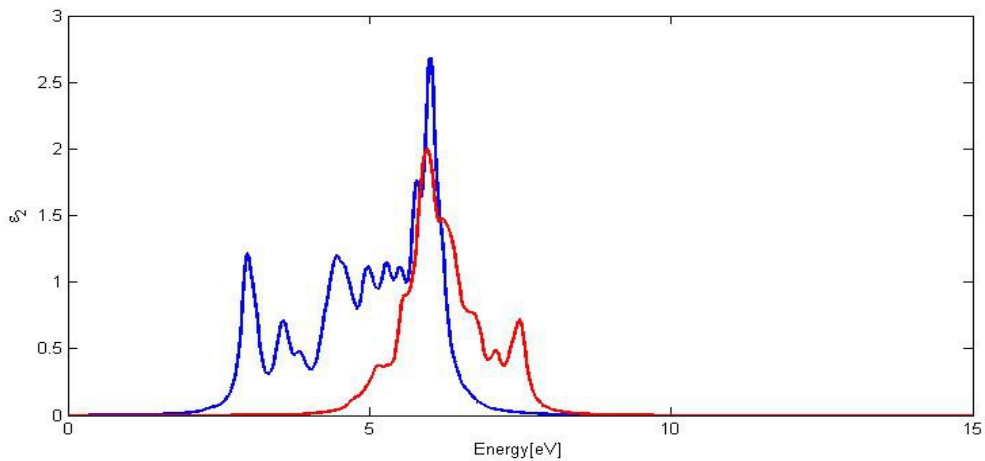


Figure 4.94 Optical spectrum of a (7,0) AlAs nanotube for wavevector x

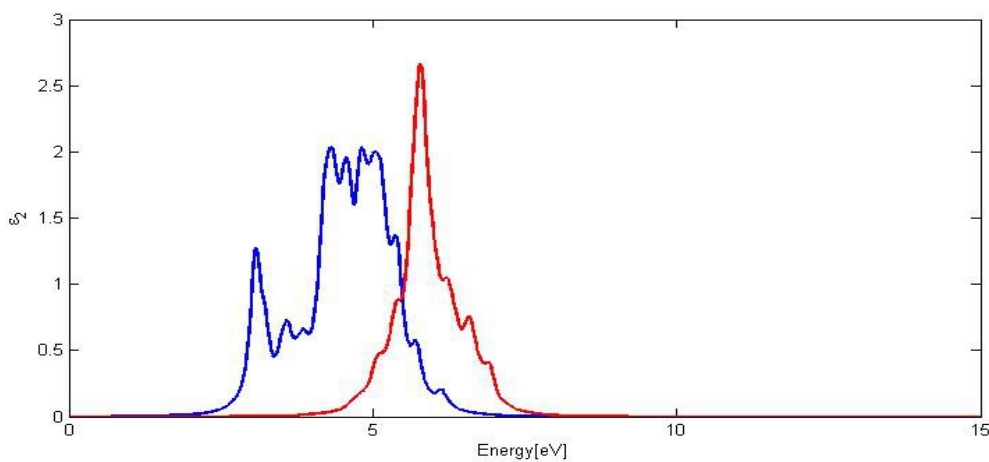


Figure 4.95 Optical spectrum of a (8,0) AlAs nanotube for wavevector x

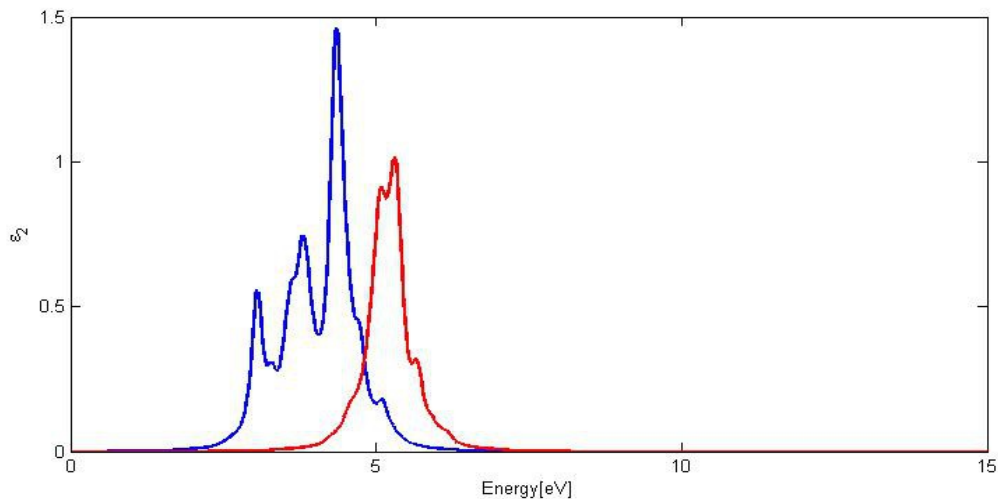


Figure 4.96 Optical spectrum of a (10,0) AlAs nanotube for wavevector x

In the case of wavevector x , one can observe in the spectrum of (7,0) a first peak at 2.97 eV, after which a broad hill comes, bordered by a peak at 4.46 eV and the main peak at 6 eV. For the (8,0) nanotube, the first peak occurs at 3 eV, and then a hill between two high peaks at 4.3 eV and 5 eV comes. Moreover, the spectrum of (10,0) possesses a series of increasing peaks at 3 eV, 3.8 eV and 4.35 eV. So it seems obvious that the optical spectrum of smaller diameter nanotubes tend to higher frequencies than for bigger diameters. Additionally, it is notable that the electron-hole coupling does not influence the spectrum so massively as it does in other systems discussed before.

4.3.3 AIP nanotubes

Now let's pay attention to the nanotube structures of AIP. The ones we are going to work on are these :

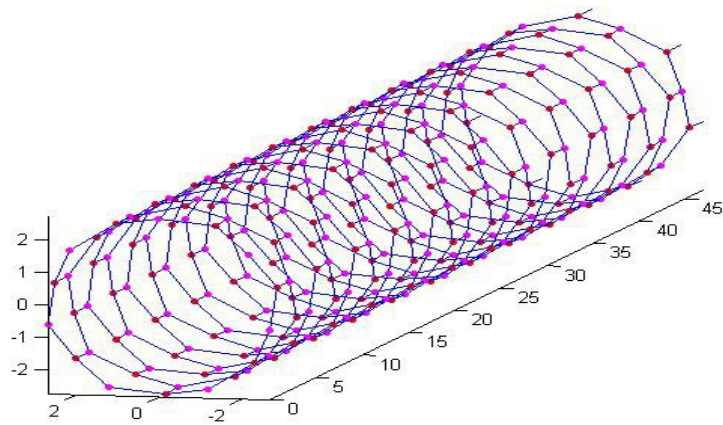


Figure 4.97 (7,0) AlP nanotube, aluminum atoms red and phosphorous atoms magenta

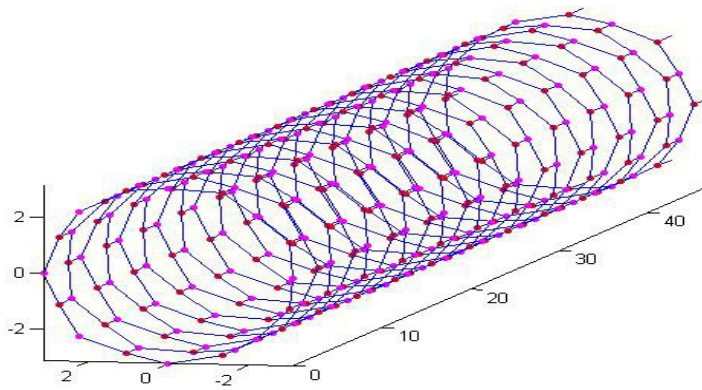


Figure 4.98 (8,0) AlP nanotube, aluminum atoms red and phosphorous atoms magenta

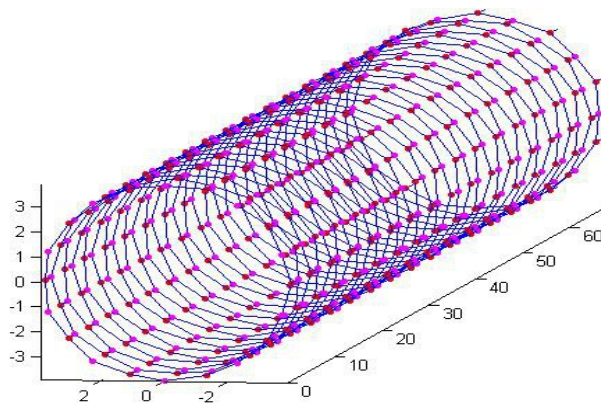


Figure 4.99 (10,0) AlP nanotube, aluminum atoms red and phosphorous atoms magenta

We receive the following band structures from DFT for these nanotubes:

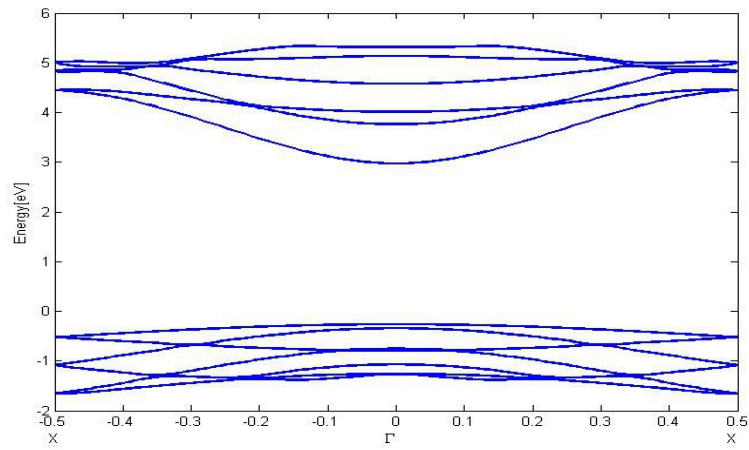


Figure 4.100 DFT bandstructure of a (7,0) AIP nanotube

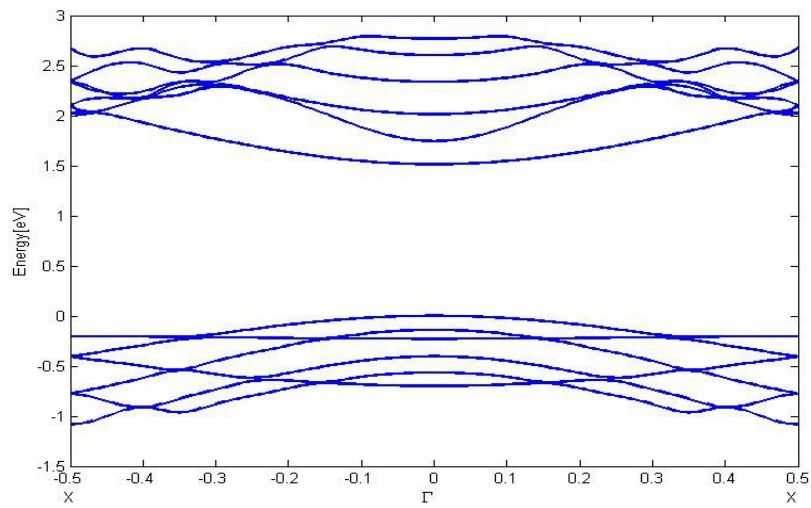


Figure 4.101 DFT bandstructure of a (8,0) AIP nanotube

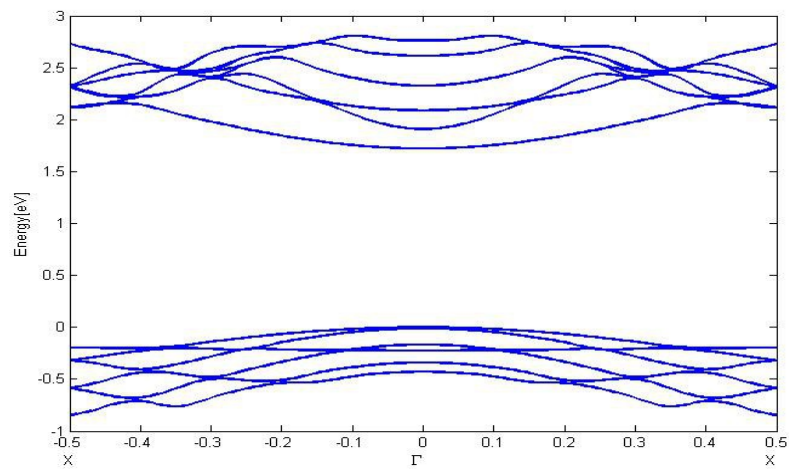


Figure 4.102 DFT bandstructure of a (10,0) AIP nanotube

From the results above one can find that (7,0) has a band gap of 3.23 eV, (8,0) a band gap of

1.51 eV and (10,0) a band gap of 1.72 eV. So there is no clear order in the band gap. Let us take a look at what GWA says :

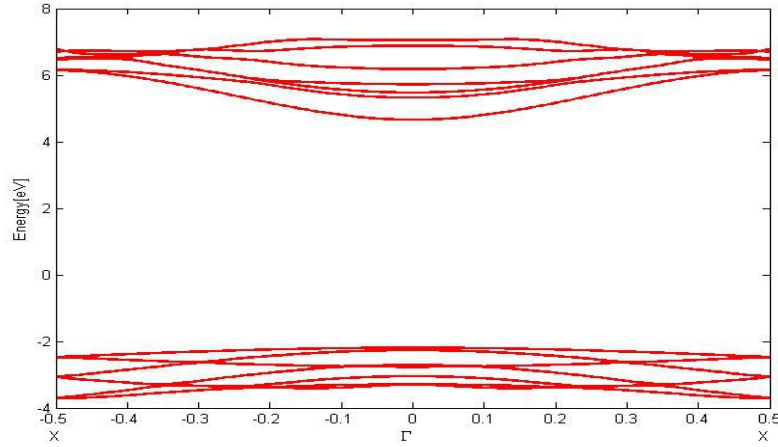


Figure 4.103 GWA band structure of (7,0) AIP nanotube

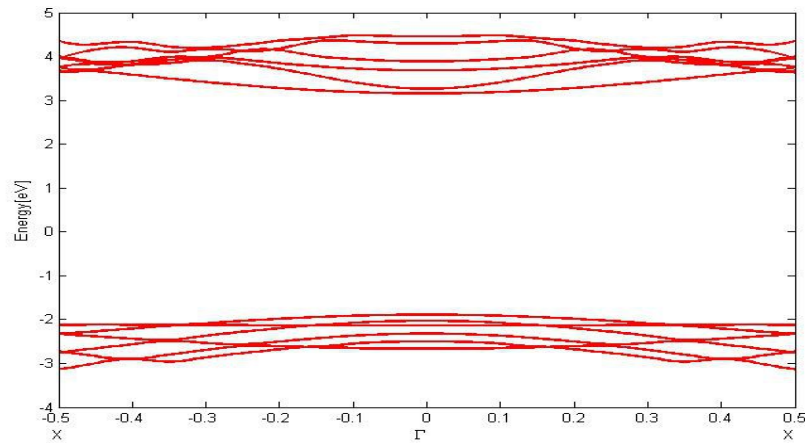


Figure 4.104 GWA band structure of (8,0) AIP nanotube

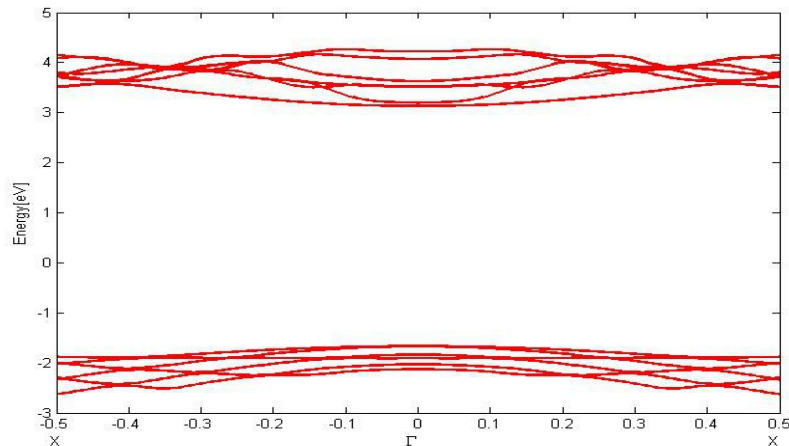


Figure 4.105 GWA band structure of (10,0) AIP nanotube

In contrast, GWA gives the band structures a clear order, 6.85 eV for the (7,0) nanotube, 5.05 eV for the (8,0) and 4.85 eV for the (10,0) nanotube. Furthermore, a similar relationship holds for the GWA corrections. These reveal nearly no dispersion and decrease with nanotube size by their size, falling from 3.5 eV for (7,0) to 3.2 eV for (10,0).

Next we regard the optical properties of these nanotubes. If the incoming plane has the propagation vector z , then the dielectric functions are as listed below. The dielectric function for wavevector y has no mentionable difference to z is therefore not listed.

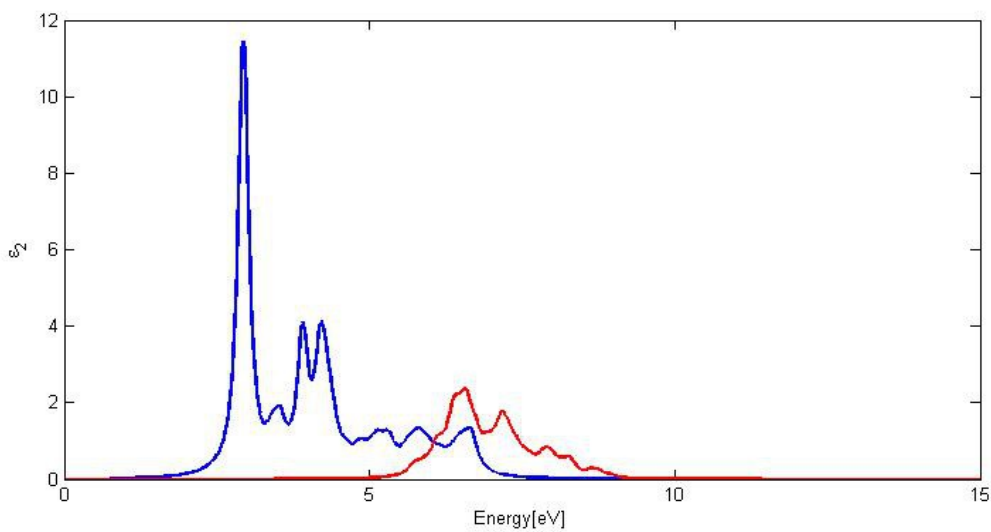


Figure 4.106 Optical spectrum of (7,0) AIP nanotube for wavevector z

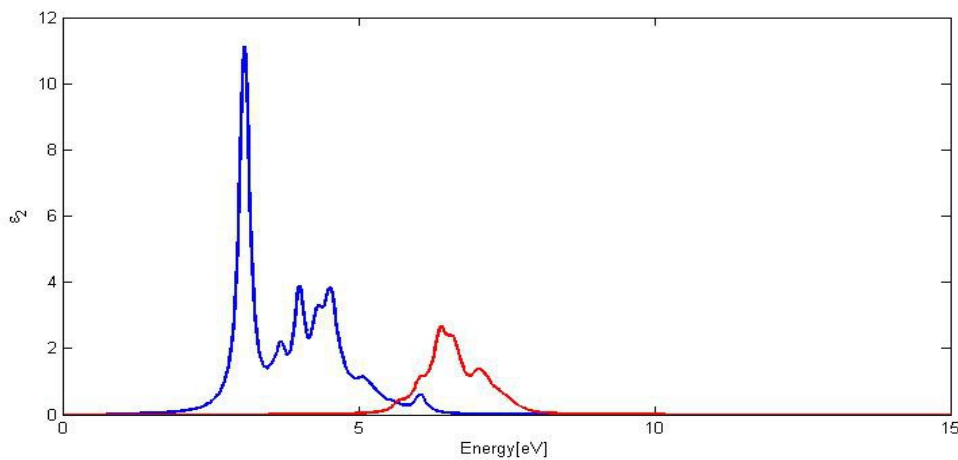


Figure 4.107 Optical spectrum of (8,0) AIP nanotube for wavevector z

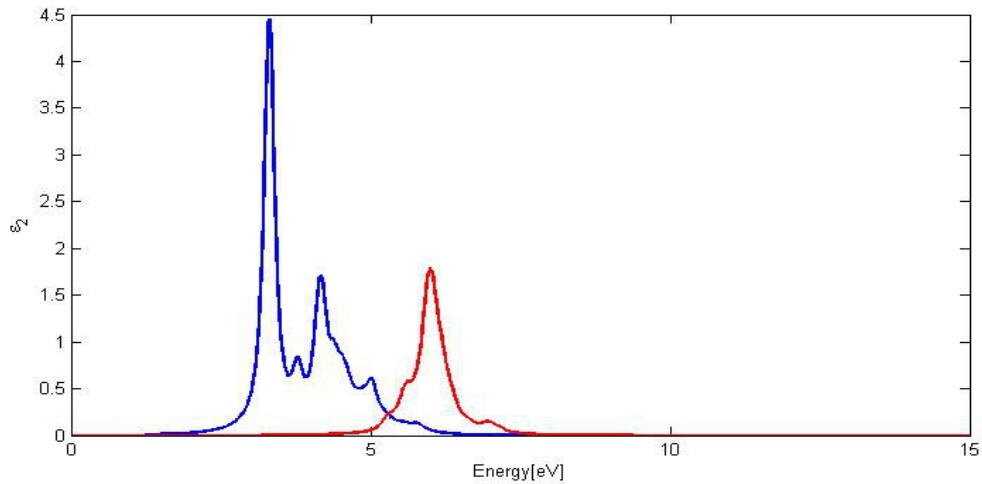


Figure 4.108 Optical spectrum of (10,0) AIP nanotube for wavevector z

The position of the peaks moves to higher frequencies for increasing nanotube size. In the (7,0) nanotube, the main peak is at 2.93 eV with two side peaks at 3.91 eV and 4.2 eV, in case of (8,0) the main peak is located at 3.07 eV with side peaks at 4 eV and 4.52 eV, and in the (10,0) nanotube one has a main peak at 3.31 eV followed by a smaller peak at 4.17 eV. This can be explained by the strong electron-hole interaction in the (7,0) nanotube.

At the end, we analyze the spectrum caused by a plane wave with propagation vector x :

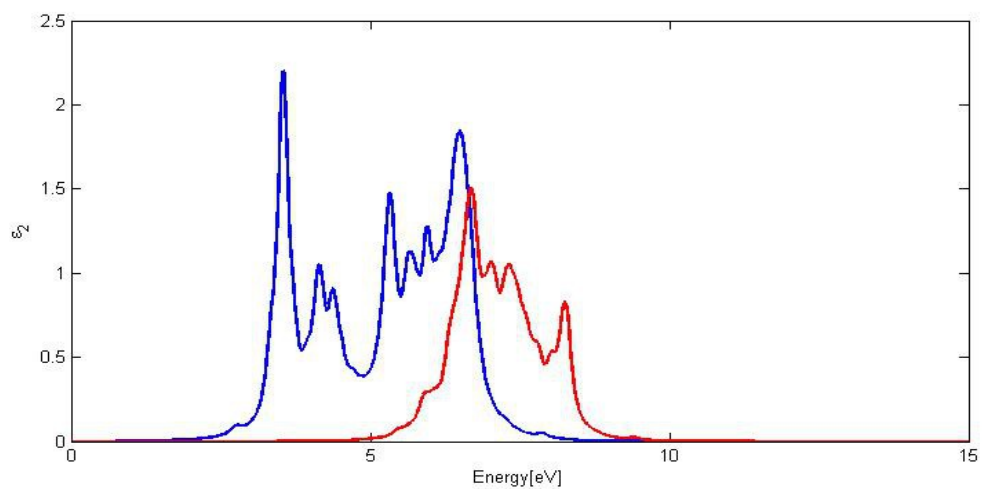


Figure 4.109 Optical spectrum of (7,0) AIP nanotube for wavevector x

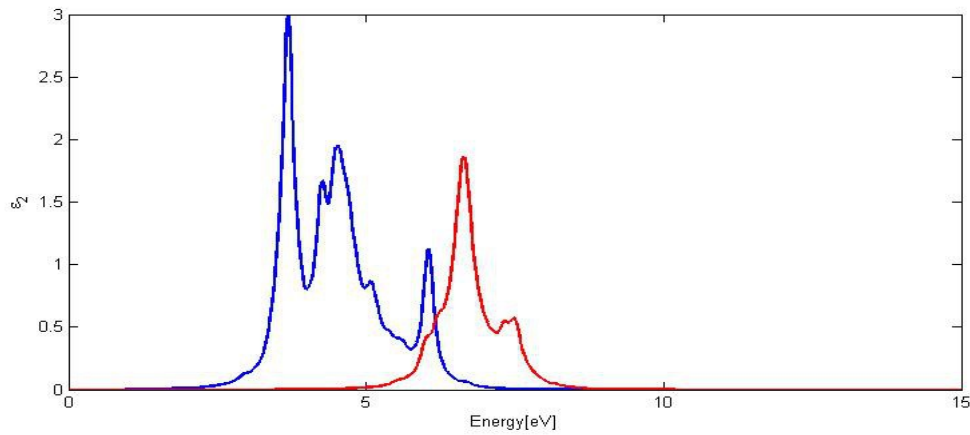


Figure 4.110 Optical spectrum of (8,0) AIP nanotube for wavevector x

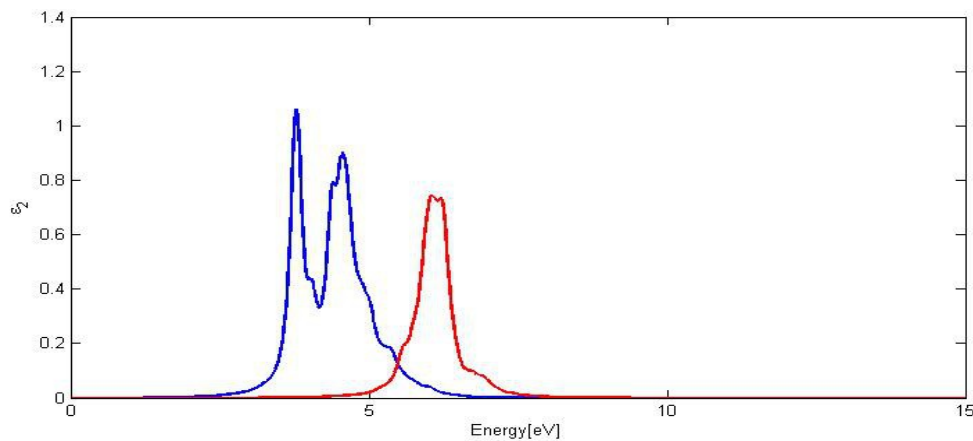


Figure 4.111 Optical spectrum of (10,0) AIP nanotube for wavevector x

One can observe a forest of peaks in the spectrum of the (7,0) nanotube, beginning with the main peak at 3.54 eV and closing with the second strong peak at 6.5 eV. In the case of the (8,0) nanotube, there is a sequence of peaks being located at 3.69 eV, 4.51 eV and 6.05 eV, starting with the main peak and finishing with a small peak. Furthermore, the spectrum of the (10,0) nanotube has its main peak at 3.78 eV and another peak at 4.56 eV. From these results we can draw the conclusion that the optical spectrum for wavevector x is pushed to the lower frequency spectrum for larger nanotubes.

4.3.4 GaN nanotubes

Finally, we discuss the last optoelectronic nanotubes of this section, namely GaN nanotubes. After this, all nanotube equivalents to the optoelectronic planar nanostructures of 3.3 have been handled. Like before the chiralities (7,0), (8,0) and (10,0) are taken into account. Below pictures of them are listed :

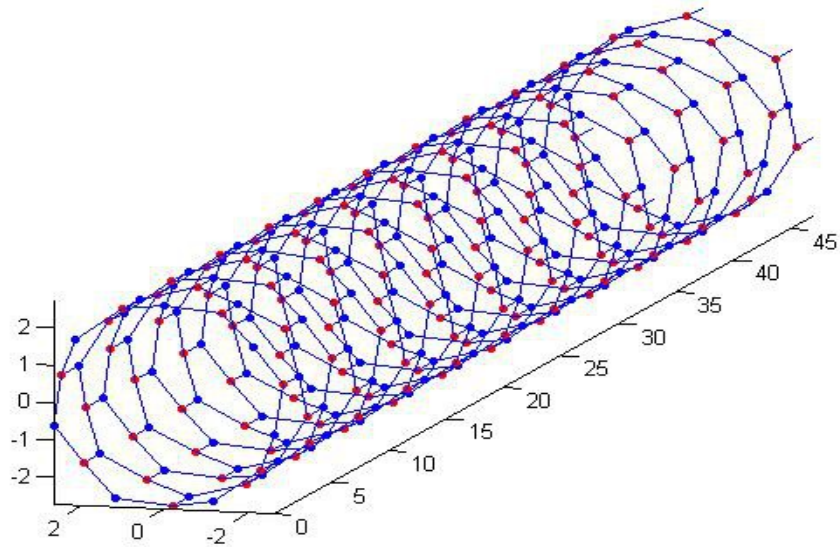


Figure 4.112 (7,0) GaN nanotube, gallium atoms in blue and nitrogen atoms in red

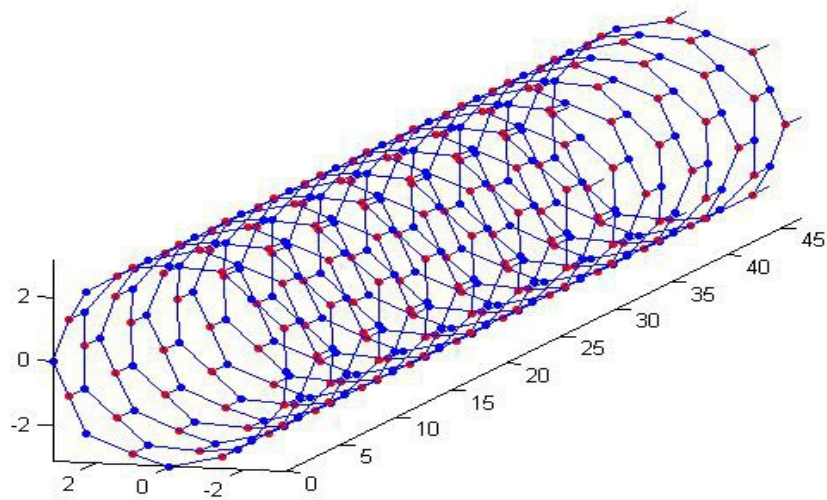


Figure 4.113 (8,0) GaN nanotube, gallium atoms in blue and nitrogen atoms in red

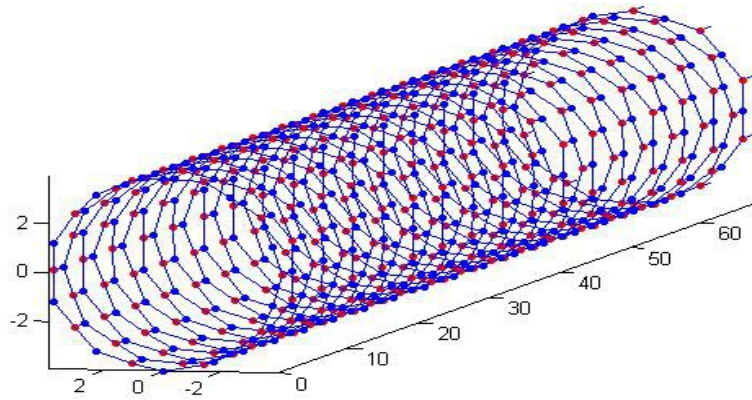


Figure 4.114 (10,0) GaN nanotube, gallium atoms in blue and nitrogen atoms in red

We obtain the following electronic band structures using DFT :

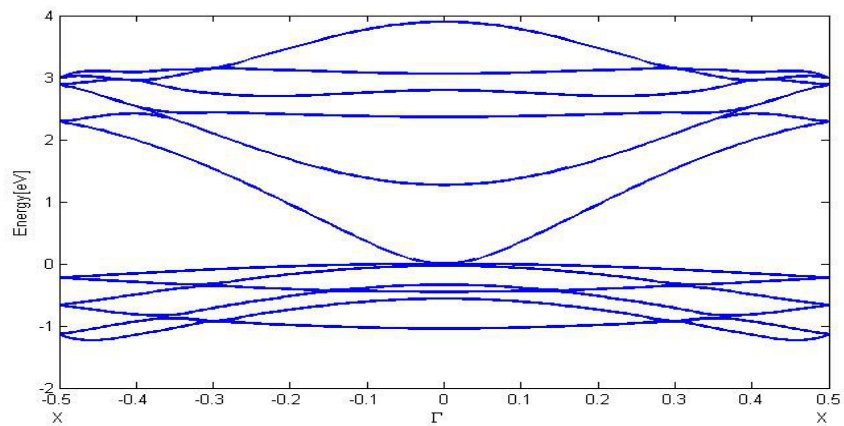


Figure 4.115 DFT band structure of a (7,0) GaN nanotube

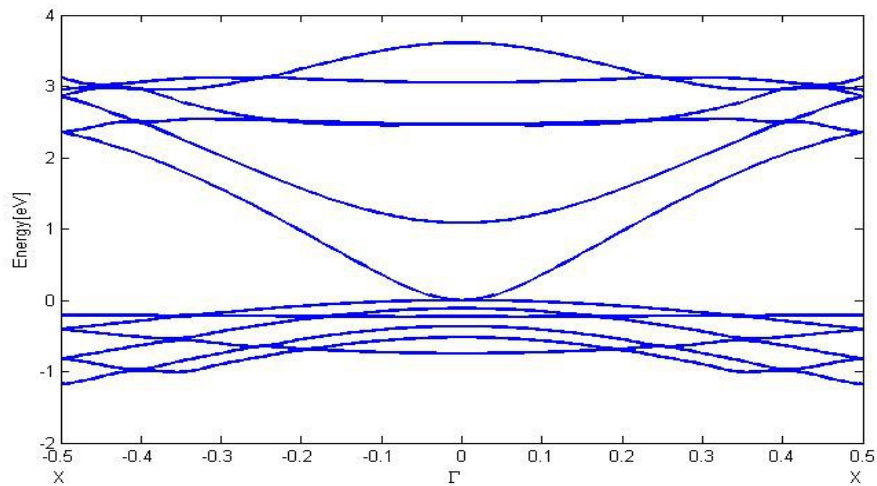


Figure 4.116 DFT band structure of a (8,0) GaN nanotube

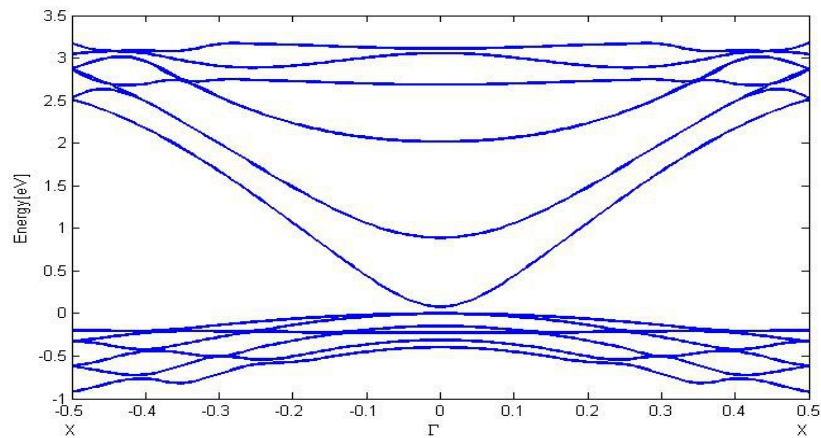


Figure 4.117 DFT band structure of a (10,0) GaN nanotube

DFT predicts no band gaps for (7,0) and (8,0) GaN nanotubes, and a very small band gap of 0.08 eV for (10,0) GaN. These system illustrate the crucial role that GWA plays in solid state physics, as these results are extremely corrected by GWA :

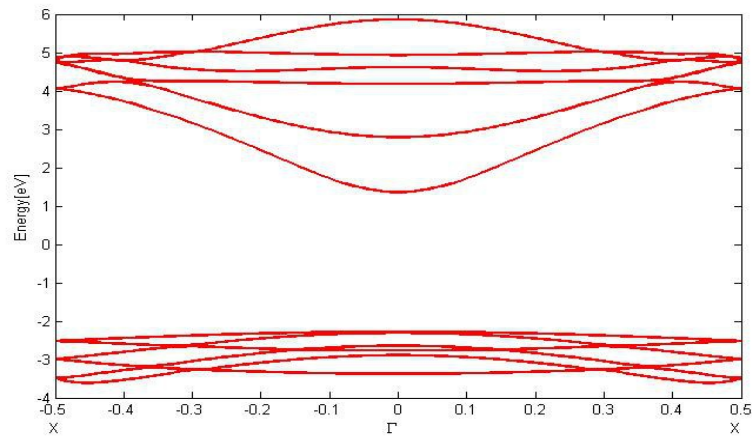


Figure 4.118 GWA band structure of a (7,0) GaN nanotube

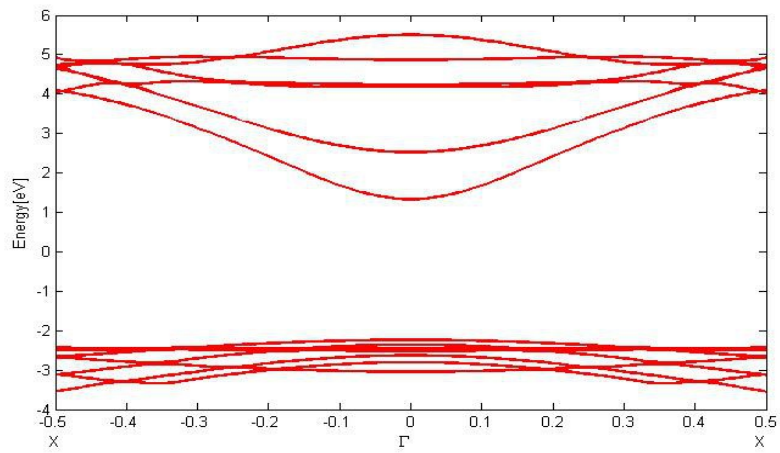


Figure 4.119 GWA band structure of a (8,0) GaN nanotube

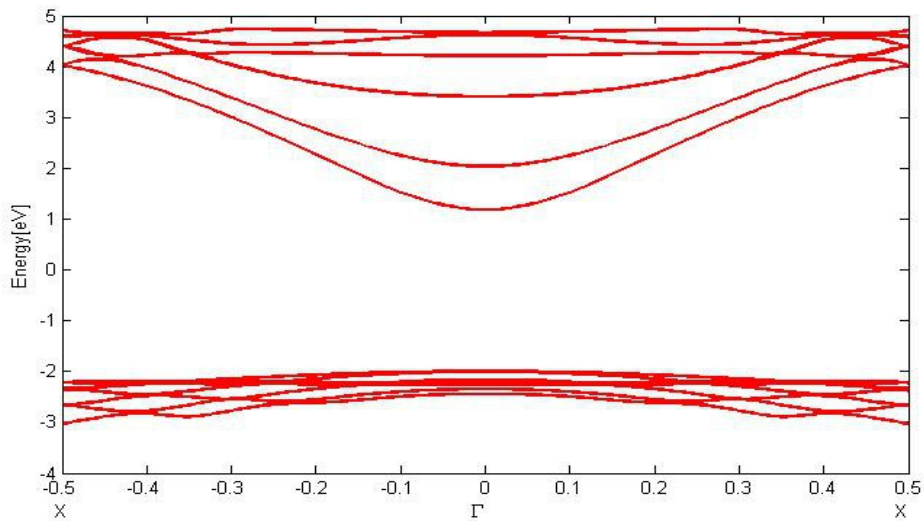


Figure 4.120 GWA band structure of a (10,0) GaN nanotube

GWA yields quite different results, a band gap of 3.63 eV for (7,0), 3.55 eV for (8,0) and 3.18 eV for (10,0). Like for the systems before, the band gap decreases for bigger nano-

tubes. GWA corrections achieve their strongest values at X and are weakest at Γ . For the (7,0) nanotube, they are 3.6 eV at Γ and the same for (8,0), and only around 3 eV at Γ for (10,0).

At the end, we examine the optical of these GaN nanotubes. Their dielectric functions for an incoming plane wave with propagation vector x with nearly identical spectra for wavevector y :

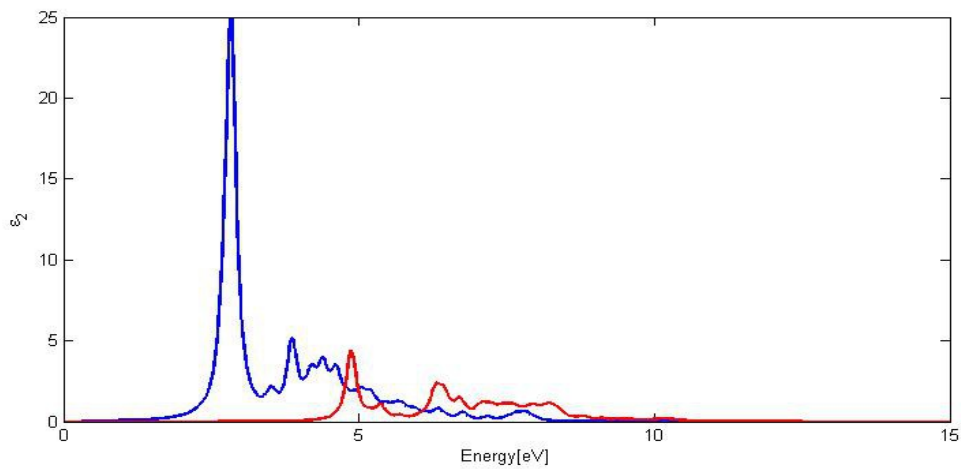


Figure 4.121 Optical spectrum of a (7,0) GaN nanotube for wavevector z

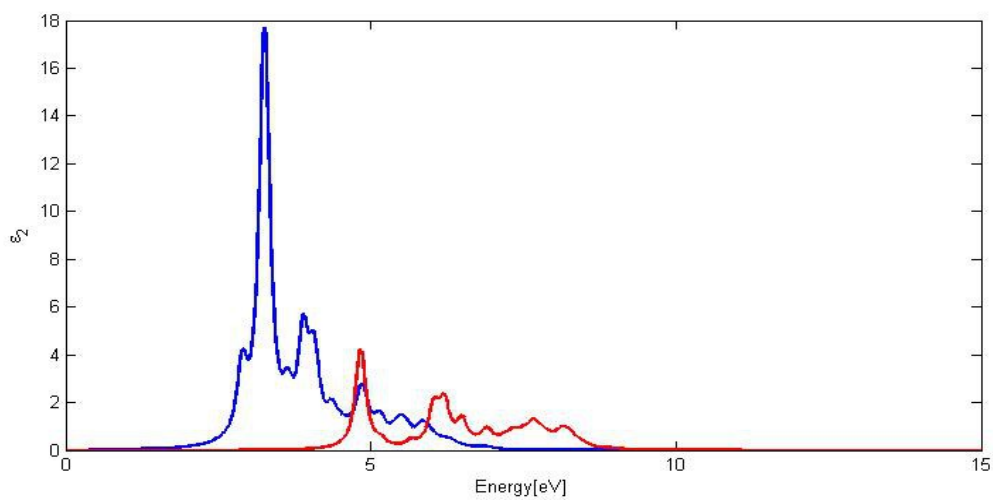


Figure 4.122 Optical spectrum of a (8,0) GaN nanotube for wavevector z

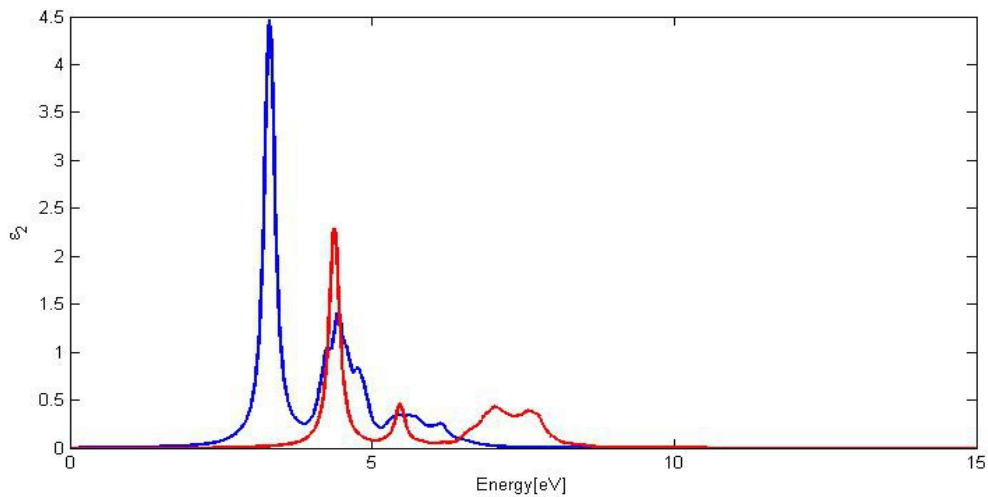


Figure 4.123 Optical spectrum of a (10,0) GaN nanotube for wavevector z

The results depicted above lead to the conclusion that the optical spectrum moves to higher frequency for taller diameters. In detail, the (7,0) nanotube has a main peak at 2.83 eV, followed by a small peak at 3.87 eV. The (8,0) nanotube shows its main peak at 3.26 eV with another peak after it at 3.89 eV, and in the case of the (10,0) nanotube a sharp main peak occurs at 3.3 eV, followed by a side peak at 4.46 eV. Once again, this is due to the stronger electron-hole interaction in the (7,0) nanotube, which outweighs the larger bandgap.

Now let's regard what happens in the case of a plane wave propagating along x :

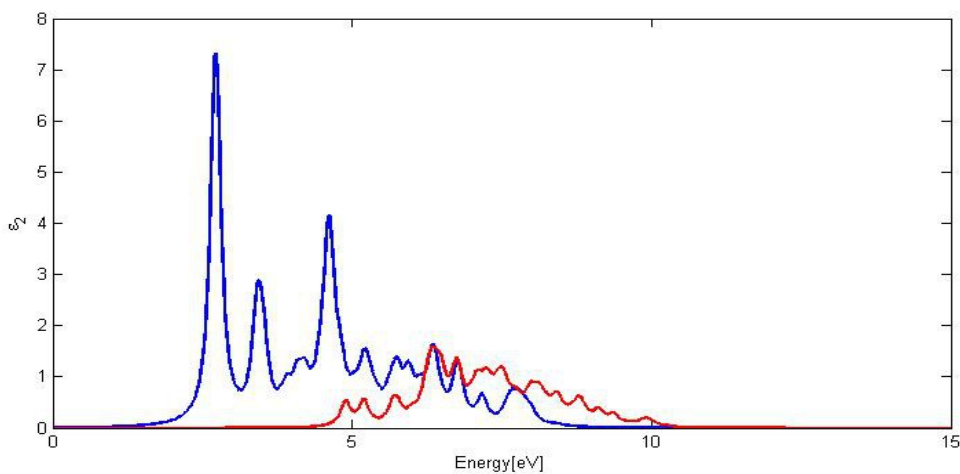


Figure 4.124 Optical spectrum of a (7,0) GaN nanotube for wavevector x

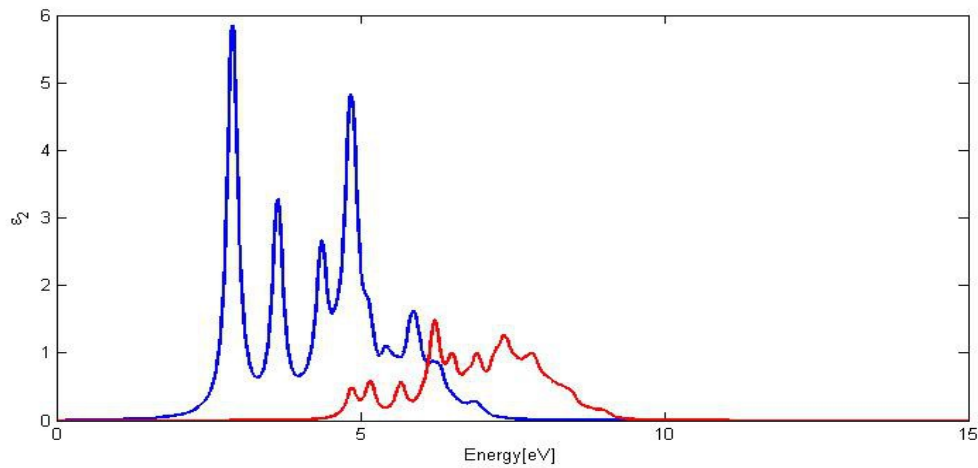


Figure 4.125 Optical spectrum of a (8,0) GaN nanotube for wavevector x

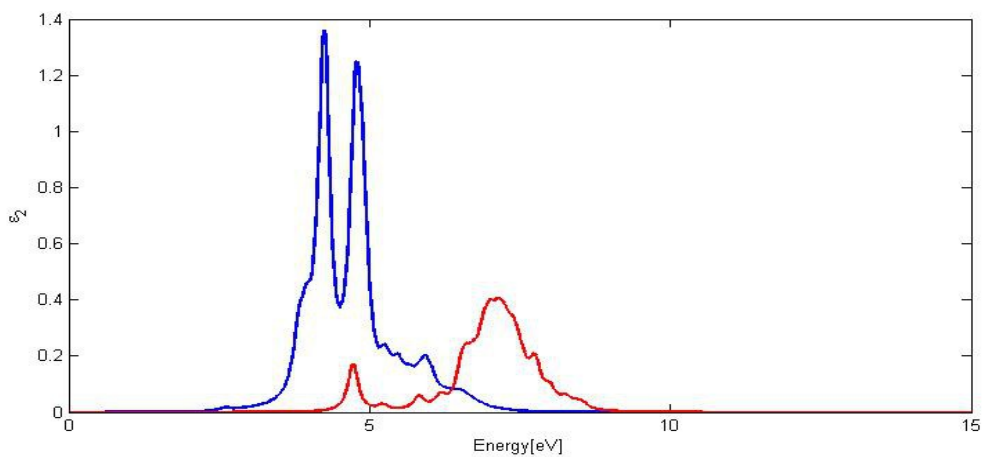


Figure 4.126 Optical spectrum of a (10,0) GaN nanotube for wavevector x

As for wavevector z , the spectra go to higher frequencies for increasing nanotube size. In the spectrum of (7,0), one has peaks at 2.72 eV, 3.43 eV and 4.61 eV, in the (8,0) nanotube they are at 2.89 eV, 3.64 eV and 4.84 eV. In the (10,0) the first peak emerges at 4.25 eV followed by the second strong peak at 4.79 eV. Once again, the strong electron-hole coupling in the (7,0) nanotube causes this.

4.4 SiC and GeC

At last, we investigate the nanotubes belonging to the planar nanostructures of SiC and Ge-C. The nanotubes of SiC we consider are shown below and possess a lattice constant of around 5.40 obtained from calculations :

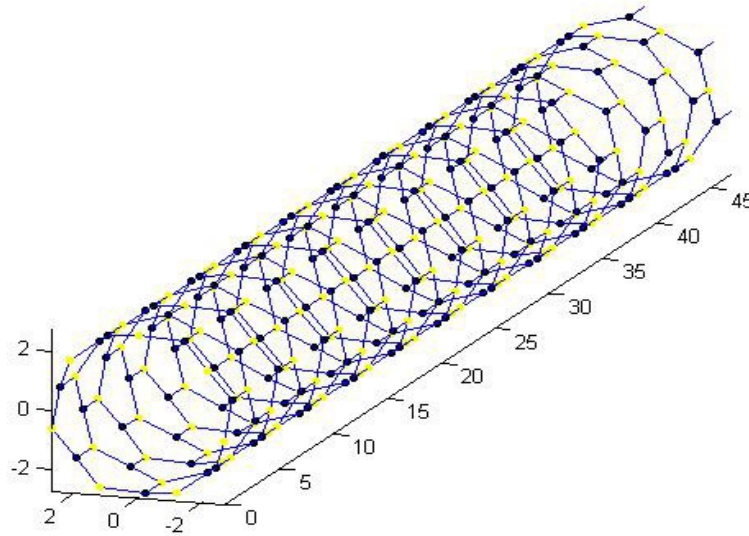


Figure 4.127 (7,0) SiC nanotube, silicon atoms in yellow and carbon atoms in black

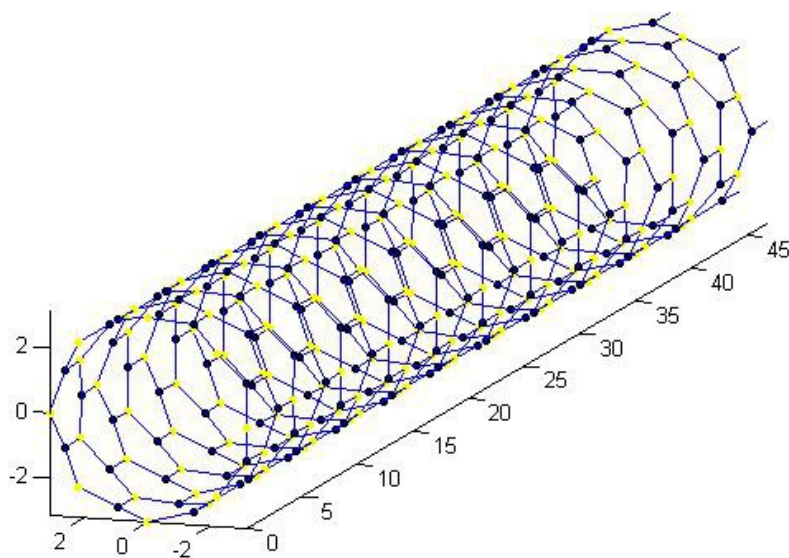


Figure 4.128 (8,0) SiC nanotube, silicon atoms in yellow and carbon atoms in black

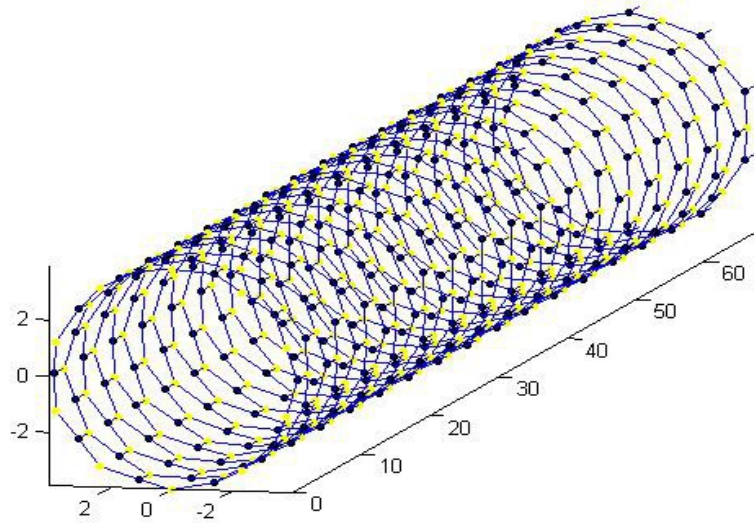


Figure 4.129 (10,0) SiC nanotube, silicon atoms yellow and carbon atoms black

Their electronic band structure is the following according to DFT :

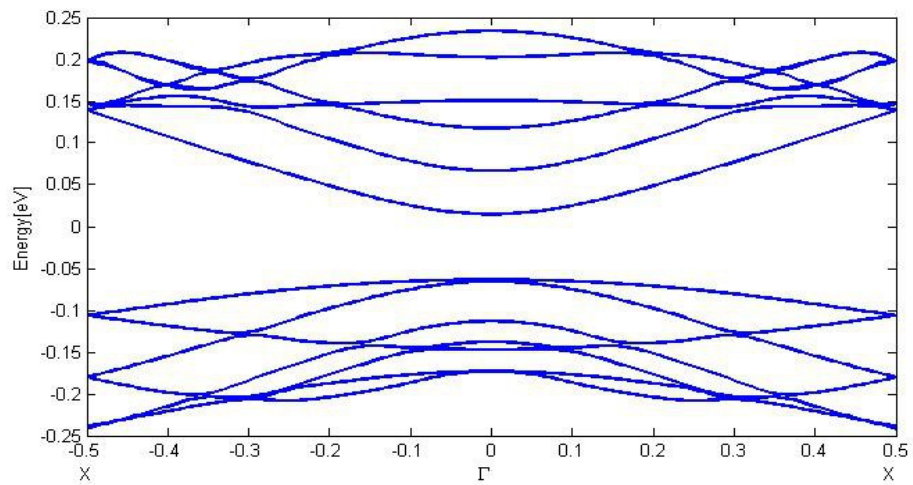


Figure 4.130 DFT band structure of a (7,0) SiC nanotube

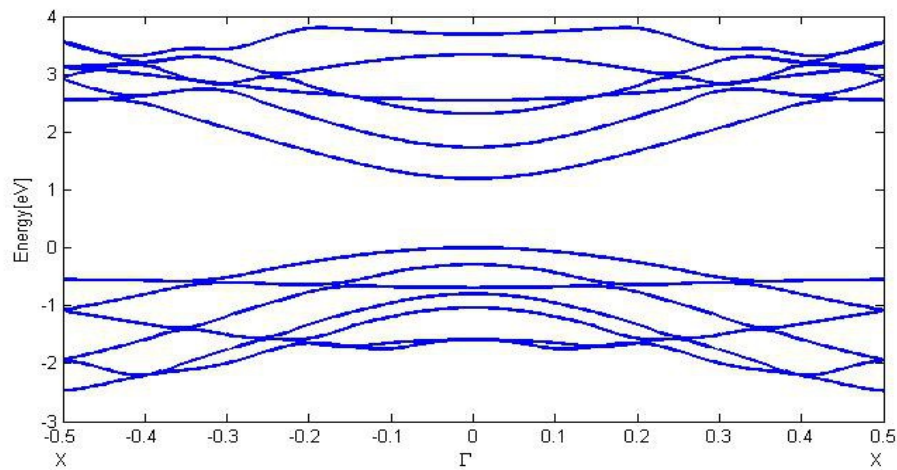


Figure 4.131 DFT band structure of a (8,0) SiC nanotube

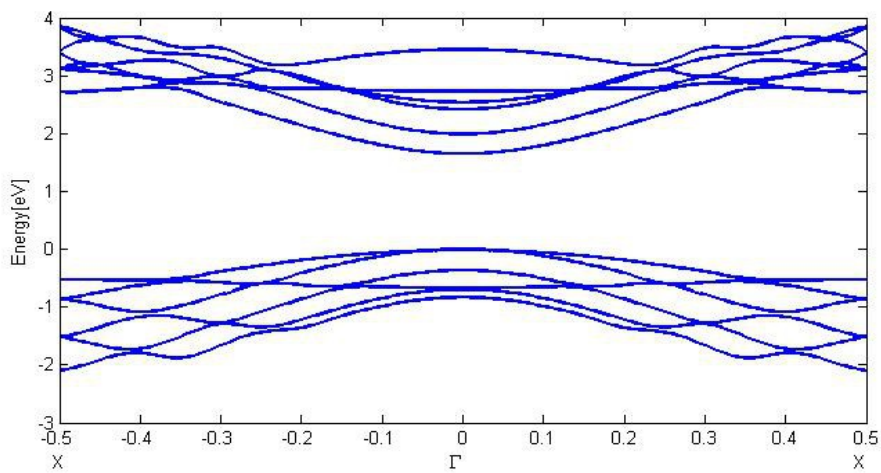


Figure 4.132 DFT band structure of a (10,0) SiC nanotube

One can realize a clear tendency from the results above. The band gap gets larger for bigger nanotubes, namely the band gap is only 0.07 eV for the (7,0) SiC nanotube, then 1.19 eV for the (8,0) SiC nanotube and 1.65 eV for the SiC nanotube. GWA provides the following corrected band structures :

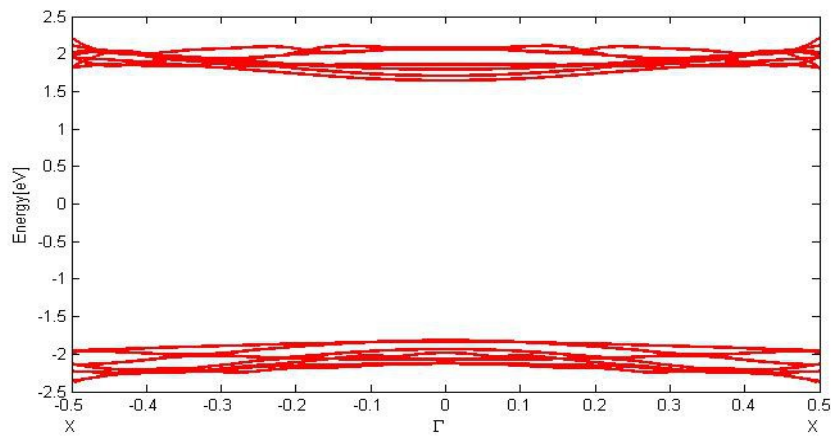


Figure 4.133 GWA band structure of a (7,0) SiC nanotube

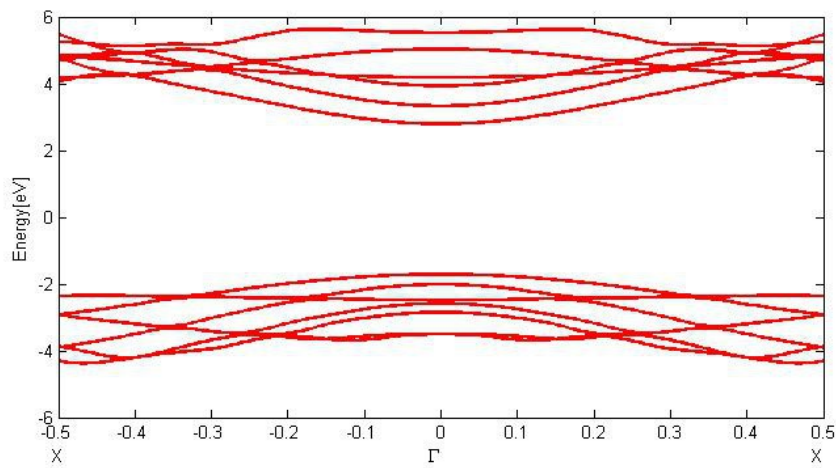


Figure 4.134 GWA band structure of a (8,0) SiC nanotube

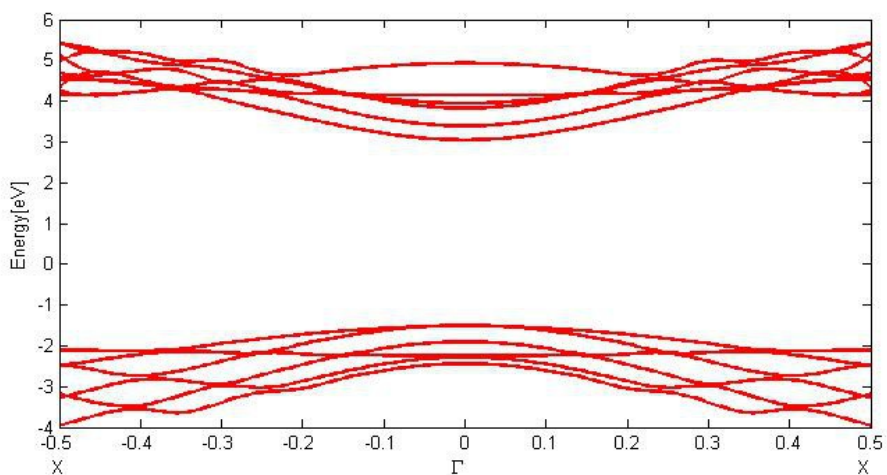


Figure 4.135 GWA band structure of a (10,0) SiC nanotube

GWA corrections preserve the order of band gaps, they predict a band gap of 3.4 eV for the (7,0) nanotube, 4.5 eV for the (8,0) nanotube and 4.54 eV for the (10,0) nanotube. One sees

that the GWA corrections immensely enlarge the band gaps. The GWA show negligible dispersion in all nanotubes, and take their largest values for small nanotubes. In the case of the (7,0) nanotube, they account around 3.3 eV, whereas in the case of the (10,0) nanotube, they only account 2.8 eV.

Now let us take a look at the optics of them. For a plane wave with propagation vector z , the optical spectra of them are :

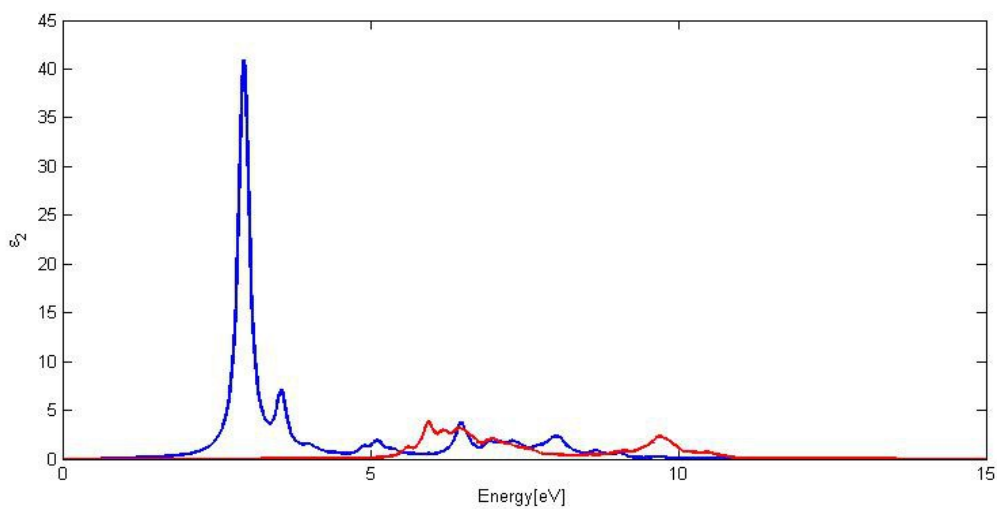


Figure 4.136 Optical spectrum of a (7,0) SiC nanotube for wavevector z

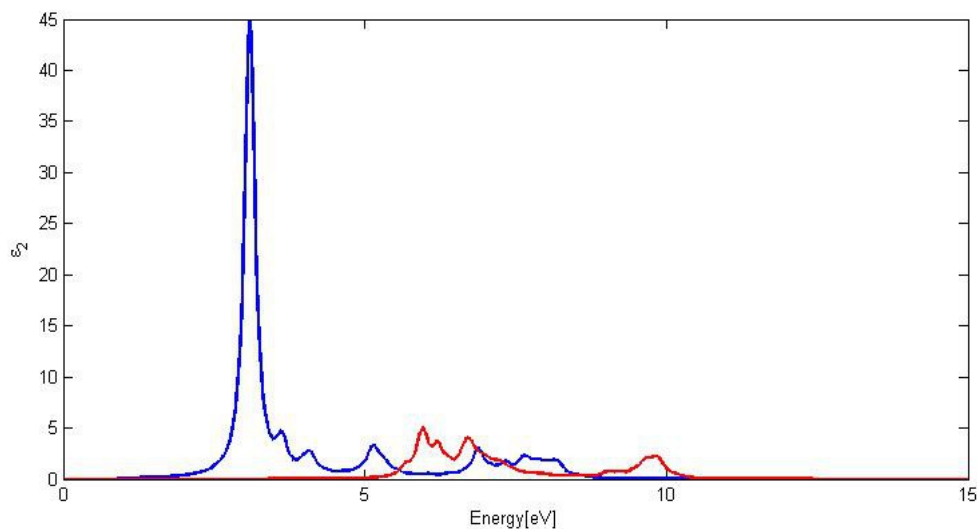


Figure 4.137 Optical spectrum of a (8,0) SiC nanotube for wavevector z

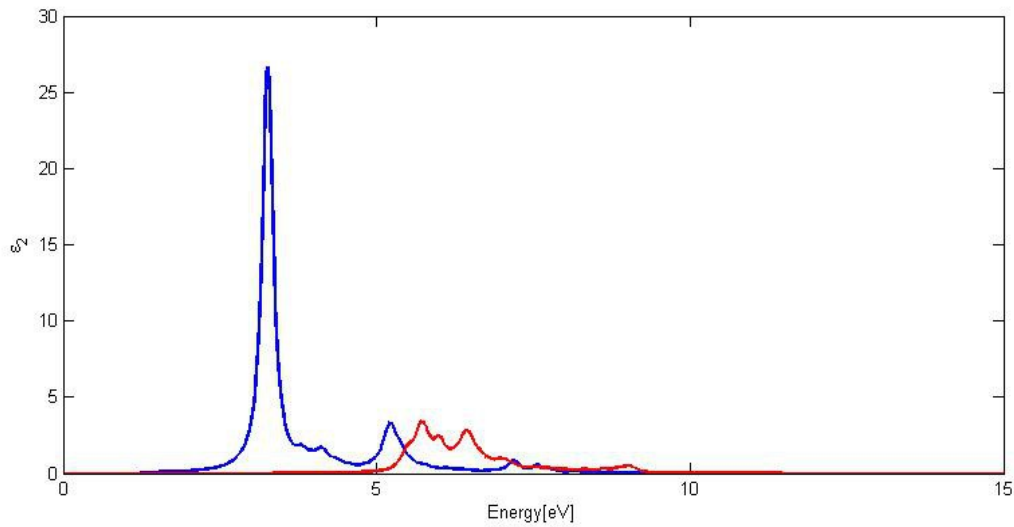


Figure 4.138 Optical spectrum of a (10,0) SiC nanotube for wavevector z

All spectra possess one characteristic sharp peak, which occurs at 2.94 eV in the case of the (7,0) nanotube, at 3.09 eV in the case of the (8,0) nanotube and at 3.26 eV in the case of the (10,0) nanotube. Consequently the peaks occur at higher frequencies for larger nanotubes, which can be explained by the higher band gaps.

Next, we regard the optical spectra in case of wavevector x :

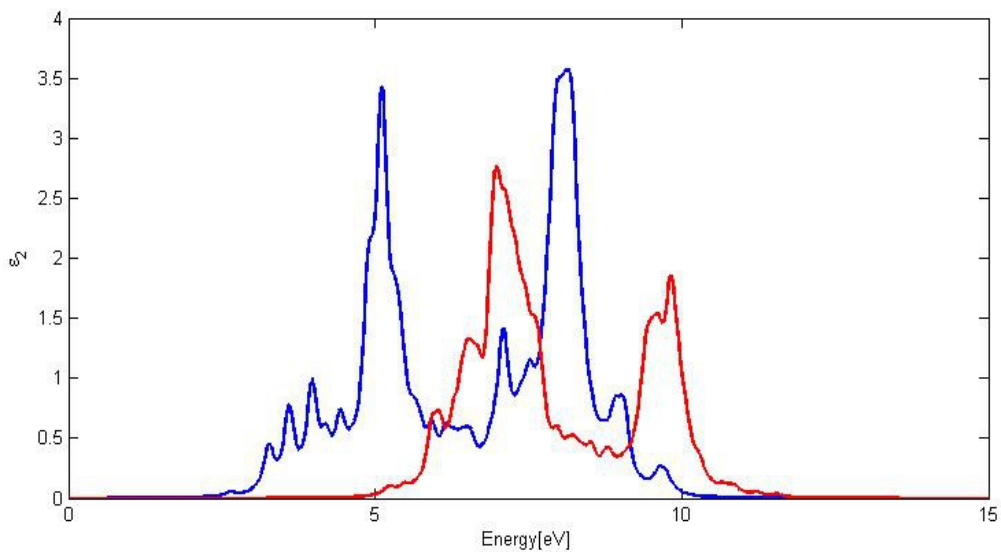


Figure 4.139 Optical spectrum of a (7,0) SiC nanotube for wavevector x

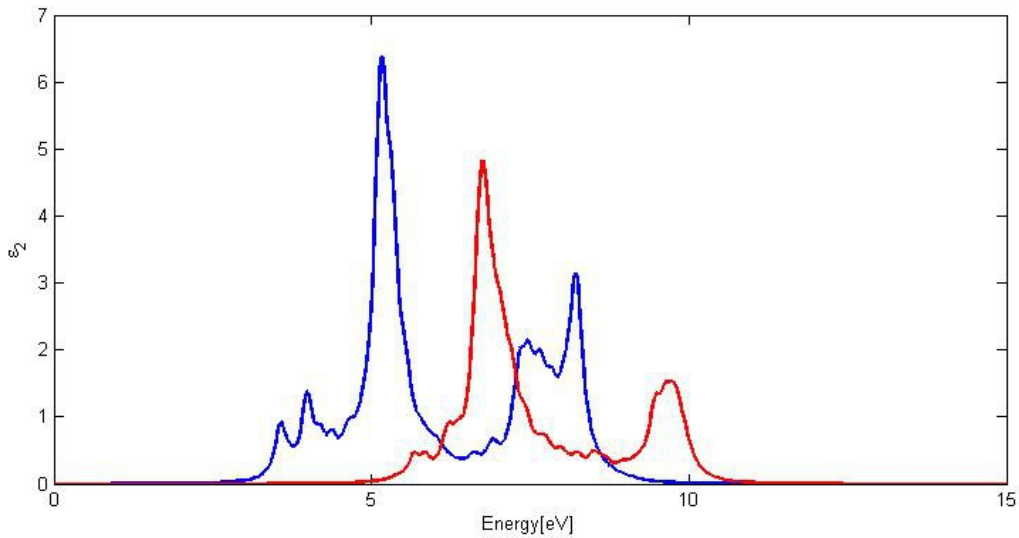


Figure 4.140 Optical spectrum of a (8,0) SiC nanotube for wavevector x

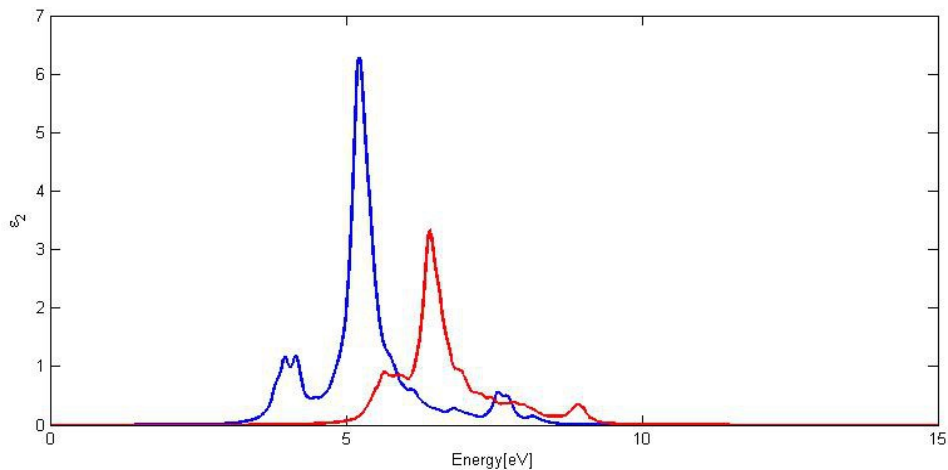


Figure 4.141 Optical spectrum of a (10,0) SiC nanotube for wavevector x

It seems obvious that the spectrum gets broader and touches higher frequencies for smaller nanotubes. The (7,0) nanotube reveals very broad with a peak hill limited by two strong peaks at 5.11 eV and at 8.14 eV, the (8,0) nanotube has a peak with two outstanding peaks at 5.16 eV and at 8.22 eV, while the (10,0) nanotube has only one sharp peak at 5.21 eV.

After having discussed SiC nanotubes, our focus attention goes to their germanium counterparts, GeC nanotubes. Their lattice constant is predicted to be 6.12 Angstrom from SIESTA, and they have the following structure:

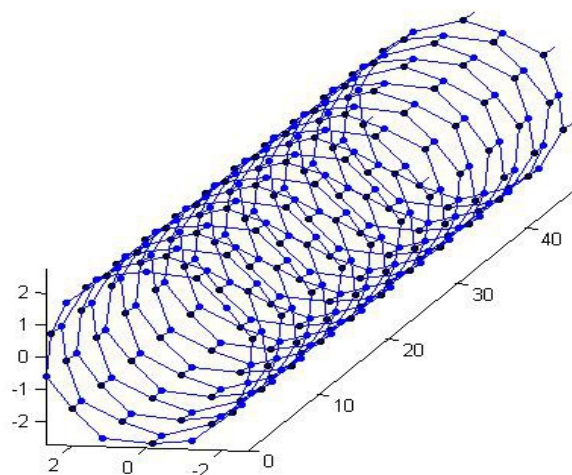


Figure 4.142 (7,0) GeC nanotube, germanium atoms blue and carbon atoms black

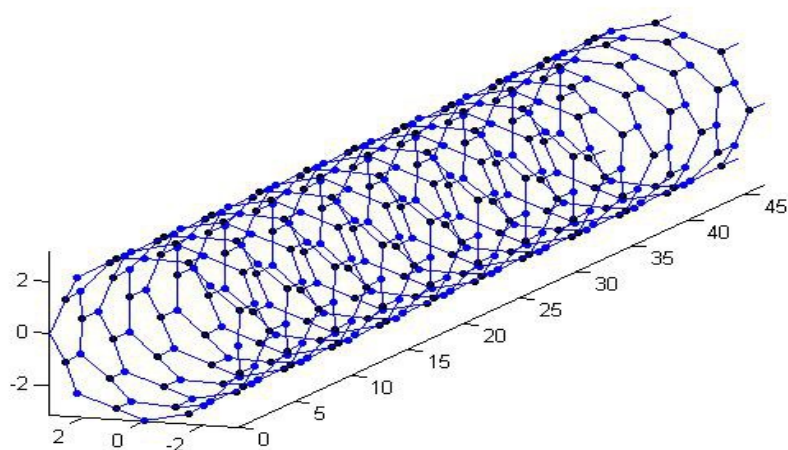


Figure 4.143 (8,0) nanotube, germanium atoms blue and carbon atoms black

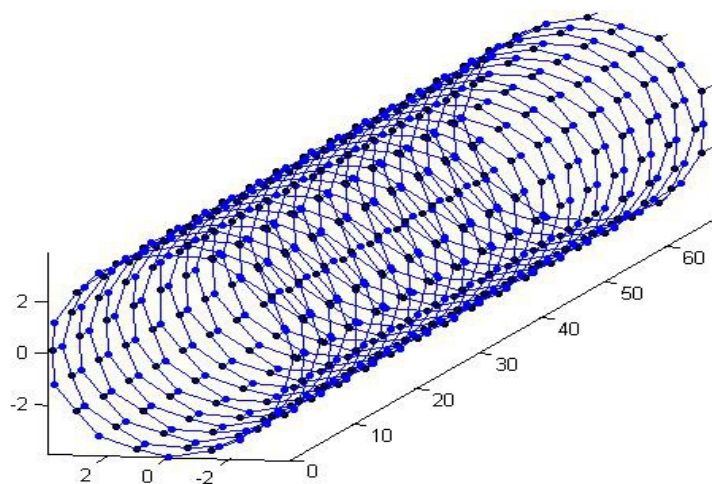


Figure 4.144 (10,0) GeC nanotube, germanium atoms blue and carbon atoms black

We get the following electronic band structures from DFT calculations:

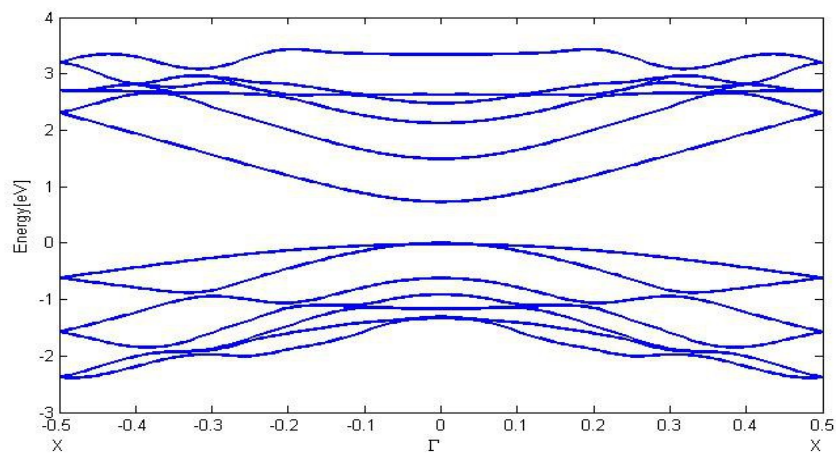


Figure 4.145 DFT band structure of a (7,0) GeC nanotube

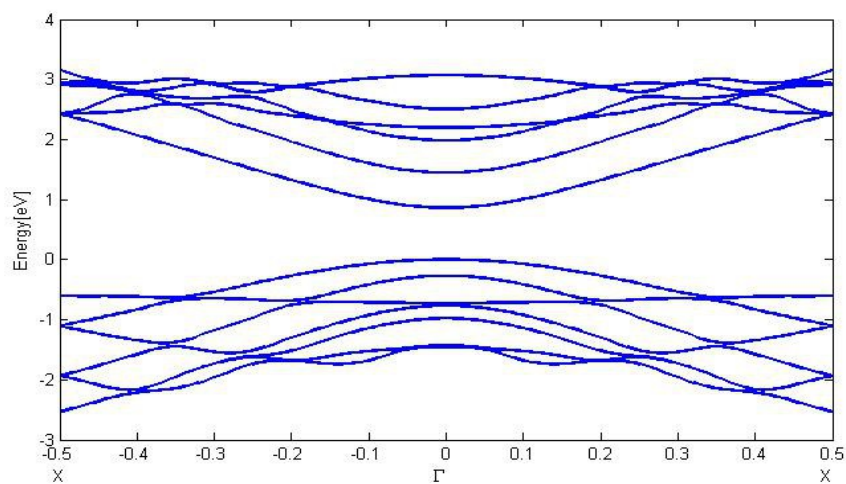


Figure 4.146 DFT band structure of a (8,0) GeC nanotube

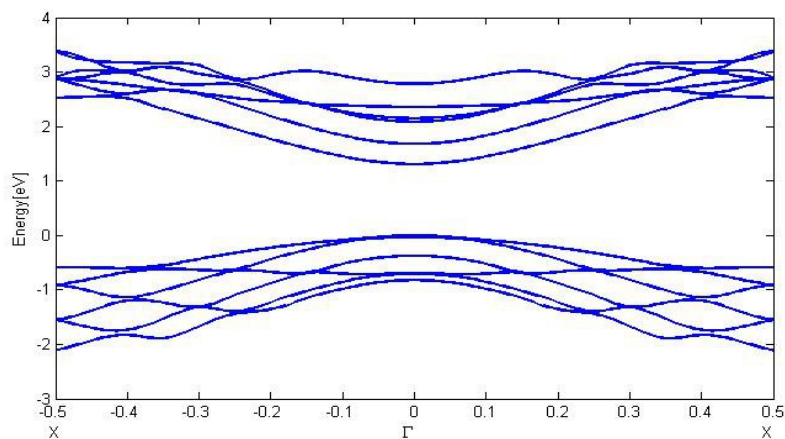


Figure 4.147 DFT band structure of a (10,0) GeC nanotube

From DFT, we receive a band gap of 0.73 eV for the (7,0) nanotube, a band gap of 0.86 eV for the (8,0) nanotube and a band gap of 1.3 eV for the (10,0) nanotube. Thus the band gap gets larger for bigger nanotubes.

Furthermore, the corrected band structures are given by GWA :

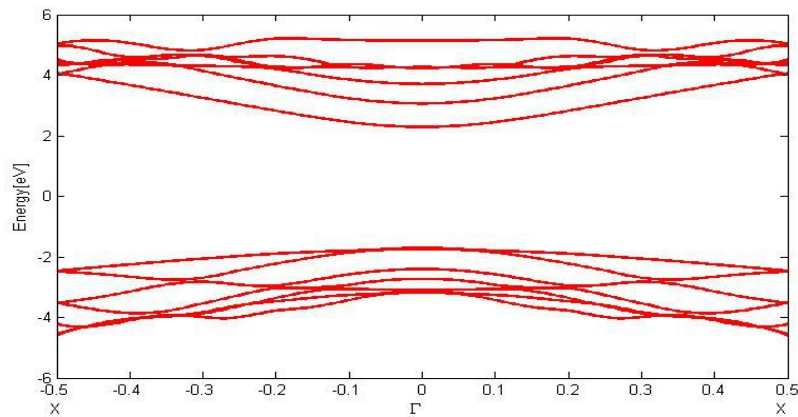


Figure 4.148 GWA band structure of a (7,0) GeC nanotube

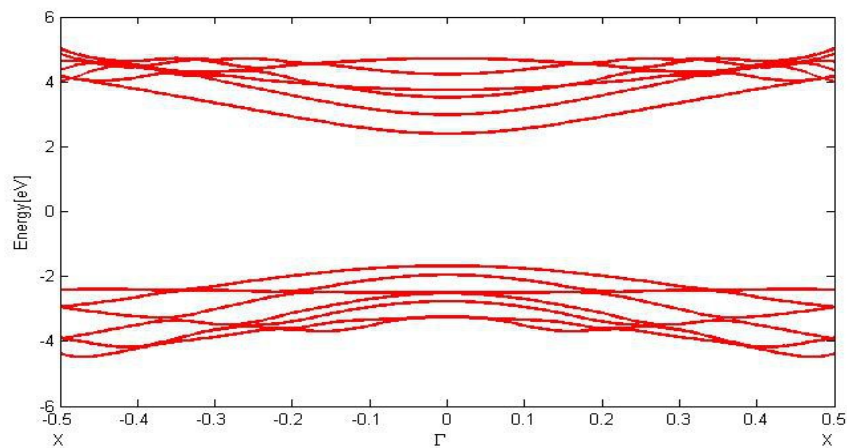


Figure 4.149 GWA band structure of a (8,0) GeC nanotube

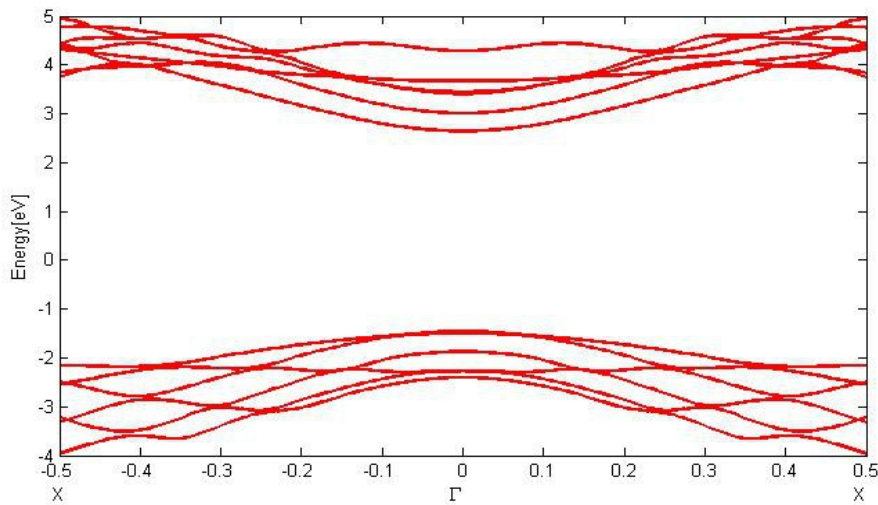


Figure 4.150 GWA band structure of a (10,0) GeC nanotube

GWA corrections deeply change the magnitude of the band gaps, making them nearly equal. Nevertheless, the order of band gap sizes remains the same, being 4 eV for the (7,0) nanotube, 4.07 eV for the (8,0) nanotube and 4.09 eV for the (10,0) nanotube. The size of the corrections gets smaller for larger nanotubes, being around 3.3 eV in the case of the (7,0) nanotube, 3.2 eV in the case of the (8,0) and only 2.8 eV for the (10,0) nanotube. One sees that the correction play a big role for all nanotubes, extending all band gaps to a large degree. All corrections reveal only very small dispersion.

The optical responses of these nanotubes are as follows :

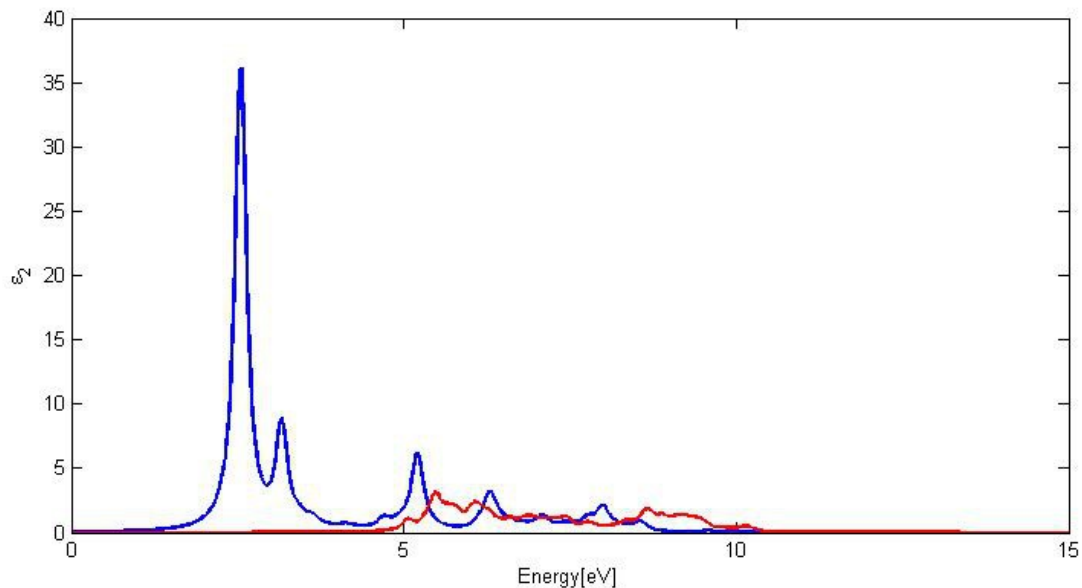


Figure 4.151 Optical spectrum of a (7,0) GeC nanotube for wavevector z

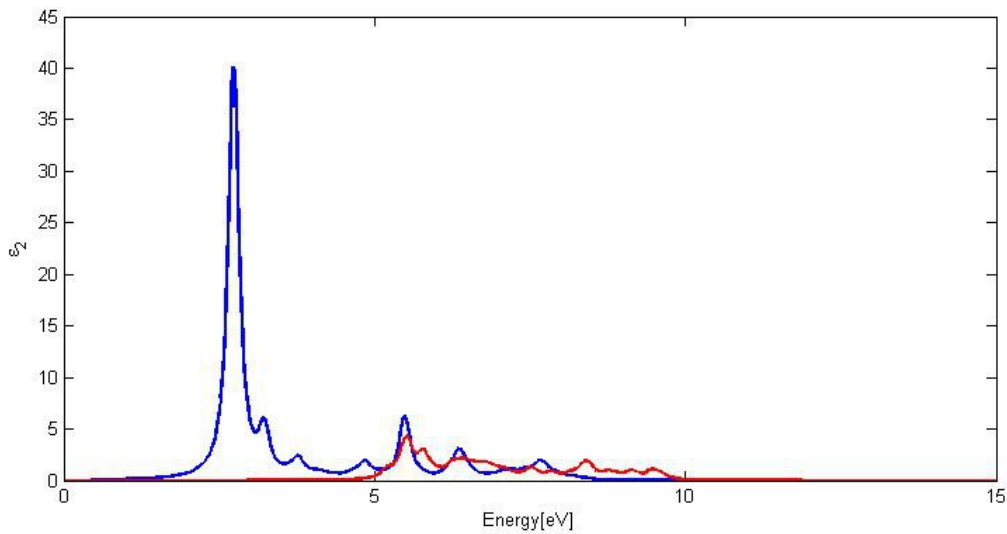


Figure 4.152 Optical spectrum of a (8,0) GeC nanotube for wavevector z

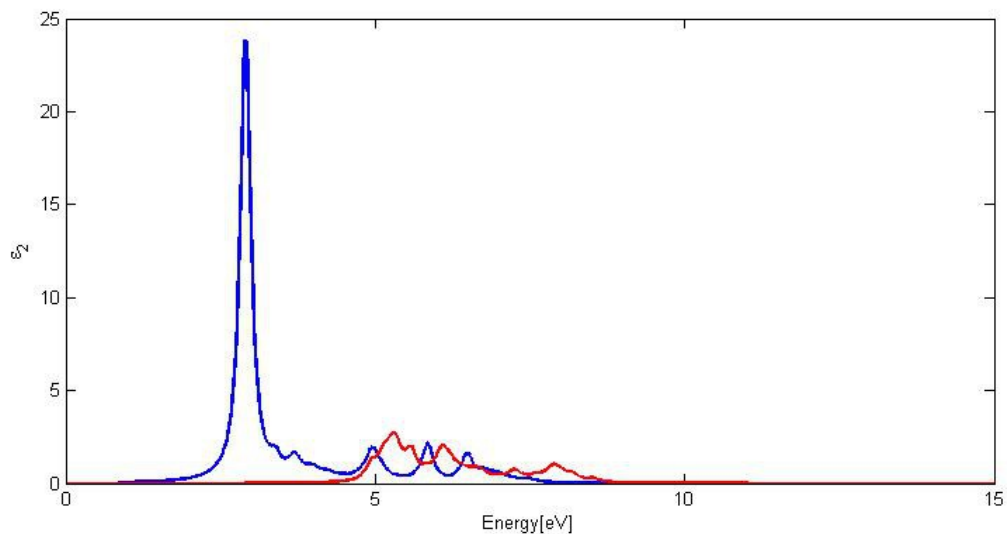


Figure 4.153 Optical spectrum of a (10,0) GeC nanotube for wavevector z

The spectra all show a sharp peak, which position moves to higher energies for bigger nanotubes. For the (7,0) nanotube, the peak is located at 2.55 eV, for the (8,0) nanotube at 2.73 eV and for the (10,0) nanotube at 2.9 eV. These results harmonize with the increasing band gap for larger nanotubes. The spectra for wavevector y are nearly identical, and are therefore not mentioned separately.

Now lets look at the optical spectra for wavevector x :

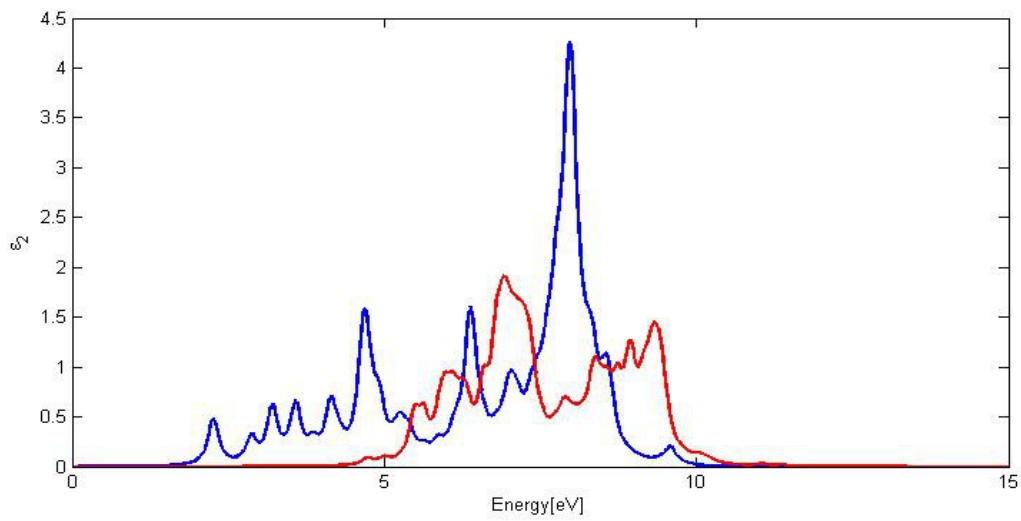


Figure 4.154 Optical spectrum of a (7,0) GeC nanotube for wavevector x

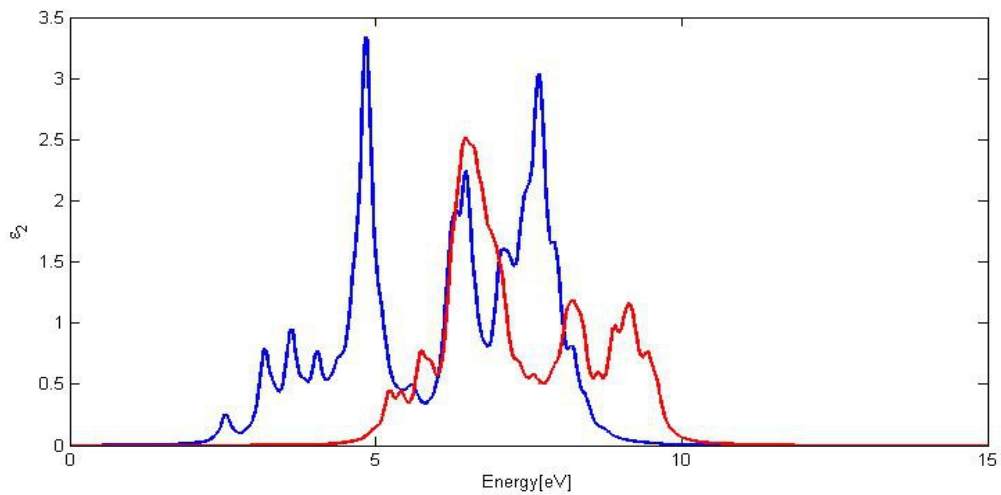


Figure 4.155 Optical spectrum of a (8,0) GeC nanotube for wavevector x

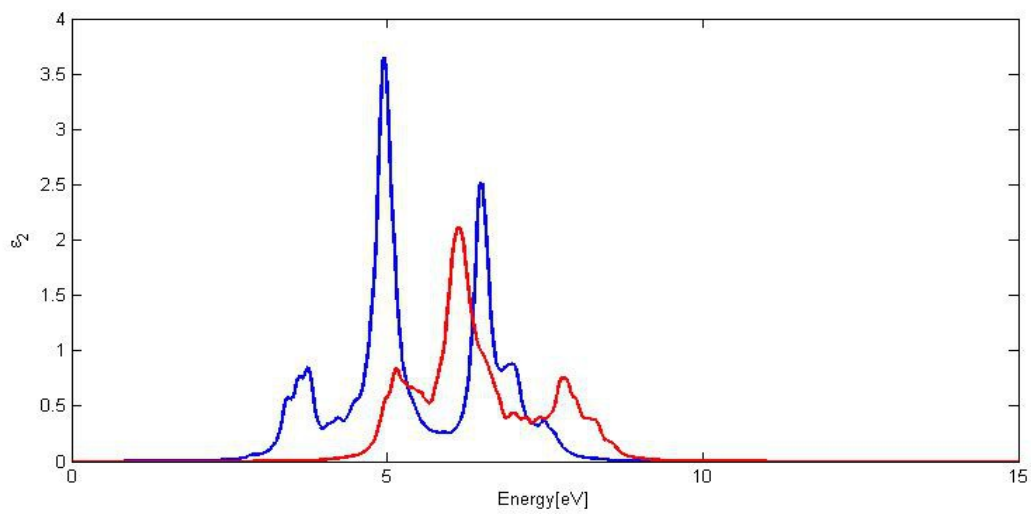


Figure 4.156 Optical spectrum of a (10,0) GeC nanotube for wavevector x

The spectra depicted above have many peaks. In case of the (7,0) nanotube, peaks emerge at 4.68 eV, 6.38 eV and 7.97 eV, in the (8,0) nanotube peaks emerge at 4.84 eV, 6.46 eV and 7.66 eV, and in case of the (10,0) nanotube, one can see peaks at 4.95 eV and at 6.49 eV. All nanotubes exhibit a very broad optical spectrum, and the frequency of the highest energy peak is higher for smaller nanotubes.

5. Heterostructures of nanomaterials

In the last two chapter, we have always concentrated on planar nanostructures and nanotubes of one material. This will change in this chapter. The focus of interest is now to investigate planar heterostructures of two different nanomaterials, where one nanomaterial is embedded in another one. We will consider two cases, boron nitride embedded in graphene, and GaN embedded in planar AlN.

5.1 Boron nitride embedded in graphene

First we regard boron nitride stripes of several width embedded in graphen. The systems have the following structures :

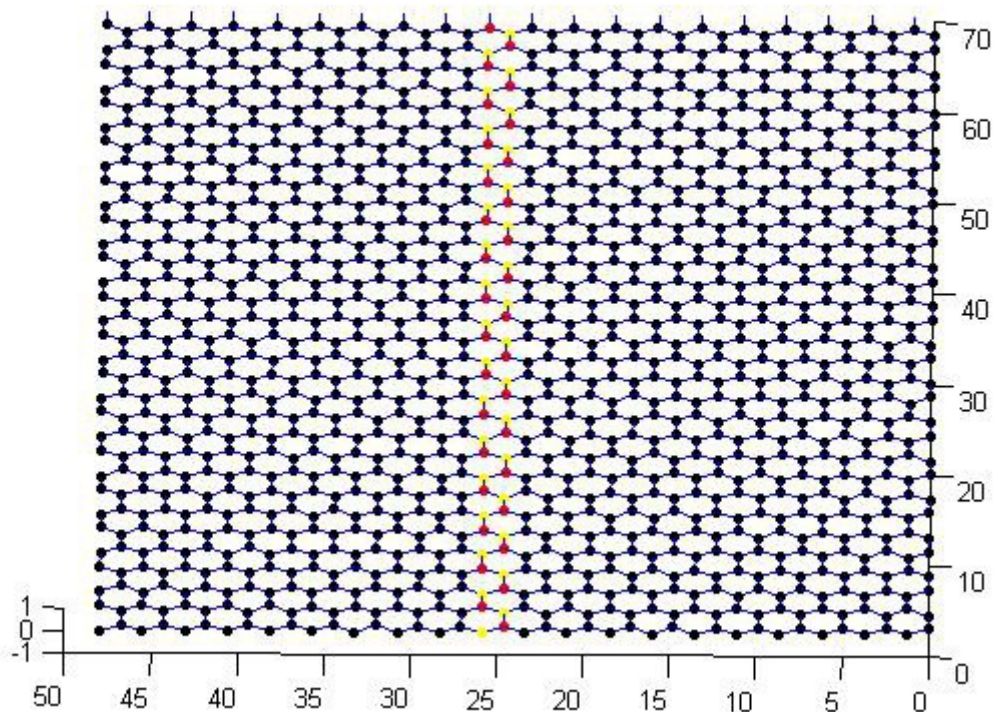


Figure 5.1 Boron nitride embedded in graphene, boron in yellow, nitrogen in red and carbon in black, $n = 1$

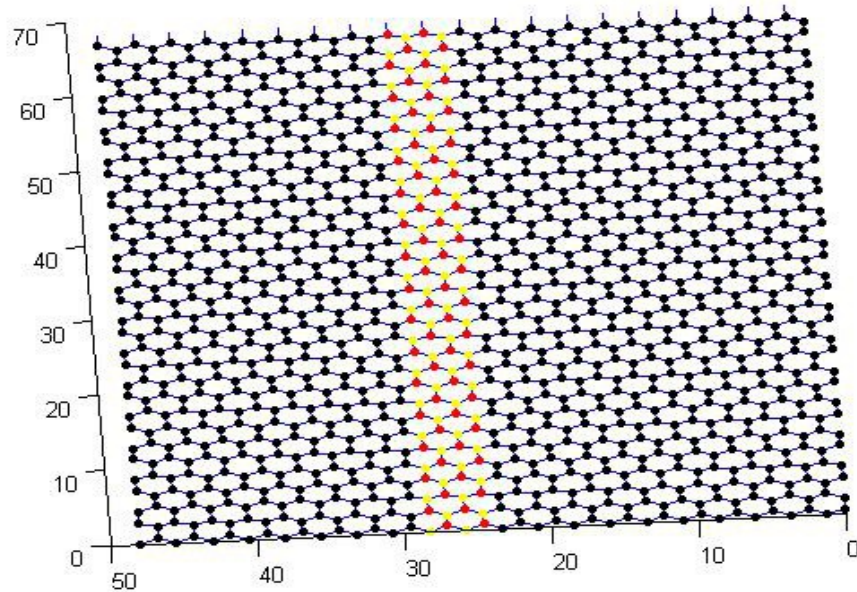


Figure 5.2 Boron nitride embedded in graphene, boron in yellow, nitrogen in red and carbon in black, $n = 2$

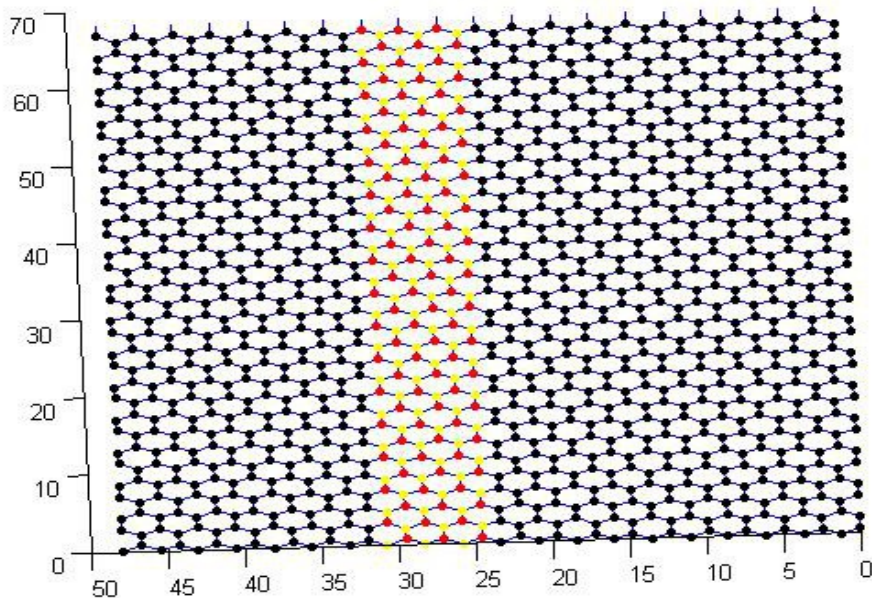


Figure 5.3 Boron nitride embedded in graphene, boron in yellow, nitrogen in red and carbon in black, $n = 3$

We consider boron nitride stripes of several widths, labeled $n = 1, 2, 3$. The stripes all have zig-zag structure, and $n = 1, 2, 3$ stands for $(1, 0)$, $(2, 0)$ and $(3, 0)$. In our model, the boron and nitrogen atoms are initially placed on the lattice position of the graphene lattice. Then the complete systems, whose size is $(30, 0)$, is relaxed using the program SIESTA, and the re-

sulting atom positions are used as basis for all calculations.

DFT yields the following electronic band structures :

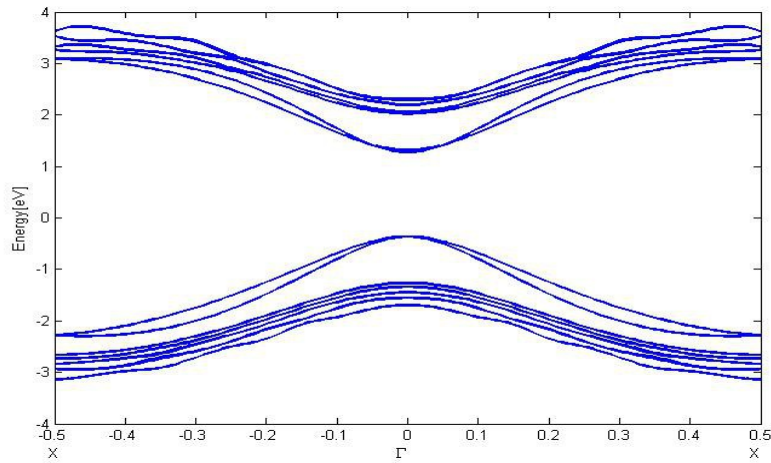


Figure 5.4 DFT band structure of boron nitride embedded in graphene, $n = 1$

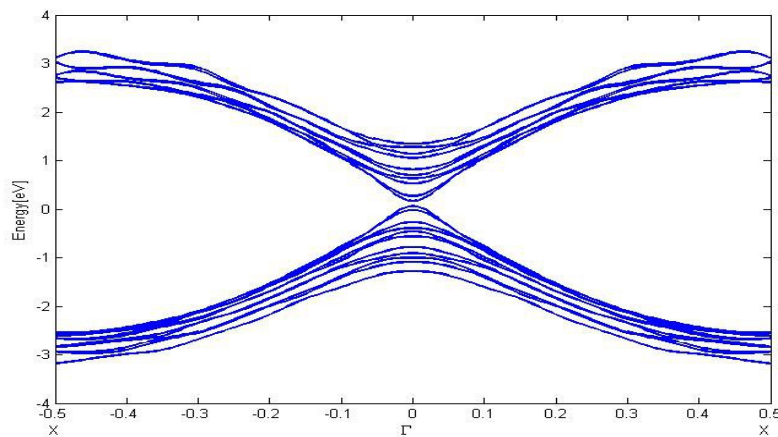


Figure 5.5 DFT band structure of boron nitride embedded in graphene, $n = 2$

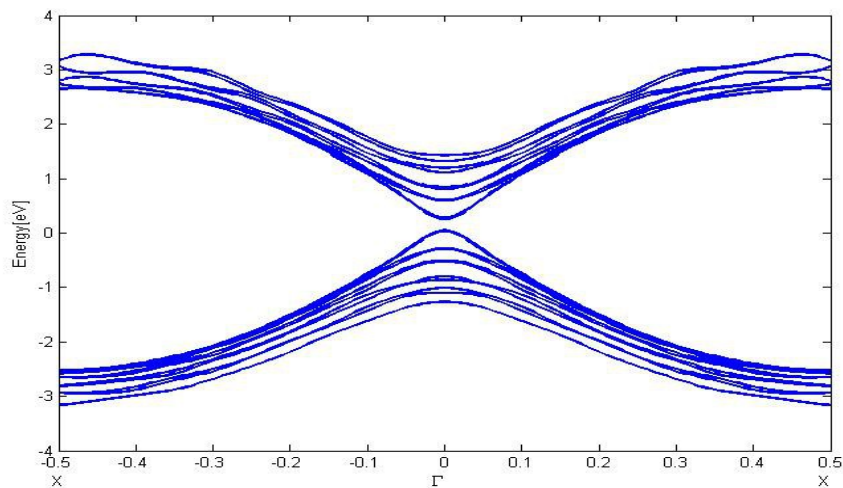


Figure 5.6 DFT band structure of boron nitride embedded in graphene, $n = 3$

According to DFT, one obtains a band gap of 1.68 eV for $n = 1$, only 0.1 eV for $n = 2$ and eV for $n = 3$. GWA significantly corrects these results :

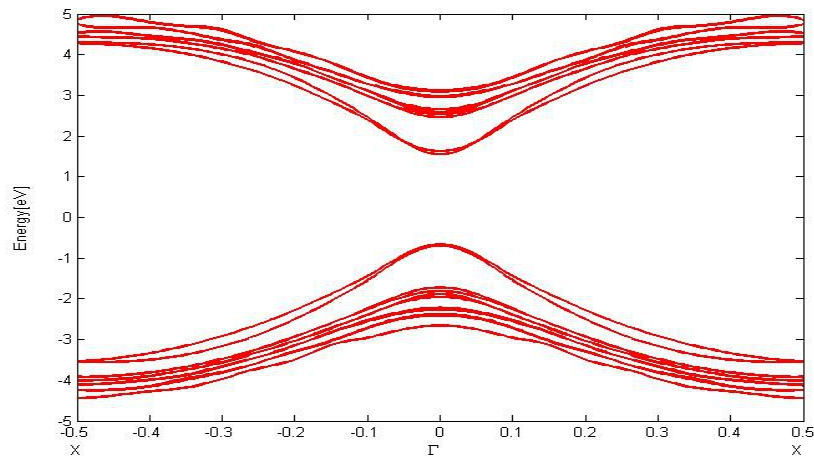


Figure 5.7 GWA band structure of boron nitride embedded in graphene, $n = 1$

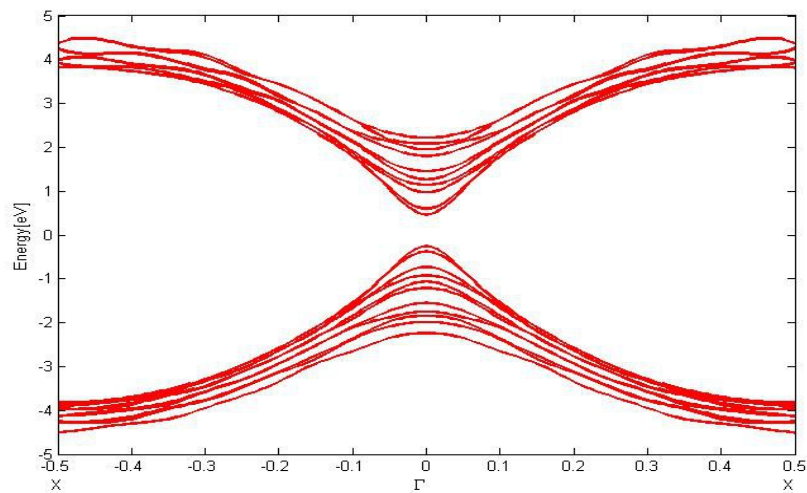


Figure 5.8 GWA band structure of boron nitride embedded in graphene, $n = 2$

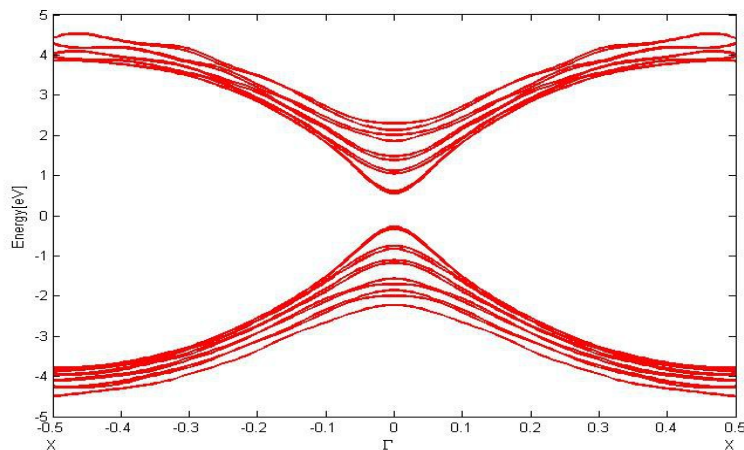


Figure 5.9 GWA band structure of boron nitride embedded in graphene, $n = 3$

From GWA, we receive a band gap of 2.21 eV for $n = 1$, a band gap of 0.72 eV for $n = 2$, and a band gap of 0.82 eV for $n = 3$. The overwhelming band gap size of $n = 1$ remains under GWA corrections, but then the band gap increases with n . The large band gap for $n = 1$ can be explained by the distortion caused by a single boron nitride stripes which is completely surrounded by graphene. In the case of $n=2,3$, the situation becomes more like boron nitride between graphene borders, and the band gap increases between $n = 2$ and $n = 3$ because the contribution of boron nitride is stronger.

We proceed now with the optical response. For wavevector z , the dielectric functions are :

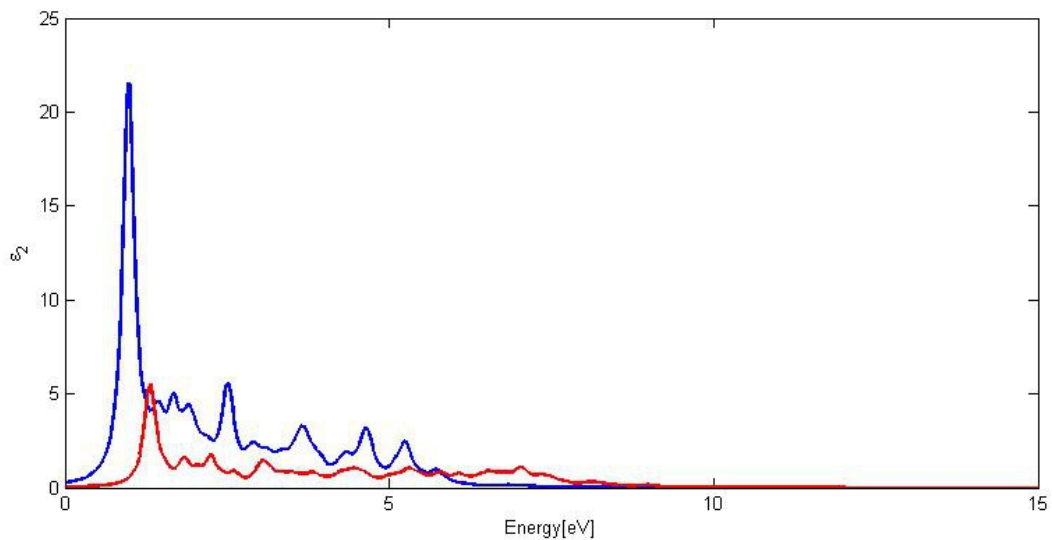


Figure 5.10 Optical spectrum of boron nitride embedded in graphene for wavevector z , $n = 1$

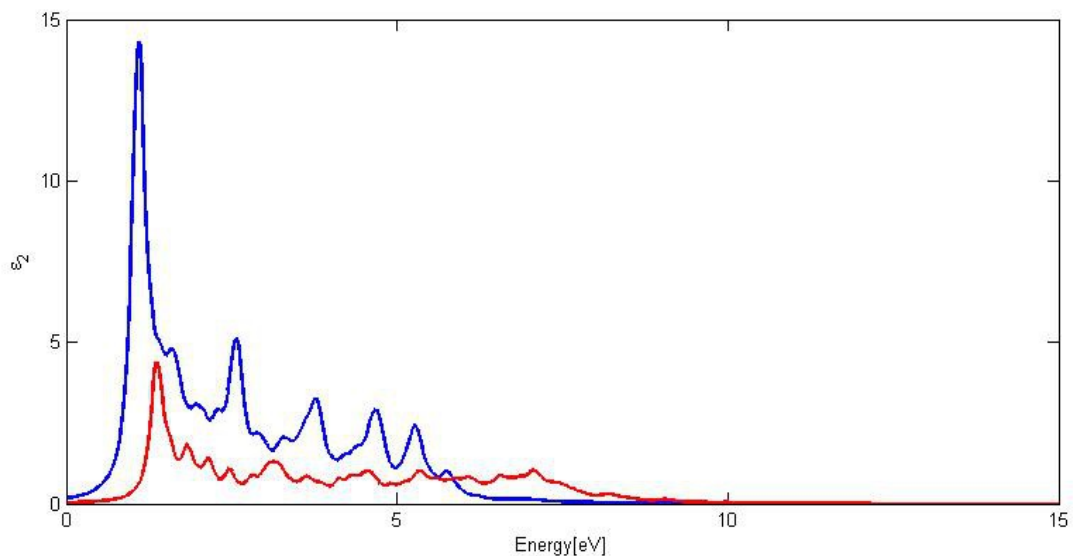


Figure 5.11 Optical spectrum of boron nitride embedded in graphene for wavevector z , $n = 2$

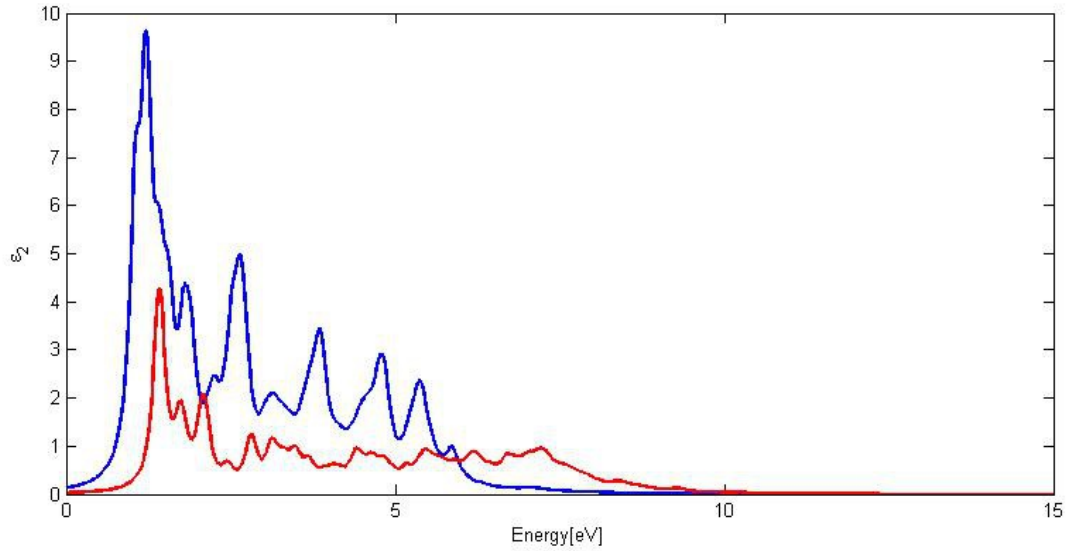


Figure 5.12 Optical spectrum of boron nitride embedded in graphene for wavevector z , $n = 3$

Regarding the optical properties, we get a clear relationship between the boron nitride with n and the spectrum. For higher n , the position of the strongest peak is pushed to higher energy, for $n = 1$ it is 0.98 eV, for $n = 2$ its is 1.1 eV, and for $n = 3$ the strongest peak is at 1.21 eV. Additionally, one can observe much more optical response in the higher frequency area for higher n . This makes sense as the contribution of boron nitride increases.

Now lets take a look at the other wavevectors :

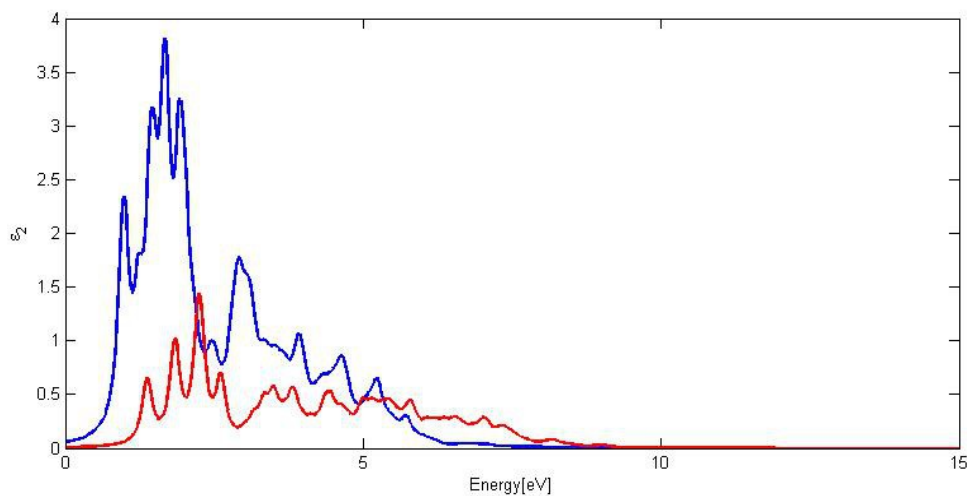


Figure 5.13 Optical spectrum of boron nitride embedded in graphene for wavevector y , $n = 1$

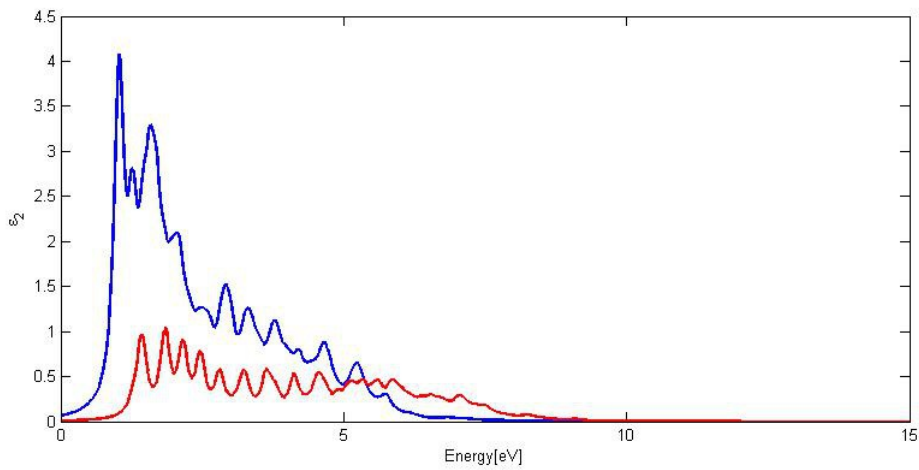


Figure 5.14 Optical spectrum of boron nitride embedded in graphene for wavevector y , $n = 2$

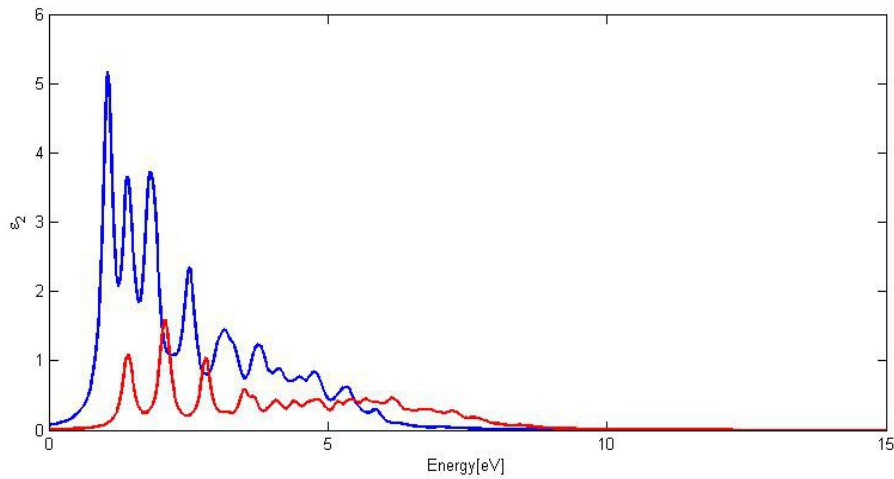


Figure 5.15 Optical spectrum of boron nitride embedded in graphene for wavevector y , $n = 3$

and for wavevector x

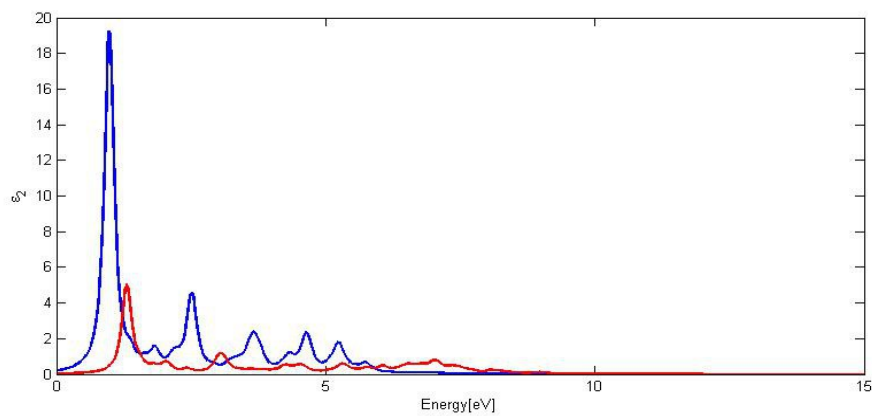


Figure 5.16 Optical spectrum of boron nitride embedded in graphene for wavevector x , $n = 1$

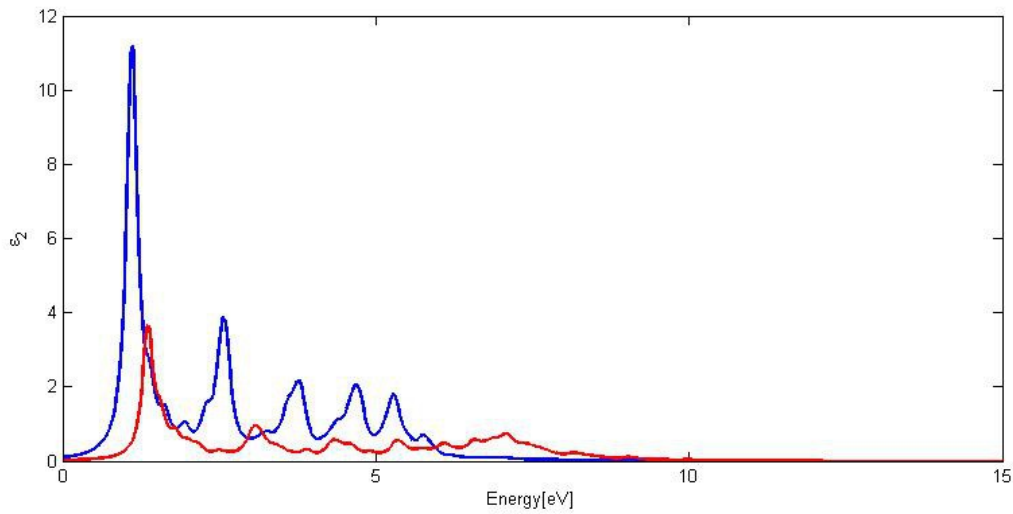


Figure 5.17 Optical spectrum of boron nitride embedded in graphene for wavevector x , $n = 2$

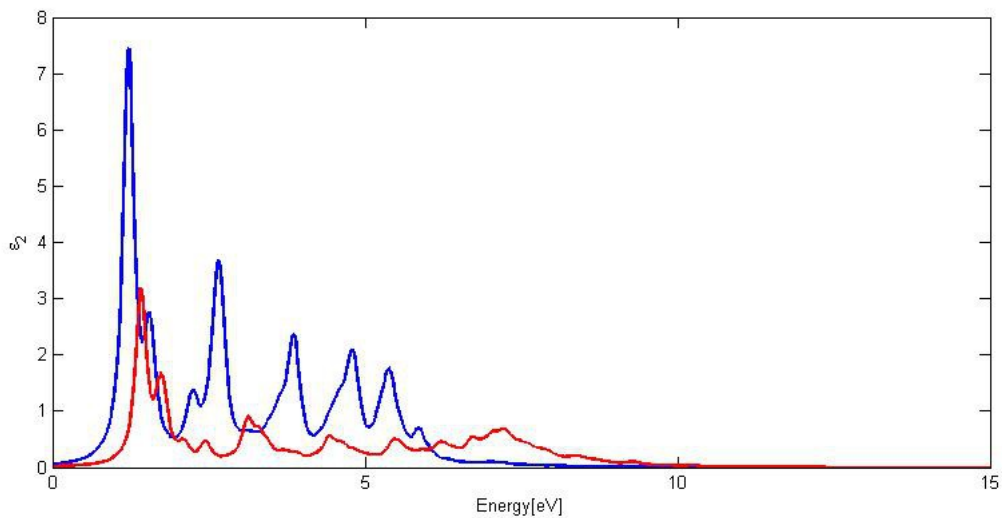


Figure 5.18 Optical spectrum of boron nitride embedded in graphene for wavevector x , $n = 3$

The position of the main peaks of wavevector z seems to originate from the spectra of wavevector y . However, the spectra of wavevector y show high values after the first peak, but the spectra belonging to wavevector x rapidly decline after the first peak. So one can realize that the spectra of wavevector z are the superposition of wavevector x and y .

5.2 GaN embedded in planar AlN

The second system we consider in this chapter is GaN embedded in planar AlN, with the same widths as in the previous section. The systems we deal with are depicted below:

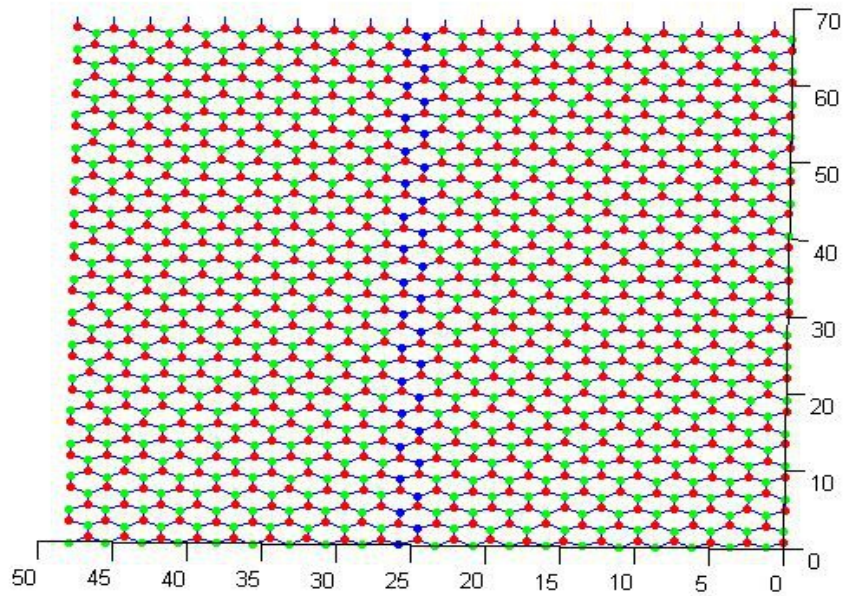


Figure 5.19 GaN embedded in planar AlN, aluminum green, nitrogen red and gallium blue, $n = 1$

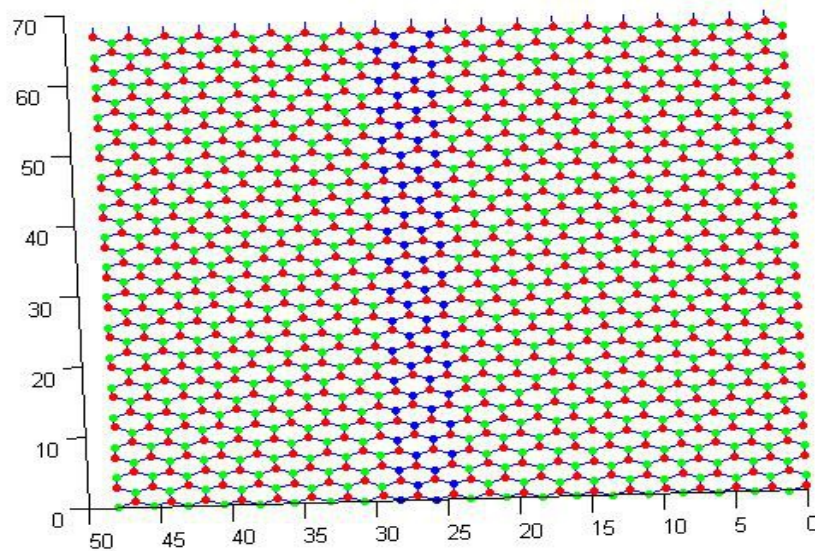


Figure 5.20 GaN embedded in planar AlN, aluminum green, nitrogen red and gallium blue, $n = 2$

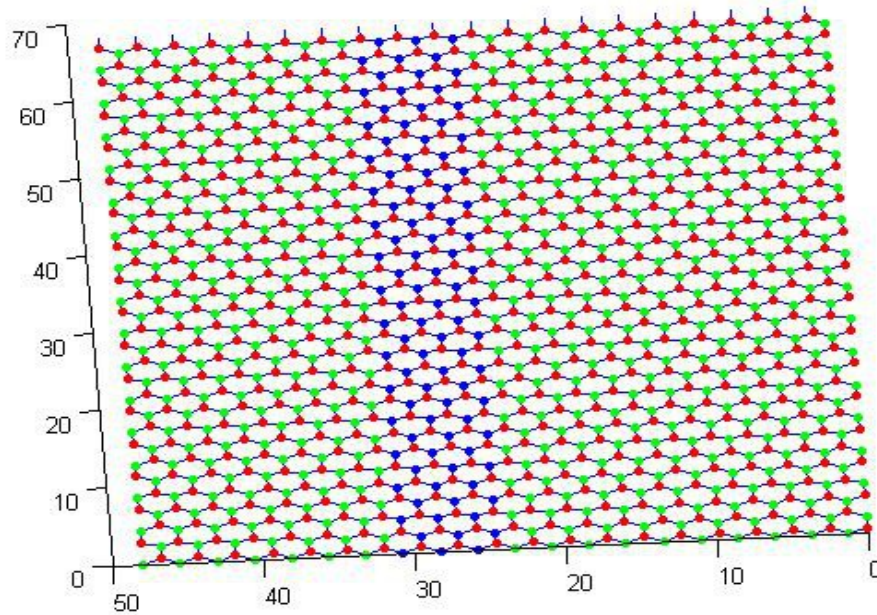


Figure 5.21 GaN embedded in planar AlN, aluminum green, nitrogen red and gallium blue, $n = 3$

As in the case of boron nitride embedded in graphene, the gallium nitride atoms have been inserted on the atomic positions of the planar hexagonal AlN lattice, and then all atomic coordinates have been relaxed with SIESTA. We have taken again a size of (30,0) for the total system. The electronic band structures of these systems are the following according to DFT :

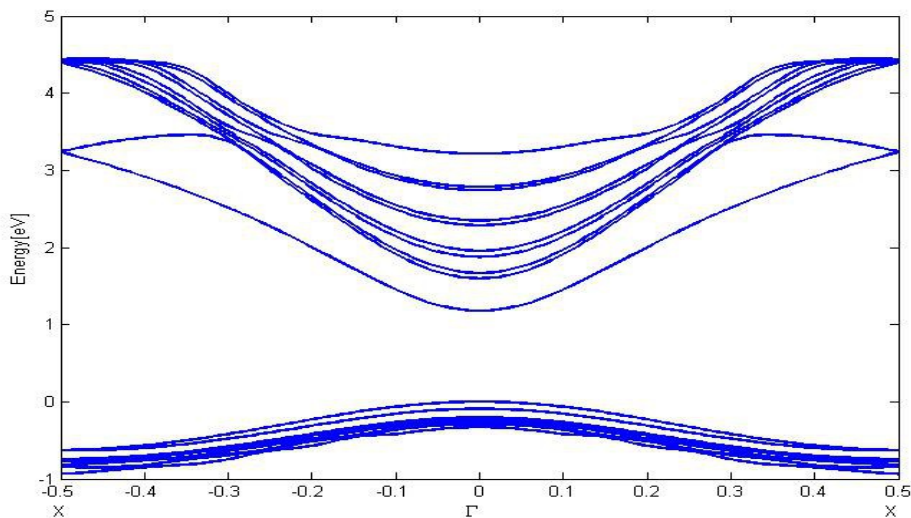


Figure 5.22 DFT band structure of GaN embedded into planar AlN, $n = 1$

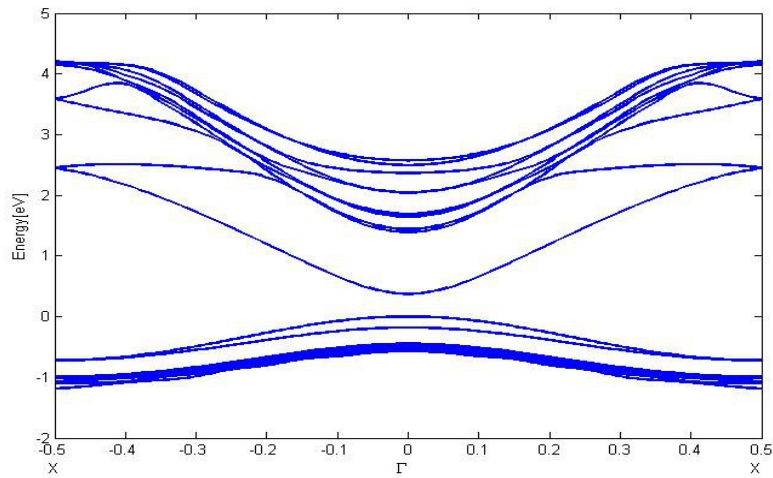


Figure 5.23 DFT band structure of GaN embedded into planar AlN, $n = 2$

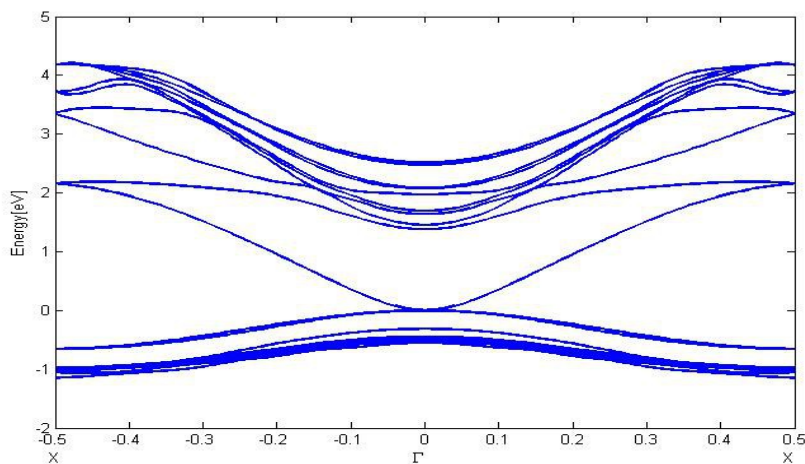
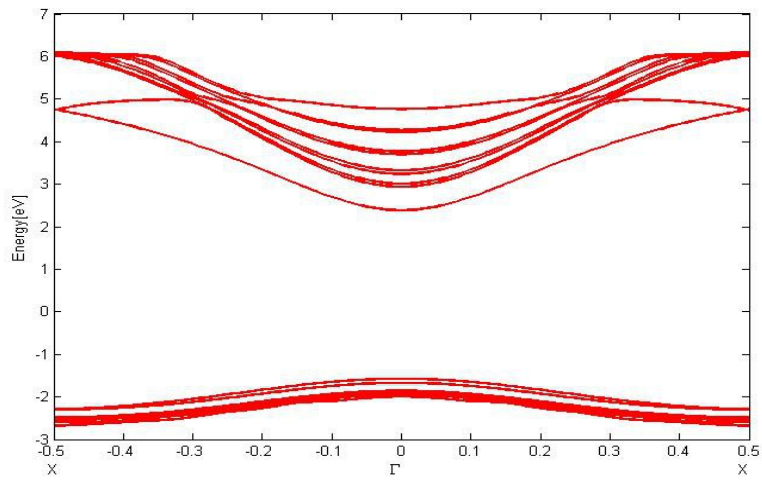
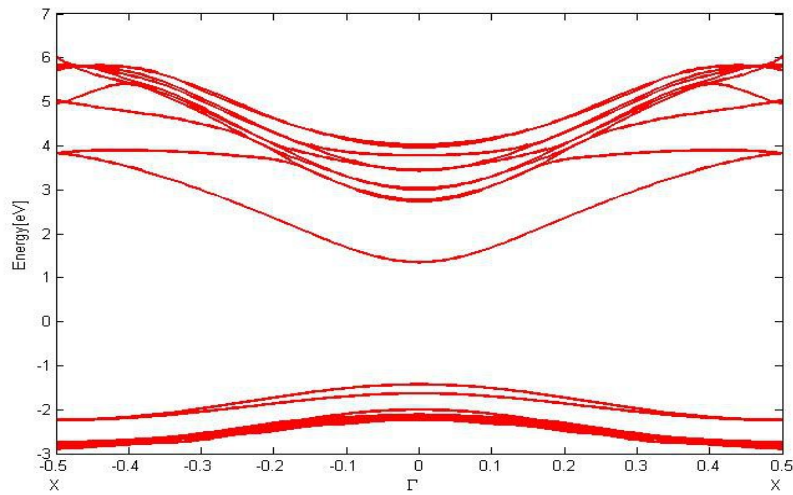
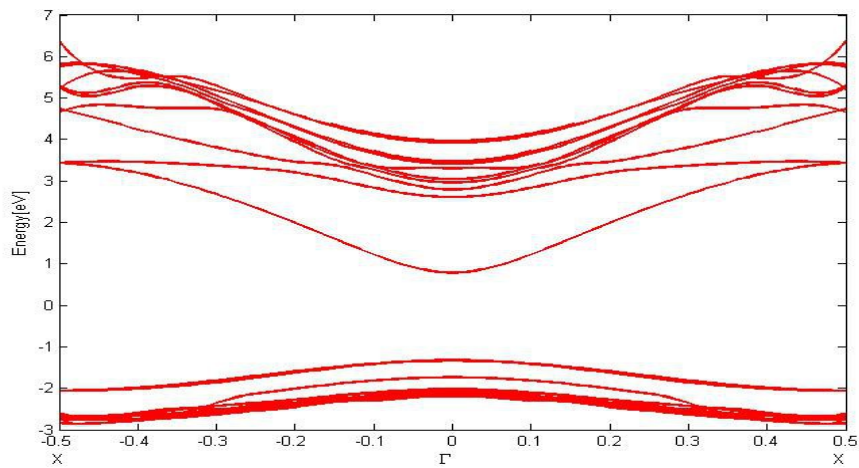


Figure 5.24 DFT band structure of GaN embedded into planar AlN, $n = 3$

DFT predicts a band gap of 1.17 eV for $n = 1$, 0.37 eV for $n = 2$ and a closing band gap for $n = 3$. Now we take look at the band structures resulting from GWA :

Figure 5.25 GWA band structure of GaN embedded in planar AlN, $n = 1$ Figure 5.26 GWA band structure of GaN embedded in planar AlN, $n = 2$ Figure 5.27 GWA band structure of GaN embedded in planar AlN, $n = 3$

We obtain a clear dependence of the band gap from n . According to GWA, the band gap is 3.95 eV for $n = 1$, 2.78 eV for $n = 2$ and 2.1 eV for $n = 3$. The situation here is different from boron nitride embedded in graphene, as AlN and GaN are much more similar to each other than boron nitride and graphene. For comparison, planar AlN possesses a band gap of 6.7 eV and planar GaN a band gap of 5.15 eV. As with higher n the influence of GaN rises and planar GaN has a smaller band gap than planar AlN, consequently the band gap of the systems decreases.

Finally, we regard the optical response of these systems :

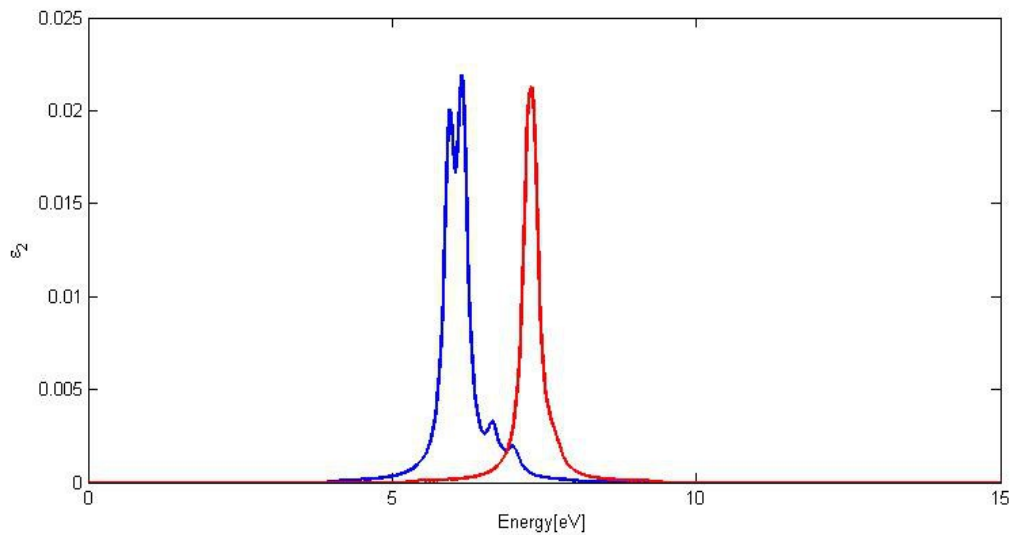


Figure 5.28 Optical spectrum of GaN embedded in planar AlN for wavevector z , $n = 1$

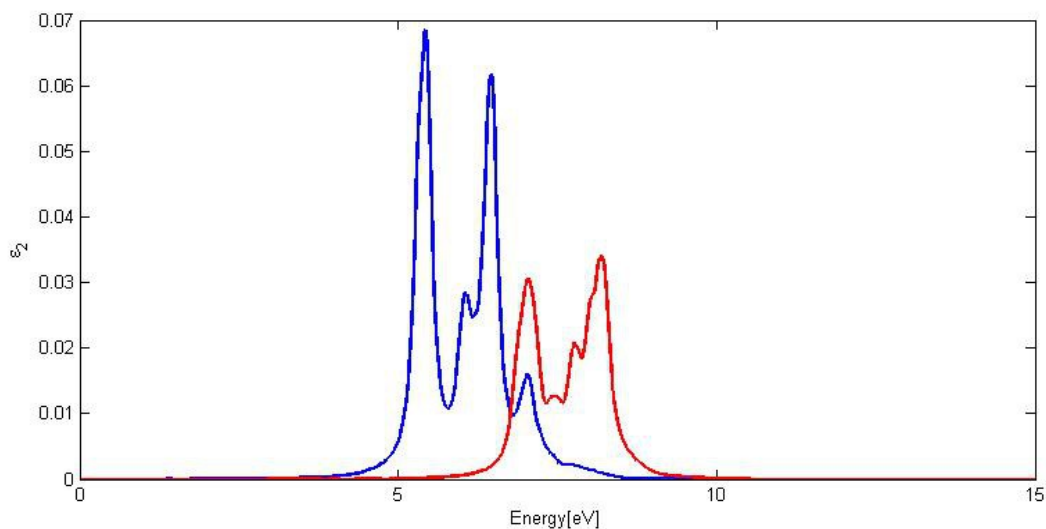


Figure 5.29 Optical spectrum of GaN embedded in planar AlN for wavevector z , $n = 2$

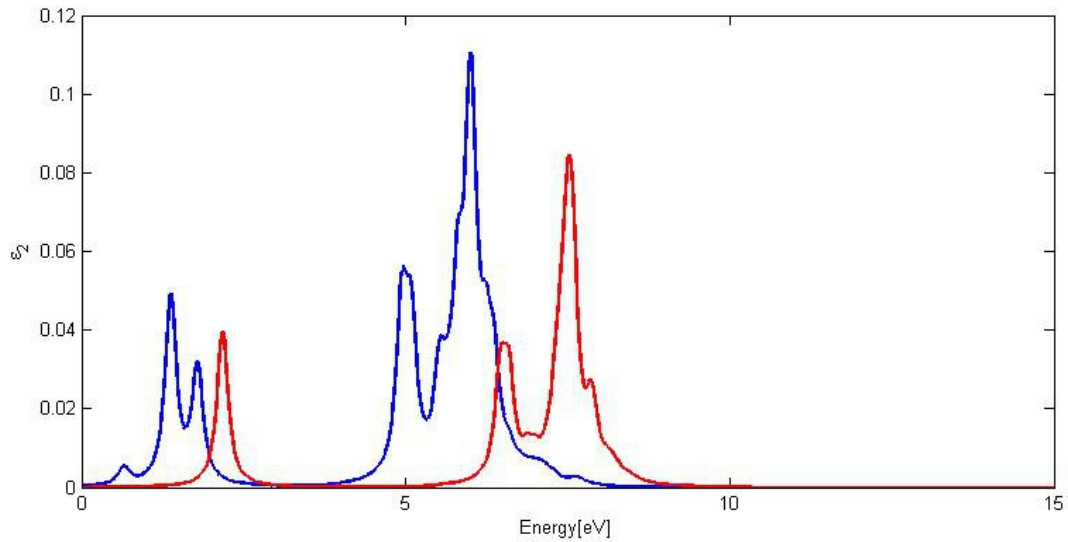


Figure 5.30 Optical spectrum of GaN embedded in planar AlN for wavevector z , $n = 3$

One can see that for $n = 1$, a double peak emerges at 5.95 eV and 6.14 eV, for $n = 2$ one has peaks at 5.43 eV and 6.45 eV, and in case of $n = 3$ peaks emerge at 1.37 eV and 6 eV. Thus the positions of the peaks move to lower energies for increasing n . This is logical in physical sense, as the spectrum of planar GaN is located at lower frequencies than that of planar AlN, and the influence of GaN increases with higher n .

For the other wavevectors, the optical spectra are :

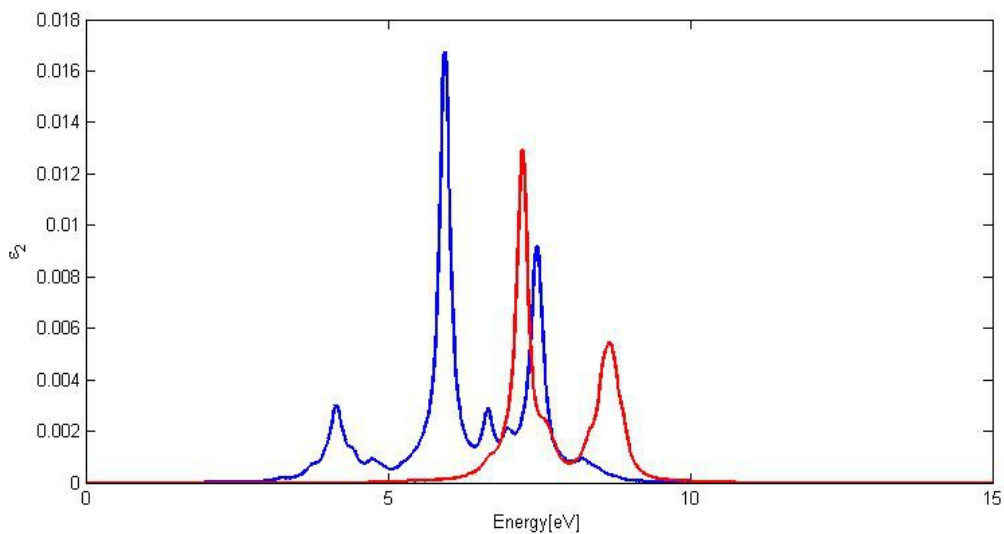


Figure 5.31 Optical spectrum of GaN embedded in planar AlN for wavevector y , $n = 1$

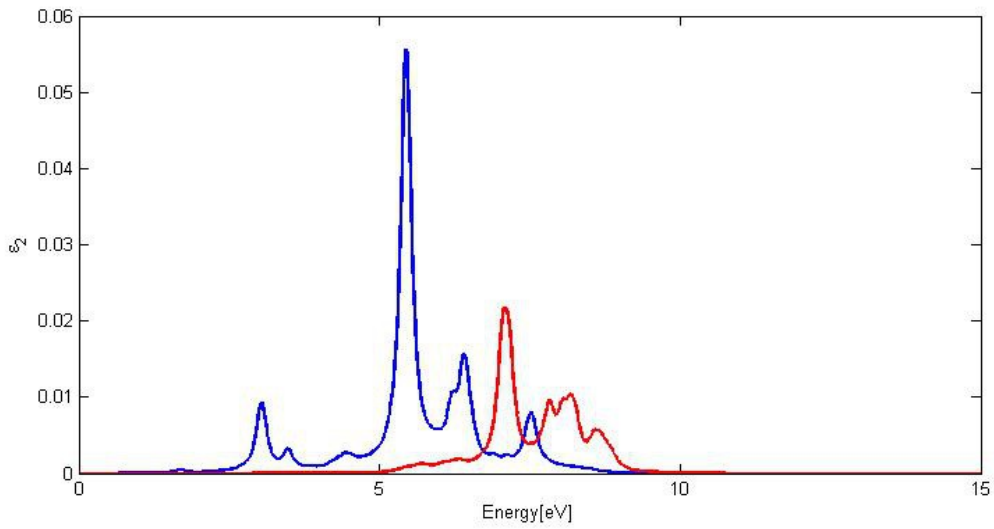


Figure 5.32 Optical spectrum of GaN embedded in planar AlN for wavevector y , $n = 2$

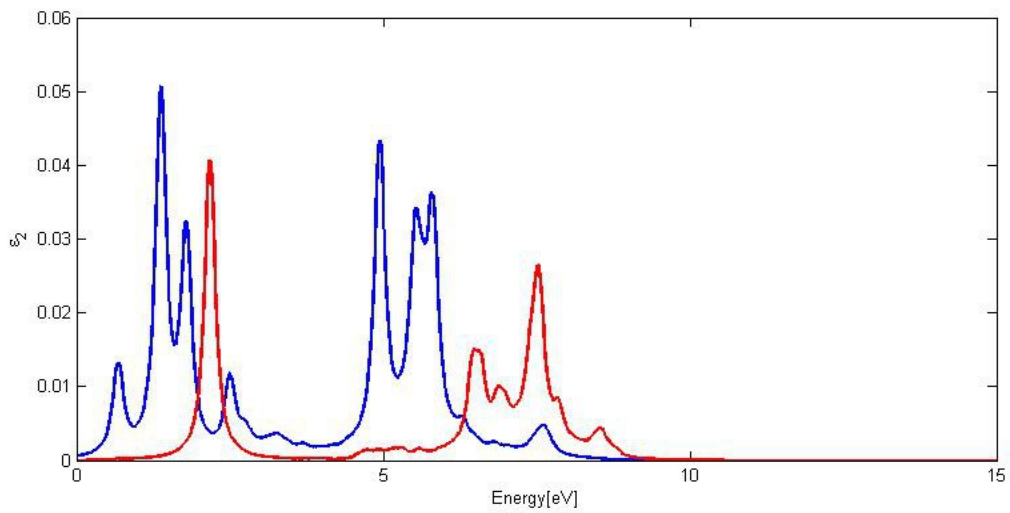


Figure 5.33 Optical spectrum of GaN embedded in planar AlN for wavevector y , $n = 3$

and for wavevector x :

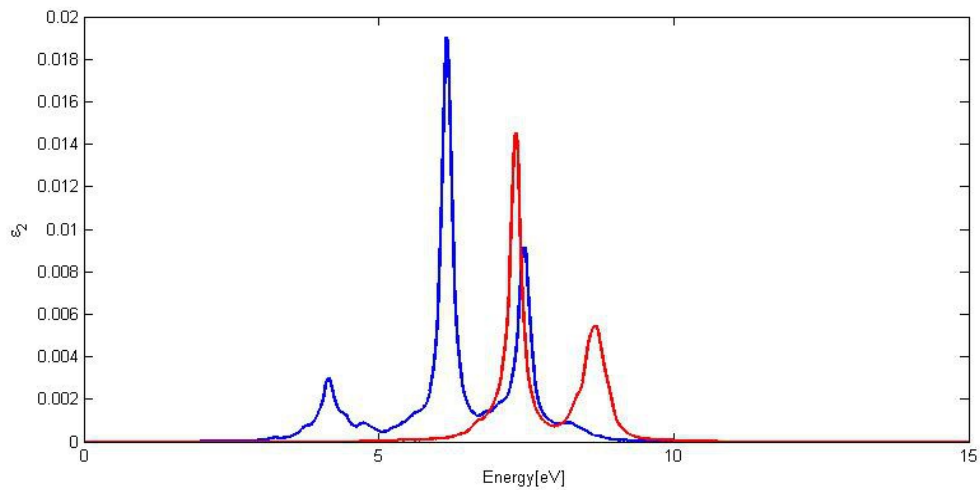


Figure 5.34 Optical spectrum of GaN embedded in planar AlN for wavevector x , $n = 1$

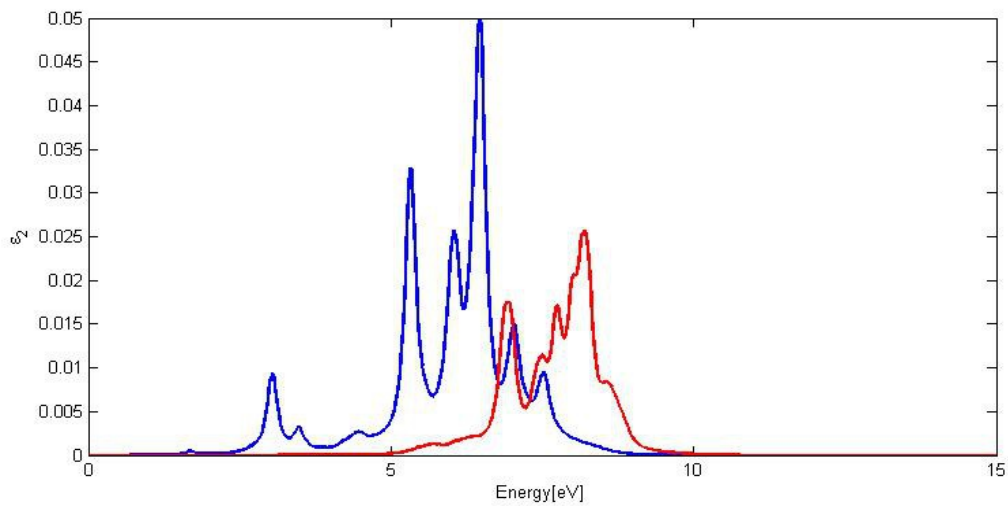


Figure 5.35 Optical spectrum of GaN embedded in planar AlN for wavevector x , $n = 2$

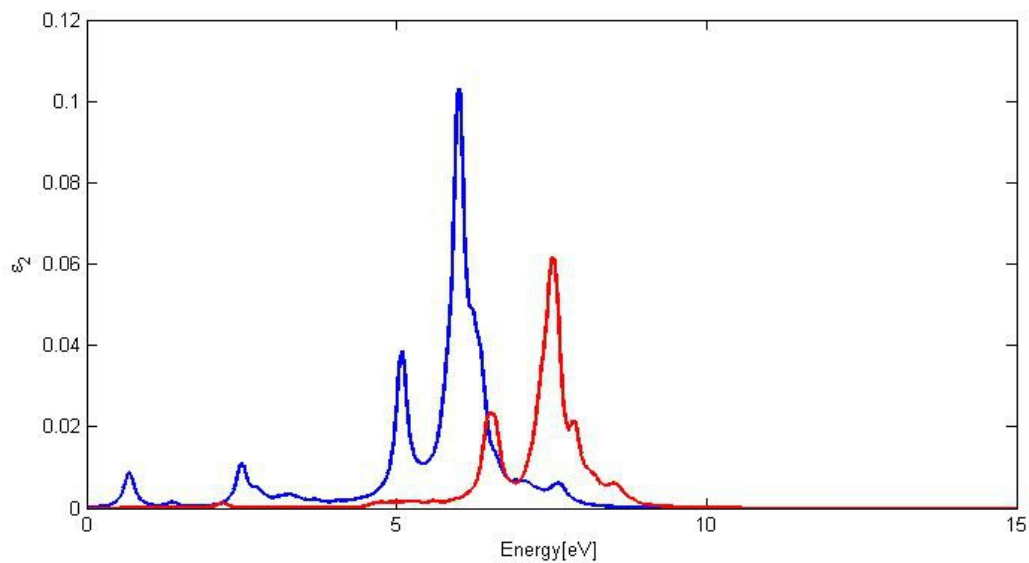


Figure 5.36 Optical spectrum of GaN embedded in planar AlN for wavevector x , $n = 3$

One realizes that the spectra belonging to wavevector x are more concentrated in higher frequencies, whereas the spectra for wavevector show stronger response at lower frequencies. This trend becomes stronger for higher n . Their superpositions result in the spectra for wavevector z , which can be seen visually from the figures shown above.

6. Summary

In this work, several nanostructures have been analyzed using *ab initio* simulations. The materials investigated can be divided in three types, firstly planar nanostructures, secondly the nanotubes corresponding to these planar systems, and finally the heterostructures of planar nanosystems. All calculations start with DFT, which provided the basic electronic structure. Following this, the resulting band structure undergoes corrections by GWA. The final step of all calculations was computing the dielectric function. Thereby the electron-hole interaction was taken into account using the Bethe-Salpeter equation.

We started with planar graphene-like structures. Graphene and silicene showed to possess basically the same electronic structure, which is plausible as both are hexagonal lattices with only one type of atom. Then we considered hexagonal lattices consisting of boron and another element. A clear relationship between the band gap size and the atomic number of the second element could be observed, namely the band gap decreases with increasing atomic number of the second element. The same behavior could be seen for the optoelectronic materials. At the end, we considered planar SiC and GeC. Planar SiC revealed a slightly larger band gap than GeC. GWA corrections were very significant for all planar systems, which is typical for spatially confined systems. As these contain a lot of vacuum, dielectric screening is weaker than for bulk systems, and the self energy is proportional to its inverse.

Next, we took a look at the nanotubes corresponding to the planar nanostructures. All nanotubes exhibited a larger band gap than their planar counterparts, most extremely in the case of carbon nanotubes, where graphene does not have any band gap. Furthermore, we found that the band gap size declines for bigger nanotube diameter. The same behavior takes place regarding the strength of the GWA corrections, which get weaker for larger nanotubes.

The last type of systems considered in this work were heterostructures of planar nanomaterials. We investigated boron nitride embedded in graphene and GaN embedded in planar AlN. The size of the embedded material was varied. Before starting DFT band structure calculations, we first determined the position of the atoms using SIESTA. Then we obtained interesting results for the electronic structure and the optical spectrum. In both cases, the band gap was surprisingly large for $n=1$, then got smaller for $n=2$, and rose again for $n=3$. The large band gap for $n = 1$ can be explained by the strong distortion caused by a very thin stripe of a material which is completely surrounded by another material. However, the optical spectra give a clear picture about the relationship between the position of peaks and the width of the embedded stripe. For bigger width of the embedded stripe, the position of peaks moved to higher frequencies. This makes sense as the optical spectrum of the embedded is located at higher frequencies than that of the surrounding material.

So one can see the crucial role *ab initio* simulations play for nanotechnology. They offer the ability to predict properties of nanomaterials before these have been synthesized and measured. Using relaxation of atom positions allows one to calculate the structure of a nanomaterial which is a combination of two different ones. GWA is very important especially for

nanomaterials in comparison to bulk crystals, as their spatial confinement causes strong corrections by GWA. Finally, the optical response can be described successfully by the widely used Bethe-Salpeter equation, taken the electron-hole interaction into account. So investigating future nanomaterials with the help of simulations will be very amazing.....

References

- [1] <http://accelrys.com/products/materials-studio/>
- [2] <http://www.quantumwise.com/applications>
- [3] Czycholl, "Theoretische Festkörperphysik" , 3rd edition, 2007
- [4] Rohlfing, M. und S. G. Louie: Electron-hole excitations and optical spectra from first principles. Phys. Rev. B, 62(8):4927{4944, Aug 2000.
- [5] Rohlfing, M., P. Krüger und J. Pollmann: Efficient scheme for GW quasiparticle band-structure calculations with applications to bulk Si and to the Si(001)-(2x1) surface. Phys. Rev. B, 52(3):1905{1917, Jul 1995.
- [6] Rohlfing, M.: Quasiteilchen-Bandstrukturen von Halbleitern und Halbleiter-Oberflächen. Doktorarbeit, Universität Münster, 1996
- [7] <http://icmab.cat/leem/siesta/>
- [8] http://www.nobelprize.org/nobel_prizes/physics/laureates/2010/press.html
- [9] Novoselov, K. S. et al. (2004). "Electric Field Effect in Atomically Thin Carbon Films" Science 306 (5696): 666-9
- [10] Oshima, C. and Nagashima, A. (1997). "Ultra-thin epitaxial films of graphite and hexagonal boron nitride on solid surfaces" J. Phys.: Condens. Matter 9: 1.
- [11] Wallace, P. R. (1947) "The Band Theory of Graphite" Physical Review 71 (9): 622.
- [12] H.P. Boehm, R. Setton, E. Stumpp (1994) "Nomenclature and terminology of graphite intercalation compounds" Pure and Applied Chemistry 66(9): 1893-1901.

[13] H.P. Boehm, A.Clauss, G. O. Fischer, U.Hofmann (1962) "Das Adsorptions-verhalten sehr dünner Kohlenstoffolien". *Zeitschrift für anorganische und allgemeine Chemie* 316 (3-4): 119-127

[14] Raji Heyrovská(2008) "Atomic Structures of Graphene, Benzene and Methane with Bond Lengths as Sums of the Single, Double and Resonance Bond Radii of Carbon"

[15] Geim, A.K. And Novoselov, "The rise of graphene", *Nature Materials* 6(3): 183-191.

[16] O.B. Shenderova, V.V. Zhirnov, D.W.Brenner (2002) "Carbon Nanostructures" *Critical Reviews in Solid State and Materials Sciences* 27 (3-4): 227.

[17] Charlier, J.-C.; Eklund, P.C. ; Zhu, J. and Ferrari, A.C. (2008). "Electron and Phonon Properties of Graphene: Their Relationship with Carbon Nanotubes" from *Carbon Nanotubes: Advanced Topics in the Synthesis, Structure Properties and Applications*, Ed. A. Jorio, G.Dresselhaus, and M.S.Dresselhaus. Berlin/Heidelberg: Springer-Verlag.

[18] Kuzmenko, A. B.; van Heumen, E.; Carbone, F.; van der Marel, D. (2008). "Universal infrared conductance of graphite". *Phys Rev Lett* 100 (11): 117401.

[19] Bao, Qiaoliang et al. (2009). "[Atomic-Layer Graphene as a Saturable Absorber for Ultrafast Pulsed Lasers](#)". *Advanced Functional Materials* 19 (19): 3077.

[20] Zhang, H.*et al.*; Bao; Tang; Zhao; Loh (2009)."[Large energy soliton erbium-doped fiber laser with a graphene-polymer composite mode locker](#)". *Applied Physics Letters* 95 (14): P141103.

[21] Zheng, Z. *et al.* (2012). "[Microwave and optical saturable absorption in graphene](#)" (PDF). *Optics Express* 20 (21): 23201–23214.

[22] Ekiz, O.O., et al. (2011). "Reversible Electrical Reduction and Oxidation of Graphene Oxide". *ACS Nano* 5 (4): 2475–2482.

[23] Ekiz, O.O., et al. (2011). "Supporting information for Reversible Electrical Reduction and Oxidation of Graphene Oxide". *ACS Nano* 5 (4): 2475–2482.

- [24] K.V.Sreekanth *et al.*; Zeng, Shuwen; Shang, Jingzhi; Yong, Ken-Tye; Yu, Ting (2012). "Excitation of surface electromagnetic waves in a graphene-based Bragg grating". *Scientific Reports* **2**.
- [25] http://www.nobelprize.org/nobel_prizes/physics/laureates/2010/advanced-physicsprize2010.pdf
- [26] Lee, C. *et al.* (2008). "Measurement of the Elastic Properties and Intrinsic Strength of Monolayer Graphene". *Science* **321** (5887): 385–8
- [27] Sanderson, Bill (2008-08-25). "Toughest Stuff Known to Man: Discovery Opens Door to Space Elevator". nypost.com. Retrieved 2008-10-09.
- [28] "Breakthrough in Developing Super-Material Graphene". ScienceDaily. 2010-01-20. Retrieved 2010-02-21.
- [29] <http://newsroom.uts.edu.au/news/2011/04/a-breakthrough-on-paper-thats-stronger-than-steel>
- [30] Chen, J., Ishigami, M., Jang, C., Hines, D. R., Fuhrer, M. S., and Williams, E. D. (2007). "Printed graphene circuits". *Advanced Materials* **19** (21): 3623–3627.
- [31] Ponomarenko, L. A. *et al.* (2008). "Chaotic Dirac Billiard in Graphene Quantum Dots". *Science* **320** (5874): 356–8.
- [32] "Graphene transistors clocked at 26 GHz Arxiv article". Arxivblog.com. 2008-12-11. Retrieved 2009-08-15.
- [33] Wang, X.; Li, X.; Zhang, L.; Yoon, Y.; Weber, P. K.; Wang, H.; Guo, J.; Dai, H. (2009). "N-Doping of Graphene Through Electrothermal Reactions with Ammonia". *Science* **324** (5928): 768–71.
- [34] Traversi, F.; Russo, V.; Sordan, R. (2009). "Integrated complementary graphene inverter". *Appl. Phys. Lett.* **94** (22): 223312.
- [35] Wang, X.; et al. (2007). "Transparent, Conductive Graphene Electrodes for Dye-

Sensitized Solar Cells". *Nano Letters* **8** (1): 323–7.

[36] Eda G, Fanchini G, Chhowalla M (2008). "Large-area ultrathin films of reduced graphene oxide as a transparent and flexible electronic material". *Nat Nanotechnol* **3** (5): 270–4.

[37] Wu, J.B.; et al. (2010). "Organic Light-Emitting Diodes on Solution-Processed Graphene Transparent Electrodes". *ACS Nano* **4**: 43.

[38] Mukhopadhyay, Prithu (2013). *Graphite, Graphene and their Polymer Nanocomposites*. Boca Raton, Florida: Taylor & Francis Group. pp. 202–213.

[39] Mukhopadhyay, Prithu (2013). *Graphite, Graphene and their Polymer Nanocomposites*. Boca Raton, Florida: Taylor & Francis Group. p. 211.

[40] <http://inhabitat.com/graphene-based-solar-cells-could-yield-60-efficiency/>

[41] Dan, Yaping; Lu, Ye; Kybert, Nicholas J.; Luo, Zhengtang; Johnson, A. T. Charlie (4 2009). "Intrinsic Response of Graphene Vapor Sensors". *Nano Letters* **9**(4): 1472–1475.

[42] Schedin, F. *et al.* (2007). "Detection of individual gas molecules adsorbed on graphene". *Nature Mater* **6**(9): 652–655.

[43] Stoller, Meryl D.; Sungjin Park, Yanwu Zhu, Jinho An, and Rodney S. Ruoff (2008). ["Graphene-Based Ultracapacitors"](#) (PDF). *Nano Lett* **8** (10): 3498–502.

[44] Mohanty, Nihar; Vikas Berry (2008). "Graphene-based Single-Bacterium Resolution Biodevice and DNA-Transistor – Interfacing Graphene-Derivatives with Nano and Micro Scale Biocomponents". *Nano Letters* **8** (12): 4469–76.

[45] Xu, M. S. Xu; D. Fujita and N. Hanagata (2009). "Perspectives and Challenges of Emerging Single-Molecule DNA Sequencing Technologies". *Small* **5** (23): 2638–49.

[46] "Carbon Wonderland". *Scientific American*. April 2008. Retrieved 2009-05-05. ".. bits of graphene are undoubtedly present in every pencil mark"

- [47] Geim, A. K. & MacDonald, A. H. (2007). "Graphene: Exploring carbon flatland". *Physics Today* **60** (8): 35–41.
- [48] Sutter, P. (2009). "Epitaxial graphene: How silicon leaves the scene". *Nature Materials* **8** (3): 171–2.
- [49] Ohta, T. *et al.* (2007). "Interlayer Interaction and Electronic Screening in Multilayer Graphene Investigated with Angle-Resolved Photoemission Spectroscopy". *Physical Review Letters* **98** (20): 206802.
- [50] Bostwick, A. *et al.* (2007). "Symmetry breaking in few layer graphene films". *New Journal of Physics* **9** (10): 385.
- [51] Zhou, S.Y. *et al.* (2006). "First direct observation of Dirac fermions in graphite". *Nature Physics* **2** (9): 595–599.
- [52] Yenny Hernandez *et al.* (2008). " High-yield production of graphene by liquid-phase exfoliation of graphite" . *Nature Nanotechnology* **3**, 563 - 568 (2008)
- [53] Alberto Mariani *et al.* (2011) "Graphene-containing thermoresponsive nanocomposite hydrogels of poly(N-isopropylacrylamide) prepared by frontal polymerization " *J. Mater. Chem.*, 2011,**21**, 8727-8733.
- [54] Alberto Mariani *et al.* (2011) " High concentration few-layer graphene sheets obtained by liquid phase exfoliation of graphite in ionic liquid " *J. Mater. Chem.*, 2011,**21**, 3428-3431.
- [55] Chakrabarti, A; Lu, J.; Skrabutenas, J. C.; Xu, T.; Xiao, Z.; Maguire, J. A.; Hosmane, N. S. (2011). "Conversion of carbon dioxide to few-layer graphene". *Journal of Materials Chemistry* **21** (26): 9491–9493.
- [56] <http://www.graphenetechnologies.com/>
- [57] Stankovich, S.; Piner, R. D.; Chen, X.; Wu, N.; Nguyen, S. T.; Ruoff, R. S. (2006).

"Stable aqueous dispersions of graphitic nanoplatelets via the reduction of exfoliated graphite oxide in the presence of poly(sodium 4-styrenesulfonate)". *Journal of Materials Chemistry* **16** (2): 155.

[58] Gómez-Navarro, C.; Weitz, R. T.; Bittner, A. M.; Scolari, M.; Mews, A.; Burghard, M.; Kern, K. (2007). "Electronic Transport Properties of Individual Chemically Reduced Graphene Oxide Sheets". *Nano Letters* **7** (11): 3499–3503.

[59] Cote, L. J.; Cruz-Silva, R.; Huang, J. (2009). "Flash Reduction and Patterning of Graphite Oxide and Its Polymer Composite". *Journal of the American Chemical Society* **131** (31): 11027–11032.

[60] Gómez-Navarro, C.; Weitz, R. T.; Bittner, A. M.; Scolari, M.; Mews, A.; Burghard, M.; Kern, K. (2007). "Electronic Transport Properties of Individual Chemically Reduced Graphene Oxide Sheets". *Nano Letters* **7** (11): 3499–3503.

[61] El-Kady, M. F.; Strong, V.; Dubin, S.; Kaner, R. B. (2012). "Laser Scribing of High-Performance and Flexible Graphene-Based Electrochemical Capacitors". *Science* **335** (6074): 1326–1330.

[62] M. Corso *et al.* (2004). "Boron Nitride Nanomesh". *Science* **303** (5655): 217–220.

[63] A. Goriachko *et al.*; He, Y; Knapp, M; Over, H; Corso, M; Brugger, T; Berner, S; Osterwalder, J *et al.* (2007). "Self-assembly of a hexagonal boron nitride nanomesh on Ru(0001)". *Langmuir Lett.* **23** (6): 2928–2931.

[64] S. Berner, M. Corso *et al.* (2007). "Boron Nitride Nanomesh: Functionality from a Corrugated Monolayer". *Angew. Chem. Int. Ed.* **46** (27): 5115–5119.

[65] R. Widmer *et al.*; Berner, S; Groning, O; Brugger, T; Osterwalder, J; Greber, T (2007). "Electrolytic in situ STM investigation of h-BN-Nanomesh". *Electrochem. Comm.* **9** (10): 2484–2488.

[66] G. G. Guzman-Verri and L. C. Lew Yan Voon (2007). "Electronic structure of silicon-based nanostructures". *Physical Review B* **76** (7): 075131.

- [67] B. Aufray, A. Kara, S. Vizzini, H. Oughaddou, C. Léandri, B. Ealet and G. Le Lay (2010). "Graphene-like silicon nanoribbons on Ag(110): A possible formation of silicene". *Applied Physics Letters* **96**: 183102.
- [68] B. Lalmi, H. Oughaddou, H. Enriquez, A. Kara, S. Vizzini, B. Ealet and B. Aufray (2010). "Epitaxial growth of a silicene sheet". *Applied Physics Letters* **97**: 223109.
- [69] Deepthi Jose, Ayan Datta (2011). "Structures and Electronic Properties of Silicene clusters: A promising material for FET and hydrogen storage". *Phys. Chem. Chem. Phys.* **13**: 7304.
- [70] Monthieux, Marc; Kuznetsov, V (2006). "[Who should be given the credit for the discovery of carbon nanotubes?](#)" (PDF). *Carbon* **44** (9): 1621.
- [71] Радужкевич, Л. В. (1952). "[О Структуре Углерода, Образующегося При Термическом Разложении Окиси Углерода На Железном Контакте](#)" (PDF). *Журнал Физической Химии* (in Russian) **26**: 88–95.
- [72] Abrahamson, John; Wiles, Peter G.; Rhoades, Brian L. (1999). "Structure of Carbon Fibers Found on Carbon Arc Anodes". *Carbon* **37** (11): 1873.
- [73] Izvestiya Akademii Nauk SSSR, Metals. 1982, #3, pp.12–17 (in Russian)
- [74] Yu, M.-F.; Lourie, O; Dyer, MJ; Moloni, K; Kelly, TF; Ruoff, RS (2000). "Strength and Breaking Mechanism of Multiwalled Carbon Nanotubes Under Tensile Load". *Science* **287** (5453): 637–640.
- [75] Peng, B.; Locascio, Mark; Zapol, Peter; Li, Shuyou; Mielke, Steven L.; Schatz, George C.; Espinosa, Horacio D. (2008). "Measurements of near-ultimate strength for multiwalled carbon nanotubes and irradiation-induced crosslinking improvements". *Nature Nanotechnology* **3** (10): 626–631.
- [76] Collins, P.G. (2000). "Nanotubes for Electronics". *Scientific American*: 67–69.
- [77] Popov, M.; Kyotani, M.; Nemanich, R.; Koga, Y. (2002). "Superhard phase composed

of single-wall carbon nanotubes". *Phys. Rev. B* **65** (3): 033408.

[78] Lu, X.; Chen, Z. (2005). "Curved Pi-Conjugation, Aromaticity, and the Related Chemistry of Small Fullerenes (C₆₀) and Single-Walled Carbon Nanotubes". *Chemical Reviews* **105** (10): 3643–3696.

[79] Pop, Eric; Mann, David; Wang, Qian; Goodson, Kenneth; Dai, Hongjie (2005-12-22). "Thermal conductance of an individual single-wall carbon nanotube above room temperature". *Nano Letters* **6** (1): 96–100.

[80] Sinha, Saion; Barjami, Saimir; Iannacchione, Germano; Schwab, Alexander; Muench, George (2005-06-05). "Off-axis thermal properties of carbon nanotube films". *Journal of Nanoparticle Research* **7** (6): 651–657.

[81] Thostenson, Erik; Li, C; Chou, T (2005). "Nanocomposites in context". *Composites Science and Technology* **65** (3–4): 491–516.

[82] "Pirahna USV built using nano-enhanced carbon prepreg". *ReinforcedPlastics.com*. 19 February December 2009. Retrieved 25 February 2010.

[83] Pagni, John (5 March 2010). "Amroy aims to become nano-leader". *European Plastics News*. Retrieved 2010-11-21.

[84] Edwards, Brad C. (2003). *The Space Elevator*. BC Edwards. ISBN 0-9746517-1-0.

[85] Yildirim, T.; Gülseren, O.; Kılıç, Ç.; Ciraci, S. (2000). "Pressure-induced interlinking of carbon nanotubes". *Phys. Rev. B* **62** (19): 19.

[86] Postma, Henk W. Ch.; Teepen, T; Yao, Z; Grifoni, M; Dekker, C (2001). "Carbon Nanotube Single-Electron Transistors at Room temperature". *Science* **293** (5527): 76–9.

[87] Collins, Philip G.; Arnold, MS; Avouris, P (2001). "Engineering Carbon Nanotubes and Nanotube Circuits Using Electrical Breakdown". *Science* **292** (5517): 706–709.

[88] "Nanocables light way to the future". YouTube. September 9, 2011.

- [89] Zhao, Yao; Wei, Jinqun; Vajtai, Robert; Ajayan, Pulickel M.; Barrera, Enrique V. (September 6, 2011). "Iodine doped carbon nanotube cables exceeding specific electrical conductivity of metals". *Scientific Reports (Nature)* **1**.
- [90] "Beyond Batteries: Storing Power in a Sheet of Paper". EurekaAlert.org. August 13, 2007. Retrieved 2008-09-15.
- [91] "Paper battery offers future power". *BBC News*. August 14, 2007. Retrieved 2008-01-15.
- [92] Halber, Deborah. [MIT LEES on Batteries](#). Lees.mit.edu. Retrieved on 2012-06-06.
- [93] Bourzac, Katherine. "[Nano Paint Could Make Airplanes Invisible to Radar.](#)" Technology Review. MIT, 5 December 2011.
- [94] <http://www.nantero.com/>
- [95] S. Bamrungsap, J. A. Phillips, X. Xiong, Y. Kim, H. Wang, H. Liu, A. Hebard, and W. Tan, "Magnetically driven single DNA nanomotor," *Small*, vol. 7, no. 5, pp. 601-605, 2011.
- [96] T. E. Mallouk and A. Sen, "Powering nanorobots," *Scientific American*, May 2009, pp. 72-77
- [97] Bailey, S. W. D.; I. Amanatidis and C. J. Lambert (2008). "Carbon Nanotube Electron Windmills: A Novel Design for Nanomotors". *Physical Review Letters*. 256802 (25): 1–4.
- [98] Simmons, Trevor; Hashim, D; Vajtai, R; Ajayan, PM (2007). "Large Area-Aligned Arrays from Direct Deposition of Single-Wall Carbon Nanotubes". *J. Am. Chem. Soc.* **129** (33): 10088–10089.
- [99] Castelvechi, Davide (May 19, 2007). "[Spinning into control: High-tech reincarnations of an ancient way of storing energy](#)". *Science News* **171** (20): 312–313.

- [100] Hill, F A; Havel, T F; Hart, A J; Livermore, C (2010). "Storing elastic energy in carbon nanotubes". *Micromechanics and Microengineering* **20** (9): 104012–104019.
- [101] José-Yacamán, M.; Miki-Yoshida, M.; Rendón, L.; Santiesteban, J. G. (1993). "Catalytic growth of carbon microtubules with fullerene structure". *Appl. Phys. Lett.* **62** (6): 657.
- [102] Naha, Sayangdev, and Ishwar K. Puri (2008). "A model for catalytic growth of carbon nanotubes". *Journal of Physics D: Applied Physics* **41**: 065304.
- [103] Banerjee, Soumik, Naha, Sayangdev, and Ishwar K. Puri (2008). "Molecular simulation of the carbon nanotube growth mode during catalytic synthesis". *Applied Physics Letters* **92**: 233121.
- [104] Nami, Nobuhito; Ambri Mohamed, Mohd; Shikoh, Eiji; Fujiwara, Akihiko (2007). "[Synthesis-condition dependence of carbon nanotube growth by alcohol catalytic chemical vapor deposition method](#)" (PDF). *Sci. Technol. Adv. Mater.* **8** (4): 292.
- [105] N. Ishigami; Ago, H; Imamoto, K; Tsuji, M; Iakoubovskii, K; Minami, N (2008). "Crystal Plane Dependent Growth of Aligned Single-Walled Carbon Nanotubes on Sapphire". *J. Am. Chem. Soc.* **130**(30): 9918–9924.
- [106] Hata, K.; Futaba, DN; Mizuno, K; Namai, T; Yumura, M; Iijima, S (2004). "Water-Assisted Highly Efficient Synthesis of Impurity-Free Single-Walled Carbon Nanotubes". *Science* **306** (5700): 1362–1365
- [107] Iijima, Sumio (1991). "Helical microtubules of graphitic carbon". *Nature* **354** (6348): 56–58.
- [108] Ebbesen, T. W.; Ajayan, P. M. (1992). "Large-scale synthesis of carbon nanotubes". *Nature* **358**(6383): 220–222.
- [109] Guo, Ting; Nikolaev, Pavel; Rinzler, Andrew G.; Tomanek, David; Colbert, Daniel T.; Smalley, Richard E. (1995). "[Self-Assembly of Tubular Fullerenes](#)". *J. Phys. Chem.* **99** (27): 10694–10697.

- [110] Guo, Ting; Nikolaev, P; Thess, A; Colbert, D; Smalley, R (1995). "[Catalytic growth of single-walled nanotubes by laser vaporization](#)" (PDF). *Chem. Phys. Lett.* **243**: 49–54.
- [111] Kim, K.S.; Cota-Sanchez, German; Kingston, Chris; Imris, M.; Simard, Benoît; Soucy, Gervais (2007). "Large-scale production of single-wall carbon nanotubes by induction thermal plasma". *Journal of Physics D: Applied Physics* **40**: 2375.
- [112] O. O. Kit, T.Tallinen, L.Mahadevan, J.Timonen and P.Koskinen (2012). "Twisting graphene nanoribbons into carbon nanotubes" *Physical Review B*, 2012; 85 (8) .
- [113] Jean-Christophe Charlier, Xavier Blase, Stephan Roche (2007) . "Electronic and transport properties of nanotubes". *Rev. Mod. Phys.* 79, 677-732
- [114] Y. Zhao and D.G. Truhlar (2008). *Journal of Chemical Theory and Computation* **4**: 1849.
- [115] L. Hedin and S. Lundqvist, in *Solid State Physics, Advances in Research and Application*, edited by F. Seitz, D. Turnbull, and H. Ehrenreich (Academic, New York, 1969), Vol. 23, p. 1.
- [116] Michael Rohlfing (2010) "Electronic excitations from a perturbative LDA + GdW approach " *Physical Review B* 82, 205127.
- [117] G. Strinati, *Phys. Rev. Lett.* 49, 1519 (1982); *Phys. Rev. B* 29, 5718 (1984); *Rivista del Nouvo Cimento* 11, 1 (1988).
- [118] M. Rohlfing, P. Krüger, and J. Pollmann, *Efficient scheme for GW quasiparticle band-structure calculations with applications to bulk Si and to the Si(001)-(2×1) surface*, *Phys. Rev. B* 52, 1905 (1995).
- [119] A.Mahmood, L.Enrique Sansores "Band structure and bulk modulus calculations of germanium carbide " *J. Mater. Res.* , Vol. 20 , No. 5 . May 2005

